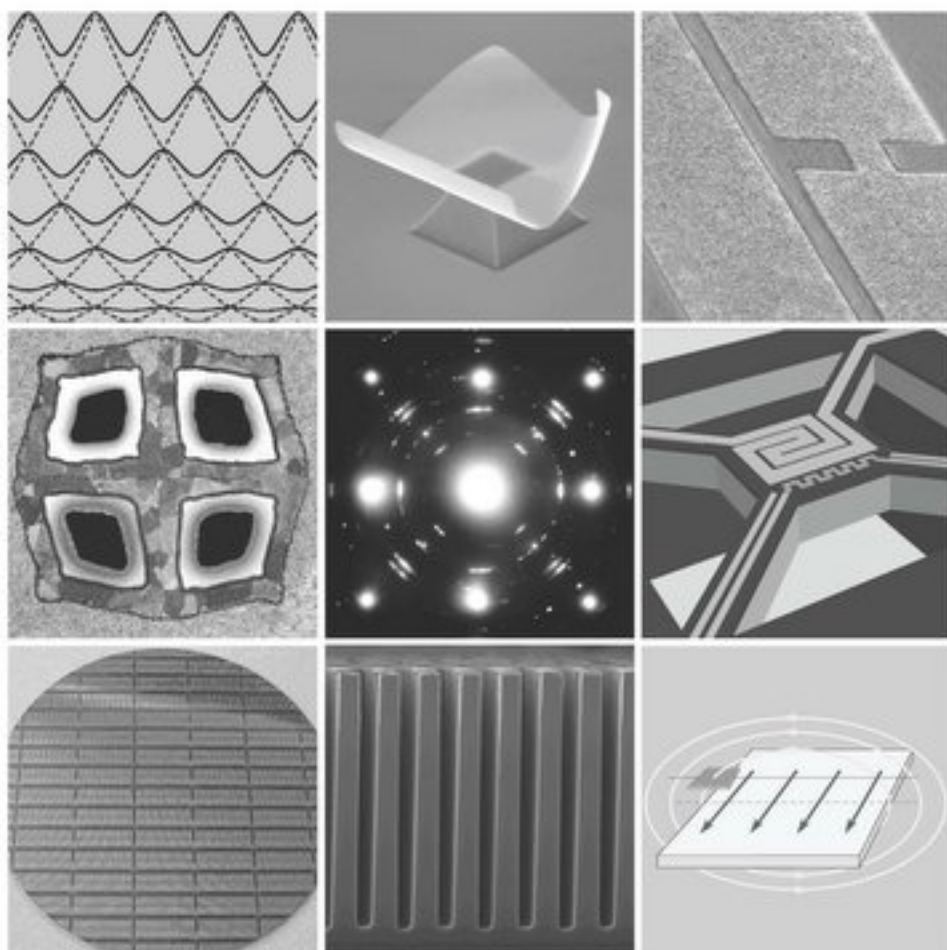


INSTITUTE OF ELECTRICAL ENGINEERING

SLOVAK ACADEMY OF SCIENCES



BIENNIAL REPORT 2007 - 2008

INSTITUTE OF ELECTRICAL ENGINEERING

SLOVAK ACADEMY OF SCIENCES

BIENNIAL REPORT

1. January 2007 – 31. December 2008

Institute of Electrical Engineering
Slovak Academy of Sciences

Dúbravská cesta 9

841 04 BRATISLAVA, SLOVAK REPUBLIC

Phone: (# 421-2) 54775806

Fax: (# 421-2) 54775816

Homepage: www.elu.sav.sk

Edited by:

Marianna	Španková
Vladimír	Štrbík
Anton	Pevala
Peter	Eliáš
Edmund	Dobročka

Cover: Jakub Fröhlich

Photo: Anton Sládek

Bratislava 2009

Contents

I. GENERAL OVERVIEW	1
Organization Scheme of the Institute	2
Thematic Focus of the Institute	3
Summary of Scientific Output	5
PhD Study at the Institute	6
Funding of Research	6
Conferences	7
II. RESEARCH ACTIVITIES	9
Department of Superconductor Physics	10
Stabilized MgB ₂ composite wire with Ti barrier P. Kováč, I. Hušek, T. Melišek, and T. Holúbek	12
Filament and interface structure of in-situ MgB ₂ wires I. Hušek and P. Kováč	13
Electro-mechanical characterization of selected superconductors E. Kopera, P. Kováč, and T. Melišek	14
MgB ₂ cable made of two-axially rolled wires P. Kováč, I. Hušek, and T. Melišek	15
Coupling losses in coated conductors at industrial frequencies S. Takács	16
Calculation of critical state in superconducting/ferromagnetic composite tapes F. Gömöry, M. Vojenčiak, E. Pardo, and J. Šouc	17
Theoretical and experimental study of AC loss in high-temperature superconducting pancake coils E. Pardo, J. Šouc, M. Vojenčiak, and F. Gömöry	18
Performance improvement of superconducting tapes due to ferromagnetic cover on edges M. Vojenčiak, J. Šouc, and F. Gömöry	20
AC susceptibility measurements of superconductors in high magnetic fields at various temperatures L. Frolek, E. Seiler, and F. Gömöry	21
Department of the Electrodynamics of Superconductors	22
The current distribution in a striated YBCO tape subjected to both a magnetization and a transport current P. Ušák, M. Polák, E. Demenčík, and J. Kvitkovič	24
Current distribution in thermally degraded superconductor of 2 nd generation P. Ušák, M. Polák, and E. Demenčík	25
Current distribution in the winding of a superconducting coil P. Ušák, M. Polák, J. Kvitkovič, and P. Mozola	26
Distribution of magnetic field inside the winding of a BSCCO coil J. Kvitkovič, M. Polák, and P. Mozola	27
Hall probe based system for study of AC transport current distribution in YBCO coated conductors E. Demenčík, P. Ušák, and M. Polák	28

Frequency dependence of AC loss in YBCO tapes and pancake coils M. Polák	29
Department of Cryoelectronics	30
YBa ₂ Cu ₃ O _x films prepared on advanced semiconductor substrates Š. Chromik, M. Španková, Š. Gaži, T. Lalinský, and I. Vávra	32
Epitaxial LSMO films grown on GaAs substrates with MgO buffer layer M. Španková, Š. Chromik, I. Vávra, V. Štrbík, and P. Lobotka	33
Transport and magnetic properties of LSMO thin films grown on MgO single-crystalline substrates V. Štrbík and M. Španková	34
Thin film HTS / FM / HTS heterostructures V. Štrbík and Š. Beňačka	35
Influence of the buffer layer on the growth of superconducting films based on mercury M. Sojková, Š. Chromik, V. Štrbík, and M. Polák	36
The influence of the rhenium in the precursor film on the properties of the thin superconducting films based on thallium A. Dujavová, M. Sojková-Valeriánová, V. Štrbík, Š. Chromik, and M. Polák	37
YBa ₂ Cu ₃ O _x bi-epitaxial junctions on the substrate with axis tilted out-of-plane Š. Beňačka and V. Štrbík	38
The influence of technological process on magnetic properties of MgB ₂ films Š. Chromik and V. Štrbík	39
Growth of thin aluminium oxide films for microelectronic applications Š. Gaži, D. Gregušová, and R. Stoklas	40
Department of Superlattices	42
Polymer based nanocomposites with carbon nano-fillers Z. Križanová, I. Vávra, and P. Lobotka	44
Multilayered metal/insulator metamaterials I. Vávra and J. Dérer	45
Structural stability of metal oxide sensors V. Šmatko, E. Kováčová, and V. Štrbík	46
Department of Thin Oxide Films	48
Growth of thin oxide films by liquid injection metal organic chemical vapour deposition K. Hušeková, K. Čičo, R. Lupták, E. Dobročka, A. Rosová, D. Machajdík, and K. Fröhlich	50
High growth rate deposition of ruthenium films by liquid injection atomic layer deposition K. Hušeková, E. Dobročka, A. Rosová, J. Martaus, D. Machajdík, and K. Fröhlich	51
Characterization of thin oxide films by X-ray diffraction and X-ray reflectivity E. Dobročka, K. Čičo, K. Hušeková, A. Rosová, and K. Fröhlich	52
Contribution of Rutherford backscattering spectroscopy to thin oxide films characterization D. Machajdík, K. Hušeková, and K. Fröhlich	53
Effect of forming gas annealing on stability of RuO ₂ -rich Ru-Si-O polycrystalline gate electrodes A. Rosová, M. Ťapajna, E. Dobročka, V. Štrbík, Š. Gaži, and K. Fröhlich	54
Work function thermal stability of RuO ₂ -rich Ru-Si-O p-channel metal-oxide-semiconductor field-effect transistor gate electrodes M. Ťapajna, A. Rosová, E. Dobročka, V. Štrbík, Š. Gaži, and K. Fröhlich	55

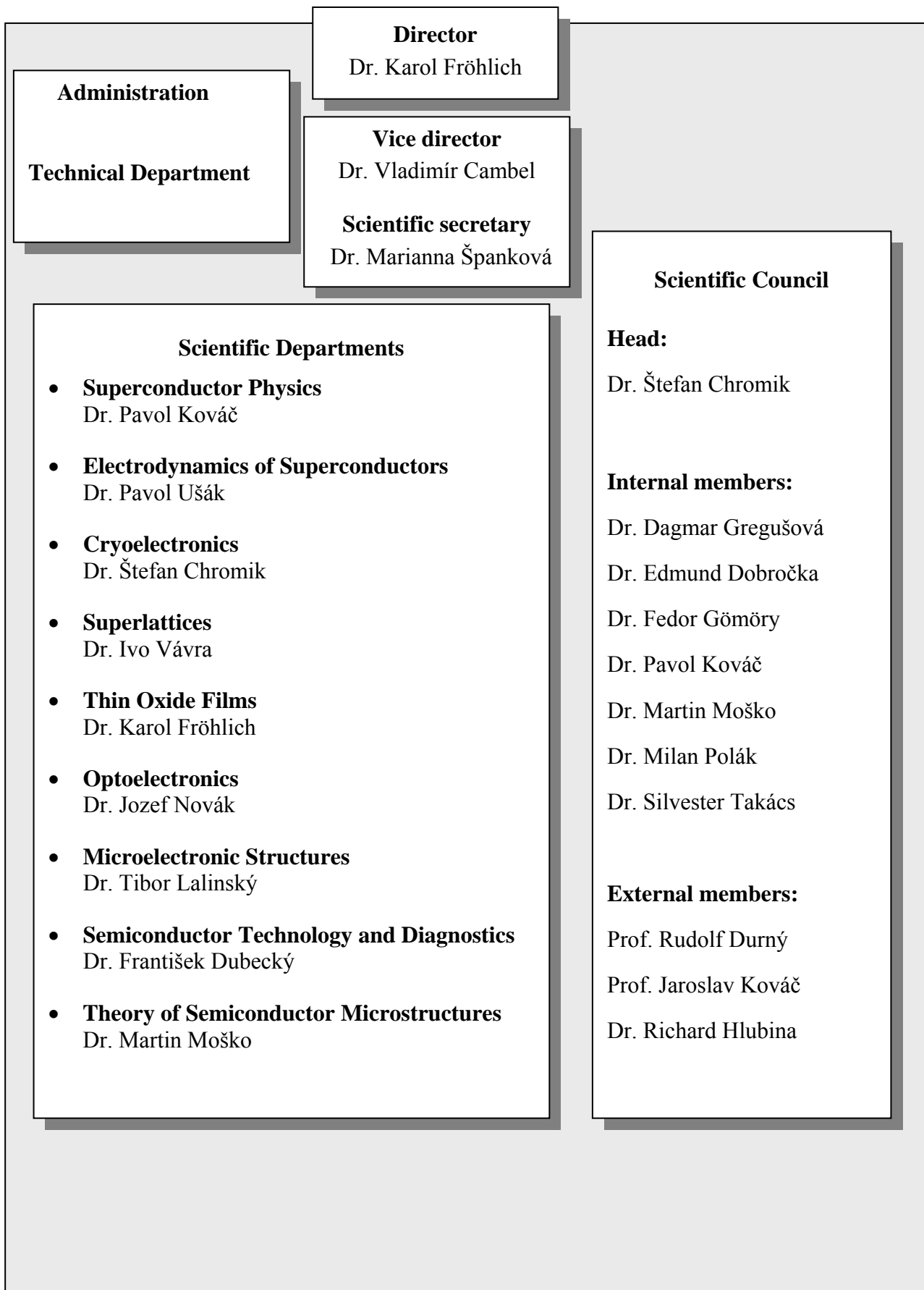
Evidence of hafnia oxygen vacancy defects in MOCVD grown $\text{Hf}_x\text{Si}_{1-x}\text{O}_y$ ultrathin gate dielectrics gated with Ru electrode	56
M. Ľapajna, A. Rosova, K. Hušekova, E. Dobročka, and K. Fröhlich	
Effect of Ti doping on Ta_2O_5 stacks with Ru and Al gates	57
M. Ľapajna, E. Dobročka, and K. Fröhlich	
Growth of high-dielectric-constant TiO_2 films in capacitors with RuO_2 electrodes	58
K. Fröhlich, M. Ľapajna, A. Rosova, E. Dobročka, B. Hudec, and K. Hušekova	
Leakage currents in $\text{RuO}_2/\text{TiO}_2/\text{RuO}_2$ structures with high-dielectric-constant TiO_2 rutile films	59
K. Fröhlich, M. Ľapajna, A. Rosova, E. Dobročka, and K. Hušekova	
Transmission electron microscopy of epitaxially grown $\text{RuO}_2/\text{TiO}_2/\text{RuO}_2$ structures	60
A. Rosova, K. Fröhlich, M. Ľapajna, E. Dobročka, and K. Hušekova	
Al_2O_3 insulating films grown by MOCVD using Ar or NH_3 carrier gas on InAlN/GaN heterostructures	61
K. Čičo, J. Kuzmık, K. Hušekova, and K. Fröhlich	
Current conduction and saturation in III-nitride MOS HEMTs	62
J. Kuzmık, K. Čičo, and K. Fröhlich	
Evaluation of the interface state density on Ni/ Al_2O_3 /InAlN/GaN and Ni/ ZrO_2 /InAlN/GaN MOS contacts	63
M. Ľapajna, K. Čičo, J. Kuzmık, and K. Fröhlich	
Department of Optoelectronics	64
Formation of AlGaAs/InGaP interfaces	66
R. Kudela, J. Šoltys, and M. Kučera	
50-nm local anodic oxidation technology of semiconductor heterostructures	67
J. Martaus, V. Cambel, D. Gregušova, R. Kudela, and J. Fedor	
Wet-etch revelation of {n11}-related facets in (100) GaAs at dynamic mask pattern edges	68
P. Eliaš, R. Kudela, and J. Novak	
Study of the growth and structural properties of InMnAs dots grown on high-index surfaces by MOVPE	69
J. Novak, P. Eliaš, J. Šoltys, S. Hasenöhr, and I. Vavra	
Technology of ‘active’ tips for magnetic and electric force microscopy	70
J. Šoltys, R. Kudela, M. Kučera, I. Vavra, J. Novak, and V. Cambel	
Photoluminescence diagnostics of AlGaAs/GaAs/AlGaAs QWs prepared on non-planar, wet-etch-formed objects of pyramidal shape	71
M. Kučera, J. Šoltys, R. Kudela, and V. Cambel	
Investigation of structural properties of GaAs based heterostructures by EDX and FIB	72
P. Štrichovanec, J. Novak, S. Hasenöhr, and I. Vavra	
Switching magnetization magnetic force microscopy – an alternative to conventional lift-mode MFM	73
V. Cambel, D. Gregušova, J. Fedor, J. Martaus, P. Eliaš, and R. Kudela	
On-tip sub-micrometer Hall probes for magnetic probe microscopy prepared by non-planar optical and AFM lithography	74
D. Gregušova, J. Martaus, J. Fedor, R. Kudela, and V. Cambel	
Micromagnetic permalloy element on a Hall probe: design and technology	75
P. Eliaš, V. Cambel, R. Kudela, Š. Gaži, J. Šoltys, and J. Martaus	
AlGaN/GaN metal-oxide-semiconductor heterostructure field-effect transistors with Al_2O_3 gate oxide	76
D. Gregušova, R. Stoklas, K. Čičo, Š. Gaži, J. Novak, and P. Kordoš	
Trapping effects in AlGaN/GaN-on-Si field-effect transistors by frequency dependent capacitance and conductance measurements	77
R. Stoklas, D. Gregušova, J. Novak, P. Kordoš, K. Čičo, and K. Fröhlich	

Influence of InMnAs layer on the properties of GaAs/AlGaAs MQW LEDs P. Telek, S. Hasenöhrl, J. Šoltýs, I. Vávra, and J. Novák	78
Department of Microelectronic Structures	80
Impact of SF ₆ plasma on performance of AlGaIn/GaN HEMT Structures T. Lalinský, G. Vanko, Š. Haščík, I. Rýger, and Ž. Mozolová	82
Surface acoustic wave excitation on SF ₆ plasma treated AlGaIn/GaN heterostructure T. Lalinský, I. Rýger, G. Vanko, Š. Haščík, and Ž. Mozolová	83
Polarization effects and energy band diagram in AlGaIn/GaN heterostructure J. Osvald	84
Numerical study of tunneling currents in GaN Schottky diodes J. Osvald	85
Department of Semiconductor Technology and Diagnostics	86
Development of mobile X-CT & SCAN system with monolithic GaAs detectors working in single photon counting and photon energy separation mode B. Zařko, F. Dubecký, and D. Korytár	88
Concept and performance of 2×64 channel input mini-module with monolithic semi-insulating GaAs two-line X-ray detectors coupled to DX64 ASICs B. Zařko, F. Dubecký, P. Boháček, M. Sekáčová, and J. Huran	89
Application of quantum digital X-ray scanner in CT reconstruction B. Zařko and F. Dubecký	90
Anomalous charge current transport in semi-insulating GaAs with a new quasi-ohmic metallization F. Dubecký, B. Zařko, P. Boháček, J. Huran, and M. Sekáčová	91
Basic parameters of a high resolution X-ray system with a microfocus source D. Korytár, P. Vagovič, F. Dubecký, and P. Boháček	92
Spectral-angular function of X-ray diffractive optics P. Vagovič and D. Korytár	93
Application of semi-insulating GaAs detectors in registration of fast neutrons emissions from hot plasmas F. Dubecký, B. Zařko, P. Boháček, M. Sekáčová, and J. Huran	94
Silicon carbon nitride thin films prepared by plasma enhanced chemical vapour deposition J. Huran and P. Boháček	95
Department of Theory of Semiconductor Microstructures	96
Persistent current in mesoscopic multichannel ring with disordered edges J. Feilhauer and M. Mořko	98
Persistent current in a ring made of the perfect crystalline insulator A. Mořková, M. Mořko, R. Németh, and A. Gendiar	99
Luttinger liquid and persistent current in continuous mesoscopic ring with weak link M. Mořko, R. Németh, R. Krčmár, and A. Gendiar	100
A new algorithm based on renormalization group study for negatively curved lattices R. Krčmár and A. Gendiar	101
Determination of the tri-critical point and phase transition classification on hyperbolic lattices R. Krčmár and A. Gendiar	102
III. PROJECTS	103
National projects	104

International projects	106
IV. INVITED PRESENTATIONS.....	107
Invited presentations at international conferences	108
V. PUBLICATIONS	109
2007	110
2008	115

I. General Overview

Organisation Scheme of the Institute



Thematic focus of the Institute

The Institute deals with current challenges in solid-state physics, information technology, microelectronics, and electrical engineering. The research performed at the Institute falls into the following domains:

- Study of selected theoretical problems of solid-state physics, aimed at potential applications in modern mesoscopic devices, and superconductivity;
- Research of new materials and technologies for information technologies, microelectronics, and electrical power devices;
- Characterisation and application of new structures for sensors and advanced microelectronic devices;
- Applied superconductivity.

In 2007 and 2008 the Institute published more than 130 papers in international scientific journals.

We participated in several projects under the 6th Framework Programme in the fields of microelectronics and applied superconductivity. Important results were achieved within the projects ULTRAGaN, SUPER3C and HIPERMAG.

At the end of 2008 we started an integrated project “*More Robust Gallium Nitride*” (MORGaN) within the 7th Framework Programme. The project includes 23 research laboratories and companies from France, Germany, the Czech Republic, the United Kingdom, Switzerland, Sweden, Greece, Poland, Hungary, and Austria. The project addresses the need for a new material basis for electronic devices and sensors that could be operated in extreme conditions, especially at high temperatures and in high electric fields.

Our efforts in applied superconductivity were supported within a Marie Curie Training Network project entitled “*Nano-Engineering Superconductors for Power Applications*” (NESPA), which started at the end of 2006.

The NESPA project involves 13 European partners. The project activities are focused on the involvement of young researchers in applied superconductivity.

Since 2005, the Institute has held the title Centre of Excellence of the Slovak Academy of Sciences in the field of advanced devices in electronic and electrical engineering (CENG). The Centre has co-operated with the following partners: the Faculty of Electrical Engineering and Information Technology of the Slovak University of Technology; the Department of Physics and the Faculty of Mathematics and Physics of Comenius University; the Department of Experimental Physics. The work of the Centre is directed mainly at:

- Information technology,
- Energy and power engineering,
- Development of new devices and sensors.

The activities of the Centre are detailed on its website: <http://www.ceng.sav.sk/>. They included the organization of a seminar each year at which young researchers presented their results. More than 70 publications registered in the Current Content database acknowledged support from the Centre during the 2007-2008 period.

The Institute received support from the European Social Fund to help young researchers pursue their research careers under a project entitled “*Educational Centre of Information Technologies and Power Engineering*” from September 2005 until February 2008.

The Institute significantly improved its research infrastructure in 2008 by opening a small clean room facility for electronic devices processing. The clean room with an area of 55 m² conforms to class 100 of the US standard.



Panaromic view of the clean room: photolithography part.

Selected outstanding results

Several outstanding results were achieved in 2007 and 2008. An overview of the achievements in the fields of advanced microelectronic devices and applied superconductivity is presented below.

Advanced microelectronic structures and devices

Local anodic oxidation (LAO) realized by the tip of an atomic force microscope (AFM) was employed to define nano-scale devices. We studied the influence of electric field distributions between the sample and the tip on local anodic oxidation. It was shown theoretically and experimentally that the conductivity of a sample is the most important parameter which controls the thickness of oxide lines prepared by LAO. A low conductivity of a sample is conducive to the formation of wide double maxima oxide lines under the tip. We explained the effect using numerical simulations using a finite element method. The results helped us to introduce a novel AFM LAO technique based on the use of an innovative material system (GaAs/AlGaAs/InGaP) and on the removal of oxide lines. The technique was used to form oxide lines as thin as 50 nm, which is a 50% reduction compared with lines formed by traditional approaches. Hence, even thinner nano-scale elements for quantum informatics and other applications can be realized using the technique.

We also focused on the development of high permittivity (high- κ) structures for nano-scale random access memories (DRAM). For DRAM cells to be further down-scaled, it is necessary to use a charge storage capacitor with very a high- κ dielectric. In our approach, RuO₂ layers, deposited by metal organic chemical vapour deposition, were used for the bottom electrode. As the second step, titanium dioxide thin films were grown using atomic layer deposition by our colleagues from Tartu University, Estonia. A stabilizing effect of the bottom rutile-type RuO₂ layer resulted in the growth of TiO₂ rutile films at low temperatures. The stabilization of the TiO₂ rutile phase occurred due to the local epitaxial growth of a polycrystalline RuO₂/TiO₂/RuO₂ structure, as was revealed by transmission electron microscopy. The capacitance-voltage measurement showed that the TiO₂ films exhibited a dielectric constant as high as 155. An SiO₂ equivalent thickness as low as 0.5 nm was obtained for the 20 nm TiO₂ thin film prepared at 425 °C.

Interesting results were achieved in the development of GaN-based high electron mobility transistors (HEMT) for high-power and high-frequency applications, such as mobile communications. High leakage current flowing through the control gate of a classical HEMT transistor with a Schottky barrier (SB) substantially limits this application. A decrease in the leakage currents of about 6 orders of magnitude was achieved in metal-oxide-semiconductor (MOS) HEMTs that had 12 nm thin insulating Al₂O₃ film deposited by metal organic chemical vapour deposition. The MOS HEMT also

showed an improvement in the maximal drain current density and extrinsic transconductance. Analytical modelling showed that a higher mobility of electrons in the channel of the MOS HEMT and consequently a higher number of electrons attaining the velocity saturation may explain the observed increase of the transconductance after the gate insulation.

Research activities in the field of passivation of AlGaN/GaN HEMTs were devoted to the investigation of plasma recess-gate etching and the passivation of the AlGaN barrier layer. We proposed a novel approach to the plasma passivation of the Schottky barrier gate interface of the HEMT structures. It lies in a shallow recess-gate CCl₄ plasma etching of the AlGaN barrier layer in combination with “in-situ” SF₆ surface plasma treatment applied selectively under the Schottky gate. A significant impact of the plasma passivation on both the current gain cut-off frequency (F_t) and maximum oscillation frequency (F_{max}) was observed. We discovered that the plasma treatment additionally performed under the Schottky gate improved F_t and F_{max} almost by about 60 %. One can therefore expect that such plasma passivation treatment should be beneficial for the development of the sub-micrometer gate length AlGaN/GaN HEMT for millimeter wave band applications.

Applied superconductivity

Our superconductivity research was focused on the development of technical superconductors and the application of high- T_c superconductors for laboratory use and energy transmission.

The transport current densities of stabilized multi-core MgB₂ composite wires were significantly increased within the 6th Framework Programme project HIPERMAG. The level of critical current density $J_c=10\,000\text{ Acm}^{-2}$ measured in an external field of 6 T at the beginning of the project (2005) was due to the current carrying capacity improvement obtained at a much higher field of 11.3 T at the end of project (2008). In addition to high J_c values at liquid helium temperatures due to the depression of secondary phase formation, the thermal stability and the resistance of MgB₂ wires to mechanical stresses were also improved. The achievements increase the potential of the material in future industrial applications, e.g. superconducting magnets for magnetic resonance imaging (MRI) or current limiters for safety energy distribution systems. The results achieved by the team dealing with superconductivity were published in 9 scientific papers in 2007 and 2008.

The electromagnetic properties of a superconducting pancake coil in an AC regime as a function of the number of turns were studied theoretically and experimentally. In particular, the AC loss, the coil critical current and the voltage signal were analysed. The coils were made from a Bi₂Sr₂Ca₂Cu₃O₁₀/Ag (BiSCCO) tape, although the main qualitative results are also applicable to other kinds of superconducting tape, such as coated conductors. The AC loss and the voltage signal were electrically measured

using different pick-up coils with the help of a transformer. The application of the technique avoided the effect of huge coil inductance. In addition, the critical current of the coil was experimentally determined by a conventional DC measurement. The critical current, the AC loss and the voltage signal were simulated, showing a

good agreement with the experiments. For all simulations, the field dependent critical current density inferred from DC measurements on a short tape sample was taken into account.

Summary of scientific Outputs

The most important results of our research were published in international scientific journals. Figure 1 shows the number of publications per year published since 2000, including the number of publications with the first author from the Institute. In recent years, the Institute has published 60 – 80 publications a year. In 2008, we unfortunately reached a low point in our publication activity. We strongly believe that this is an exception, and we will see an increase in the number of papers published in the future. The statistics show that we published on average of nearly two publications per research scientist a year.

expressed by their citation impact. Figure 2 depicts the number of citations from the Web of Science (WoS) database since 1999. We note that the citation statistics are issued with a one-year-long delay. The number of citations in a particular year includes responses to papers published over the whole period before a given year. The number of citations has increased annually even though the annual publication rate has been more-or-less at saturation point. The increase of the citation number above 500 in 2007 is encouraging. We believe that this trend reflects the increasing quality and recognition of the scientific output of the Institute.

The scientific significance of the publications is

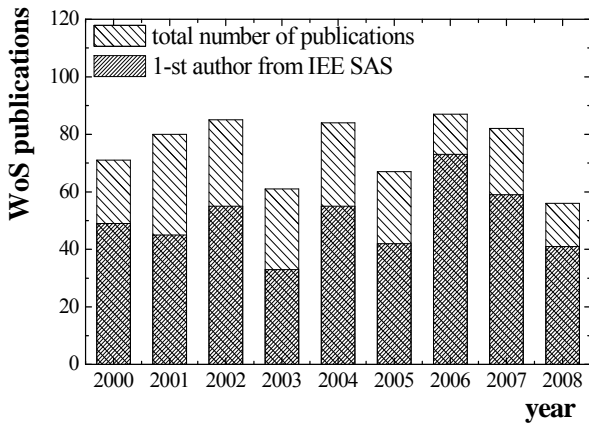


Fig. 1. Number of publications of the Institute in international journals according to the Web of Science database.

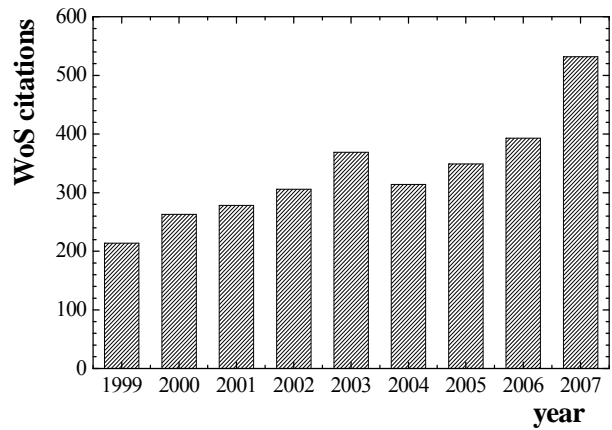


Fig. 2. Number of citations of the Institute according to the Web of Science database.

PhD study at the Institute

The Institute is accredited in the following scientific areas until 2010:

- Physics of condensed matter and acoustics,
- Theory of electrical engineering,
- Electronics,
- Electro-technology and materials.

In 2005, a change of the legislation of PhD education came into effect. Since 2005, the Institute has received an accreditation in new PhD study programmes:

- Physics of condensed matter and acoustics,
- Microelectronics,
- Physical engineering.

The programmes are realised in co-operation with the Faculty of Electrical Engineering and Information Technology, Slovak University of Technology, (Dept. of Microelectronics, Dept. of Physics), and the Faculty of Mathematics, Physics, and Informatics, Comenius University, (Dept. of Experimental Physics).

Twelve PhD students were trained at the Institute each year. Thanks to the Marie Curie Training Network project NESPA, there were PhD students from Finland and Ukraine among them. Six PhD students successfully defended their PhD thesis in 2007 and 2008.

A PhD should officially be completed within three years. However, most of our PhD theses were experimental works, which typically required more than four years for completion.

Funding of Research

The Institute of Electrical Engineering is a contribution-based governmental research organisation. The institutional contribution to the budget of the Institute was mostly spent on personnel costs. The second part of the budget was obtained from research grant agencies to fund research projects. Our research work was supported mainly by two national agencies: (1) the Slovak Academy of Sciences grant agency - VEGA, and (2) the Slovak Research and Development Agency - APVV. In addition, important funding was obtained within the Framework Programme of the European Commission.

Figure 3 shows the development of the total budget and institutional part from 2000 to 2008. The institutional contribution to the budget increased especially from 2000

to 2004. The contribution then levelled off. Fortunately, we increased the total budget of the Institute via our successful projects that obtained resources from the agencies and because the budget of the Slovak Research and Development Agency had significantly increased since 2002.

The total 2008 budget of the Institute was € 2,600 mil. (SKK 78,314 mil.). Figure 4 shows the breakdown of the budget. It is evident that the funds from the national and international projects and from the European Social Fund (ESF) and our own resources almost matched the institutional contribution.

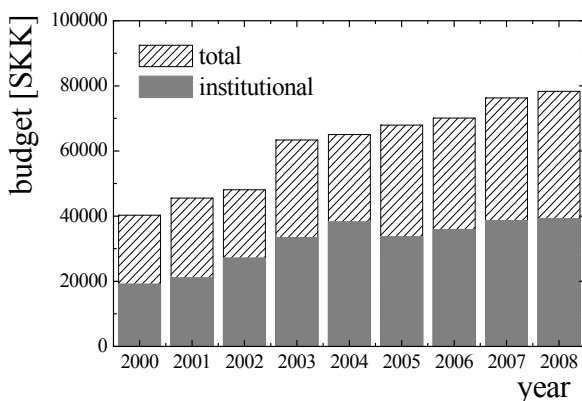


Fig. 3. Budget development from 2000 to 2008.

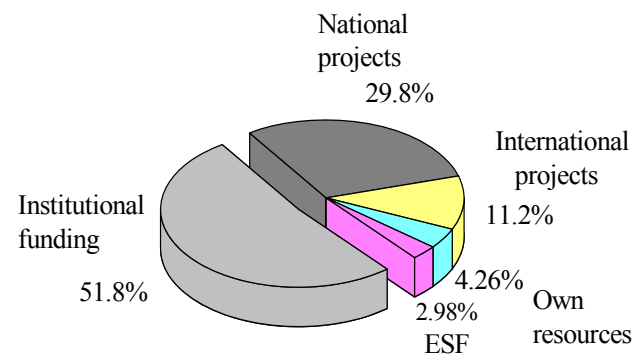


Fig. 4. Approximate budget composition in 2008.

Conferences

In 2007 and 2008, the Institute organized the following international scientific events:

The 12th European Workshop on Metalorganic Vapour Phase Epitaxy - EW-MOVPE 2007, Bratislava

The 7th Autumn School on X-ray Scattering, Smolenice

NANOVED 2007, a conference on nanoscience, Bratislava,

The 7th International Conference on Advanced Semiconductor Devices and Microsystems - ASDAM '08, Smolenice.

In June 3-6, 2007 we organized the 12th European Workshop on MOVPE technology in Bratislava (EW-MOVPE), a top European conference in the field. More than 200 scientists from Europe, the USA and Japan participated in it. The conference helped to support the position of our MOVPE experts within the community of MOVPE growers in Europe. Its successful organization was made possible thanks to the efforts of every member of the Department of Optoelectronics.

The 7th Autumn School on X-ray Scattering focused traditionally on the topic of X-ray scattering from surfaces and interfaces. As in the previous years, this school introduced the participants to techniques and applications of high resolution X-ray scattering and data analysis of thin films and lateral nanostructures. In addition to the tutorial talks given by experienced scientists, graduate and post-graduate students and other young scientists presented their current results at the School, which was

organized at the Conference Centre of the Slovak Academy of Sciences in Smolenice, Slovakia in October 4-6, 2007. The autumn school was attended by about 78 participants.

The NANOVED 2007 conference (November 11 – 14, 2007) was devoted mainly (but not solely) to the presentation of current trends and achievements in the field of nanoscience, nanotechnology and nanomaterials and to their applications in the diverse fields of physics, materials science, electronics, chemistry, biology, medicine, etc. A Young Researchers' workshop and the award ceremony for the best oral and poster presentations were an integral part of the conference. An important part of the conference was devoted to activities stimulating the assembly of interdisciplinary teams focused on nanoscience research. The teams would potentially form consortia and apply for projects within FP7. A total of 88 registered participants from 14 countries took part in the conference.

The ASDAM '08 conference was held in October 12-16, 2008 at the Congress Centre of the Slovak Academy of Sciences in Smolenice Castle, Slovakia. The workshop brought together scientists, engineers and post-graduate students who specialized in semiconductor devices and microsystems and related technologies. The invited and contributed papers provided detailed views on the latest results in the research field. The meeting gave young scientists an opportunity to discuss their work and to initiate intensive and fruitful discussions on the relevant topics. Over 90 participants from 16 countries presented 8 invited, 45 oral and 40 poster presentations. The ASDAM Conference proceeding was published by the IEEE Electron Devices Society.

II. Research activities

Department of Superconductor Physics

Pavol Kováč

Research scientists

Silvester Takács
Fedor Gömöry
Ján Šouc
Eugen Seiler
Tomáš Holúbek
Enric Pardo

Research Engineers

Imrich Hušek
Tibor Melíšek
Lubomír Frolek

Technical staff

Lubomír Kopera
Juraj Tančár
Stanislav Štefanik

PhD Students

Miloslav Kulich
Michal Vojenčiak
Mikolaj Solovjov
Jonna Viljammaa

Students

Lukáš Havrila



The Department of Superconductor Physics (DSP) has been developing and studying applicable superconducting materials and high-current superconducting systems. Composite wires and tapes both from low- and high-temperature superconductors have been produced by means of a variety of fabrication procedures using comprehensive tools and facilities at the DSP. The wires and tapes are fully characterized by electrical measurements and mechanical tests also carried out at the department.

We developed and applied various unconventional deformation techniques. They were used to prepare high-performance low-temperature (LTS) Nb₃Sn wires and cables, high-temperature (HTS) Bi-2223/Ag tapes, and recently medium-temperature (MTS) MgB₂/metal composites.

The MgB₂ binary metallic compound, discovered in 2001, exhibits superconductivity below the critical temperature $T_c = 39$ K. The advantages of using MgB₂ in applications outweigh those of using HTS and LTS: MgB₂ wires are produced more easily than ceramic HTS ones, because of favourable MgB₂ intrinsic properties. They are also cheaper, as their raw materials are considerably less expensive than ceramic HTS ones. The estimated cost to produce a MgB₂-based conductor is at least ten times lower than that necessary to make a HTS wire. Compared with LTS, the higher T_c of MgB₂ enables systems to be operated in the 20 – 30 K range, which can easily be reached by direct conduction cooling.

In general, MgB₂-based systems are inherently safer, easier to design, and more compact. Their production and maintenance are less costly. Cryo-cooled MgB₂ systems can thus potentially replace the existing NbTi ones, which would bring significant cost cuts. Such low cost superconducting prototype systems could then become more widely used in the electro-technical (generators, motors) and energy sectors (transformers, SMES).

To achieve thermally stable MgB₂/metal composite wires exhibiting high critical currents, the metallic elements should show low chemical reactivity with the Mg +B system and the MgB₂ compound. They should also exhibit sufficient mechanical workability and high thermal and electrical conductivities.

We produced a stable, four-filament *in-situ* MgB₂/Ti/Cu/Monel composite wire using a rectangular wire-in-tube (RWIT) technique. Nano-sized SiC was added into a Mg-B powder mixture (10 wt %), which was packed into Ti/Cu and Monel tubes. Two-axially rolled 1.2×1.2 mm² wires sintered at 650 - 850 °C / 0.5 h showed excellent $J_c(\mu_0 H)$ characteristics crossing over the level of $J_c = 10^4$ Acm⁻² between 8.9 T and 10.3 T. *I-V* characteristics of the MgB₂/Ti/Cu/Monel square wires measured far above the electric field criterion for critical current (I_c) showed good thermal stability. Above the I_c value, some part of the transport current flowed parallel through the metallic sheath, which generated heat and increased the temperature of the wires. When the temperature of a composite reaches the critical

temperature of MgB₂, the current is excluded from the filaments into the less resistive metallic sheath, and the corresponding transition can be observed at current I_t . The power density calculated for this point as $p_t = (U_t \times I_t) / F_s$ (where F_s is the outer surface area of the wire) was only 1mWmm⁻².

A stable seven-core MgB₂ cable was made from two-axially rolled single-core wires with a Ti/Cu sheath. It was shown that the drawing deformation applied prior to the braiding affected the core density and consequently also the transport current densities J_c . An appropriate drawing deformation technique prevented the J_c degradation. The cable reached a critical current density of 10^4 Acm⁻² at 9.5 T and 10^5 Acm⁻² at 4.5 T at 4.2K.

Superconducting filaments in a ferromagnetic matrix are a system whose features can be influenced by both the quality of the materials used and the arrangement of filaments. The electromagnetic properties of Y-123 and Bi-2223/Ag composites were studied experimentally and theoretically using finite element commercial codes. Such studies are essential for the future applications of composite superconductors in electric power devices. When electrical currents are expected to be transported in the range of kA, superconducting wires should inevitably be cabled. We have dedicated a systematic effort to the understanding of the distribution of current, magnetic field, and the resulting energy loss in flat cables used in the nuclear fusion technology. Concerning the cables for power transmission, we have designed, manufactured and tested short laboratory models to investigate some peculiarities in the current distribution, AC transport capacity and AC loss.

The activities of DSP have been financially supported by national agencies VEGA and APVV. VEGA supported two of our projects: “*The effect of magnetic field on the properties of superconductors with ac transport current*” and “*Superconducting MgB₂ wires with artificial pinning centers*”. APVV supported the three other projects: “*Superconductors in conditions of high current equipments*”, “*Composite superconductors for cryogen-free devices*”, and “*Advanced filamentary composite MgB₂ superconductors*”.

DSP has intensively collaborated for a long time with the INFN, Genua, Italy, the Materials Department of Oxford University, UK, the High Pressure Institute, Warsaw, Poland, Twente University, Enschede, The Netherlands, Tampere University, Finland, and others.

DSP was significantly involved in international collaboration within multilateral projects of the 6th Framework Program of the EC: “*Superconducting coated conductor cable*”, “*Nano- and micro-scale engineering of higher-performance MgB₂ composite superconductors for macro-scale applications*”, and the Centre of Excellence “*Applied Superconductivity Training and Research Advanced Centre*” or net NESPA “*Nano-Engineering Superconductors for Power Applications*”.

Pavol Kováč

Stabilized MgB₂ composite wire with Ti barrier

P. Kováč, I. Hušek, T. Melišek, and T. Holúbek

Stabilized four-filament *in-situ* MgB₂/Ti/Cu/Monel composite wire was produced by the rectangular wire-in-tube (RWIT) technique. 10 wt% of nano-size SiC was added into the Mg-B powder mixture, which was packed into the Ti/Cu and Monel tubes, respectively. Assembled composite was two-axially rolled into the wire and/or tape form and sintered at temperatures 650-850 °C/0.5 h. Stabilized MgB₂ wire with Ti barrier is studied in terms of field-dependent transport critical current density, effects of filament size reduction and thermal stability [1]. Cross section of composite in Fig. 1 presents well uniform Ti barrier separating the filaments from OFHC copper.

Critical current densities J_c of square wires $1.2 \times 1.2 \text{ mm}^2$ annealed at temperatures ranging from 650 °C to 850 °C were measured. $J_c(\mu_0 H)$ characteristics are crossing-over the level of $J_c = 10^4 \text{ Acm}^{-2}$ between 8.9 T and 10.3 T. It is apparent that increased temperature leads to improved current density and the highest J_c is measured for 850 °C. Surprising is the apparent increase of current density for annealing above 800 °C. While the $J_c(10 \text{ T})$ increase between 650 °C and 800 °C is only 23 %, 56 % improvement of $J_c(10 \text{ T})$ occurred between 800 °C and 850 °C.

Figure 2 shows I - V characteristics for MgB₂/Ti, MgB₂/Ti/Cu and MgB₂/Ti/Cu/Monel square wires 1.2 mm annealed at the same conditions (650 °C/30 min) and measured above the electric field criterion for critical current (I_c) in the external field 8.5 T for increasing and decreasing current. Above the I_c value, some part of the transport current is flowing parallel through the metallic sheath, which generates the heat and increases the temperature of the whole sample. When the temperature

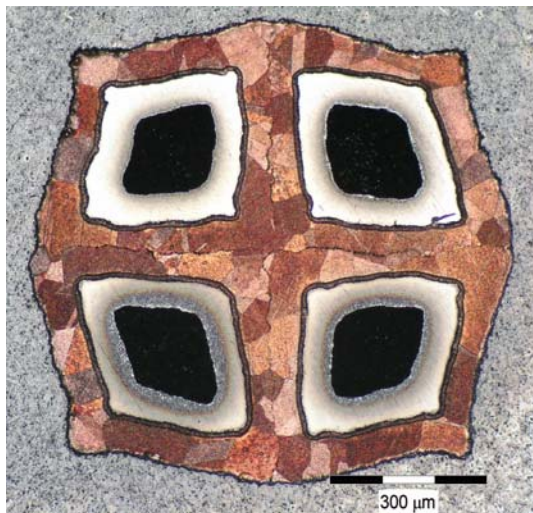


Fig. 1. Cross-section of MgB₂/Ti/Cu/Monel composite wire treated at 850 °C.

of composite reaches the critical temperature of MgB₂, the current is excluded from the filaments into less resistive metallic sheath and corresponding transition can be observed at the current I_t . If the current is ramping down the temperature of sample is decreased and opposite transition occur at the recovery current I_r . MgB₂/Ti wire shows a typical low thermal stability behavior with the sudden transition of MgB₂ core into normal state at the transition current $I_t = 2.32 I_c$. The power density calculated for this point as $p_t = (U_t \times I_t) / F_s$ (where F_s is the wire's outer surface area) is only 1 mWmm^{-2} [2].

The same p_t values were estimated for this wire at lower fields and also at the quench current (I_q), which occurred at 7.5 T. Below the quench current the reversible part of I - V curve can be measured for decreasing current and the recovery current $I_r = 0.855 I_t$. While the large transition-recovery loop was measured for not stabilized MgB₂/Ti wire, only very small one is observed for MgB₂/Ti/Cu (see the insert in Fig. 2) with $p_t = 3.5 \text{ mWmm}^{-2}$ reflecting the improved thermal stability by the added highly conductive copper sheath.

This work was supported by the Science Agency VEGA 2/5088/25, and by the EU FP6 contract No. NMP3-CT2004-505724.

- [1] Kováč, P., Hušek, I., Melišek, T., and Holúbek, T.: *Supercond. Sci. Technol.* **20** (2007) 771.
- [2] Kováč, P., Hušek, I., Melišek, T., Martínez, E., and Dhallé, M.: *Supercond. Sci. Technol.* **19** (2006) 1076.

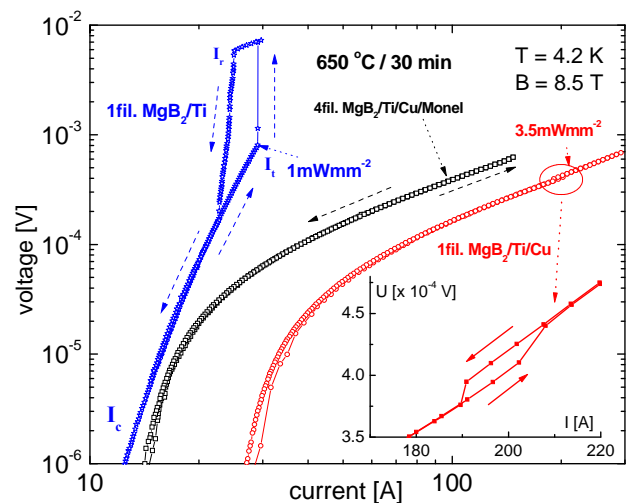


Fig. 2. I - V characteristics of MgB₂/Ti, MgB₂/Ti/Cu and MgB₂/Ti/Cu/Monel wires.

Filament and interface structure of *in-situ* MgB₂ wires

I. Hušek and P. Kováč

The structure of MgB₂ filaments and interface areas of *in-situ* made composite MgB₂/Ti/Cu/Monel wires sintered at temperatures 650-850 °C were studied by polarized light optical microscopy and Vickers microhardness. The presented results give useful information above how the applied composition and annealing can affect the core density, J_c and interface diffusion/reaction [1].

The averaged HV 0.05 values for MgB₂ filaments are plotted in Fig. 1 together with the filament critical current densities (J_c) measured at 5 T. While an initial hardness HV 0.05 = 170 was measured for the as-deformed Mg+B filaments, MgB₂ phase creation leads to an apparent increase of HV 0.05 > 400 and it continued to increase with annealing temperature. The highest value HV 0.05 = 535 is measured for the sample annealed at 850 °C. The J_c also increases with temperature and increases by 40 % between 800 and 850 °C (from 73 to 92 kAcm⁻²). This J_c

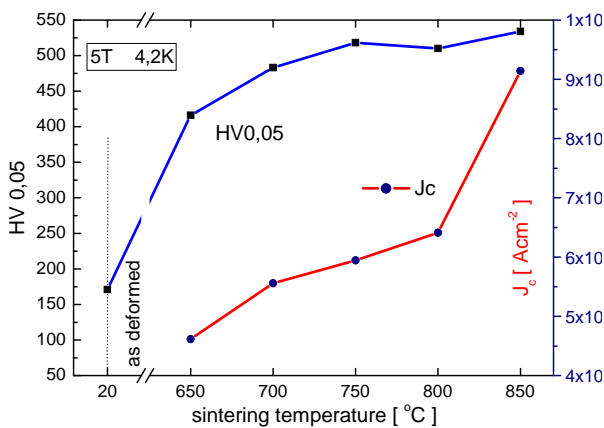


Fig. 1. The filament microhardness HV 0.05 and transport current densities at 5 T and 4.2 K.

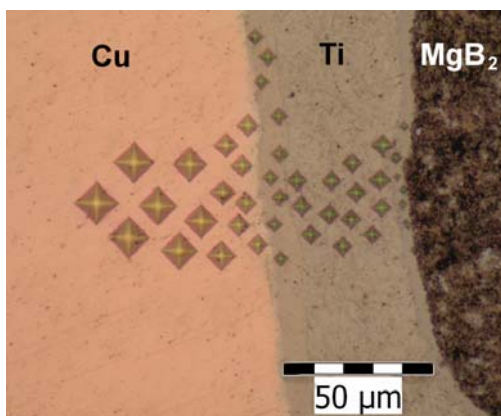


Fig. 2. MgB₂/Ti/Cu area with Vickers indentations after annealing at 850 °C.

improvement cannot be explained by the small filament density increase between 800 °C (510) and 850 °C (535). The strengthening of Ti barrier for $T_s > 700$ °C was measured. The increased hardness of titanium barrier can be caused by possible diffusion/reaction of elements from MgB₂ filaments on the one side and with Cu stabilizer on the opposite side [2]. Figure 2 shows polarized optical microscopy (POM) picture of the MgB₂/Ti/Cu area with Vickers indentations made after annealing at $T_s = 850$ °C. One can see that the size of the indentations in the Ti barrier is dependent on their distance from the MgB₂ filament and also from the Cu stabilizer. It means that some inter-diffusion/reaction took part at both sides of the Ti barrier leading to the creation of multiphase layers.

More selective etching and POM allowed finding the reactive layer at MgB₂/Ti (see Fig. 3) and the Ti/Cu interface which consisted of several separated layers. Therefore, HV 0.01 measurements across the Ti barrier and also in the separate layers 1 (at MgB₂/Ti) and 2, 3 and 4 (marked from Ti to Cu side) have been done for all temperatures.

This work was supported by the Grant Agency of the Slovak Academy of Sciences VEGA 2/5088/25 and by the EU FP6 contract No. NMP3-CT2004-505724.

- [1] Hušek, I. and Kováč, P.: *Physica C* **432** (2005) 153.
- [2] Kováč, P., Hušek, I., Melišek, T. and Holúbek, T.: *Supercond. Sci. Technol.* **20** (2007) 771.

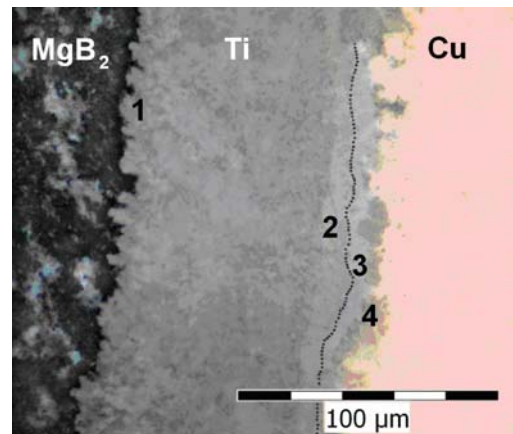


Fig. 3. Ti/Cu interface layers (2,3 and 4) after annealing at 850 °C/30 min.

Electro-mechanical characterization of selected superconductors

E. Kopera, P. Kováč, and T. Melišek

This work describes the design and performance of tension test instrument aimed for freestanding sample stress-strain characterisation and critical current degradation of superconducting wires and tapes under variable tension and magnetic field.

The tension test instrument was designed to elongate the sample and measure the applied load and corresponding elongation simultaneously using the Nyilas type (NT) extensometer [1]. Figure 1 illustrates details of the tension test instrument.

The instrument is mounted to the fibreglass tube holder with outer diameter OD = 60 mm. The measured sample of the maximum length 50 mm is fixed by its ends into the holding grips in between the tension and flexible arms. Uniaxial tensile load up to 1000 N applied to the sample is transferred from slide motion of the pusher along bevel edge of the tension arm. Flexible arm is manufactured from the titanium alloy and functioned as a load cell. The sample elongation is measured by extensometer clamped by springs to the sample. The presented system allows to obtain: $\sigma(\varepsilon)$ characteristics and Young modulus of samples measured at room and

cryogenic temperatures (293 K, 77 K and 4.2 K); $I-V$ characteristics of composite superconductors measured under variable applied uniaxial tension load in the presence of external magnetic field (parallel or perpendicular in the range of 0 - 7.5 T) and the corresponding $I_c(\varepsilon)$ dependences. Critical currents (I_c) were determined by a standard four-probe method with a criterion of 1 $\mu\text{V}/\text{cm}$.

Stress-strain and I_c -strain characteristics of advanced Bi-2223, Y-123 and MgB_2 composite superconductors were measured. Cross-sectional views and specifications are summarised in Fig. 2.

Obtained results show the best electro-mechanical properties for the tapes mechanically reinforced by the soldered stainless steel strips (Fig. 3). Sample #3 has the best mechanical strength ($E=108 \text{ GPa}$, $\sigma_y=274 \text{ MPa}$) and also very good electro-mechanical properties ($\sigma_{95}=454 \text{ MPa}$, $\varepsilon_{95}=0.51\%$). MgB_2 tape with Ti-barrier and Monel sheath is less reinforced due to an apparent softening of these materials after the final heat treatment at 800 °C / 30 min [2]. Therefore, more effective mechanical reinforcement of superconducting tape could be achieved e.g. by stainless steel strips soldered after the final heat treatment [3].

This work was supported by the Slovak Scientific Agency under the project APVV-0398-07 and partially by APVT-51-029902.

[1] Kopera, L., Kováč, P., and Melišek, T.: *Supercond. Sci. Technol.* **21** (2008) 115001.
 [2] Kováč, P., Dhalle, M., Melišek, T., van Eck, H.J.N., Wessel, W.A.J., ten Haken, B., and Husek, I.: *Supercond. Sci. Technol.* **16** (2003) 600.
 [3] Kováč, P., Hušek, I., Melišek, T., and Holúbek, T.: *Supercond. Sci. Technol.* **20** (2007) 771.

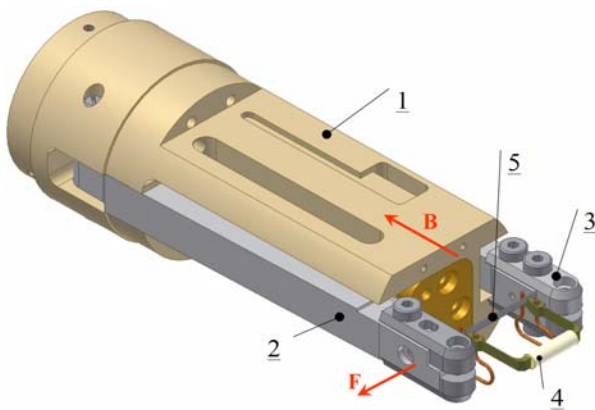


Fig. 1. The tension test instrument: (1) fibreglass holder, (2) tension arm, (3) flexible arm (load cell), (4) Nyilas type extensometer, (5) measured sample, (6) pusher.

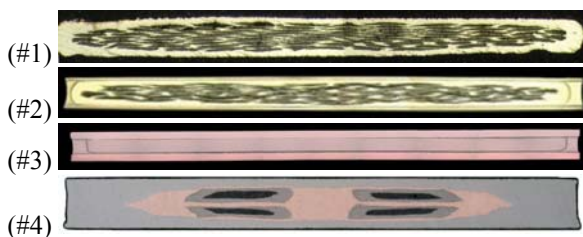


Fig. 2. Cross sections of tested superconductors: (#1) Bi-2223/Ag alloy tape, (#2) High Strength Bi-2223 tape, (#3) SS stabilized YBCO 344S tape, (#4) $\text{MgB}_2/\text{Ti}/\text{Cu}/\text{Monel}$ tape.

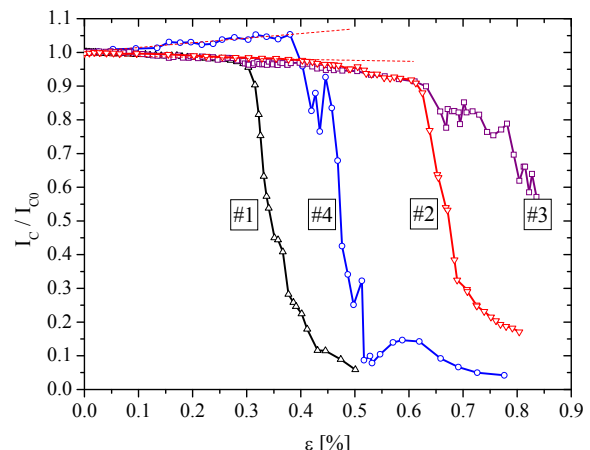


Fig. 3. Relative I_c degradation of the measured superconductors.

MgB₂ cable made of two-axially rolled wires

P. Kováč, I. Hušek, and T. Melišek

Stabilized seven-core MgB₂ cable has been made from two-axially rolled single-core wires with Ti/Cu sheath. It was shown that drawing deformation applied prior to braiding is influencing the core density and consequently also the transport current densities J_c . The proper drawing deformation allows avoiding J_c degradation and cable critical current density 10^4 Acm^{-2} at 9.5 T and 10^5 Acm^{-2} at 4.5 T can be reached at 4.2 K [1]. Several shapes of single-core wires (Fig. 1) were used for cabling (Fig. 2).

To check the effect of braiding in advance, the wire WS of $0.28 \times 0.28 \text{ mm}^2$ was wrapped around the quartz capillary of 2 mm in diameter with different spiral slope (twist pitch L_t) 45, 30 and 15 mm. No current degradation but even slight improvement was observed for all wrapped WS wires.

Critical current densities of seven strands cables CS 0.28 and CSR 0.35 and CSR 0.335 braided with the same twist of 15 mm are plotted in Fig. 3 together with the J_c of single strand WSR 0.35. It should be noted that J_c of not braided wires WS 0.28, WSR 0.35 and WSR 0.335 were very similar. Figure 3 clearly shows that no and/or only very small J_c decrease occurred by braiding of wires WSR

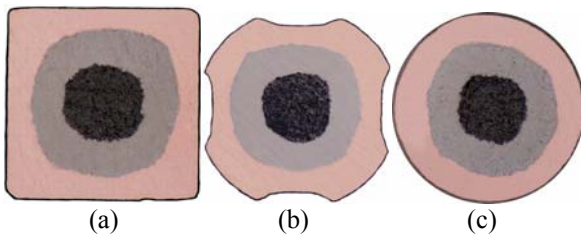


Fig. 1. Cross sections of single core wires containing 15% of MgB₂, 35% Ti - barrier and 50% oxygen free high conductivity Copper stabilization (a) WS, 0.30 x 0.30 mm, (b) WSR, 0.35 mm and (c) WR, 0.30 mm.

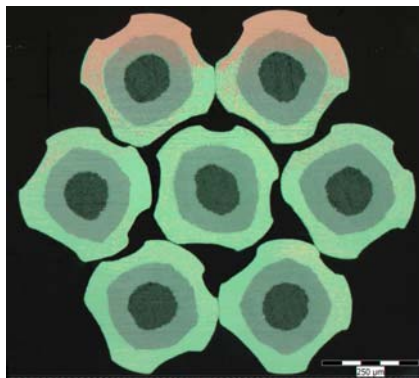


Fig. 2. Seven strands MgB₂/Ti/Cu cable made of WSR wire 0.35 mm in diameter.

0.35 and WSR 0.335, respectively. Lowered J_c of cable CS 0.28 can be attributed to not uniform cabling of square wires WS 0.28 (see Fig. 1a) into circularly symmetrical 1 + 6 braid configuration. The insert in Fig. 3 shows the field dependence of n - exponent derived from I - V curves of WSR 0.335 ranging from 34 (at 8.5 T) up to 272 (for 3 T).

No quenching was observed during the I - V measurements in the field range ≥ 3 T. The n values for cables CSR 0.35 and CSR 0.335 were more scattered than for individual wires due to possible current redistribution among the strands. But, very similar n magnitudes were measured in the range of 4.5 - 5.5 T for CSR 0.35 and CSR 0.335 (80-100), which confirm the excellent cables quality. Critical currents of 90-100A were measured CSR cables (0.335-0.35 mm) at external field 4 T and 4.2 K, which represent the engineering current density (J_e) of 16400 - 18220 Acm^{-2} . Critical current of 785 A was extrapolated for the double triplet cable at the same field and temperature [2], which gives $J_e = 16122 \text{ Acm}^{-2}$.

This work was supported by the Slovak Scientific Agency under the project APVV- 0398-07.

- [1] Kováč, P., Hušek, I., and Melišek, T.: *Supercond. Sci. Technol.* **21** (2008) 125003.
 [2] Musenich, R., Greco, M., Razeti, M., and Tavilla, G.: *Supercond. Sci. Technol.* **20** (2007) 235.

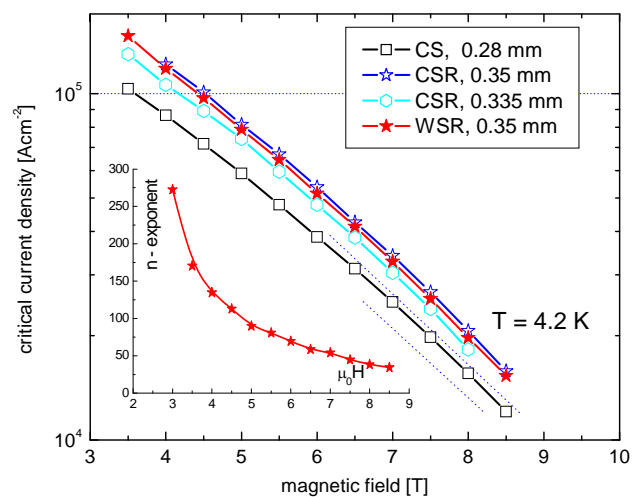


Fig. 3. Critical current densities of three different cables (CS and CSR) compared to J_c of individual straight wire (WSR), the insert shows the field dependence of n - exponent for WSR 0.335.

Coupling losses in coated conductors at industrial frequencies

S. Takács

The present activities in producing $\text{YBa}_2\text{Cu}_3\text{O}_7$ (YBCO) coated conductors with very high critical current densities j_c and decreasing the hysteresis losses by striating or scratching the layers into thinner stripes increased the hopes for applicability of these conductors in AC regimes. The superconductors may replace copper in many areas, like high-power transformers, motors, and generators, substantially reducing the size and weight of the corresponding designs. The coupling losses between the individual stripes could be decreased also radically by striating or scratching. To maintain high critical current density values also in long length samples, the current sharing between the stripes is necessary, enabling thus the redistribution of the current into the neighbouring stripes. Otherwise, some small defects or electromagnetic perturbations can be detrimental to the individual stripes, and even to the whole tape. The current sharing between the stripes can be nearly completely restricted in the striated samples. But any type of connection between the stripes increases the coupling losses between them. The suggested full coating of the tape with normal metal results in dramatic increase of the coupling losses [1].

Therefore, I proposed a model of coated conductors, which does not require *any twisting* procedure for the tapes. By partial coating of the tapes with segmented pieces of normal metal (NM), the coupling losses should be decreased to an acceptable level even at industrial frequencies [2]. The basic feature of the model is to allow the induced currents to close *partially* in loops between the NM plates. This is analogous to the currents flowing at the crossing points of twisted superconducting filaments or strands. The remaining current is then not proportional to the total length of the conductor. Thus, the distance between the NM segments plays the same role as the twist pitch in the twisted structure.

Subsequently, more precise considerations for the induced currents in the proposed structure were performed and the coupling losses recalculated [3].

The induced current density in the superconductor was shown to be below the critical current density of best YBCO coated conductors. At applied magnetic field amplitude $B_m = 0.1$ T and with the frequency $f = 50$ Hz, the maximum induced current density j_0 was calculated. Its value is about

$$j_0 = 1.26 \times 10^{10} \text{ A/m}^2,$$

which is below the achieved critical current density of present YBCO coated conductors.

The allowed frequency range for the model and the validity of the proposed structure – hence its relevance for practical applications – were examined, too.

The frequency limitation for penetrating the flux *between the individual stripes* was determined by calculating the time constant τ of the individual circuits consisting from the stripes and the normal metal plates. For parameters of the magnetic field given above, the full flux penetration is restricted by the condition

$$f < (2.9 \div 22) \times 10^2 \text{ Hz}$$

for the number of included stripes on the striated coated conductors $n \in (2, \dots, 10)$, respectively.

The frequency limitation for entering the flux *into the normal metal plates* is about $f < 2 \times 10^3$ Hz. Both these limits are well above the industrial frequency. Therefore, the flux penetration into the proposed structure is possible at industrial frequency without any restriction.

Thus, the proposed model of covering the striated YBCO coated conductors by segments of normal metal can be the solution to having a compromise between acceptable coupling losses and current sharing. In analogy to the twisted structure, an essential part of the induced currents is closed on a finite length, hence the induced currents between the normal metal plates do not depend on the total length of the conductor. As the value of the induced current density in the superconductor is below the critical current densities in best YBCO coated conductors, and the flux penetration is practically unrestricted at industrial frequencies, it seems to be no need for twisting the stripes on small length. The presented model can be applied to the actually produced YBCO coated conductors. The difficult task of twisting the YBCO coated conductors seems to be therefore a secondary problem. This could be good news for the superconducting materials research. Therefore, the chance for AC applications of coated conductors in the near future should increase.

This work was supported by the Slovak Grant Agency for Science VEGA 2/6098/26, and from the Slovak Research and Development Agency, No. APVV-51-045605.

[1] Takács, S.: *Supercond. Sci. Technol.* **20** (2007) 180.

[2] Takács, S.: *Appl. Phys. Letters* **90** (2007) 242505.

[3] Takács, S.: *J. Appl. Phys.* **103** (2008) 05397.

Calculation of critical state in superconducting/ferromagnetic composite tapes

F. Gömöry, M. Vojenčiak, E. Pardo, and J. Šouc

The knowledge of local distributions of electrical current density and magnetic field is essential when the dissipation in AC regime should be predicted for a superconducting wire. Numerical methods for solving this problem in the case of tape conductors based on high-temperature superconducting materials have been developed and tested. The challenge met recently is the insertion of ferromagnetic layers to allow the simulation of Bi-2223/Ag tapes covered on edges by nickel or YBCO coated tapes on magnetic substrates.

We developed for this purpose a new numerical calculation procedure based on the idea proposed by A.M. Campbell [1]. The finite-element code resolves the distribution of vector potential of magnetic field, \vec{A} , in the cross-section of the composite tape. The properties of both superconducting and ferromagnetic material must be expressed as functions of \vec{A} or its derivatives i.e. the magnetic field components B_x, B_y . It is essential to allow non-linearity in these dependences, otherwise the comparison with experiments is not plausible. We have developed the expression for the current density in superconductor in terms of the time derivative of the magnetic vector potential. Because the evolution of currents and fields in time is represented by a series calculated for a finite time steps, the time derivative is replaced by the difference between the value at the actual instant, \vec{A}_z , with respect to the previous one, \vec{A}_p . Vectorial notation can be omitted in our two-dimensional calculation performed in the plane perpendicular to the tape longitudinal axis. In the finite-element calculation, the current density in superconductor obeys the following expression that represents the critical-state principle [2]:

$$j_s(x, y) = j_c(B) \tanh\left(\frac{A_p(x, y) - A_z(x, y)}{A_n}\right)$$

Here, A_n is the factor controlling the sharpness of the transition between two polarities of the current density. The critical current density of superconductor, j_c , depends on magnetic field and is also sensitive to its orientation.

The properties of ferromagnetic material required for the prediction of AC dissipation is the field

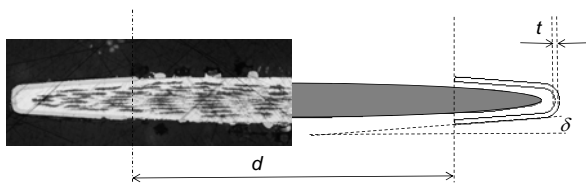


Fig. 1. Cross-section of the commercial Bi-2223/Ag tape covered on edges by Ni layer (left) and the simplified geometry used in calculations (right).

dependence of the relative permeability, and of the volume density of hysteresis loss. Suitable choice of the boundary condition allows to simulate the application of an external magnetic field or transporting an electrical current.

In Fig. 2 is illustrated the suitability of this calculation procedure to predict the AC loss in Bi-2223/Ag tape covered by galvanic process on edges by 30 μm thick layer of Ni (cross-section shown in Fig. 1). Properties of the nickel layer were determined from the magnetization measurement of a 10 μm Ni layer prepared on Ag sheet by identical process [3]. The field and angular dependence of critical current density in superconducting material was determined from the critical current dependence on magnetic field taken at different field orientations [4].

As one can see from this example, the validity of theoretical prediction is rather high: the transport loss reduction by one order of magnitude has been successfully explained.

This work was supported by the Slovak Research and Development Agency under No. APVV-51-045605.

- [1] Campbell, A.M.: *Supercond. Sci. Technol.* **20** (2007) 292.
- [2] Gömöry, F., Vojenčiak, M., Pardo, E., Šouc, J.: *Supercond. Sci. Technol.* **22** (2009) 034017.
- [3] Gömöry, F., Šouc, J., Seiler E., Vojenčiak, M., and Granados, X.: *J. Phys.: Conf. Ser.* **97** (2008) 012096.
- [4] Gömöry, F., Šouc, J., Vojenčiak, M., and Klinčok, B.: *Supercond. Sci. Technol.* **20** (2007) S271.

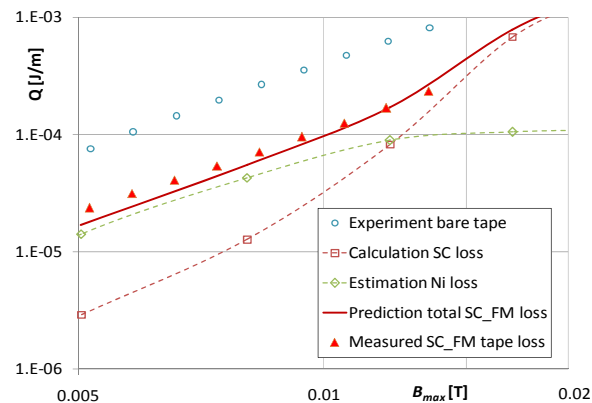


Fig. 2. Comparison of calculated magnetization loss (full line) with experimental data (triangles) for Bi-2223/Ag tape with cross-section shown in Fig. 1. Total predicted loss is the sum of loss in superconductor (squares) and Ni cover (diamonds). Reduction of the loss in respect to the original tape (circles) is evident.

Theoretical and experimental study of AC loss in high-temperature superconducting pancake coils

E. Pardo, J. Šouc, M. Vojenčiak, and F. Gömöry

ReBCO coated conductor tapes are the most promising high-temperature superconductors. However, they present too high AC loss for commercial applications. Many AC devices contain coils, such as motors, generators and transformers. In this case, the tapes strongly interact with each other, presenting different AC loss behaviour than the isolated tape [1-4]. Therefore, the AC loss in a coil has to be analysed as a whole in order to predict and, eventually, reduce the AC loss. Here, we present a numerical and experimental study of high-temperature superconductor pancake coils. The numerical simulations are for either ReBCO coated conductors or $\text{Bi}_2\text{Sr}_2\text{Ca}_2\text{Cu}_3\text{O}_{10}$ (Bi2223). We made our experiments on Bi2223 coils in order to develop the measuring technique for coated conductors.

Our simulation technique is based on the minimum magnetic energy variation (MMEV) method, which assumes the critical state model [5,6]. For a constant critical current density, J_c , this method is very fast. Thanks to this, we could simulate a generic coated conductor pancake coils (Fig. 1) with a large number of turns, up to 200 [4]. We have further developed the method in order to solve an anisotropic J_c with field and position dependence [7]. For this case, the calculations take a larger computing time. A common feature for both coated conductors and Bi2223 pancake coils is that the current density which contributes to the net transport current distributes close to the upper and lower parts of the tapes. Moreover, this current distribution is similar for all the tapes (Fig. 2). Another feature is that the magnetic field is parallel to the tape surface in the region with null current density on the tape thickness (Figs. 1 and 2).

The numerical model above can solve the current distribution and the AC loss in a pancake coil with an anisotropic magnetic field dependent J_c . In order to apply the simulations in practice, it is necessary to know the

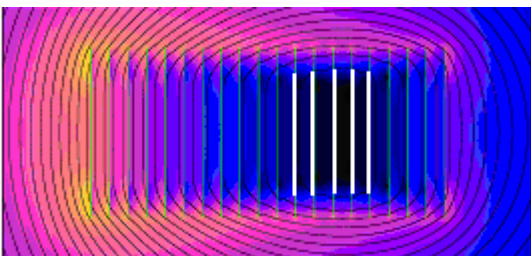


Fig. 1. Magnetic field magnitude (grayscale) and magnetic field lines for a generic coated conductor pancake coils [4] (d in the legend is the superconductor thickness). The shown area is in a coil cross-section (the left and right limits are the inner and outer coil radius). The broad white straight lines represent the superconductor position.

field dependence of J_c . We extracted this information from measurements of the critical current as a function of the applied field for several orientations. In order to do this, it has been necessary to use a self-consistent numerical method to take into account the self-field effects on the critical current [8,9].

The pancake coils that we experimentally studied are made of Bi2223 superconducting tape (Trithor superconductor) and were made of 1, 3, 5, 10, 19 and 32 turns, respectively [7].

The coil critical current in the pancake coils is significantly lower than the tape (Fig. 3), evidencing that the field dependence of J_c is important. Moreover, the critical current saturates for a large number of turns. This is due to two reasons: first, J_c becomes less sensitive to the magnetic field at large magnetic fields, and, second, J_c

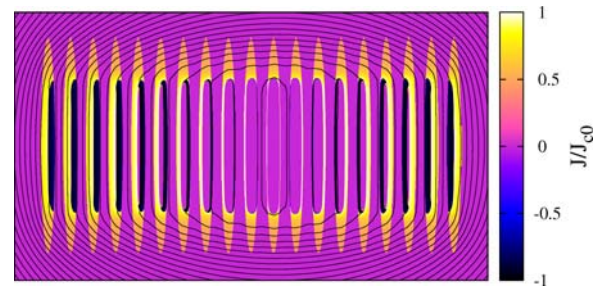


Fig. 2. Current density normalized to the intrinsic value at zero field, $J_c(0)$, inside a Bi2223 coil [7] (grayscale) at the peak of the AC cycle. The AC amplitude is 14.1 A and the critical current is 29.4 A. The lines are magnetic field lines. The radial coordinate increases from left to right.

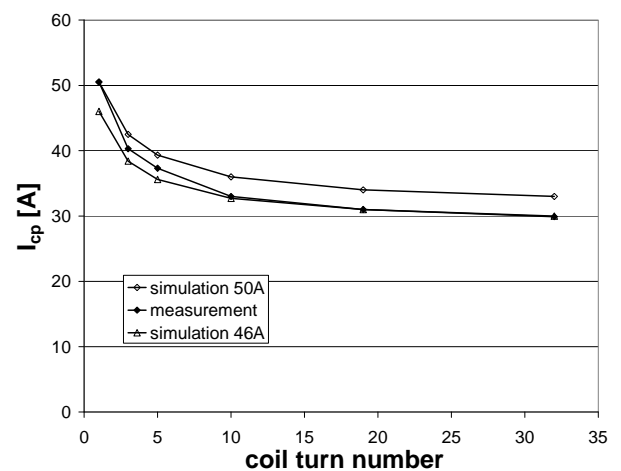


Fig. 3. Measured and simulated critical current density of a Bi2223 pancake coil, I_{cp} , as a function of the number of turns [7].

is much more sensitive to the radial field than the vertical one and the radial field saturates for a large number of turns [4]. We also predicted the critical current density from the internal $J_c(\mathbf{B})$ characteristics and the self-consistent method introduced above, showing a very good agreement (Fig. 3). The discrepancy is due to the length inhomogeneity of the tape, which critical current presented a 10 % variation.

We measured the coil AC loss by means of a transformer. The coil is short-circuited and is the secondary of the transformer. The details of the measurements can be found in Ref. [7]. Summing up, the current, which is sinusoidal, is measured by means of a Robowsky coil around the copper wire that short-circuits the pancake coil; the voltage is measured by means of a pick-up coil around the transformer core; and the AC loss is the product of the rms values of the current and the first in-phase harmonic of the voltage. This harmonic is measured by means of a lock-in amplifier. We also explored other measuring alternatives in Ref. [7].

The AC loss measurements agree very well with the simulations (Fig. 4). The AC loss per unit tape length increases with increasing the number of turns in the coil (Figs. 4 and 5). This is because the average magnetic field increases with the number of turns. As we showed in [4], a larger mean magnetic field in the radial direction increases the AC loss also if J_c is constant. This explains why the AC loss increases from 19 to 32 turns, while the critical current practically does not change. A possible origin of the discrepancy between the experiments and the calculations at the large number of turns can be the tape inhomogeneity. Indeed, the extraction of the $J_c(\mathbf{B})$

dependence has been done assuming a uniform J_c . A position dependence would change the field dependence of $J_c(\mathbf{B})$ extracted from critical current measurements.

In conclusion, the AC loss and the critical current in a pancake coil can be predicted by the simulation tools we have presented above. Besides, we have shown that it is very convenient to measure the coil AC loss by means of a transformer. This work settles the basis for the simulation and measurement of coated conductor coils.

This work was supported by the Slovak Research and Development Agency under the contract No. APVV-51-045605, the European Atomic Energy Community under the contract FU07-CT-2007-00051 and the European Commission under contract No. MRTN-CT-2006-035619.

- [1] Claassen, J. H.: *Appl. Phys. Lett.* **88** (2006) 122512.
- [2] Polak, M., Demenčík, E., Jansak, L., Mozola, P., Aized, D., Thieme, C.L.H., Levin, G.A., and Barnes, P.N.: *Appl. Phys. Lett.* **88** (2006) 232501.
- [3] Grilli, F. and Ashworth, S.P.: *Supercond. Sci. Technol.* **20** (2007) 794.
- [4] Pardo, E.: *Supercond. Sci. Technol.* **21** (2008) 065014.
- [5] Pardo, E., Sanchez, A., and Navau, C.: *Phys. Rev. B* **67** (2003) 104517.
- [6] Pardo, E., Gömöry, F., Šouc, J., and Ceballos, J.M.: *Supercond. Sci. Technol.* **20** (2007) 351.
- [7] Šouc, J., Pardo, E., Vojenčiak, M., and Gömöry, F.: *Supercond. Sci. Technol.* **22** (2009) 015006.
- [8] Gömöry, F.: *Appl. Phys. Lett.* **89** (2006) 072506.
- [9] Rostila, L., Lehtonen, J., Mikkonen, R., Šouc, J., Seiler, E., Melišek, T., and Vojenčiak, M.: *Supercond. Sci. Tech.* **20** (2007) 1097.

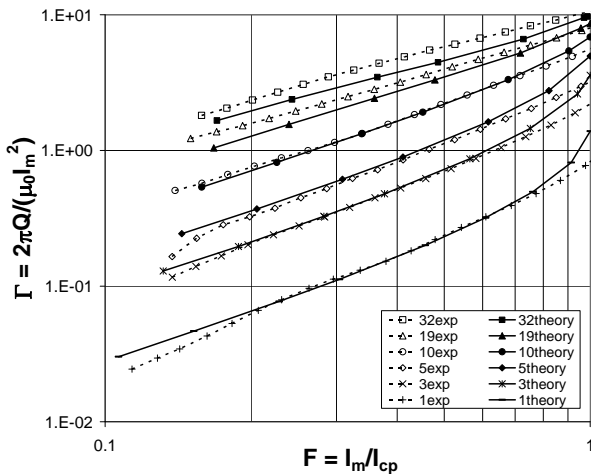


Fig. 4. AC loss per cycle and unit tape length, Q , normalized to the current amplitude, I_m , square for Bi2223 coils with 1, 3, 5, 10, 19 and 32 turns [7]. The horizontal axis is the current amplitude normalized to the coil critical current, I_{cp} . The simulations (symbols with solid lines) agree with the experiments (symbols with dash lines).

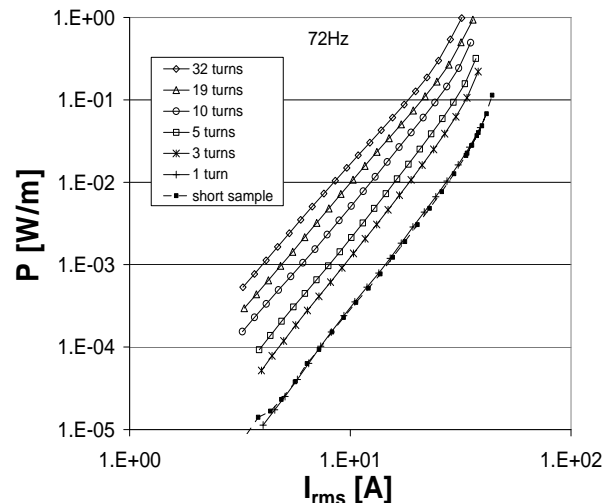


Fig. 5. Power AC loss at 72 Hz for the same pancake coils as in Fig. 4. The AC loss for one turn is the same as for a short straight sample.

Performance improvement of superconducting tapes due to ferromagnetic cover on edges

M. Vojenčiak, J. Šouc, and F. Gömöry

The critical current density of superconductor strongly depends on local magnetic field. Moreover, this dependence is nonlinear and anisotropic with respect to the ab-plane of superconductor crystal structure. As was experimentally found [1] and confirmed by numerical simulations [2] it is possible to improve the critical current of BiSCCO-2223 tape using ferromagnetic material deposited on the tape edges. This material makes the distribution of magnetic flux density in the tape more parallel to ab-plane of the crystal structure.

Improvement of the self-field critical current up to 15 % has been achieved by this procedure. The critical current of such tape strongly depends on geometric and magnetic properties of both the superconducting tape as well as the ferromagnetic cover. Numerical method, based on the critical state model using commercial finite element method (FEM) code, has been developed. Using these calculations, optimization of the cover thickness and width was performed to achieve the best improvement of the self-field critical current.

Besides the confirmed improvement of the critical current it is important to know how the edge cover would influence the AC loss. The results achieved experimentally for the superconducting conductors partially covered by ferromagnetic material have shown significant reduction of the AC loss [3]. We observed that both the transport (i.e. self-field) loss as well as the loss in applied magnetic field is lower for the tapes with Ni-covered edges.

Samples of commercially available BiSCCO-2223/Ag tape have been partially covered by the ferromagnetic material following suggestions of the optimization

calculations. Electroplated nickel layer has width of 1 mm and thickness of 30 μm . Critical current of the sample was improved of 14.8 % from 100.8 A to 115.7 A. This sample was then investigated from the AC loss point of view.

In the case of applied AC transport current, classical method using two voltage taps was employed. Measured AC transport loss of the bare tape and the tape with nickel edges are compared in Fig. 1. Measured losses are reduced in the whole range of applied transport current.

Magnetization loss was measured in conditions of homogenous applied AC magnetic field up to 70 mT, perpendicular to the wide face of the tape. Calibration-free method was utilized for these measurements [4]. Loss is again essentially reduced, as it is shown in Fig. 2. Indeed magnetization curves of nickel layer, at higher applied magnetic fields ferromagnetic cover starts to saturate. This results in suppressing of magnetic shielding and increase of loss to the level of non-covered tape.

Concluding that, by using a ferromagnetic layer tens of micrometers thick it is possible to increase the critical current by 15 %, to reduce magnetization and transport loss to less than 30 % and 40 %, respectively, comparing with values of non-covered tape.

[1] Alamgir, A.K.M., Gu, C., and Han, Z.: *Physica C* **432** (2005) 153.

[2] Gömöry, F.: *Appl. Phys. Lett.* **89** (2006) 072506-1.

[3] Gömöry, F., Šouc, J., Seiler, E., Klinčok, B., Vojenčiak, M., Alamgir, A.K.M., Han, Z., and Gu, C.: *IEEE Trans. Appl. Supercond.* **17** (2007) 3083.

[4] Šouc, J., Gömöry, F., and Vojenčiak, M.: *Supercond. Sci. Technol.* **18** (2005) 592.

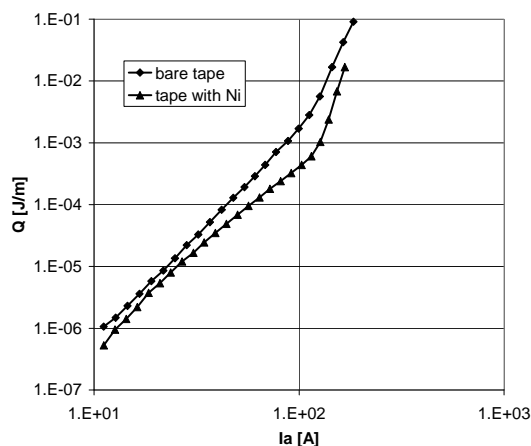


Fig. 1. Comparison measured AC transport loss (superconductor carries AC transport current) of non-covered tape and tape partially covered by nickel.

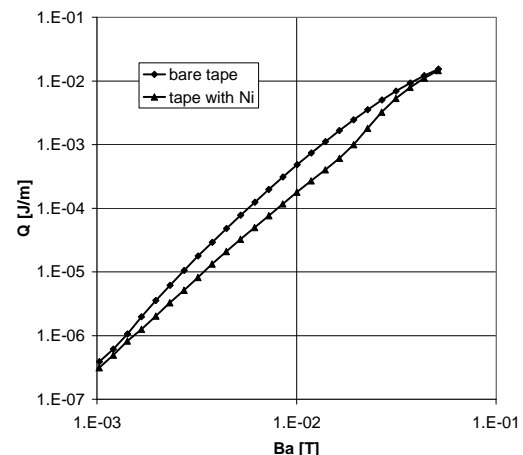


Fig. 2. Comparison measured AC magnetization loss (perpendicular field) of non-covered tape and tape partially covered by nickel.

AC susceptibility measurements of superconductors in high magnetic fields at various temperatures

L. Frolek, E. Seiler, and F. Gömöry

Study of AC susceptibility (χ_{AC}) in high magnetic fields provides information relevant for some applications e.g. tokamak fusion machines. AC loss in superconductor can be determined from the AC susceptibility data. AC susceptibility measurements for these purposes require a measurement setup designed for a wide range of magnetic fields and temperatures. The main problem is the sample holder [1] which must be designed to work in small space and has to satisfy all the requirements of the measurements (creation of relatively high amplitudes of AC magnetic fields, operation in a wide temperature range, measuring of the sample temperature, possibility to measure properties of samples of different thickness and magnetic field probing).

The sample holder (Fig. 1) was designed for operation inside the working diameter of the variable temperature insert (VTI) of the LHe cryostat which is 30 mm. The sample holder includes primary AC coil, measurement coil, compensation coils and a position adjustable insert. This insert contains a Cernox thermometer for the temperature measurement and a Hall probe for the magnetic field probing. Due to the position adjustable insert this sample holder allowed us to measure wires and tapes of different thickness. Achieved amplitudes of AC magnetic field are 50 to 90 mT depending on the cooling power. The transfer function of primary AC coil is 14.7 mT/A, the compensation of pure inductive signal is better than 99.75 % and the sample space diameter is 10 mm. The achieved AC magnetic field amplitude is worthy of remark because it is ten times higher than those in commercial susceptometers.

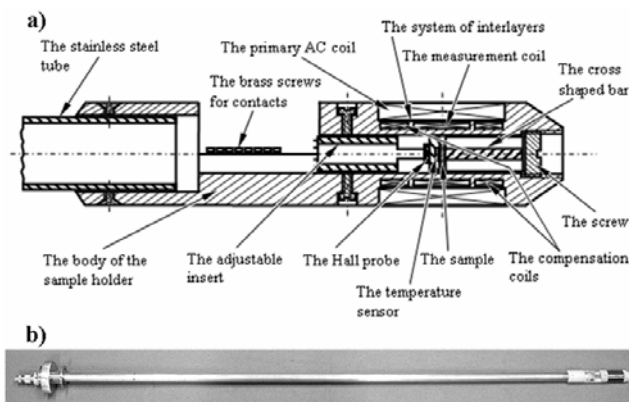


Fig. 1. a) Graphic cross section of the body of the sample holder with all its components (it is non in scale). b) All-inclusive view of the complete sample holder.

Our experimental set-up [2] enables to determine AC susceptibility in the temperature range 1.5-300 K at magnetic fields up to 14 T. The Oxford Instruments superconducting magnet, cryostat and variable temperature insert is used in this set-up. A lock-in amplifier is used for voltage measurement.

The real χ' and imaginary χ'' components of the χ_{AC} measured by this system for YBCO-coated conductor are shown in Fig. 2 for two values of the DC magnetic field. In [3] other AC susceptibility measurements were presented at several constant temperatures in the range 3-50 K and in background DC fields 8-14 T. The AC losses determined from measured AC susceptibility data are shown in [4]. From the obtained results it can be concluded that in high magnetic fields (~10 T and more) the working temperature is crucial for the loss performance of the wire and the magnetic field has only small impact.

This work was supported by the European Commission (contract No. FU06-CT-2006-00441) and grant agency APVV (contract No. APVV-51-45605).

[1] Frolek, L., Gömöry, F., and Seiler, E.: *Supercond.. Sci. Technol.* **21** (2008) 105009.
 [2] Frolek, L., Seiler, E., and Gömöry, F.: *Proc. of the Inter. Cryogenic Material Conf. '06*, Eds. D. Evans et al. Praha: Icaris 2007. Vol. 2 (2007) p. 117.
 [3] Seiler, E. and Frolek, L.: *Acta Physica Polonica* **113** (2008) 379.
 [4] Seiler, E. and Frolek, L.: *J. Phys.: Conf. Ser.* **97** (2008) 012028.

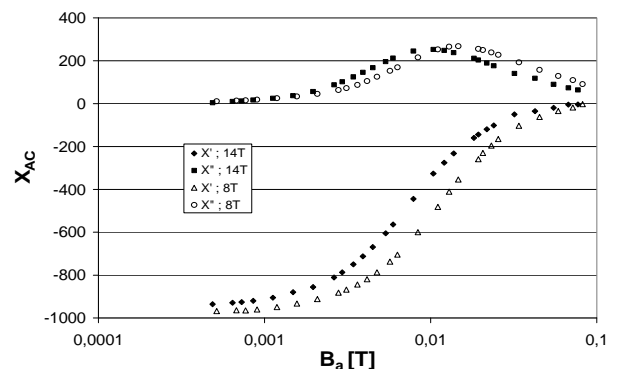


Fig. 2. Graph of real part χ' and imaginary part χ'' of complex AC susceptibility χ_{AC} measured at applied DC magnetic fields of 14 T and 8 T and a temperature of 20 K for a YBCO coated conductor sample. B_a is the amplitude of the applied AC magnetic field and the frequency is 21 Hz.

Department of Electrodynamics of Superconductors

Pavol Ušák

Research scientists

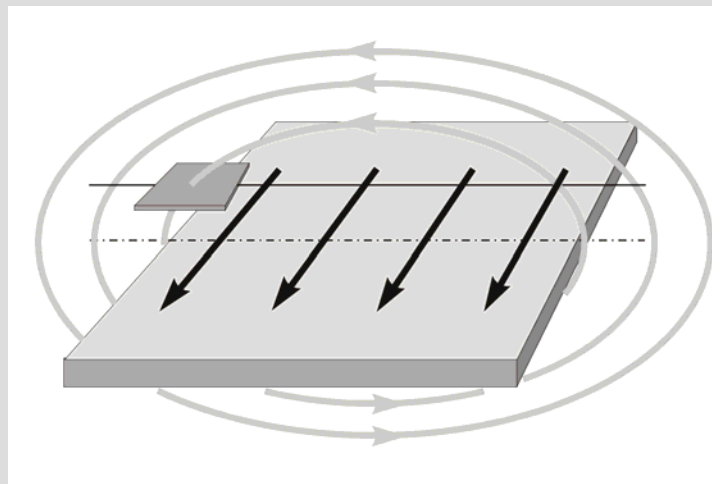
Milan Polák
Eduard Demenčík

Technical staff

Jozef Talapa
Dagmar Erbenová

Research Engineers

Jozef Kvitkovič
Pavol Mozola



The profile and research orientation of the Department of Electrodynamics of Superconductors are determined by the available instrumentation, up to now accumulated knowledge and achieved skills of staff, confronted with expected new opportunities and challenges. The emphasis is put on the study of superconductors and technical or physical problems encountered in connection with their practical applications in the transport and production of electrical energy (windings of magnets and magnetic vessels, transformers, electrical generators, cables). Both, classical LTS (e.g. well established NbTi, Nb₃Sn) and HTS (e.g. 1st generation BiSCCO or perspective 2nd generation YBCO, DyBCO), are the objects of our interest.

The activities of the department were framed by the projects APVV-51-002305 („*The Study of current distribution in superconductors for DC and AC applications*”, principal investigator P. Ušák) and LPP-0245-06 (“*The Dynamics of current distribution in superconductors of 2nd generation intended for AC applications*”, principal investigator P. Ušák, a supportive project for post-doc position of our PhD absolvent E. Demenčík). In parallel we solved the AFOSR project (FA 8655-07-1-3005, “*Electromagnetic and thermal properties of YBCO coils in AC regime*”, principal investigator M. Polák, international cooperation with Dayton Air Force Base, USA) and VEGA project (“*Temperature aspects of dissipative processes in superconductors*”, principal investigator P. Ušák). We have been interested in the study of dissipative effects in superconductors and superconducting windings, inevitably connected with their operation, especially in AC and pulse applications. We applied a thermal method, relating the steady heat input to the temperature response of a sample, to the measurement of losses for a variable phase shift between external ac magnetic field and sample ac transport current. The temperature increase was used as an indicator of the losses. We built an experimental set-up, including an appropriate software control of the frequency, phase shift and independent definition of amplitudes for I_{tr} , B_{ext} (LabView). We had the ambition to broaden our interest to a more general concept of the stability, i.e. to take into account also the disturbance spectrum generated during the loading of a superconducting device, the thermal properties of the superconductor and the cooling conditions. We measured the voltage and temperature response to a local heat pulse applied to a superconducting tape with current. The axial distribution of a heat input, amplitude and duration of the pulse, as well as cooled surface changed in experiments (HTS, LN₂ at 77K).

The fact, that we combined our experience in the field of superconductivity with the technology of semiconducting Hall probes, developed in our Department, had positive synergetic effect. The probes were used as sensors to map the magnetic fields of superconductors and superconducting windings.

We implemented the procedures for solving the inverse problem based on Biot-Savart relation. We improved them and successfully applied to the measurement of current distribution in superconducting object (tape, wire, cable, winding), using the mapped data of its self magnetic field. We were motivated by the importance of current distributions in superconductors and superconducting windings with regard to the losses, stability and current load threshold of superconductors and cables. We also had the ambitions to boost the application potential of our Hall probes. The publication of our measurement and mapping procedures and the procedures of data evaluation were intended to attract an attention of researchers to this field of non-destructive characterization of superconductors and to make other people interested in our Hall probes.

One of the applications of the method of non-contact measurement of the current distribution is connected with the mechanical load imposed on a superconducting winding of a superconducting device during its operation or during process of cabling. Especially cables, composed of fragile Nb₃Sn wires, are sensitive to mechanically involved degradation of their critical currents. We performed several experiments dealing with the problem. We deformed a Nb₃Sn wire by bending it to a given radius and compared the profiles of $B_z(self)$ component of self-magnetic field of remnant current loops, induced by an external magnetic field B_z , before and after the deformation. Analogical experiments were done on the wire supplied with DC transport current I_x . The mapping of self magnetic field $B_y(self)$ of the wire was realized at the background of an external magnetic field B_z , as well as at a zero level of external field. The appropriate level of an external magnetic field is necessary to approach the region of the critical current ($I_c = I_c(B)$ is a decreasing function) of the wire, where the degradation effects are most pronounced. The selection of B_y component (perpendicular to the external field B_z) for mapping (and inverse calculation of the current) allowed to emphasize the role of self field of the sample and to diminish the impact of the external field to input data for the calculation. The current distribution under I_c was heavily influenced by the history of the external magnetic field and less by the history of current. This matches the reality encountered in expected applications. The measured sample was a type intended for use in a cable for the winding of magnetic vessels of ITER. The maximum external magnetic field applied in our test experiments was half of the level expected in the real windings, and the maximum current achieved was well under the critical value. We encountered problems with the precision of localization of the field sensor. The high precision is inevitable for inverse calculations.

Our agenda in brief: the dissipative processes related to losses and stability, current distribution in superconductors, applications.

Pavol Ušák

The current distribution in a striated YBCO tape subjected to both a magnetization and a transport current

P. Ušák, M. Polák, E. Demenčík, and J. Kvitkovič

High temperature superconducting (HTS) wire has achieved a new milestone as the $\text{YBa}_2\text{Cu}_3\text{O}_{7-x}$ (YBCO) coated conductor length now exceeds 300 m with high critical currents. To reduce hysteretic losses in the coated conductor, the YBCO tape is divided into a multifilamentary layer. Understanding of the current distribution in such a conductor is imperative as it is placed into applications. From a practical standpoint, the superconducting current is a result of induced magnetization currents caused by an appropriate change in an external magnetic field, a transport current due to an applied potential difference, or a combination of these two sources of current. Often, when the current distribution in the conductor is investigated, it generally considers transport current or the induced magnetization current, but seldom the combination of these two. Applications such as the HTS generator provide an environment where the YBCO conductor can be subject simultaneously to both current sources.

A non-destructive method of determining the current distribution can be achieved by measuring the self magnetic field in the vicinity of the tape and solving the inverse problem for the corresponding current distribution. Generally, this method has been used to examine applied transport currents, especially the longitudinal component of the current distribution in the lateral direction. We showed that the magnetization currents, induced in superconducting tape by an external magnetic field, can be reconstructed in the same way. We present here the results of an initial investigation of the current distribution in a multifilamentary YBCO tape, subjected to both magnetization and applied DC currents

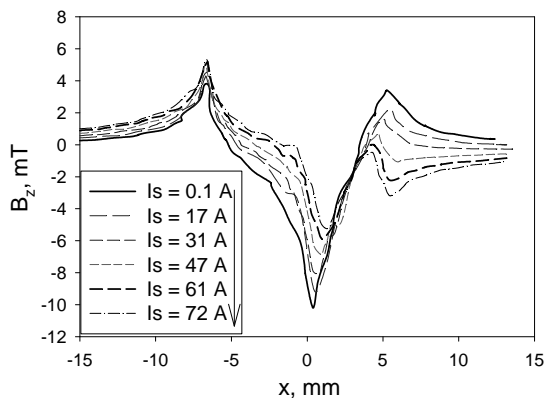


Fig. 1. Transversal magnetic field profiles of B_z component of the tape self field at $y = y_0$ (y is along the sample). The parameter is the gradually increasing transport current, applied after finishing the whole cycle of the external magnetic field, when $B_{z(\text{ext})} = 0$ mT.

[1]. The magnetization currents were induced by gradually changing the external magnetic field, sequentially from 0 to +60 mT, +60 to 0 mT, 0 to -60 mT, and then -60 to 0 mT. After the end of the cycle, we have applied gradually increasing transport current. The self-field profiles (see e.g. Fig. 1) were post-processed and prepared as an input for the inverse calculations to determine the current distribution. The application of the gradually increasing positive transport current into the sample results in the asymmetric change of the current distribution as evident in Fig. 2. In a superposition with the current loops, induced after falling external magnetic field to zero, we get an asymmetric change of the current distribution, seen here as sheet current profile at $y = y_0$. Left side of the tape is saturated by the positive branch of the induced currents, and the current change takes place on the right side only, with the negative branch. This asymmetry was up to now demonstrated only on a qualitative level.

This work was supported by the AFOSR grant, number FA8655-05-1-3062. The work was partially supported also by projects VEGA 2/5089/25, CENG, APVV-51-002305 and LPP-0245-06.

[1] Ušák, P., Polák, M., Demenčík, E., Kvitkovič, J., Levin, G.A., and Barnes, P.N.: *Supercond. Sci Technol.* **20** (2007) 994.

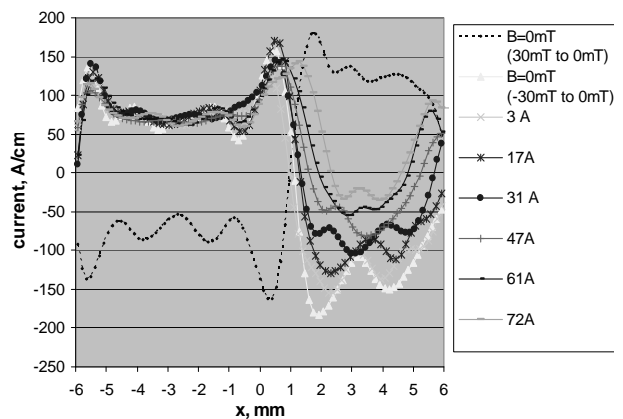


Fig. 2. The gradually increasing positive transport current in a superposition with the current loops, induced after falling external magnetic field to zero, result in an asymmetric change of the lateral current distribution, seen here as sheet current profile at $y = y_0$.

Current distribution in thermally degraded superconductor of 2nd generation

P. Ušák, M. Polák, and E. Demenčík

The current distribution in coated conductors has impact on their AC losses. Obviously, simplified assumptions are made concerning current distribution, e.g. in Norris theory for AC transport current losses a uniform critical current distribution is assumed. More realistic current distribution in superconducting tape was calculated by Brandt and Indebom (see ref. in [1]). To measure the current distribution in a real sample, both destructive and non-destructive methods are used: e.g. longitudinal cutting of the tape into sub-tapes, magnetic knife approach, lateral mapping of the self magnetic field profiles and inverse calculation of the corresponding transversal current distribution profiles, in a selected cross-sections along the tape. The most general and fruitful is the last one, successfully implemented also in our laboratory. As a mapping sensors are used InSb Hall probes, developed in our group. Biot-Savart inverse is realized by means of well established procedure, based on Tikhonov regularization, successfully tested numerically, as well as by comparing the experimental results with the results achieved on the same sample by principally different experimental method of magnetic knife.

Under certain circumstances a superconducting tape can be locally overheated. Most frequently this can occur in the vicinity of bad current contacts, or in the tape sections with reduced critical current. Up to now there are no papers dealing with the problem of current distribution change as a consequence of local overheating. The exceptions are one dealing with switches and parallel and serial configurations of thin layers of YBCO used in the current limiters. But even here the direct determination of the current distribution is absent. We have studied the influence of thermally induced local degradation on the current distribution at the vicinity of the destroyed portion of the tape. The burned out place was easily resolved even optically and was cut out. Transport current was applied to remnant tape to search the degree of degradation and to look for current distribution in the part adjacent to the burned one, but without any visually detectable traces of the damage.

Comparing the current distribution profiles, measured before (Fig. 1) and after (Fig. 2) the thermal destruction at one place, with the one (Fig. 3) measured at its vicinity, further from the destroyed portion, we demonstrated that the thermal damage was local and limited to several centimeters.

The project was supported by APVV-51-002305, LPP-0245-06 and VEGA 2/5089/25.

[1] Ušák, P., Polák, M., and Demenčík, E.: *Physica C* **455** (2007) 67.

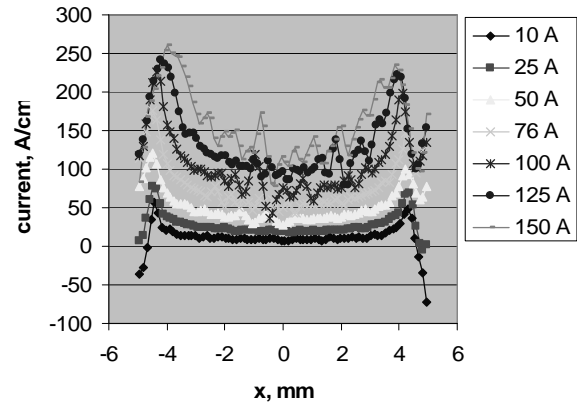


Fig. 1. Lateral transport current distribution during gradual increase of the current in intact DyBCO tape.

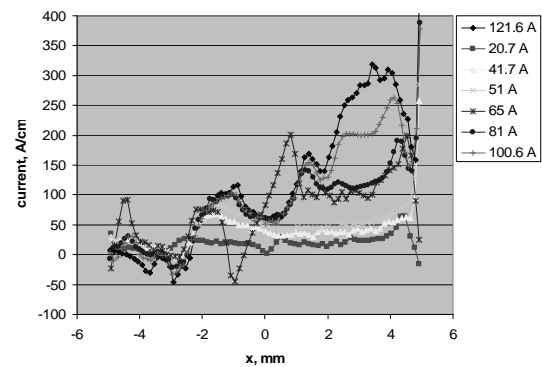


Fig. 2. Current profiles practically at the same place like in Fig. 1, but after burning. Burned portion is distanced 3 cm.

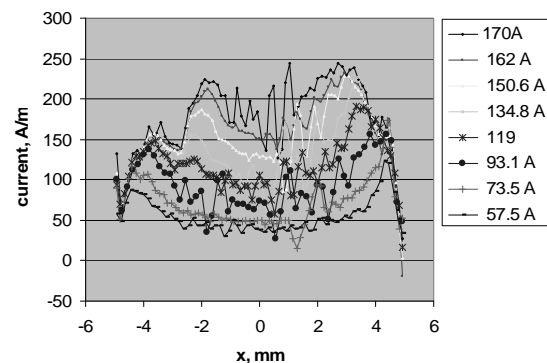


Fig. 3. The current profiles measured at somewhat larger distance (5 cm) from the burned portion. The profiles, corresponding to increasing transport current, resemble the one of intact tape, i.e. the damage is local and limited to several centimeters.

Current distribution in the winding of a superconducting coil

P. Ušák, M. Polák, J. Kvitkovič, and P. Mozola

The actual current distribution in the superconducting winding is a superposition of the magnetization and transport currents. It reflects a recent history and may be distributed non-homogeneously even within a single turn.

It is hard to reconstruct the current distribution dynamics and its history from the first principles, relying on the material properties of the superconducting tape. However, we can use the data of the radial component B_r of the self magnetic field of the coil, mapped outside the coil in the plane and in close vicinity around the selected cross section of the winding, and put it into inverse calculation of distribution of current circumferential component within the cross section. We have used principally the same approach as in the case of the cable. The discrete mesh of the straight virtual conductors in the cross section of the cable is, however, replaced by a discrete mesh of equal rectangles covering the winding cross section. The rectangles are cross sections of independent virtual circular turns (sub-coils), replacing the real winding (see Fig. 1). We are to determine the circumferential component of the current I_{yi} , perpendicular to the winding cross section plane, for each rectangle of the virtual current mesh, from the B_r field data mapped outside. Both, the circular currents ($I = I_{yi}$ in a virtual turn) in the discrete mesh of the sub-coils and discrete mesh of the B_{ri} data, gathered on a mapping track outside, are to reasonable degree related by Biot-Savart law, i.e. inverse calculation has sense. Since our pancake coil had 20 turns and each actual tape turn was replaced by 10 virtual sub-turns arranged axially, for the same radius, full number of knots was $n = 20 \times 10 = 200$. The smooth current distribution across the tape width, i.e. height of the pancake winding (horizontal axis in Fig. 2, Fig. 3 or vertical in Fig. 1), was approximated by 10 values of sheet current density i_i [A/cm]. The results have to be checked further, to avoid artifacts, especially the role

of the distance of mapping line from individual turn (at a given radial parameter).

This work was supported in part by the APVV-51-002305, LPP-0245-06, VEGA2/5089/25, AFOSR grant number FA8655-05-1-3062 and CENG.

[1] Ušák, P., Polák, M., Kvitkovič, J., Mozola, P., Barnes, P.N., and Levin, G.A.: *IEEE Trans. Applied Supercond.* **18** (2008) 1597.

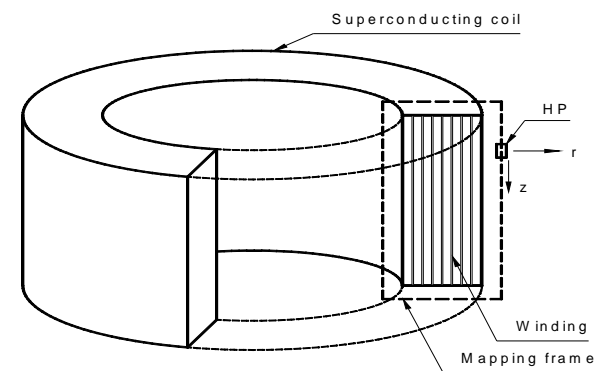


Fig. 1. Schema of possible mapping frame around coil winding cross-section.

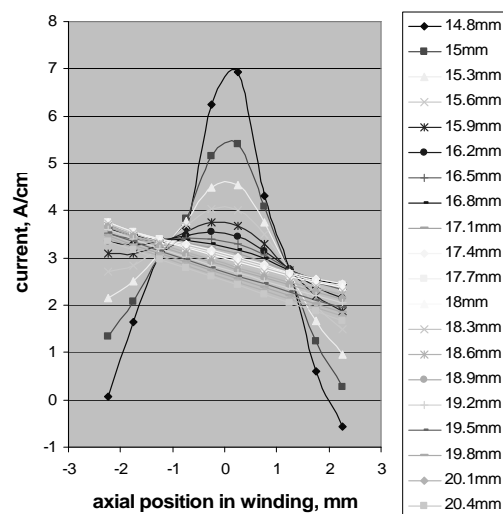


Fig. 2. Current distribution in cross section of the YBCO coil after reaching $I = 30$ A in virgin run. Parameter is radial position.

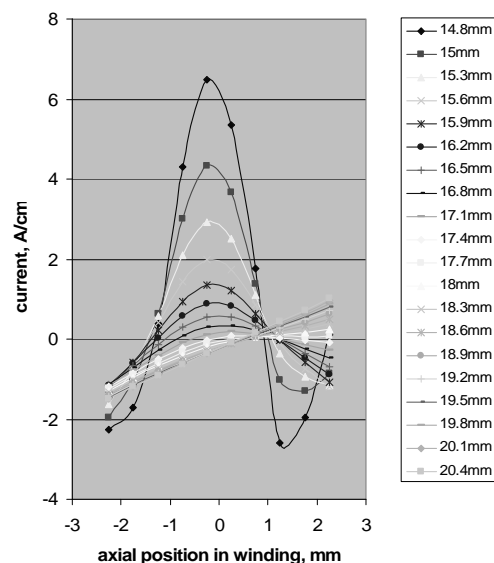


Fig. 3. Current distribution in cross section of the coil after current decrease to $I = 0$ A (from level $I = 30$ A).

Distribution of magnetic field inside the winding of a BSCCO coil

J. Kvitkovič, M. Polák, and P. Mozola

Recent development of the BSCCO tapes resulted in relatively long tapes with improved electrical and mechanical parameters. They can be used in windings of various electrical devices as motors, generators, transformers and cables.

However, the BSCCO tapes suffer from anisotropy of critical current with respect to the orientation of magnetic field. If the magnetic field vector B is applied perpendicular to the flat face of the tape, the critical current is lower, comparing to the parallel configuration. This behavior is directly related to the structure and orientation of grains in filaments. In a pancake winding it is just radial component B_r of the coil field B which is perpendicular to the tape face. For every turn its maximum is at tape edges. Reduction of the critical current density at tape edges can be, to some degree, improved by magnetic shielding, diverting magnetic flux around the most exposed parts of the tape. The drawback is an increase of the total AC loss, because of the presence of magnetization effects of the shield. The superconducting part of the loss of the pancake winding, still present even without the magnetic shield, is influenced by the winding geometry and local value and orientation of the magnetic field. Intrinsic properties of the BSCCO tape itself are decisive for the loss.

Because of the complicated structure of the local value and orientation of the magnetic field B within the winding, it is worth of attention to try to estimate it, at least in selected parts, directly by a measurement. We present the results of the measurements of the radial component B_r of the magnetic field distribution inside the BSCCO pancake coil [1]. The tracks of B_r field mapping were in axial direction, parallel to the coil axis, in different slots between the turns, arranged radially from inner to outward (Fig. 1). The mapping track well overlapped the tape width (4 mm). There were 3 slots. We mapped also in coil hole, in vicinity of the innermost turn of the winding and along the outer winding surface. Also here, the mapping track of the Hall probe, used as

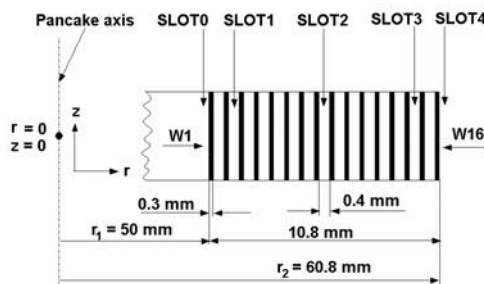


Fig. 1. The cross-section of the pancake winding. $W1-W16$ are the turns. The vertical arrows mark the positions of the mapping tracks. (Sketch is not to the scale.)

a sensor, was parallel to the tape surface. Additional mapping was done also in radial direction, over the pancake upper side.

The $B_r(z)$ profiles at maximum current 75 A, achieved in virgin run, are shown in Fig. 2. To demonstrate the role of magnetization currents and the history of feeding, we show, for comparison, also the profiles $B_r(z)$ mapped at the same tracks but after current change to -20 A.

The current ramping up and down over the 60 A level has only a little influence on the measured $B_r(z)$ field profiles. The role of the magnetization currents is small. The observed differences in shape between these profiles, and profiles calculated under the assumption of the homogeneous sheet current distribution across the tape width, can be explained as a result of inhomogeneities in critical current density distribution. Intrinsic one, as well as one influenced by the local value of the magnetic field.

This work was supported by AFOSR under Grant FA8655-07-1-3005, in part by Projects VEGA 2/5089/25, Center of Excellence CENG, Slovak Academy of Sciences, and APVV-51-002305.

[1] Kvitkovič, J., Polák, M., and Mozola, P.: *IEEE Trans. Applied Supercond.* **18** (2008) 1621.

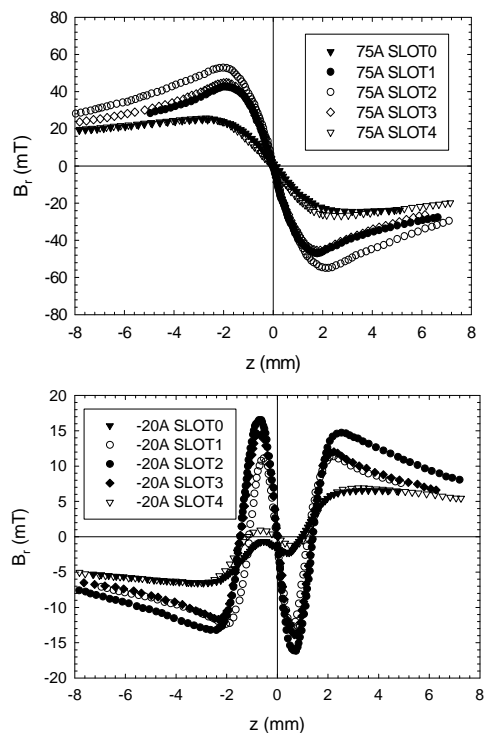


Fig. 2. Comparison of measured $B_r(z)$ profiles in slots 0 – 4 at maximum coil current 75 A and after current change to -20 A.

Hall probe based system for study of AC transport current distribution in YBCO coated conductors

E. Demenčík, P. Ušák, and M. Polák

High temperature superconductors (HTS) are potential candidates for the AC applications in systems related to electrical power generation and transport. These applications require operation at AC, typically with frequencies up to 1 kHz. The operation under mentioned conditions introduces loss in HTS tapes. In the real HTS tapes the current distribution can significantly differ from the homogeneous one, supposed in simplified theoretical models, used in loss calculations. It is therefore extremely important to study the tape behavior when operating under ac transport current at higher frequencies.

We have focused on the study of the lateral current distribution in perspective YBCO tape carrying AC transport current [1]. We compared the current distributions, measured at various phases of the AC current, with those for DC current, set to the level equal to the magnitude of the AC current for a given phase. We have deduced on current distribution from Hall probe mapping of self magnetic field of the tape. Two ways can be used in gathering the mapped data: we can trigger sampling by a given level of current, e.g. $I = 0$ A, and sample the time evolution of the component $B_z(t)$, perpendicular to the tape plane, during all the cycle, for every point x of the mapping track. Then, in numerical evaluation, we can reconstruct the field distribution $B_z(x)$ for a desired phase, or alternatively, we can repeatedly trigger the sampling just to one value, corresponding to a

selected phase of the current and directly map the field $B_z(x)$ just for this phase. In both methods, the profiles $B_z(x)$ are used in inverse calculation of the lateral sheet current distribution across the width of the tape, for a given phase of the current. In the measurements, presented here, we have used the second approach (see results in Fig. 1, Fig. 2).

The mapping track was in the tape center, only several hundreds micrometers distanced from the superconducting layer. The tape was 4.2 mm wide and several centimeters long. The current flows mainly in y direction and cumulative input to the B_{zi} value, measured at a given point $x_i, z_i, y = 0$ mm, from the currents, distant in y direction, is small. The inverse calculation from $B_z(x)$ gives the lateral current distribution close to the real one and just under the mapping line. Artifacts may arise from incorrect phase determination, encountered in measurement.

This work was supported by the projects VEGA 2/5089/25, EFDA/EURATOM project FU06-CT-2005-00007, APVV-51-002305, and CENG.

[1] Demenčík, E., Ušák, P., Polák, M., Levin, G.A., and Barnes, P.N.: *IEEE Trans. Applied Supercond.* **17** (2007) 3175.

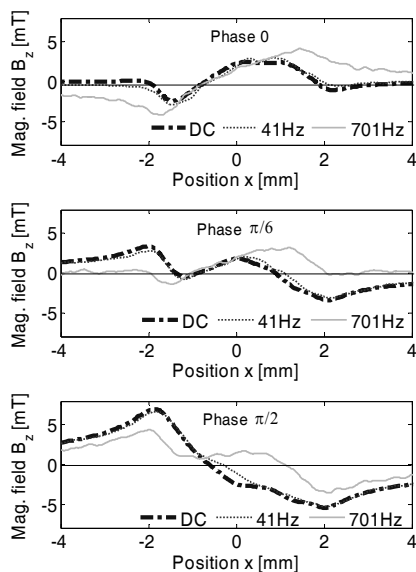


Fig. 1. Comparison of $B_z(x)$ distributions sampled for different phases of AC cycle with the one of DC transport current. The DC current equals to the AC current value for a given phase. The comparison is made for frequencies 41 Hz and 701 Hz.

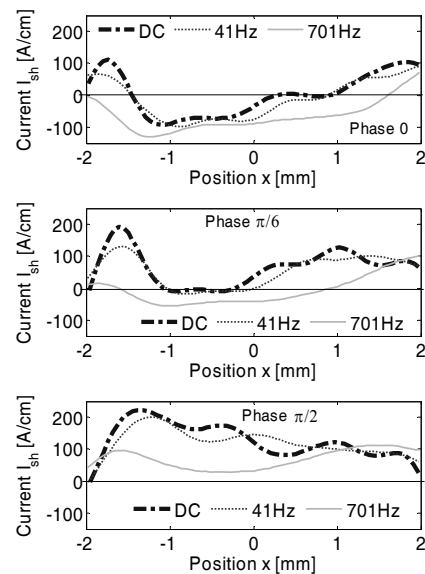


Fig. 2. The lateral sheet current distributions across the width of YBCO tape calculated from the mapped data. We have used Biot-Savart formula.

Frequency dependence of AC loss in YBCO tapes and pancake coils

M. Polák

The energy dissipation in a superconductor exposed to AC electromagnetic field (AC loss) is very important for its application. As known, AC loss in several millimeter wide YBCO tape, exposed to perpendicular AC magnetic field, is unacceptably high. The wide thin film tape is subdivided into narrow filaments to reduce the large hysteretic loss. Finite resistance between filaments causes so called coupling losses. They can be reduced by a filament twisting.

For the successful development of low AC loss YBCO conductors, we need reliable methods for evaluation of the total loss and determination of its components, related to material and structural parameters. The hysteretic loss, which is supposed to have small frequency dependence, and the coupling loss, proportional to the square of the sweep rate or frequency of AC field, are the most important components [1].

We studied the frequency dependence of the loss in simple and also striated YBCO tapes [1], as well as in YBCO coils, wound with non-striated YBCO tapes [2]. As an example, in Fig. 1 we show the dependence of the loss on frequency for an YBCO filamentary tape in wide frequency range from 1 mHz up to 700 Hz. Below 20 Hz the loss is predominantly hysteretic. Still present small increase of the loss with frequency may be attributed to non-linear shape of the voltage-current curves. Above 20 Hz the contribution of coupling loss to the total loss is distinctive. The sample was striated using the laser ablation. This procedure led to finite resistances between the filaments.

To study the properties of the coils made out of the second generation superconducting wire (YBCO), in

particular their AC behavior, we designed, manufactured and tested an experimental double pancake coil wound with copper stabilized YBCO coated conductor, 4.2 m long and 4 mm wide. The critical current of a short sample was 53 A at 77 K, in self-field. The critical current of the single pancake coil, according to the same voltage criterion 1 μ V/cm, was approximately $I_c = 30$ A.

The AC loss in the double pancake coil ($I_c = 23$ A) was measured at frequencies 54 Hz, 108 Hz, 216 Hz, 432 Hz and 864 Hz. At the critical current ($I_{c,rms} = 16.2$ A) and frequency 432 Hz, the total coil loss was 0.9 W. Only very small frequency dependence of the loss per cycle was observed in the frequency range from 27 Hz up to 864 Hz (Fig. 2). This indicates predominantly hysteretic character of the coil loss at this range.

This work was supported by European Office of Aerospace Research and Development (EOARD), Award No FA8655_07-1-3005.

- [1] Polák, M., Kvitkovič, J., Mozola, P., Ušák, P., Barnes, P.N., and Levin, G.A.: *Supercond. Sci. Technol.* **20** (2007) S293.
- [2] Polák, M., Barnes, P.N., Kvitkovič, J., Levin, G.A., Mozola, P., and Ušák, P.: *IEEE Trans. Applied Supercond.* **18** (2008) 1240.

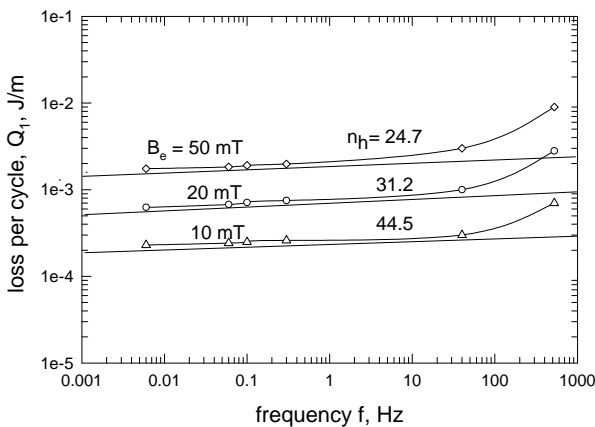


Fig. 1. The frequency dependence of loss per cycle and meter, at various magnetic field amplitudes, for sample YBCO 10 mm wide, 20 filaments 0.47 mm wide, on Hastelloy substrate.

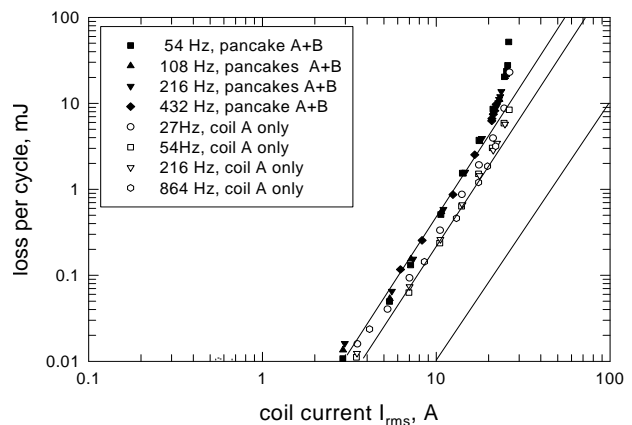


Fig. 2. Loss per cycle vs. coil current for the double pancake YBCO coil (pancakes A and B are in series) and for one pancake coil (A) measured separately.

Department of Cryoelectronics

Štefan Chromik

Research scientists

Štefan Beňačka
Vladimír Štrbík
Marianna Španková
Michaela Sojková-Valeriánová
Ondrej Vávra
Jozef Vincenc Oboňa

Research Engineers

Štefan Gaži

Technical staff

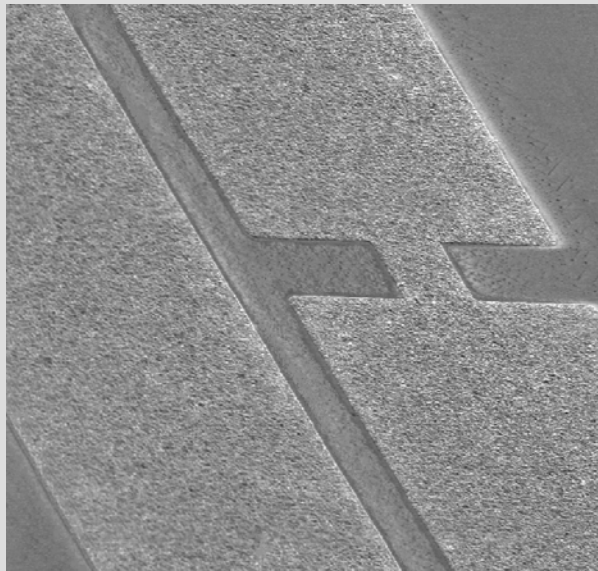
Peter Drlička
Alexander Taldík

PhD Students

Agáta Dujavová

Students

Michal Kovačič



The main research activities of the Department of Cryoelectronics in 2007-2008 can be divided into the following areas:

- Thin superconductor and manganite oxide films and structures,
- Superconducting MgB_2 films,
- Dielectric oxide films for cryoelectronics,
- Films and structures based on conventional superconductors,
- High-temperature superconductor (HTS) weak links.

We prepared and studied thin manganite LSMO films on MgO and MgO-buffered GaAs substrates. The structural and magnetic properties of the films were analysed. The YBCO/LSMO/YBCO heterostructures were investigated. Bi-epitaxial YBCO Josephson contacts on tilted YSZ/NGO substrates were also studied. We found out a good agreement of the angle influence on the critical current of bi-epitaxial contact localized between d-wave superconductors with the Siegrid-Rice theoretical prediction.

We continued to prepare thin MgB_2 superconducting films by sequential evaporation. We studied the link between the technology of the MgB_2 films and their magnetic properties.

We observed that our MgB_2 films prepared on the SiC/Si substrate at high temperatures behaved like a film consisting of two different superconducting layers, as the consequence of a diffusion process between the SiC/Si substrate and the MgB_2 film.

Our activities were supported mainly by the Slovak Grant Agencies for Science and Technology: (1) Under VEGA project No. 2/3116/23 "*Josephson effects in superconducting weak links and their application in cryoelectronics circuits*", and (2) under VEGA project No. 2/7125/27 "*Josephson effects in the structures of unconventional superconductors*". We studied the possibility of integration of passive HTS with active semiconductor GaAs and GaN devices for the millimeter wave band. To combine superconducting and semiconducting elements, it is necessary to deposit a suitable buffer film on top of semiconductor substrates: We applied thin MgO dielectric films as buffer layers on GaAs and GaN substrates. We have studied the structural properties of MgO films and the growth of superconducting YBCO films to achieve suitable properties. The research has been supported mainly by APVV project No. APVV-51-040605 "*Monolithically integrated circuits based on GaAs (GaN) with passive superconducting filters for millimeter wave band*", and VEGA project No. 2/0139/08 "*Perspective thin films and structures for cryoelectronics on semiconducting substrates*." Besides that we worked on similar problems related to the preparation of thin perovskite manganite films on GaAs substrate under APVT project No. APVT-51-03-2902 "*Integrated micromechanical sensors of electromagnetic radiation on the basis of thin manganite*

films". The department also coordinated an international INTAS project entitled "*Metal oxide thin film heterostructures on tilted – axes substrates*".

We have studied HTS films with the zero critical temperature above 100K. We have been focused on the influence of rhenium on Hg and Tl-based films. We developed a non-contact method of a mercuration process to prepare the first successful coplanar structures suitable for ultrafast photodetectors. The influence of rhenium on structural and electrical properties of the resultant thin HTS films was investigated. We worked on this task along with the Laboratoire de Cristallographie CNRS, Grenoble (supported by the international mobility project ECONET) and with the University of Rochester. The research was supported by the Slovak national VEGA projects. The Department of Cryoelectronics has been involved in the international networks, "*Nanoscience and Engineering in Superconductivity – NES*", "*Arrays of quantum dots and Josephson junction- AQDJJ*".

The Department of Cryoelectronics has co-operated on the development of HTS Josephson arrays with the Slovak Institute of Metrology.

Štefan Chromik

YBa₂Cu₃O_x films prepared on advanced semiconductor substrates

Š. Chromik, M. Španková, Š. Gaži, T. Lalinský, and I. Vávra

Recently, the field of new electronics based on III-V and III-N semiconductor materials with their main representatives such as GaAs, AlAs, GaN, AlN has rapidly developed. These materials seem to be usable in the design of new sub-millimeter wave devices and MEMS (Micro-Electro-Mechanical structures) [1]. Active elements on the base of these materials (HEMT structures and diodes) and passive elements are very efficient at temperature of liquid nitrogen 77 K. This gives a possibility of the integration of passive high-temperature superconductor (HTS) devices with active GaAs and GaN devices in the form of millimeter wave devices. The direct growth of HTS thin films on GaAs, however, may not only produce film with suppressed critical temperature but can as well cause damage to the GaAs substrate [2]. The suitable buffer film is necessary on the top of GaAs which will work as an efficient diffusion barrier and enable an oriented growth of the HTS film. We have prepared epitaxial MgO film on semiconducting cubic GaAs substrate [3] and hexagonal GaN substrates. In case of the MgO films grown on the GaAs we observed a cube on cube growth, while the MgO films prepared on the GaN grow with (111) plane parallel to GaN substrate surface.

YBa₂Cu₃O_x (YBCO) superconducting films were prepared using pulsed laser deposition method on both types of the substrates. X-ray diffraction analysis

confirmed *c*-axes oriented YBCO films for both cases (Fig. 1a). The films are superconducting, however, the T_{C0} is suppressed to ~65 K (Fig. 1b). In case of the GaAs substrate the properties of the final YBCO films are very sensitive to the deposition temperature and the duration of the deposition. For example, the sputtering method which needs much longer deposition time (few hours) was not able to offer superconducting YBCO films due to an interdiffusion process. On the other hand, MgO buffered hexagonal GaN substrate surprisingly enables to prepare *c*-axis oriented YBCO superconducting films by both methods at the substrate temperature ~700 °C. However, we observe a broad transition into superconducting state in spite of the fact that the GaN substrates are more resistive against high temperature treatment. We have used Φ -scan and transmission electron microscopy to study the situation in the *a*-*b* plane. Φ -scan showed twelve periodic peaks instead of expected four peaks. We revealed an interesting selected area diffraction (SAD) pattern which can be interpreted as the superposition of three single crystalline patterns rotated by 30° (Fig. 2) Such population of grains creates a network of weak links. Microwave measurements confirmed Josephson losses immediately after the transition into superconducting state through all temperatures down to 4.2 K. Josephson weak links produce noise undesirable for microwave applications.

This work was performed in cooperation with Dr. P. Gierlowski from the Institute of Physics PAN, Warsaw, Poland.

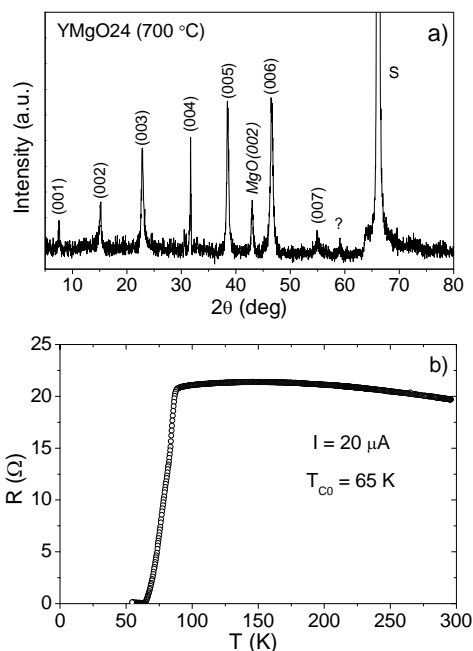


Fig. 1. a) Typical XRD pattern of YBCO film on GaAs containing only (00 l) peaks. b) Typical R(T) dependence of YBCO film grown on MgO buffered GaAs substrate.

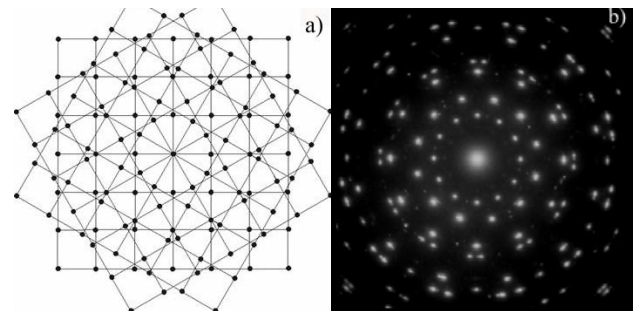


Fig. 2. a) Schematic SAD pattern – superposition of 3 single crystalline pattern rotated by 30°. b) Experimental SAD pattern of upper YBCO layer.

Epitaxial LSMO films grown on GaAs substrates with MgO buffer layer

M. Španková, Š. Chromik, I. Vávra, V. Štrbík, and P. Lobotka

On cooling of a manganese perovskite material, a spontaneous transition from paramagnetic to ferromagnetic state occurs characterized by a peak in resistance vs. temperature ($R(T)$) dependence. The large temperature coefficient of the resistance (TCR), defined as $1/R \times dR/dT$ is a prerequisite for intended fabrication of uncooled microbolometer based on GaAs MEMS (Micro-Electro-Mechanical structure) providing very good thermal isolation with manganite $\text{La}_{0.67}\text{Sr}_{0.33}\text{MnO}_3$ (LSMO) as a sensing film. Since there is a lattice mismatch and interdiffusion between the LSMO film and the GaAs substrate, it is necessary to insert between them an epitaxial MgO buffer film.

The MgO deposition was carried out using e-beam evaporation at a heater temperature of 600 °C at a partial pressure of oxygen $\sim 10^{-2}$ Pa. The deposition was followed by slow cooling down to a temperature of 300 °C at a rate of 0.6 °C/s [1]. In order to eliminate the arsenic desorption from the GaAs substrate the backside and the edges of the substrate were covered by a thin MgO film.

The LSMO films were deposited using a dc magnetron sputtering onto GaAs substrate with MgO buffer layer. The deposition was performed in an Ar + O₂ atmosphere at a total pressure of 40 Pa. The substrate holder was heated to 700 °C. In order to increase the oxygen content, the LSMO films were subsequently in-situ annealed in O₂ (10^4 Pa) at 690 °C for 40 min.

X-ray diffraction measurements indicate that the LSMO/MgO films exhibit only (00 ℓ) orientation. The FWHM values (ω -scan) measured on the (002) MgO and LSMO diffraction peaks were 1.8° and 1.7°, respectively.

Transmission electron microscopy (TEM) analyses revealed an epitaxial growth of the LSMO/MgO on the GaAs. The LSMO film exhibits a columnar epitaxial growth with typical block sizes up to 35 nm. The analysis

also revealed a polycrystalline growth of the LSMO on the surface of the epitaxial LSMO film (typical block size 40–45 nm). We have observed similar polycrystalline LSMO film growth in the case of the LSMO films deposited on the MgO single crystalline substrates [2]. In both cases the polycrystalline part of the LSMO can be a consequence of the post-deposition an-nealing process or it could be formed during the cooling period after the completion of the deposition.

Using Auger electron spectroscopy (AES) we detect a small amount of As and Mg on the LSMO/MgO/GaAs sample surface but not in the bulk of the thin film structure (Fig. 1). The origin of this contamination seems to be a consequence of the postannealing process where we suppose some local escape of As through the passivated backside and edges of the substrate. Some traces of In are also present on the LSMO film surface as a residua originating from the In contacts used for electrical measurements. We observe no Ga diffusion through the MgO barrier but a slight diffusion of Mn and La into the MgO barrier.

The temperature dependence of the resistance $R(T)$ for the LSMO/MgO/GaAs exhibits metal-insulator like transition (Fig. 2). The resistance peak occurs at 280 K. The maximal TCR ($\sim 2.3\% \text{ K}^{-1}$) occurs at $T = 249 \text{ K}$ [3].

We thank to J. Liday, SUT Bratislava for AES and J.P. Espinós, ICM Sevilla for XPS analyses.

- [1] Chromik, Š., Španková, M., Vávra, I., Liday, J., Vogrinčič, P., and Lobotka, P.: *Appl. Surf. Sci.* **254** (2008) 3635.
- [2] Španková, M., Chromik, Š., Vávra, I., Sedláčková, K., Lobotka, P., Lucas, S., and Stanček, S.: *Appl. Surf. Sci.* **253** (2007) 7599.
- [3] Španková, M., Chromik, Š., Vávra, I., Štrbík, V., Liday, J., Vogrinčič, P., Espinós, J.P., and Lobotka, P.: *accepted in Physica Status Solidi (a)*.

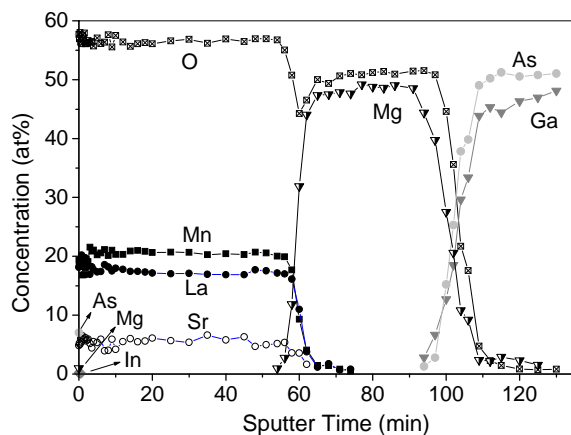


Fig. 1. AES depth profile of the LSMO/MgO film grown on the GaAs substrate.

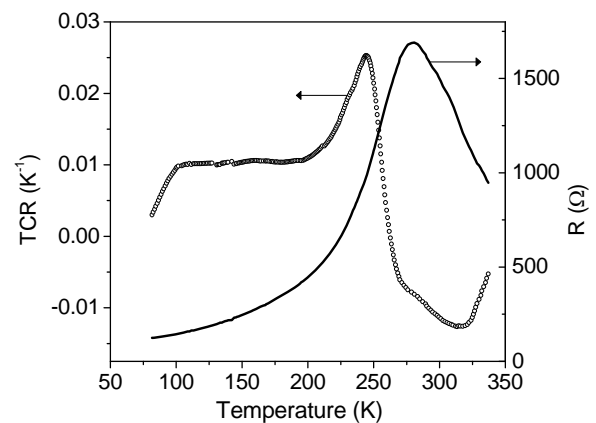


Fig. 2. TCR(T) and $R(T)$ dependences of the LSMO/MgO/GaAs.

Transport and magnetic properties of LSMO thin films grown on MgO single-crystalline substrates

V. Štrbík and M. Španková

The effect of colossal magnetoresistance in perovskite manganites like $\text{La}_{0.67}\text{Sr}_{0.33}\text{MnO}_3$ (LSMO) has triggered a lot of scientific and industrial attention. Our attempt was to applied the LSMO thin films for bolometric purposes using an abrupt change in resistivity at the transition of LSMO from paramagnetic into ferromagnetic state [1,2].

The LSMO films were deposited by an on-axis dc magnetron sputtering onto single crystal MgO (001) substrates at a temperature of 800 °C. The thickness of the LSMO films was about 500 nm. Our LSMO films exhibited only (00 l) growth orientation (X-ray diffraction in θ -2 θ configuration). Transmission electron microscopy confirmed an epitaxial growth of the LSMO films besides a 20 nm thin film surface layer of a polycrystalline character. We detected the growth of the polycrystalline surface layer only in the case of the annealed samples.

The electrical resistivity ρ of the LSMO thin films was investigated in the temperature range 4 – 330 K. For high quality film at the temperature $T_p \gtrsim 300$ K a peak of resistivity (transition metal – insulator) was observed. For temperatures higher than T_p (insulating character) the resistivity vs. temperature dependence ($\rho(T)$) can be described by variable range hopping (VRH) model (Fig. 1). The rapid decrease of the resistance for $T < T_p$ (metal character) can be interpreted mainly by the electron-electron scattering, electron-magnon scattering and impurity (defects) grain boundary scattering.

The non-monotonic dependence of the resistivity on the temperature can be characterised by a temperature coefficient of resistivity (TCR) = $[1/\rho \times d\rho/dT] \times 100\%$ and its maximal value TCR_{max} indicates the most suitable temperature region for bolometric application. Our best LSMO films reached $TCR_{max} \approx 3\% \text{ K}^{-1}$ at 290 K ($TCR_{max} \approx 5\% \text{ K}^{-1}$ at 300 K is considered as a ‘good’ value).

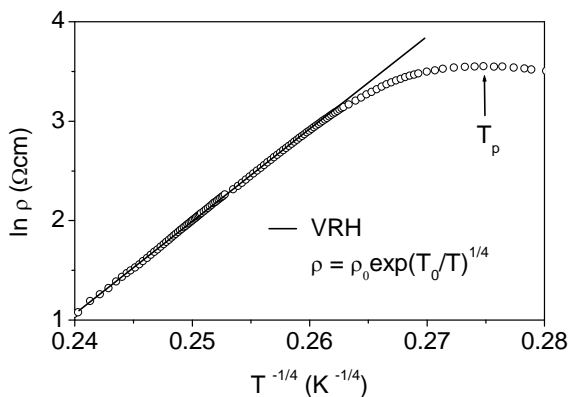


Fig. 1. Resistivity vs. temperature dependence in insulating (paramagnetic) state of the LSMO film. The solid line represents the fit by variable range hopping (VRH) model.

Magnetic properties of the thin LSMO films by SQUID equipment were also investigated. We observed the temperature of the magnetic transition from paramagnetic into ferromagnetic state (T_{Curie}) close to T_p ($T_p = 291$ K, $T_{Curie} = 293$ K). The magnetoresistivity (MR) of the LSMO film is shown in Fig. 2. The magnetoresistivity is defined by the relation $MR = [(\rho_B - \rho_0)/\rho_0] \times 100\%$, where ρ_0 and ρ_B are resistivities at zero and applied magnetic field B , respectively. The maximum of MR was registered at the temperature $T = 256$ K and MR depends nearly linearly on the applied parallel magnetic field. Dependences of MR taken at another temperature are also shown in Fig. 2.

Further study showed the strong correlation between the magnetic and transport properties of the LSMO films. The maximum of MR was achieved at $T = 256$ K, the maximum of $d\chi'/dT$ was obtained at $T = 250$ K (χ' is the real part of the susceptibility) and TCR_{max} at $T = 248$ K. The correlation of T_p and T_{Curie} was mentioned above.

Our LSMO thin films show relatively low MR effect (about 50 %) and slow decrease of the resistivity after the ferromagnetic transition. These may be caused by the lack of parallel alignments of the cluster magnetization below T_{Curie} .

This work was performed in cooperation with Dr. M. Reiffers from the Institute of Experimental Physics SAS, Košice, Slovak Republic.

- [1] Španková, M., Chromik, Š., Vávra, I., Sedláčková, K., Lobotka, P., Lucas, S., and Stanček, S.: *Appl. Surf. Sci.* **253** (2007) 7599.
- [2] Španková, M., Chromik, Š., Vávra, I., Štrbík, V., Liday, J., Espinós, J.P., and Lobotka, P.: *accepted in Physica Status Solidi* (a).

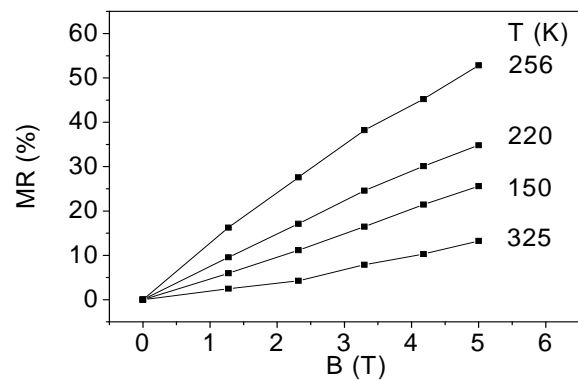


Fig. 2. Magnetoresistivity of the LSMO thin film. The maximum of MR was achieved at $B = 5$ T and $T = 256$ K. The resistivity was changed by 52% comparing to value in 0 T.

Thin film HTS / FM / HTS heterostructures

V. Štrbík and Š. Beňačka

High temperature superconducting (HTS) and ferromagnetic (FM) two or three layer heterostructures are suitable objects for physical investigation of interplay between the two fundamental condensed matter phenomena - superconductivity and ferromagnetism. On the other hand, the HTS/FM layered structures are perspective for application in new type devices (e.g. π -junctions, qubits, π -SQUIDS), or superspintronics devices manipulated by the spin-state of the charge carriers.

We have investigated [1] three layer heterostructures with upper and lower $\text{YBa}_2\text{Cu}_3\text{O}_7$ (YBCO) electrodes (70 nm thick) separated by 20 - 40 nm thick $\text{La}_{0.67}\text{Sr}_{0.33}\text{MnO}_3$ (LSMO) layer. Alternatively, FM $\text{La}_{0.67}\text{Ca}_{0.33}\text{MnO}_3$ (LCMO) thin films were used as well. The peak in the resistance vs. temperature dependence usually corresponds to Curie temperature (T_{Curie}) at which LSMO or LCMO undergoes transition into ferromagnetic state. LCMO thin films show lower T_{Curie} than LSMO (in Fig. 1 LSMO resistance peak is above 300 K). Superconducting films were prepared by DC and ferromagnetic layer by RF magnetron sputtering [1].

X-ray diffraction measurements confirmed preferential (00l) growth of all layers in heterostructure but with some increased width of reflex peaks comparing to the single YBCO or LSMO films. Such result indicates a worse growth of films when the number of layers increases. The LSMO grows in pseudocubic structure with unit cell parameter of $a = 0.3894$ nm which matches very well with YBCO base plane ($a = 0.384$ nm, $b = 0.387$ nm). YBCO c lattice parameter is equal to 1.1687 nm and corresponds to relaxed film.

Electrical properties of heterostructures were investigated by DC transport 4-point method and AC susceptibility measurements. Whereas superconducting

transition of electrodes corresponds to high quality YBCO films (zero resistance critical temperature $T_{C0} \geq 86$ K, and width of transition ΔT_C (10 - 90 %) < 1 K, critical current density $j_C > 10^6$ A/cm² at 77 K) the transition parameters of heterostructure exhibit values $T_{C0} \approx 84$ K, with a small resistance tail, and ΔT_C (10 - 90 %) $\approx 1.5 - 2.5$ K. Similar results were obtained in susceptibility measurement. Superconducting diamagnetic transition of YBCO electrodes is characterised by steep and narrow transition (curve E in Fig. 2). The onset of this transition begins approximately at T_{C0} of YBCO. The measurement of YBCO/LSMO bilayers indicate phase transitions at the lower temperatures (curve YL in Fig. 2). The curves H1 and H2 in Fig. 2 represent the diamagnetic transitions of two another heterostructures on the same substrate indicating possible influence of proximity effect. The onset of these transitions begins at lowered temperature (compared to YBCO electrodes) and their width is significantly broadened.

The presented results indicate a noticeable interplay of proximate ferromagnetic and superconducting layers at the HTS/FM interface. This effect can be more enhanced by the direct injection of spin - polarized carriers from ferromagnetic into superconducting film and it can lead to practical HTS/FM/HTS or FM/HTS/FM junctions or devices [2].

This work was performed in cooperation with Dr. T. Nurgaliev, Dr. E. Mateev, Dr. S. Miteva and Dr. B. Blagoev from the IE BAS, Sofia, Bulgaria.

[1] Nurgaliev, T., Štrbík, V., Miteva, S., Blagoev, B., Mateev, E., Neshkov, L., Beňačka, Š., and Chromik, Š.: *Central European J. Phys.* 5 (2007) 637.

[2] Štrbík, V., et al.: *paper in preparation*

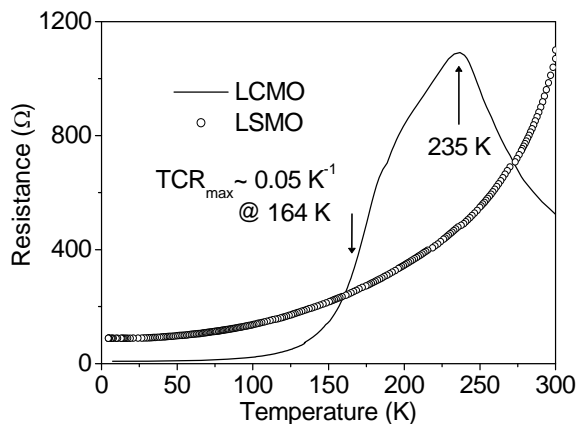


Fig. 1. Resistance vs. temperature dependences of LSMO (circles) and LCMO (full line) single layers. The resistance peak for LSMO layer occurs above 300 K.

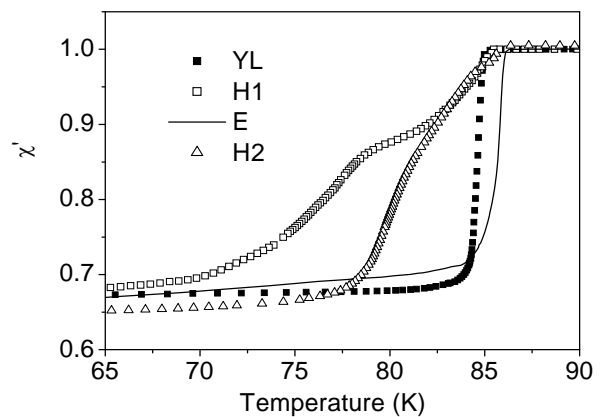


Fig. 2. Real part of susceptibility for both electrodes (E), bilayer YBCO/LSMO (YL) and heterostructure at two different trilayers on the same substrate (H1 and H2).

Influence of the buffer layer on the growth of superconducting films based on mercury

M. Sojková, Š. Chromik, V. Štrbík, and M. Polák

Hg-based superconductors $\text{HgBa}_2\text{Ca}_{n-1}\text{Cu}_n\text{O}_{2n+2}$ ($[\text{Hg}-12(n-1)n]$, HgBCCO) have the highest critical temperatures from all known superconductors. The substrate as well as the buffer layer play an important role in the formation of thin epitaxial films. De Barros et al. [1] studied the influence of the substrate on the growth of HgBCCO films. They used LaAlO_3 (LAO) (001) and MgO (001) substrates with lattice mismatches 1.4 % and -8.7 %, respectively. They found out that the Hg-1212 was formed on the LAO, while the Hg-1223 was the main phase obtained on the MgO. They suppose that this is linked with nucleation-growth conditions and with the formation path of the Hg-1223 involving the Hg-1212 as an intermediate step.

We studied the influence of the thickness of the CeO_2 buffered R-plane sapphire substrate on structural and electrical properties of the Hg-based superconducting films grown on this buffer layer.

First, three different thicknesses of the CeO_2 films were prepared – 10, 70 and 120 nm. XRD studies of the CeO_2 buffer layers showed their epitaxial character in all cases. Only (00 l) diffractions of the CeO_2 are observed in θ -2 θ scans suggests that only one orientation of the CeO_2 grains has grown in the c -axis direction. This was confirmed by ϕ -scans having FWHM's (full width at half maximum) in the range 0.2-1° and pole figures. As expected, the intensity of the diffracted peaks increased with the film thickness. The (00 l) Bragg peaks of the 10 nm thin buffer layer are shifted to higher planar spacing d (nm) values and they are very broad because of the residual strain due to the large mismatch between the substrate and the buffer layer. The lattice parameters of the strained films ($c = 0.541$ nm) are larger than those of the relaxed CeO_2 films ($c = 0.539$ nm). The strain decreases with the increasing thickness and the lattice parameter in the c -axis direction decreases, too.

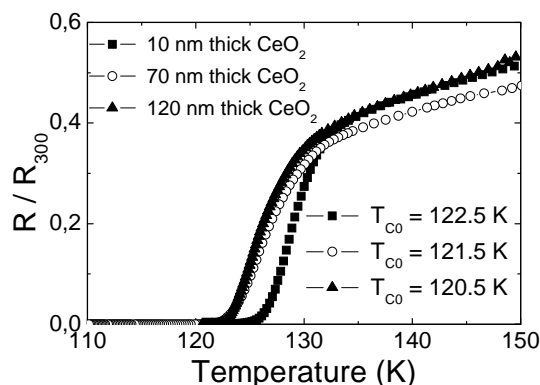


Fig. 1. $R(T)$ dependence of the mercurated films with the CeO_2 buffer layer of different thicknesses.

The precursor (Re-Ba-Ca-Cu-O) films were deposited on the CeO_2 buffered sapphire and mercurated at 800 °C during 3 hours according to [2,3]. We obtained a mixture of Hg-1223, Hg-1212 and intergrowth phases, all being c -axis oriented. The Hg-1223 phase was present in all cases, however, the ratio between the phases was thickness dependent. Interestingly, the amount of the Hg-1223 phase decreased when the thickness of the buffer layer increased.

The superconducting films (~ 300 nm thick) were relaxed in all cases; the c -parameters of the superconducting phases did not change and were close to those of the bulk samples. It seems that the strain in the CeO_2 buffer layer influenced only the growth mechanism and thus the final phase composition of the superconducting films. The mercurated films were superconducting and their zero resistance critical temperatures were above 120 K and very close to one another (Fig. 1). The highest T_{c0} ($= 122.5$ K) was observed for the sample containing the largest amount of the Hg-1223 phase prepared on the thinnest CeO_2 which is in agreement with XRD analyses. The films were studied also by scanning electron microscopy. The film prepared on the thinnest buffer layer contains less impurities comparing to the films prepared on the thicker buffer layer. Because the precursor films had the composition of $\text{Re}:\text{Ba}:\text{Ca}:\text{Cu} = 0.15:2:2:3$, the film containing the larger amount of Hg-1223 has the smaller amount of impurities. The critical current density J_C of the prepared films was estimated from the magnetic measurements using the Hall probe method. They have comparable values in the range of $1 - 4 \times 10^5$ A/cm² at 77 K. The J_C versus CeO_2 thickness dependence is complex and not monotonic. Probably several factors, like purity, strain and thickness are competing.

We found out that we can change the phase composition of the final films varying the thickness of the CeO_2 layer. Using a very thin CeO_2 film (~ 10 nm) we can prepare Hg-1223 phase on the R-plane sapphire due to the enhanced diffusion (intercalation) of the Ca-Cu-O into the dislocations network of the Hg-1212 and the consequent transformation to the Hg-1223. This shows how the growth of HgBCCO anisotropic epitaxial films is influenced by the strain developed in the buffer layer [4].

- [1] De Barros, D., et al.: *Physica C* **440** (2006) 45.
- [2] Valeriánová, M., Odier, P., Pairis, S., and Štrbík, V.: *Physica C* **435** (2006) 31.
- [3] Valeriánová, M., Chromik, Š., Odier, P., and Štrbík, V.: *Central European J. Phys.* **5** (2007) 446.
- [4] Valeriánová, M., Odier, P., Chromik, Š., Štrbík, V., Polák, M., and Kostič, I.: *Supercond. Sci. Technol.* **20** (2007) 900.

The influence of the rhenium in the precursor film on the properties of the thin superconducting films based on thallium

A. Dujavová, M. Sojková-Valeriánová, V. Štrbík, Š. Chromik, and M. Polák

Thallium based cuprates ($Tl_mBa_2Ca_{n-1}Cu_nO_{2n+m+2}$ where $m = 1 - 2$, $n = 1 - 5$; TBCCO) belong to the group of high temperature superconductors. High values of the critical temperatures provide the stability of the superconducting properties and parameters (coherent length, energy gap, etc.) at the working temperature of the superconductor (77 K) so these materials are suitable for various applications.

Thin films of thallium based superconductors were prepared on a CeO_2 buffered R-plane sapphire as well as on a $LaAlO_3$ (LAO) substrate using an RF magnetron sputtering. Two different targets were used for the deposition: a) Re-free target with a nominal composition of $Ba_2Ca_2Cu_3O_x$ prepared as a mixture of $BaCuO_2$ and Ca_2CuO_3 , and b) Re stabilized target with a nominal composition of $Re_{0.15}Ba_2Ca_2Cu_3O_x$. The thallination of the precursor films were performed in a one zone configuration where the sources of the thallium ($Tl_{1.85}Re_{0.15}Ba_2Ca_2Cu_3O_{10}$) and the precursor films were kept at the same temperature. The thallination temperature and time were 860 °C and 30 minutes, respectively. We have studied the influence of the presence of the rhenium in the precursor film on structural and electrical properties of the final films [1].

In all cases (the precursor film, with and without rhenium, prepared on the R-plane sapphire with the CeO_2 buffer layer and on the LAO substrates), the prepared films were black, homogenous and without visible defects. Using X-ray diffraction (XRD) analyses we identified only *c*-axis oriented Tl-2212 superconducting phases present in the prepared films. The presence of the rhenium was not detected by XRD analysis. We suppose that rhenium phases are not crystalline and could be present in the amorphous form between the grain boundaries.

Transport measurements of the resistance versus

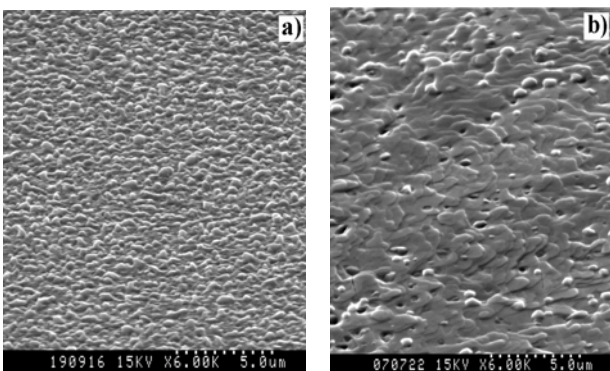


Fig. 1. SEM images of the Tl-based films prepared on the CeO_2 buffered R-plane sapphire with (a) and without (b) rhenium content in the precursor films.

temperature ($R(T)$) characteristics confirmed the presence of the superconducting phases in all types of the films. The values of the zero resistance critical temperature T_{C0} for all samples were comparable in the range of 93 – 101 K.

Although the influence of the rhenium on the phase composition and on the value of the critical temperatures was not significant, its influence on the microstructure of the prepared films was really evident. In the Fig. 1 we can see scanning electron microscope (SEM) images of the films prepared with and without rhenium on the CeO_2 buffered R-plane sapphire.

In the case of the Re-stabilized films the grains are small with an average grain size of about 0.5 μm . These grains are formed from the Tl-2212 superconducting phase. On the other hand, the Re-free films contain large epitaxial blocks (3 – 5 μm) consisting of the Tl-2212 superconducting phase. The same effect was observed on the LAO substrate, too.

Critical current density was estimated from the magnetic measurements using the Hall probe method. We found out that the value of the critical current density J_C was strongly influenced by the presence of the Re. The films prepared with the Re reached $4.1 \times 10^5 \text{ Acm}^{-2}$ at 77 K in the self field while in the case of the Re-free films it was up to $3 \times 10^6 \text{ Acm}^{-2}$. We suppose that J_C value in the case of Re-stabilized films was suppressed due to the presence of some rhenium phases in the intergranular region increasing the resistance of the grain boundaries.

We studied the influence of the rhenium in the precursor films on the structural and electrical properties of the final films. Rhenium did not have significant impact on the phase composition and on the values of the thin film critical temperature in all cases. However, we registered a noticeable difference in the grain size of the prepared films. Using the rhenium, the prepared films consist of smaller grains reducing the critical current density due to the increase of the resistance and the number of the grain boundaries. On the other hand, the rhenium stabilizes the sputtering target thus facilitates the process of the superconducting film fabrication. It will be necessary to find some optimal condition for the rhenium content in the precursor films to improve the properties of the rhenium containing Tl-based superconducting films.

[1] Dujavová, A., Sojková-Valeriánová, M., Gaži, Š., Štrbík, V., Polák, M., Kostič, I., and Chromik, Š.: accept. in *Physica C*.

YBa₂Cu₃O_x bi-epitaxial junctions on the substrate with axis tilted out-of-plane

Š. Beňačka and V. Štrbík

The physics of high temperature superconductor (HTS) weak links is different from conventional superconductors. One of the main differences is the fourfold d-wave symmetry of the order parameter (OP). When the in-plane lobes of the OP face each other a maximum value of the critical current density j_C is expected, when the lobe misorientation angle α is such that the nodes are facing ($\alpha = \pi/4$), $j_C = 0$ across the junction. This behavior was clarified in the Sigrist-Rice (SR) outstanding approach, where the Josephson current is proportional to the projection of the momentum-dependent energy gap onto the junction interface normal. In this SR phenomenological approach the Josephson current density j , of an all d -wave junction, is given by relation $j = A \cos(2\alpha_1) \cos(2\alpha_2) \sin\varphi$ where α_1, α_2 are the in-plane angles of crystallographic axes with respect to the interface normal, A is a junction characteristic constant and φ the phase difference of the junction superconductors wave functions. The SR formula is convenient for real junctions, with interfaces damaged by roughness, oxygen deficiency, strain, etc., but it is not suitable for junctions with ballistic transport [1]. It is not clear at present how the angular and temperature dependence of the HTS weak link critical current density influences angle θ of the substrate out-of-plane tilted axis.

We investigated bi-epitaxial YBa₂Cu₃O_x (YBCO) weak link junctions prepared on single crystal NdGaO₃ (NGO) substrates with different miscut angles θ tilted out-of-plane by 18-33°, which provide the best properties of the YBCO films and junctions. A part of the substrate was covered by Y:ZrO₂ (YSZ) seeding layer (15 nm thick) to build up additional 45° in-plane rotation of the YBCO on the YSZ/NGO boundary. The YBCO epitaxial films (120 nm thick) showed critical temperature T_C

higher than 89 K and critical current density j_C near 10^7 A/cm². YBCO films were patterned to bridges (5 μm wide), crossing the YSZ/NGO boundary line, with critical current of the bridge $j_{Cb}(4 K) \approx 10^5$ A/cm². The orientation of the bridges was chosen 0, 10, 20, 70, 80 and 90° from the tilt axis [001] of NGO. The samples preparation and film properties we published elsewhere [2].

Typical current voltage characteristics (CVC) of the YBCO bi-epitaxial junctions were, due to relatively high critical current density, $j_{Cb} > 10^4$ A/cm² even at 77 K, mostly flux-flow type. Fig. 1 shows the CVC of sample with out-of-plane miscut angle $\theta = 33^\circ$. Next we suppose the j_C suppression by variation of YSZ seed layer thickness. The inset of Fig. 1 illustrates normalized critical current $I_C(T)$ dependence which is close to linear, regardless of the boundary angle α or miscut angle θ . The $j_C(\alpha)$ in Fig. 2, for samples with different substrate miscut angle θ , follows the SR relation for α close to 0° and 90°. The additional $\pi/4$ in-plane tilt on NGO/YSZ boundary should result in zero j_C at $\alpha = 45^\circ$ as well, the effect which on the present is investigated in more detail [3]. The results show another variability of bi-epitaxial HTS weak link properties for cryoelectronic circuits.

The work was performed in cooperation with Dr. P. Mozhaev and Dr. J. Mozhaeva from the IPT RAS, Moscow, Russia, and Dr. C.S. Jacobsen from the DTU, Lyngby, Denmark.

- [1] Yokoyama, T., et al: *Phys. Rev. B* 75 (2007) 020502.
- [2] Mozhaev, P.B., et al.: *Proc. 29th RISO Material Science Symposium, DTU Lyngby, 2008, p. 317.*
- [3] Beňačka, Š., et al.: *paper in preparation*

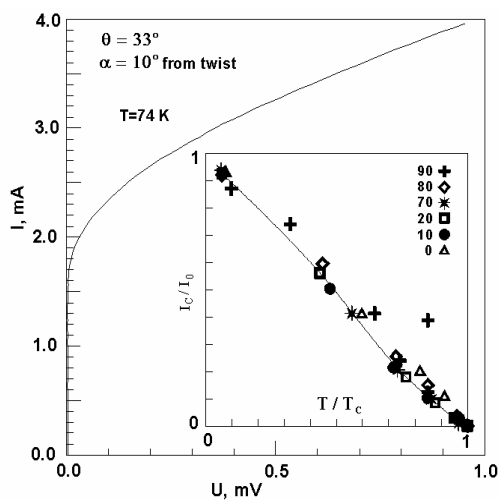


Fig. 1. CVC and $I_C(T)$ angular dependence (inset) of bi-epitaxial junctions with substrate miscut angle $\theta = 33^\circ$.

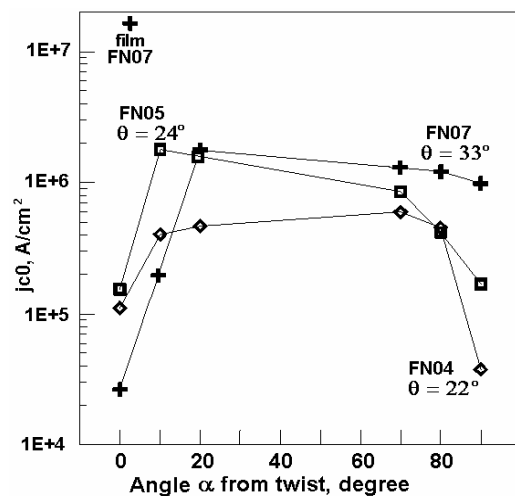


Fig. 2. Angular dependence of $j_c(0)$ for samples with different NGO substrate miscut angles: $\theta = 22^\circ, 24^\circ$ and 33° .

The influence of technological process on magnetic properties of MgB₂ films

Š. Chromik and V. Štrbík

MgB₂ thin films were prepared by sequential evaporation of boron and magnesium bilayers on SiC buffered Si substrates followed by in situ annealing [1]. The precursor Mg-B bilayers were deposited at room temperature by electron beam evaporation. The amount of B was varied so as to result in different thickness of the stoichiometric MgB₂ film after the reaction with the excess Mg top layer. As-deposited films were *in situ* heated to 280 °C for 30 min in Argon atmosphere at a pressure of 0.06 Pa. Subsequently, the pressure was increased up to 16 Pa and the temperature was increased to maximum temperature of either 750 °C or 830 °C and kept there for 10 min. The samples were then cooled down to room temperature at 10³ Pa Ar pressure. According to cross sectional Transmission electron microscopy study, the obtained thickness of the MgB₂ was about 50 nm.

We observe the influence of the deposition temperature on the magnetic properties of the films [2,3]. Figure 1 shows upper critical field H_{C2} versus temperature for 750 °C and 830 °C. The coherence length $\xi_{||}$ is related to H_{C2}^{\perp} by the equation $H_{C2}^{\perp} = \Phi_0 / 2\pi \xi_{||}^2$ with the flux quantum $\Phi_0 = h/2e$. When we compare H_{C2}^{\perp} values (Fig.1), we see higher values in the case of 830 °C and consequently shorter coherent length than the one annealed at 750 °C. This may be explained by shorter mean free path due to some impurities produced by higher annealing temperature of 830 °C. We actually observed interdiffusion [1] between the SiC buffer layer and the MgB₂ film. It is natural that the higher the annealing temperature rises, the more readily the interdiffusion takes place. The increased amount of SiC or Si as intergranular

materials should reduce the intergrain coupling and then shorten the electron mean free path and $\xi_{||}$.

We estimate the irreversibility field H_{irr} by taking critical current density $J_C = 60 \text{ kA/cm}^2$ (1/100 of the maximum J_C) as the criterion of the reversibility with magnetic field perpendicular to the film [2]. The estimated H_{irr} for the MgB₂/SiC/Si annealed at 750 °C is plotted with open diamonds in Fig. 2 as a function of $1 - t^2$. Here $t = T/T_C$ is the reduced temperature with $T_C = 34.5 \text{ K}$. H_{irr} for MgB₂/SiC/Si annealed at 830 °C is also plotted (●), which is reanalyzed by the same criterion of 1/100 of the maximum J_C . We found an interesting difference in the temperature variation of H_{irr} between the films annealed at 830 °C and annealed at 750 °C. As for the film annealed at 830 °C, H_{irr} decreases rapidly at higher temperatures probably due to the part of the film near the interface with weak links between the crystal grains with diffused impurities [2]. This is consistent with the above examinations on $|dH_{C2}^{\perp}/dT|$ and $\xi_{||}$ concerning Fig. 1. On the other hand, H_{irr} in the film annealed at 750 °C keeps steady values even at higher temperatures and follows the scaling law: $H_{irr} \propto (1 - t^2)^n$, with exponents n of 3 at all temperatures. This also indicates the good crystal quality of the 750 °C annealed film.

This work was performed in cooperation with Prof. A. Nishida from the Fukuoka University, Fukuoka, Japan.

- [1] Chromik, Š., Huran, J., Štrbík, V., Španková, M., Vávra, I., Bohne, W., Rohrich, J., Strub, E., Kováč, P., and Stanček, S.: *Supercond. Sci. Technol.* **19** (2006) 577.
- [2] Nishida, A., Taka, C., Chromik, Š., and Durný, R.: *accepted in J. Phys. Conf. (LT25)*.
- [3] Nishida, A., Taka, C., Chromik, Š., and Durný, R.: *J. Phys. Conf.* **43** (2006) 293.

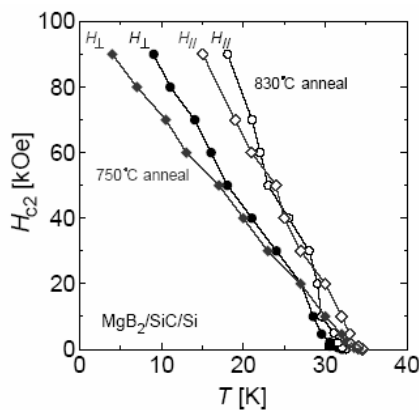


Fig. 1. Upper critical field $H_{C2}^{\perp}(T)$ under parallel (\diamond, \circ) and perpendicular (\blacklozenge, \bullet) fields for MgB₂/SiC/Si annealed at 750 °C (\diamond, \blacklozenge) and 830 °C (\circ, \bullet).

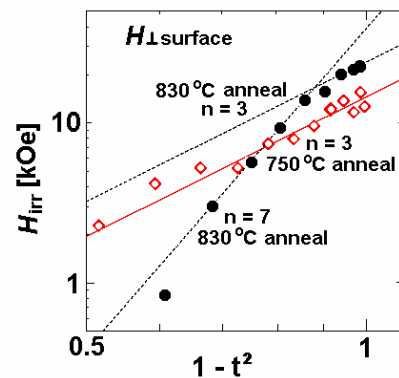


Fig. 2. Irreversibility field H_{irr} of MgB₂/SiC/Si film annealed at 750 °C (\diamond) and 830 °C (\bullet) as a function of $1 - t^2$ with $t = T/T_C$.

Growth of thin aluminium oxide films for microelectronic applications

Š. Gaži, D. Gregušová, and R. Stoklas

Our effort is focused on the preparation of very thin dielectric films for superconducting tunnel junctions as well as metal-oxide-semiconductor field effect transistors (MOSHFETs).

In the case of superconducting tunnel junctions, more than twenty years ago, the technology of Gurwitsch have offered solution to replace low quality Nb-oxide tunnel barrier by aluminium oxide [1]. It consists of 4-8 nm thin Al layer deposited immediately after the Nb base electrode sputtering. Subsequently by the room-temperature Al surface oxidation, at low oxygen pressure atmosphere, Al-oxide is formed with thickness smaller than about 2 nm. Such oxide layers are amorphous, and their excellent uniformity, up to thickness of some monolayers, prevents creation of shorts through the junction barrier. The rest of thin Al layer in close contact with Nb is superconducting due to proximity effect.

Presented technology of tunnel barrier preparation was than used for realization of SNIS and SNINS type tunnel junctions (S-superconductor, N-normal metal, I-insulator) in our niobium Josephson junction projects.

In the case of MgB_2 superconductor our attempt for the preparation of $MgB_2/AlO_x/Nb$ ramp-type junctions was realized by similar method of Al deposition and oxidation. The oxidation of Al layer was carried out on the interface of MgB_2/Al due to the adsorbed oxygen after the ex-situ MgB_2 -ramp surface preparation. Nb top electrode was deposited immediately on the Al layer. Tunnel junctions were SINS type with well defined Josephson effects. Relatively large excess current in some cases was associated with nanocrystalline MgB_2 layer and properties of intercrystalline region, rather than with the barrier oxide quality. in our niobium Josephson junction projects.

Composition of oxidized Al films was studied by X-ray photoelectron spectroscopy (XPS). Aluminium film

with thickness of 8 nm was deposited on polished Si substrate after preliminary ion cleaning and its exposure to oxygen during 10 hours. After deposition of Al layer, by sputtering in argon at 2 Pa, room temperature saturated surface oxidation succeeded in oxygen at 200 Pa during 10 hours. By the gradual removing the layer by Ar ion bombardment, we obtained Al-O and Al-Al XPS spectra. Depth profile spectra show presence of Al-oxide at the interface with Si and on the surface of the Al layer. In the middle part of the Al layer thickness there remains rest of nonoxidized aluminium (Fig. 1). From analysis of thinner layers it is clear that Al layers with thickness of about 4 nm can be fully oxidized. This type of oxide appears as an excellent gate and passivation oxide for MOSHFETs.

The presented technology of Al-oxide creation was used for gate oxide to study the properties of AlGaN/GaN metal-oxide-semiconductor heterostructure field effect transistors (MOSHFETs). Al-oxide gate was 4 nm thick. Nonpassivated HFETs were also prepared for comparison. The investigation of AlGaN/GaN MOSHFETs transport properties demonstrates enhancement of the carrier velocity as was recognized from conductance measurement and analysis of effective carrier mobility data. Drastic reduction of the drain leakage current indicates also suppression of the trap density. $C-V$ characteristics measured at 10 kHz and 1 MHz exhibited significant suppression of the capacitance dispersion and indicates similar surface traps reduction [2]. We are sure that all these effects are connected with the interaction of thin Al layer and the AlGaN surface.

From the obtained results it follows, that sputtered and subsequently oxidized thin aluminium films are very convenient for gate insulator as well as for the preparation of high-performance AlGaN/GaN MOSHFETs.

We would like to thank to Z. Sofer, Institute of Chemical Technology, Prague, Czech Republic, for XPS measurements.

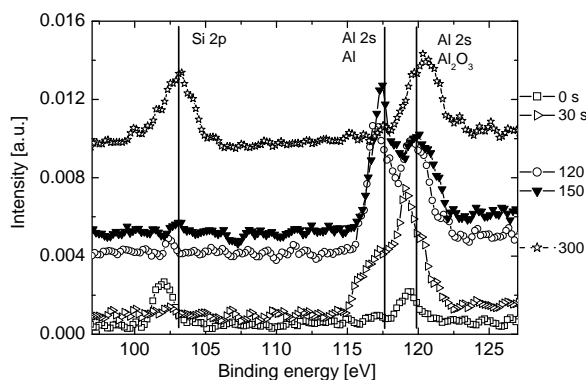


Fig. 1. XPS analysis of 8 nm Al layer after oxidation

- [1] Gurwitsch, M., et al.: *Appl. Phys. Lett.* **42** (1983) 472.
 [2] Stoklas, R., Gaži, Š., Gregušová, D., Novák, J. and Kordoš, P.: *Phys. Stat. Sol. (C)* **5** (2008) 1935.

Department of Superlattices

Ivo Vávra

Research scientist

Peter Lobotka

Research Engineers

Eva Kováčová

Vasilij Šmatko

Technical staff

Ján Dérer

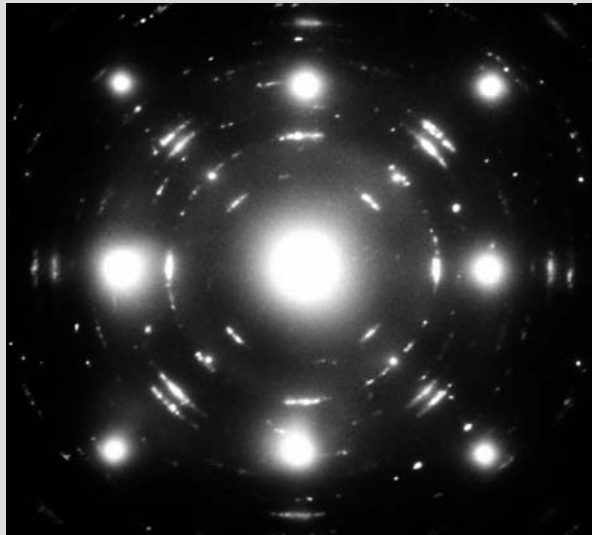
Jana Ryzá

PhD Students

Zuzana Križanová

Students

Pavol Kunzo



The main research activities of the Department of Superlattices in 2007 and 2008 were focused on a complex study of nanostructures, mainly thin nanocomposite films and their applications in electronics.

We prepared thin nanocomposite films using our deposition technology based on a modified magnetron sputtering system, previously developed and used to prepare metallic superlattices.

Our nanocomposite films are essentially periodic multilayers composed of discontinuous metallic sub-layers and continuous insulating ones.

The metallic sub-layers are composed of crystalline nucleation islands measuring a few nanometers across (in-plane dimension). The metallic sub-layers are separated by amorphous insulating ones. We have mastered the following aspects of their technology: (1) The crystallinity of the metallic particles is perfect, and (2) We can easily control the distance between particles along the normal direction to the surface plane. We also used the method to prepare nanocomposites containing metallic nanowires embedded in amorphous matrices. A structural zone growth model was used for their preparation. As the optical properties of such materials depend predominantly on their “nano-structuring”, they can be viewed as metamaterials.

Nanocomposites based on a polymer matrix were the other important topic we worked on together with the Polymer Institute of the SAS, Bratislava, Slovakia. We concentrated on nanocomposites filled with carbon nanotubes or graphene. Our task was to study the electrical properties of the thin metal/polymer-based films and to investigate their structure by transmission electron microscopy. The carbon-based nanocomposites are the basis of chemical sensors, which we worked on within our APVV project.

The department has been involved in a project entitled “*Preparation technology of monodispersed nanoparticles and their organization to the superlattice form*” supported by the Slovak Grant Agency VEGA. Risks and benefits of nanotechnologies for human health will be studied together with the Institute of Experimental Oncology, the Institute of Virology, and the Institute of Experimental Physics, SAS (VEGA project “*Molecular mechanisms of nanoparticle interactions after their internalization in the cells in vitro*”).

Besides the study of our nanocomposite films, we were also involved in the investigation of samples prepared by other techniques at collaborating organizations within bi-lateral cooperation.

We worked very effectively in the past two years on a project titled “*Thin film nanocomposites*” (the collaboration with MFA Budapest, Hungary). The results obtained were used to design chemical sensors. The department is a member of the Centre of Excellence of the SAS “*Nanostructured materials*”.

The basic experimental equipment available at the department includes:

- Cryopumped vacuum apparatus for the deposition of periodic multilayers by magnetron sputtering,
- Cryopumped vacuum apparatus for ion-assisted deposition and ion beam etching,
- JEOL1200EX transmission electron microscope, technology of cross-sectional TEM specimens,
- BS340 scanning electron microscope adapted to perform simple direct electron lithography,
- Measurement set for electro- and magneto-transport measurements in the range of 4–300 K and magnetic fields up to 1.7 T.

To perform successful research in nanomaterials, “sophisticated” vacuum technology, detailed nano-structural analysis, special lithographic techniques, and sophisticated electrical measurements are necessary. It is also a prerequisite that the staff members work together very intensively. I would like to express my gratitude for the work my colleagues have done within the two-year period.

Ivo Vávra

Polymer based nanocomposites with carbon nano-fillers

Z. Križanová, I. Vávra, and P. Lobotka

Over the last years, the conducting polymer/graphite nanocomposites have attracted considerable interests because of their exceptional properties. Polymer nanocomposites prepared from high aspect ratio layered graphite nanofillers achieve significant improvements in mechanical, thermal, electrical and barrier properties at very low filler concentrations, compared to conventional composites, without a significant increase in density. This is caused by the sheet-like structure of natural graphite where the atoms are strongly bonded on a hexagonal plane but weakly bonded normal to that plane. If these graphene layers could be separated down to a nanometer thickness through intercalation and exfoliation, they would form graphite nanosheets (Fig. 1), which possess a huge surface area and satisfy the high aspect ratio (200-1500) criterion needed for high strength composites.

Electrical, structural, thermal and mechanical properties of nanocomposites based on the ethylene-vinylacetate (EVA) matrix filled with graphite micro and nanofiller were prepared.

It was found that electrical conductivity of composites strongly depends on the carbon structure. The polymer composite structure was investigated by transmission electron microscopy. In the case of micro-sized graphite, the percolation concentration of the filler is at about 15-17 vol. %, whereas when nano-sized fillers are used the percolation concentration in composites was significantly lower. Electrical conductivity of graphite-based nanocomposites was found to be much higher than electrical conductivity of graphite based microcomposites at comparable concentrations.

The polymer composite was also investigated by Raman spectroscopy (RS) because Raman spectra show typical dependence on the graphite film thickness. This enables us to distinguish the number of graphene sheets in

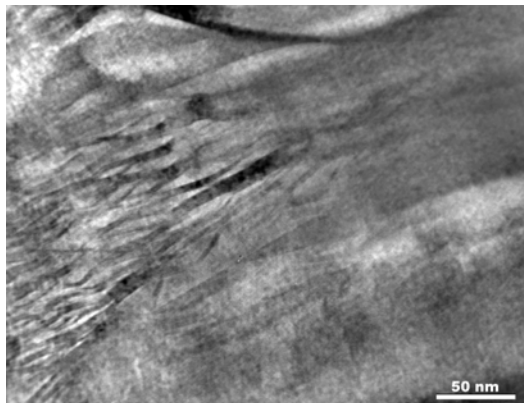


Fig. 1. Progress in exfoliation of expanded graphite (EG). The lamella width increased up to 1.5 nm. Exfoliation ends by graphene creation.

graphite particles in polymer matrix. RS of the graphite has three important peaks: the signal strength of D peak depends strongly on the degree of disorder in the graphite or graphene (Fig. 2). Position of G line shifts to the higher wave numbers with decreasing number of layers (Fig. 2). The most important peak is D' peak (Fig. 3). Its form is strongly different for 1 and few layers. Also its position is shifted down to the lower frequency with decreasing layers number.

We conclude that the most of frequent lamellas in prepared EVA/EG nanocomposite consist of 6 layers.

This work was performed in cooperation with I. Krupa, PI SAS, Bratislava, Slovak Republic and R. Srnánek, FEEIT SUT, Bratislava, Slovak Republic.

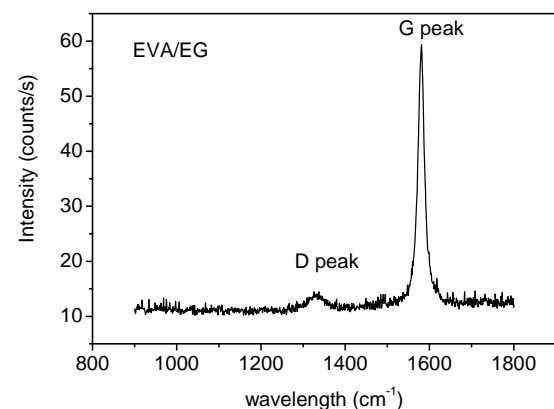


Fig. 2. The Raman spectra of nanocomposite EVA/EG has two peaks. The D peak (around 1328 cm^{-1}) looks like for more layers - graphite. The wavelength of the G peak (1580 cm^{-1}) is typical for 6 layers.

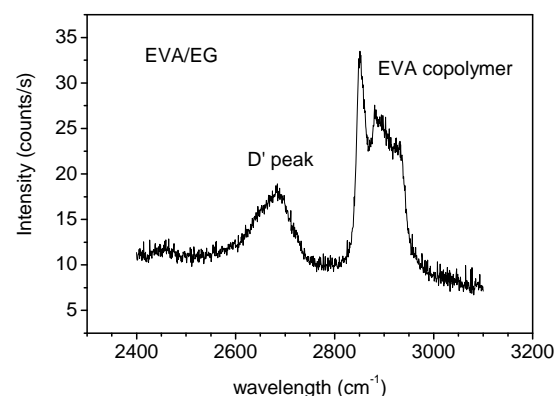


Fig. 3. The Raman spectra of nanocomposite EVA/EG. There are two peaks. First one is D' peak and the second belongs to polymer matrix. The form of the full width at half maximum of D' line (2680 cm^{-1}) indicates the presence of graphite.

Multilayered metal/insulator metamaterials

I. Vávra and J. Dérer

Metal nanoparticles embedded in amorphous matrix represent an interesting optical material. The metallic nanoparticles which are at their nanometric dimensions optically transparent contribute to the resulting optical characteristics of the nanocomposite. The topic of metal/insulator nanocomposite is relatively old; nanocomposites provide, e.g. colours in glasses [1].

On the base of our previous experience in the field of periodic multilayer technology and structure zone model for self organized structural evolution during physical vapor deposition as a function of film growth parameters [2] we developed metal/insulator nanocomposites with wide variety of nanostructuring.

The periodic multilayers and also single Mo layers were deposited in cryopumped apparatus with a base pressure of 10^{-5} Pa. The dc magnetron sputtering was used

for Mo deposition at a pressure of 10^{-1} Pa. The rf magnetron sputtering at 5×10^{-2} Pa was used for SiO_2 deposition. Sputtering rates of targets were kept constant and the deposition rate was adjusted by the velocity of substrate movement over the Mo and SiO_2 targets. The Si/ SiO_2 substrate was cooled during deposition to -20°C .

Depending on the Ar pressure during sputtering we prepared standard polycrystalline Mo layers (top layer in Fig. 1a) or non-continuous nanostructured layer (bottom layer in Fig. 1a). Dark field transmission electron microscope (TEM) image (Fig. 1b) reveals that Mo creates the “nanowires” (passing through the whole Mo layer thickness). Each nanowire is composed of Mo nanocrystals (size of approx. 10 nm).

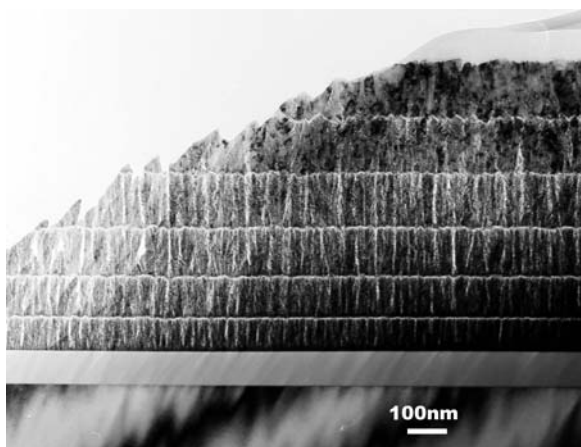
Optical properties of all the prepared Mo/ SiO_2 nanostructured layers and multilayers were measured by IR-VIS-UV ellipsometric and reflectance spectroscopies (Fig. 2). The aim is at understanding the behavior of the nano-composites and exploring the possibilities of tuning their optical properties. In particular, we focus on achieving low values of UV reflectivities of these metamaterials.

Optical response of Mo/ SiO_2 nanocomposite depends strongly on their nanostructuring. Ni/ SiO_2 and Fe/ SiO_2 provided substantially smaller variability of optical response. The optimization for specific properties (e.g. a low UV/VIS reflection) is possible.

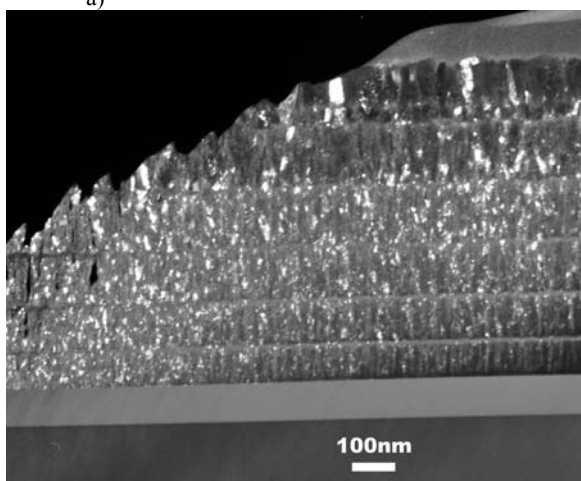
This work was performed in collaboration with Prof. J. Humlíček, Institute of Condensed Matter Physics, Masaryk University, Brno, Czech Republic.

[1] Garnett, J.C.M.: *Philos. Trans. R. Soc. Lond.* **203** (1904) 385.

[2] Petrov, I., Barna, P.B., Hultman, L., and Greene, J.E.: *J. Vac. Sci. Technol. A* **21** (2003) S117.



a)



b)

Fig. 1. a) Cross-sectional TEM micrograph of Mo/ SiO_2 multilayer. Each Mo layer is sputtered at different Ar pressure (from the bottom to the top: 10, 8, 6, 4, 2, 1 Pa). The SiO_2 layers were deposited always at 10^{-1} Pa. b) Dark field TEM image clearly reveals the nano- or micro- crystalline structure of Mo layers.

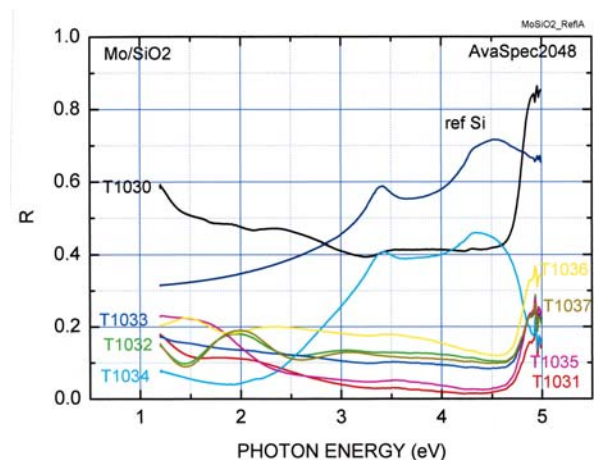


Fig. 2. Reflectivity measurements of nanostructured Mo/ SiO_2 composites (T1031-T1037). Reflectivity of Si is depicted for comparison.

Structural stability of metal oxide sensors

V. Šmatko, E. Kováčová, and V. Štrbík

Indium oxide films are widely used as solid state gas sensor materials [1]. We designed one electrode sensor with thin film platinum meander which is covered by In_2O_3 layer. The one-electrode meander acts both as the heating resistor and measuring electrode. The sensor works under a stabilized current feed. The operation principle of the one-electrode sensor is based on the shunting of the electrode (meander) by semiconductor In_2O_3 oxide. At the gas exposure, the sensor response is obtained as a voltage (U) change during the interaction of oxide with surrounding atmosphere.

The impedance matching between metal oxide and heater resistances may be achieved through the control of the metal electrode thickness and width. The distance between the strips also became a crucial factor that affects the sensor sensitivity. The considerable progress could be obtained as a result of development of high precision and resolution patterning processes, like microfabrication technology.

Service parameters of In_2O_3 based sensors were studied in conditions of their intensive exploitation at elevated temperatures. Sensor response values to H, CO and $\text{C}_3\text{H}_6\text{O}$ were measured. The devices were placed in the chamber of volume 650 ml. Experiments were performed in the temperature interval 350-400 °C.

To suppress structural changes activated by thermal effects in sensors we prepared samples on Si wafer with Si_3N_4 membranes of thickness 300 nm. For such samples thermal induced degradation processes were significantly slowed down.

Further, new samples were produced by vacuum evaporation method. The formation of In precipitates on a substrate was performed in O_2 atmosphere with addition

of He. Such way we influence crystallization centers and vary the sizes of In_2O_3 grains, we can produce oxide films of high uniformity, see Fig. 1. High dispersion films have a large active surface and hence the sensor response is larger, see Fig. 2. It was not necessary to perform a thermal annealing of produced films in the case when films were prepared in vacuum with background of He. Our previous observations showed that in some cases an annealing of oxide films leads to formation of hidden pores. We revealed that the sensitivity of sensor can be increased by addition several percentages of Sn to the composition of oxide film.

It was found that an initial structural uniformity of oxide films mainly determines structural degradation processes in sensors during their exploitation, in particular in extreme conditions. Structural inhomogeneities in In_2O_3 films stretched out along the sample were revealed. A continuous prolonged exploitation of sensors at elevated temperatures led to structural degradation accompanied by surface electromigration of In atoms. Structural degradation of studied sensors could be partly suppressed using thin substrates. Sensors with uniform oxide films and enough small grains showed improved service characteristics (larger current signal and smaller relaxation time after gas exhaust). In such sensors structural degradation processes during the time of experiment were not observed.

- [1] Korotcenkov, G., Boris, I., Brinzari, V., Golovanov, V., Lychkovsky, Yu., Karkotsky, G., Cornet, A., Rossinyol, E., Rodrigue, J., Cirera, A.: *Sensors and Actuators B* **103** (2004) 13.

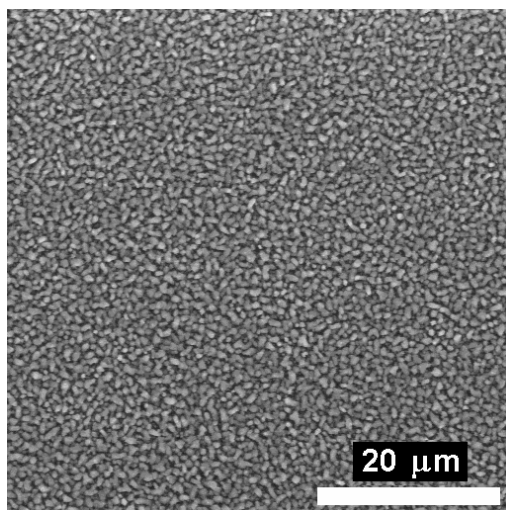


Fig. 1. SEM image of In_2O_3 film produced in vacuum with addition of He.

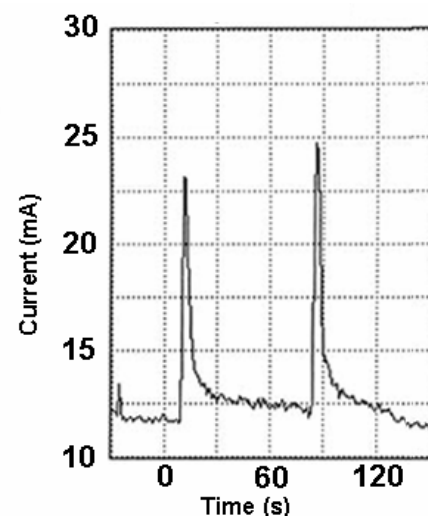


Fig. 2. Current response of In_2O_3 based sensor to gas exposure.

Department of Thin Oxide Films

Karol Fröhlich

Research scientists

Antónia Mošková
Alica Rosová
Edmund Dobročka
Ján Kuzmík
Daniel Machajdík
Milan Ťapajna

Research Engineers

Kristína Hušeková
Roman Lupták
Karol Čičo

Technical staff

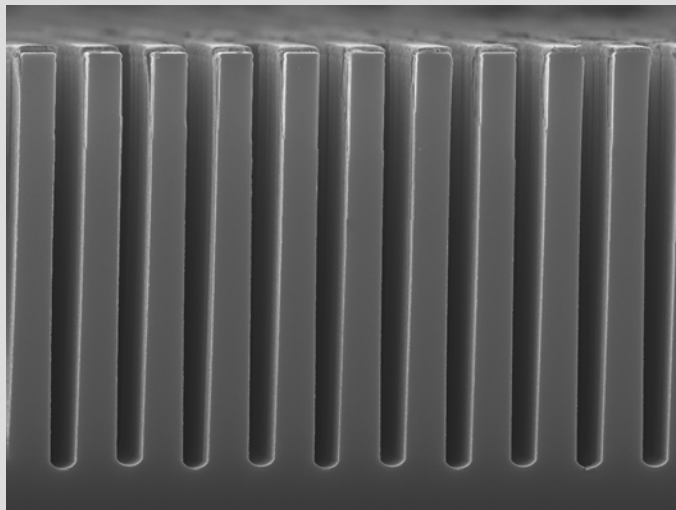
Alena Seifertová
Miroslav Pokorný

PhD Students

Boris Hudec

Students

Michal Fajta
Marek Franta
Robert Dzvonic
Michal Jurkovič
Marek Neupauer



The main research activities of the Department of Thin Oxide Films include the growth and characterization of thin metallic and oxide films and structures. We have prepared a variety of metal and oxide films in our metal organic chemical vapour deposition reactors (MOCVD). The deposition is based on a TriJet™ liquid precursor delivery technology (liquid injection).

We have recently focused on the preparation of oxide films and their application in semiconductor devices with the aim to increase their performance.

Our department was involved in the following research projects in 2007 and 2008:

- “*Thin films and structures perspective for electronics*”, VEGA project No. 2/5130/25, 2005-2007.
- “*Microstructure of very thin films for advanced microelectronics*”, VEGA project No. 2/0031/08, 2008-2010.
- “*Thin oxide films for advanced MOS structures*”, APVV project No. APVT- 51- 017004, 2005-2007.
- “*Structures metal-insulator-metal for nanoscale DRAM memories*”, APVV project No. APVV-0133-07, 2008-2011.
- “*InAlN/(In)GaN heterostructure technology for ultra-high power microwave transistor*”, ULTRAGaN, 6th Framework Programme, Specific Targeted Research Project No.006903, 2005-2008.
- “*Materials for robust Gallium Nitride, MORGaN*”, 7th Framework Programme, Integrated project No. 214610, 2008-2011.

The structural characterization of the films was performed by means of X-ray diffraction using a recently installed high-performance Bruker AXS D8 Discover Super Speed Diffraction system. Using the versatile equipment, we analyzed very thin films (~ 10 nm) via grazing incidence X-ray diffraction and X-ray reflectivity measurements.

Within the “*Thin oxide films for advanced MOS structures*” project, we concentrated on the preparation and characterization of thin high-dielectric constant films. Complex oxides GdScO₃ and LaLuO₃ were prepared and investigated as candidates for the next generation of MOSFETs.

Further efforts were devoted to the study of a gate stack for a new generation of MOSFETs. We observed a good thermal stability of Ru-Si-O-based gate electrodes during rapid thermal annealing under forming gas. Hafnia oxygen vacancy defects were observed in ultrathin MOCVD-grown Hf_xSi_{1-x}O_y gate dielectrics gated with Ru electrodes.

The effect of Ti doping on Ta₂O₅ stacks with Ru and Al gates was studied in connection with the application of Ta₂O₅ in dynamic random access memories (DRAM). We demonstrated that the Ti doping of Ta₂O₅ was conducive to a remarkable improvement in the leakage characteristics of Ru-gated capacitors by the Ti-induced suppression of the oxygen vacancy related defects.

Since 2008, we have been studying properties of RuO₂/TiO₂/RuO₂ structures containing high dielectric constant TiO₂ films under the new APVV project “*Structures metal-insulator-metal for nanoscale DRAM memories*”. The TiO₂ films have been prepared by atomic layer deposition at the Institute of Physics, University of Tartu, Estonia.

Our role within the 6th FP ULTRAGaN project was to develop insulating films for InAlN/GaN high electron mobility transistors (HEMT). Al₂O₃ dielectric films were chosen for the gate insulation of the transistors, which led to a drastic decrease in their leakage currents and to a surprising increase in their extrinsic transconductance. We will go on working on the insulation and passivation of InAlN/GaN-based HEMTs under a new 7th FP t MORGaN projec.

The Department of Thin Oxide Films enjoyed contacts with institutes and laboratories in Slovakia and Europe. We worked on our APPV-funded projects along with our research partners: (1) the Department of Microelectronics at the Faculty of Electrical Engineering and Information Technology, Slovak University of Technology, Bratislava, and (2) the International Laser Center, Bratislava.

Participation in the ULTRAGAN project helped us to establish fruitful co-operation with the project partners, in particular with the Institute for Solid State Electronics, Vienna University of Technology, Austria. We hope that the partnership will continue within the 7th FP MORGaN project, in which the ULTRAGaN partners have been included.

As already mentioned, co-operation with the Institute of Physics, University of Tartu, Estonia resulted in the successful preparation of metal-insulator-metal structure containing very high dielectric constant TiO₂ films. We should acknowledge the composition analysis of our thin films by Rutherford backscattering performed under co-operation with the Joint Institute for Nuclear Research, Dubna, Russia. The continuation of our activity in high dielectric constant films was also supported by a joint research project on the investigation of properties of Ru/high-κ capacitors with the Institute of Solid State Physics, Sofia, Bulgaria.

Karol Fröhlich

Growth of thin oxide films by liquid injection metal organic chemical vapour deposition

K. Hušková, K. Čičo, R. Lupták, E. Dobročka, A. Rosová, D. Machajdík, and K. Fröhlich

Liquid injection metal organic chemical vapour deposition (MOCVD) is suitable technique for growth of thin oxide films. In this technique a precursor is dissolved in an appropriate solvent and this solution is injected into the evaporation chamber. Injection of the solution is performed by an electromagnet micro-valve controlled by computer. Injected solution is flash evaporated in the evaporation chamber. Evaporated vapours of the precursor and solvent are transported to the deposition chamber using argon and mixed with oxygen, serving as a reactant gas. Advantage of the process is that it is possible to control the growth rate and composition of the films by dissolving of different amount of the precursors in the starting solution. Unfortunately, concentration of the solvent in reaction atmosphere is always higher than the concentration of the precursor and therefore influence of the solvent on reaction process is of great importance. The solvent, as well as its reaction by-products, participate in a chemical reaction during deposition and affect the film growth.

Using liquid injection MOCVD we have succeeded in a preparation of great variety of thin oxide films including conducting RuO_2 as well as dielectric Al_2O_3 , LaLuO_3 and GdScO_3 films. In addition, thin films of Ru and Pt were deposited by this technique as well.

Thin RuO_2 films were prepared using $\text{Ru}(\text{thd})_2(\text{cod})$ precursor dissolved in iso-octane in a concentration of 0.03 M. Growth rate of the films attains several nm/min. Deposited RuO_2 films are either polycrystalline or epitaxial, depending on the substrate. Polycrystalline RuO_2 films were obtained on Si/SiO₂ substrates at 290 °C. Resistivity of the films grown on Si/SiO₂ substrate is about 200 $\mu\Omega\text{cm}$. The films can be used as electrodes in capacitor structures for DRAM applications.

(101) and (002) oriented RuO_2 films were deposited

on R-plane and M-plane single crystal sapphire substrates, respectively. Figure 1 shows X-ray diffraction pattern of the 002 oriented epitaxial RuO_2 film grown on the M-plane oriented sapphire. Full width at half maximum (FWHM) of the (002) diffraction rocking curve of 0.8 ° indicates heteroepitaxial growth of RuO_2 on M-plane sapphire.

Al_2O_3 thin films were grown by liquid injection MOCVD technique at 600 °C using precursor aluminium acetylacetonate ($2\text{Al}(\text{C}_5\text{H}_7\text{O}_2)_3$) dissolved in toluene. The films exhibited dielectric constant equal to 9 and very low leakage currents. The films were successfully used as gate insulation in metal-oxide-semiconductor high electron mobility transistor based on AlGaIn/GaN and InAlN/GaN heterostructures.

Complex oxide films can be effectively grown using liquid injection MOCVD. GdScO_3 and LaLuO_3 thin films were prepared at temperatures from 450 up to 600 °C using $(\text{thd})_3$ precursors dissolved in toluene. The growth rate of the films was adjusted to about 0.8 nm/min. The films exhibited amorphous character that sustains under rapid thermal annealing up to 1000 °C. Figure 2 shows X-ray reflectivity of the 13.2 nm thin GdScO_3 film. Modulation of the curve up to 2 theta = 10 indicates very smooth surface and sharp GdScO_3/Si interface. Dielectric constant of the films with the thickness range from 5 to 20 nm was about 20 and only slightly depended on Gd/Sc atomic composition. The GdScO_3 films appear to be promising candidate for next generation of high dielectric constant gate dielectrics in silicon CMOS technology.

This work was supported by the Slovak grant agency APVV (projects APVT-51-017004, APVV-0133-07) and VEGA (projects 2/5130/25, 2/0031/08).

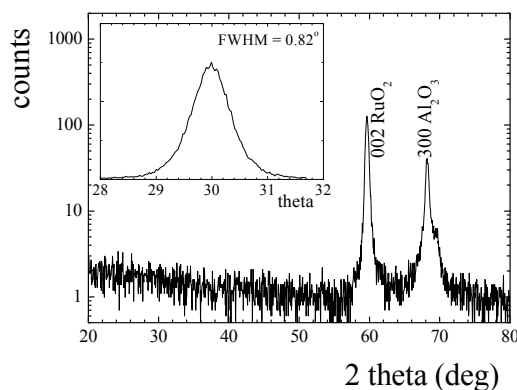


Fig. 1. X-ray diffraction pattern of epitaxial RuO_2 film deposited on M-plane sapphire.

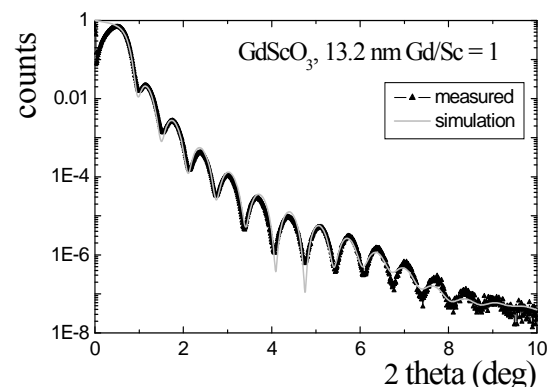


Fig. 2. X-ray reflectivity of GdScO_3 film.

High growth rate deposition of ruthenium films by liquid injection atomic layer deposition

K. Hušková, E. Dobročka, A. Rosová, J. Martaus, D. Machajdík, and K. Fröhlich

Recently several reports on Ru preparation by atomic layer deposition (ALD) have appeared [1-4]. In these reports growth rate of the Ru ALD films is between 0.04 and 0.18 nm/cycle.

We reported on preparation of ruthenium thin films using liquid injection atomic layer deposition. The process resulted in high growth rate. In the liquid injection ALD the Ru(thd)₂(cod) precursor dissolved in toluene in a concentration 0.02 M was injected into the evaporation part of the reactor. ALD deposition cycle consisted of four steps: (i) repeated injection of the precursor – 10 injections, (ii) purge of the deposition chamber by Ar, (iii) oxygen introduction, (iv) purge of the deposition chamber by Ar. Argon as a carrier gas was introduced in each deposition step. X-ray diffraction (Fig. 1) revealed growth of pure Ru phase. The growth rate exhibited saturation as a function of precursor concentration, number of injections per cycle, oxygen flow rate and oxygen pulse time, thereby indicating self-limiting mechanism. Transmission electron microscopy revealed polycrystalline Ru films with grains diameter of about 20 nm.

Thickness as a function of number of cycles exhibits two different regions (Fig. 2): from 0 up to 25 cycles the growth rate is about 0.8 nm/cycle while above 25 cycles it decreases to 0.23 nm/cycle. We suppose that the high growth rate was attained due to oxygen chemisorption on the ruthenium surface and formation of subsurface oxygen. Source of oxygen is therefore present not only during oxygen gas introduction step. At low number of cycles (5 and 10 cycles) we have observed island structure. The growth in this region presumably deviates

from the ALD due to specific nucleation mechanism on the SiO₂ surface.

SIMS analysis revealed in the ALD prepared Ru films slightly increased concentration of carbon in comparison to MOCVD grown Ru films, especially close to the surface. The ALD Ru films exhibited smooth surface with a RMS roughness less than 0.3 nm for the thickness of 22 nm, as observed by atomic force microscopy. Room temperature resistivity of the films was about 20 μΩcm. Cross-section image of the film grown in trenches with the aspect ratio 12 revealed 50 % conformal growth.

The authors are grateful to A. Šatka from the International Laser Centre, Bratislava, Slovakia and to F. Fillot, from the CEA-LETI, MINATEC, Grenoble, France.

This work was supported by the Slovak grant agency VEGA (project 2/0031/08).

- [1] Aaltonen, T., Ritala, M., Arstila, K., Keinonen, J., and Leskelä, M.: *Chem. Vap. Deposition* **10** (2004) 219.
- [2] Kwon, O.-K., Kim, J.-H., Park, H.-S., and Kang, S.-W.: *J. Electrochem. Soc.* **15** (2004) G109.
- [3] Kim, S.K., Lee, S.Y., Lee, S.W., Hwang, G.W., Hwang, C.S., Lee, J.W., and Jeong, J.: *J. Electrochem. Soc.* **154** (2007) D95.
- [4] Park, S.-J., Kim, W.-H., Lee, H.-B.-R., Maeng, W.-K., and Kim, H.: *Microelectron. Eng.* **85** (2008) 39.

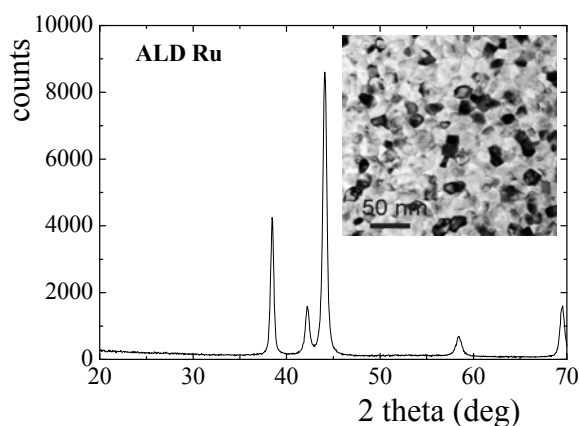


Fig. 1. X-ray diffraction pattern of Ru film. Inset shows polycrystalline structure revealed by TEM.

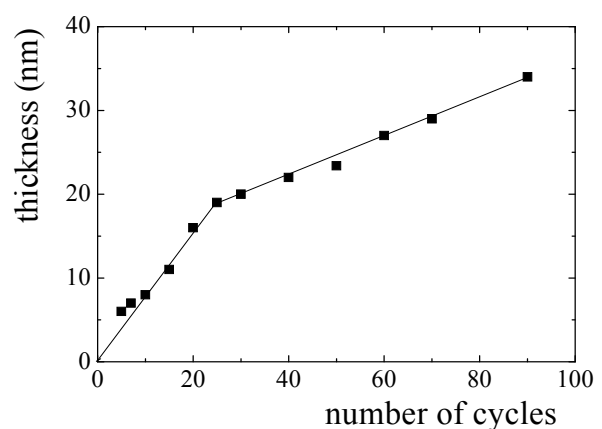


Fig. 2. Thickness as a function of number of cycles.

Characterization of thin oxide films by X-ray diffraction and X-ray reflectivity

E. Dobročka, K. Čičo, K. Hušeková, A. Rosová, and K. Fröhlich

In most thin film investigations the thickness of the films is substantially less than the penetration depth of X-rays. In the case of the nanometer range thicknesses only negligible structural information can be gained in the conventional symmetric $2\theta/\theta$ configuration. Therefore, the grazing incidence X-ray diffraction technique has been developed in which the primary beam enters the sample at very small angle of incidence. For this method the parafocusing geometry cannot be used and new beam-shaping devices for parallel X-ray optics have had to be developed. In the last decade new generation of versatile diffractometers appeared that fulfill all the requirements of thin film analysis. In this study examples of typical diffraction and reflectivity measurements are presented demonstrating the capability of the diffractometer Bruker D8 DISCOVER equipped with X-ray tube with rotating Cu anode operating at 12 kW. All measurements were performed in parallel beam geometry with parabolic Goebel mirror in the primary beam.

Rutile phase of titanium dioxide is promising material for DRAM application because of its very high dielectric constant. $\text{RuO}_2/\text{TiO}_2/\text{RuO}_2$ structures were prepared by a combination of metal organic chemical vapor deposition and atomic layer deposition techniques [1]. The layers deposited on (001) Si and (1 $\bar{1}$ 0 2) sapphire substrates were polycrystalline and epitaxial, respectively. The structure of the layers was analyzed by means of X-ray diffraction in conventional set-up as well as in the high resolution configuration. In Fig. 1a diffraction pattern of the polycrystalline $\text{TiO}_2/\text{RuO}_2/\text{Si}$ sample is shown. The measurement was performed in the grazing incidence mode. The angle of incidence was 1.5° . In Fig. 1b symmetric $2\theta/\theta$ scan of the epitaxial $\text{TiO}_2/\text{RuO}_2/\text{sapphire}$ sample is presented. The pattern was recorded in high

resolution mode using Bartels monochromator in the primary beam. Here only (101) diffraction maxima of both layers are visible – the preferred orientation of the layers is evident.

A number of gate dielectrics are used in metal-oxide-semiconductor HEMTs for the reduction of the leakage current. One of the promising materials is aluminium oxide. In this study Al_2O_3 thin films were deposited on Si substrates using MOCVD technique with N_2 or Ar as the carrier gas [2]. X-ray reflectivity (XRR) measurements were performed to analyze the structural parameters of the films. In addition to film thickness and surface roughness, XRR enables one to determine the layer density as well. In Fig. 2a typical XRR curve of Al_2O_3 thin film of the thickness 9.2 nm is shown. The thickness fringes are clearly visible only in the central part of the curve. This anomalous behavior can be explained by changes of the film density in vertical direction – i.e. perpendicular to the plane of the sample. In Fig. 2b the vertical density profile of a model consisting of two Al_2O_3 sublayers with different densities is presented. The model parameters were optimized by means of the LEPTOS 3.04 software.

This work was supported by the Slovak grant agency VEGA (project 2/0031/08).

- [1] Fröhlich, K., Aarik, J., Ľapajna, M., Rosová, A., Aidla, A., Dobročka, E., and Hušeková, K.: *J. Vac. Sci. Technol. B* 27 (2009) 266.
- [2] Čičo, K., Kuzmik, J., Gregušová, D., Stoklas, R., Lalinský, T., Georgakilas, A., Pogany, D., and Fröhlich, K.: *Microelectr. Reliability* 47 (2007) 790.

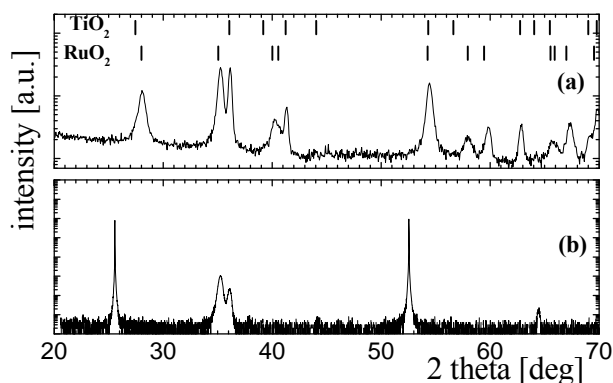


Fig. 1. X-ray diffraction pattern of TiO_2 films grown on (a) polycrystalline RuO_2 on Si – grazing incidence measurement, (b) on (1 $\bar{1}$ 0 2) sapphire – high resolution $2\theta/\theta$ scan.

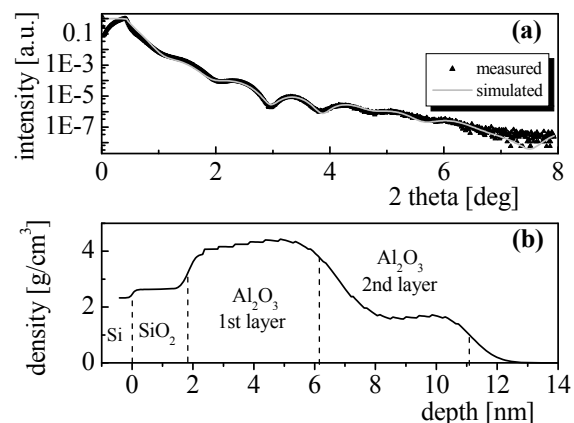


Fig. 2. (a) Measured and simulated X-ray reflectivity curves of Al_2O_3 on Si. (b) Depth density profile of the stack of layers used in the simulation model. The interfaces are marked by the dashed lines.

Contribution of Rutherford backscattering spectroscopy to thin oxide films characterization

D. Machajdík, K. Hušková, and K. Fröhlich

The development of a new technology for the formation of thin films is rather a complicated task. In the process, it is necessary to assess the quality of films produced to provide feedback for the technologist. Quality characterizations methods are therefore an integral part of an entire technology development, and they are vital for the whole optimization process.

Sophisticated methods are often used for the extraction of characteristic thin film parameters. One of the classical methods used for this purpose is Rutherford backscattering spectroscopy (RBS). It is complementary to X-ray diffraction [1].

We give an example of an RBS analysis applied to GdScO thin films. It illustrates the capability of RBS in the development of a technology. GdScO is a high dielectric constant material with a κ value of around 20, which makes it interesting for the next generation of microelectronic devices.

A set of 9 samples of thin GdScO film was prepared with a different Gd:Sc ratio in precursors. The set was investigated from several points of view. We focused particularly on the determination of film thickness, stoichiometry, gradient of the stoichiometry, mapping of

deposition conditions along the CVD reactor, the Gd:Sc ratio in the film as a function of the Gd:Sc ratio in the precursors, and on the presence of impurities.

The film thickness together with the film stoichiometry were determined by modelling and simulation of the theoretical spectra (Fig. 1a, b). Oxygen as a light element was determined from the RBS spectrum measured at energy 3.05 MeV, where the resonance of α particles on oxygen nuclei occurs. Therefore the stoichiometry of the films was revealed quantitatively.

A correlation between the Gd:Sc ratio in the precursor and in the films is shown in Fig. 2. An important conclusion can be obtained from this figure. To achieve a 1:1 ratio in a film, one should set the ratio at 4:1 in the precursor solution.

We found a peak of Ru, which represents an unexpected presence of an impurity in all spectra in Fig. 1a. It is the result of previously deposited RuO₂ in the same CVD chamber. It means that a standard cleaning procedure of the reactor does not guarantee a sufficiently clean environment in the reactor. A separate reactor should be used for each type of deposited material. Detailed analysis of the spectrum (Fig. 1b) reveals that the concentration of Ru impurity increases towards the film surface. By contrast, the Gd and Sc concentrations increase towards the interface. It indicates that the stability of the deposition parameters should be improved.

The authors are grateful to A. Macková from the Nuclear Physics Institute of ASCR, Řež, Czech Republic for cooperation with the RBS measurements.

This work was supported by the Slovak grant agency VEGA (project 2/0031/08) and APVV (project APVV-0133-07)

[1] Machajdík, D., Kobzev, A. P., and Fröhlich, K.: *Vacuum* 78 (2005) 455.

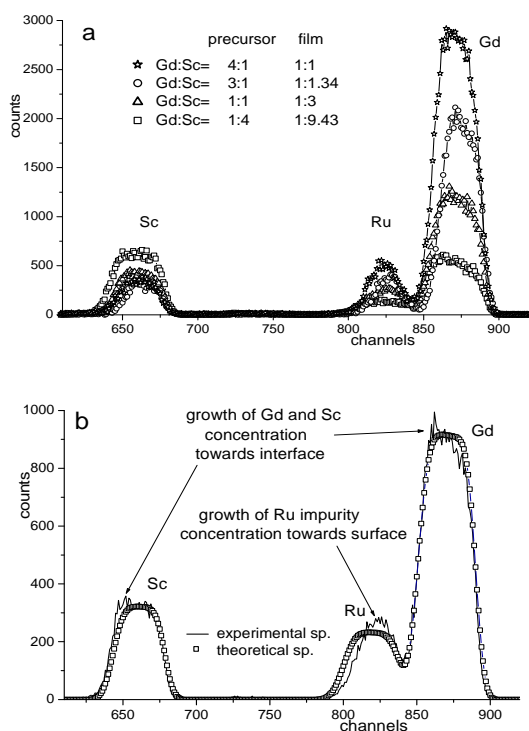


Fig. 1 a) Set of four RBS spectra measured on films deposited at different Gd:Sc precursor ratio; b) Experimental and theoretical spectrum. Comparison of them indicates gradient of Gd, Sc and Ru concentration.

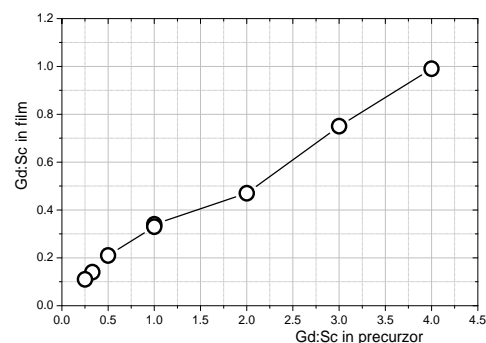


Fig. 2. Correlation between Gd:Sc ratio in precursor and in the films.

Effect of forming gas annealing on stability of RuO₂-rich Ru-Si-O polycrystalline gate electrodes

A. Rosová, M. Ľapajna, E. Dobročka, V. Štrbík, Š. Gaži, and K. Fröhlich

RuO₂ is a metallic oxide with the high work function of above 5 eV that is an important parameter for using it as a gate electrode material in modern CMOS technology. However, RuO₂ decomposes into metallic Ru during annealing in reduction atmosphere. Annealing in forming gas (10% H₂ + 90% N₂) is an inevitable technologic step that disqualifies RuO₂ as a gate electrode.

We have exposed polycrystalline RuO₂ and RuO₂-rich Ru-Si-O layers prepared by atomic vapor deposition (AVD) to forming gas annealing (FGA) to study the stability of the work function and their microstructure necessary for gate electrode integration [1].

In all samples RuO₂ phase was transformed into Ru during FGA, but the effect was different for pure RuO₂ and Ru-Si-O layers. The originally pure RuO₂ layer (Fig. 1a) exhibited not only lowering of work function below required value but also it lost its integrity. The resulting Ru layer became non-continuous due to shrinkage of material during oxygen loss and phase transformation, which corresponds to the molar volume ratio of approximately one-half (Fig. 1b).

Ru-Si-O layers were composed of RuO₂ grains of a size dependent on SiO₂ content and an amorphous matrix (Fig. 1c). The amorphous matrix in this immiscible system acted as a barrier for grain growth not only during Ru-Si-O layer growth, but also during FGA and related Ru grain recrystallization. The resulting Ru-Si-O layer consisted of Ru grains (again, their grain size depended

on SiO₂ content) distributed in amorphous matrix. In this way the SiO₂ addition helped to retain the film continuity (Fig. 1d).

The other very important effect of SiO₂ addition is the presence of an amorphous or very fine nanocrystalline interlayer between the Ru-Si-O layer and SiO₂ substrate composed of a mixture of RuO_x and SiO_x. This ultra-thin layer shows good resistance to FGA and the work function of required value (above 5 eV). Figure 2 reveals difference between diffraction pattern of SiO₂ grown on Si substrate and the sample with removed upper Ru-Si-O layer indicating a presence of such interlayer. In the second case (line with open squares) the spectrum is the sum of contributions of the SiO₂/Si surface and the ultra-thin interlayer composed of a mixture of RuO_x and SiO_x. We used ProcessDiffraction 2.1.7 software for electron diffraction analysis [2].

We would like to thank to C. Manke and P.K. Baumann for Ru-Si-O thin layers deposition and P. Benko and L. Harmatha for *C-V* measurements.

This work was financially supported by projects VEGA 2/5130/25 and APVV-51-017004

- [1] Ľapajna, M., Rosová, A., Dobročka, E., Štrbík, V., Gaži, Š., Fröhlich, K., Benko, P., Harmatha, L., Manke, C., and Baumann, P.K.: *J. Appl. Phys.* **103** (2008) 073702.
 [2] Lábár, J.L.: In: *Proc. of EUREM12*, ed. Frank, L. and F., Brno, Czech Republic, 2000, Vol. III, p. 1379.

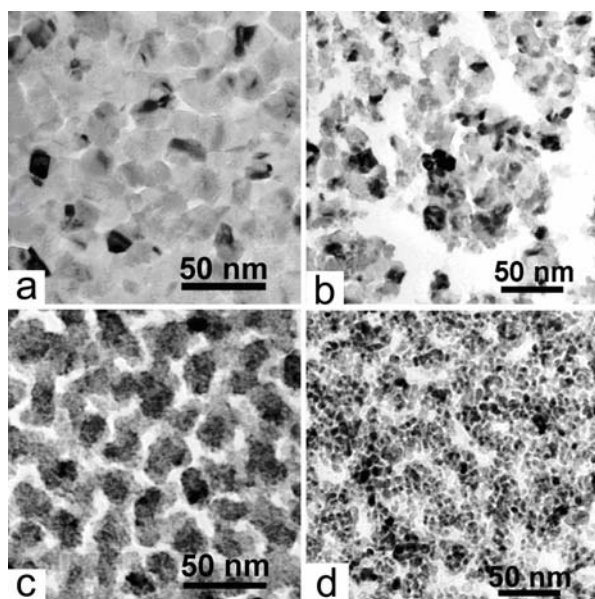


Fig. 1. Plane-view TEM micrograph of the RuO₂ film before (a) and after FGA (b) and Ru-Si-O film with 40% SiO₂ before (c) and after FGA (d).

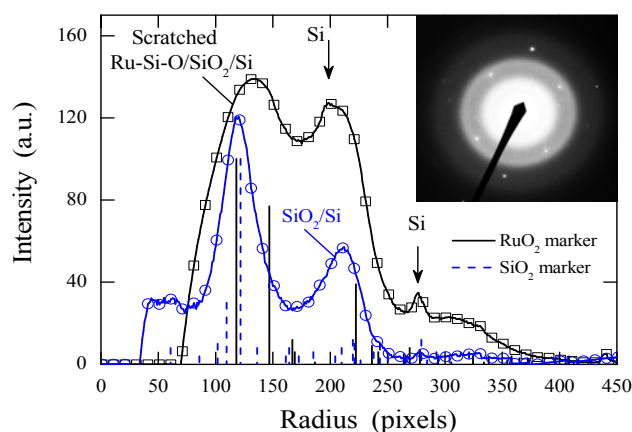


Fig. 2. Azimuthal integrated intensity dependence on radial position obtained from SAD pattern of Ru-Si-O/SiO₂/Si (Ru-Si-O film with 40% of SiO₂ after FGA) sample with scratched top Ru-Si-O layer (line with open squares) and pure thermal SiO₂ grown on Si (line with open circles). The inset shows the SAD pattern of sample with scratched Ru-Si-O layer. The vertical markers show diffraction maxima of reference RuO₂ (solid lines) and SiO₂ (dashed lines) spectra.

Work function thermal stability of RuO₂-rich Ru-Si-O p-channel metal-oxide-semiconductor field-effect transistor gate electrodes

M. Ľapajna, A. Rosová, E. Dobročka, V. Štrbík, Š. Gaži, and K. Fröhlich

In CMOS technology, dual metal gates will replace a polycrystalline Si as the gate electrode in metal-oxide-semiconductor field effect transistors (MOSFETs) [1]. Among other metals and conductive oxides, Ru-based films (Ru, RuO₂, SrRuO₃) represent promising electrode materials due to their high work function suitable for p-channel MOSFETs. However, they suffer from limited stability in H₂-enriched forming gas annealing (FGA) that is an unavoidable technological step in CMOS process. It was found that mixture of RuO₂ and SiO₂ shows robust metastability although there is not known compound of the species. In this work, thermal stability of Ru-Si-O gate electrode effective work function (EWF) during FGA and rapid thermal annealing (RTA) is systematically studied for the first time on MOS capacitors [2].

The Ru-Si-O layers were prepared by atomic vapor deposition (AVD[®]) in an Aixtron Tricent reactor. As a gate dielectric, slanted thermal SiO₂, *i.e.* oxide with varying thickness (4 – 8 nm), were used for precise determination of gate electrode EWF on MOS capacitors using capacitance-voltage (*C-V*) measurement. FGA in 10 % H₂ + 90 % N₂ atmosphere were performed at 430 °C for 30 min while RTA was carried out in N₂ ambient in the temperature range of 500 – 1000 °C for 10 s.

When grown by CVD-based technique, RuO₂ thin film shows EWF similar to 5.1 eV, however, the film reduces to Ru upon FGA and disintegrates as Ru has smaller molar volume and, if measurable, EWF falls to 4.6 eV that corresponds to bulk Ru WF. As seen from Fig. 1, Ru-Si-O thin film with 15 % of SiO₂ is much more stable, showing the EWF similar to that of RuO₂ even after four times repeating FGA.

In CMOS process, RTA at 1000 °C/10 s is used after

gate stack deposition for impurity activation followed by FGA. Gate electrode EWF of Ru-Si-O with 15 % of SiO₂ was found to be stable in RTA for temperatures up to 800 °C followed by FGA. Although EWF is stable also after RTA at 900 °C, it then drops from 5.2 to 4.8 eV during FGA. The EWF decreasing was accompanied with slight accumulation capacitance decreasing. When compare to pure RuO₂, admixture of SiO₂ leads to striking improvement of the thin film thermal stability that makes it suitable for application in future CMOS technology, although microstructure of the film has to be optimized.

This work was financially supported by projects VEGA 2/5130/25 and APVV-51-017004

[1] *International Technology Roadmap for Semiconductors*, (<http://public.itrs.net>).

[2] Ľapajna, M., Rosová, A., Dobročka, E., Štrbík, V., Gaži, Š., Fröhlich, K., Benko, P., Harmatha, L., Manke, C., and Baumann, P.K.: *J. Appl. Phys.* **103** (2008) 073702.

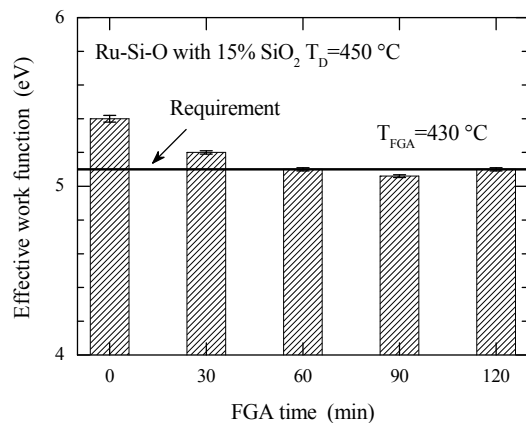
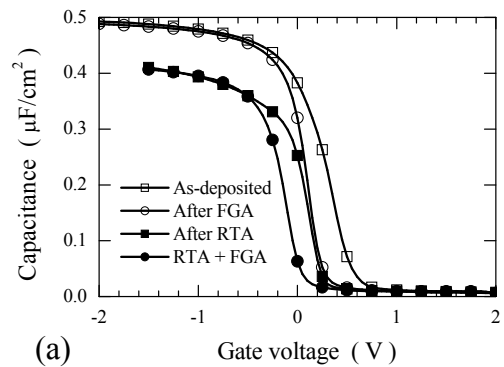
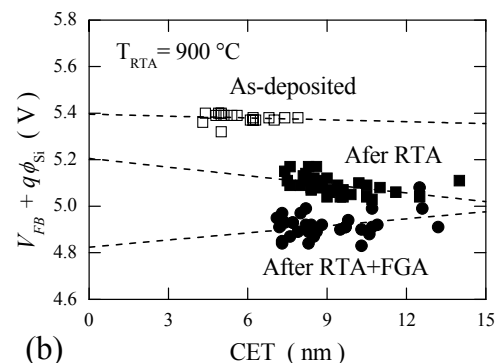


Fig. 1. Evolution of EWF of Ru-Si-O with 15% of SiO₂ deposited at 450 °C after successive FGA. Line represents the requirement for a high-performance p-MOSFET gate electrode EWF.



(a) Gate voltage (V)



(b) CET (nm)

Fig. 2. (a) *C-V* curves of MOS capacitors with Ru-Si-O (15% of SiO₂, T_d=450 °C) gate electrode after deposition, FGA, RTA at 900 °C, and subsequent FGA and the extraction of its EWFs (b) using linear fit to $V_{FB} + q\phi_{Si}$ vs. CET plots giving EWF at $x=0$.

Evidence of hafnia oxygen vacancy defects in MOCVD grown $\text{Hf}_x\text{Si}_{1-x}\text{O}_y$ ultrathin gate dielectrics gated with Ru electrode

M. Āapajna, A. Rosova, K. Huřekova, E. Dobrořka, and K. Frohlich

Hf-based dielectrics have been selected as the gate dielectric for sub-45-nm node CMOS technologies [1]. Although many papers have reported on the high-quality Hf-silicate, detail knowledge on the structural defects and their relation to electrical characteristics are still limited. Particularly, the gate leakage characteristics at low and moderate electric fields are of great interest as they will affect the device performance and are closely related to quality of ultra-thin Hf-silicate gate dielectric. Therefore, in this study, we analyze temperature dependent current-voltage (IV - T) characteristics of $\text{Hf}_x\text{Si}_{1-x}\text{O}_y$ gate dielectric annealed by a rapid thermal annealing (RTA) in oxygen in the temperature range of 700 – 1000 °C using metal-oxide-semiconductor (MOS) test structures.

$\text{Hf}_x\text{Si}_{1-x}\text{O}_y$ dielectrics with thicknesses range from 2 to 9 nm were grown by MOCVD and then annealed by RTA. The X-ray diffraction and transmission electron microscopy study revealed X-ray amorphous structure composed of HfO_2 -rich nuclei embedded in SiO_2 -rich amorphous matrix stable up to 900 °C/10 s. Annealing at 1000 °C results in re-growth of HfO_2 grains [2].

To form MOS structures, Ru gate electrodes were prepared by liquid injection MOCVD and patterned. Capacitance-voltage measurements were used to determine the interfacial layer thickness and electric field distribution over the MOS capacitor. IV - T characteristics measured on MOS capacitors with the gate dielectric annealed at 700 °C showed noticeable temperature dependence with activation energy of about 0.4 eV (Fig. 1a). Trap-assisted (or two-step) tunneling (TAT) was suggested to be responsible for such behavior as depicted in band diagrams for different gate voltages

(Fig. 1c). On contrary, IV - T characteristics for dielectric annealed at 800 °C were found to be weakly temperature dependent (Fig. 1b) indicating a direct tunneling (DT) as a dominant current mechanism. The ‘‘bump’’ on the IV characteristics originates from interface state involving in the tunneling process and affecting local distribution of the electric field. Note good correlation between the gate voltage at which the bump disappears and Si conduction band falling below the metal gate Fermi level.

Since the dielectric trap level is annealed out during RTA in oxygen ambient, we suppose that this defect corresponds to oxygen vacancy (V_O) in HfO_2 , keeping in mind the microstructure of the dielectric films. Note that V_O in SiO_2 , the so-called E' center create the level deep in SiO_2 valence band. Indeed, the position of the level is in good agreement with a plane wave density functional simulation [3]. The transition from the positive to neutral electronic state corresponds to the capture of an electron from the gate electrode.

The preparation of the $\text{Hf}_x\text{Si}_{1-x}\text{O}_y$ films by Aixtron is gratefully acknowledged. This work was financially supported by project APVV-51-017004.

- [1] *Int. Technol. Roadmap for Semicond.*, (<http://www.itrs.net>).
- [2] Āapajna, M., Rosova, A., Huřekova, K., Roozeboom, F., Dobrořka, E., and Frohlich, K.: *Microelectron. Eng.* **84** (2007) 2366.
- [3] Shluger, A.L., Foster A.S., Gavartin, J.L., and Sushko, P.V.: *Nano and Giga Challenges in Micro-Electronics*, Korkin A. ed., Elsevier, Berlin, 2003.

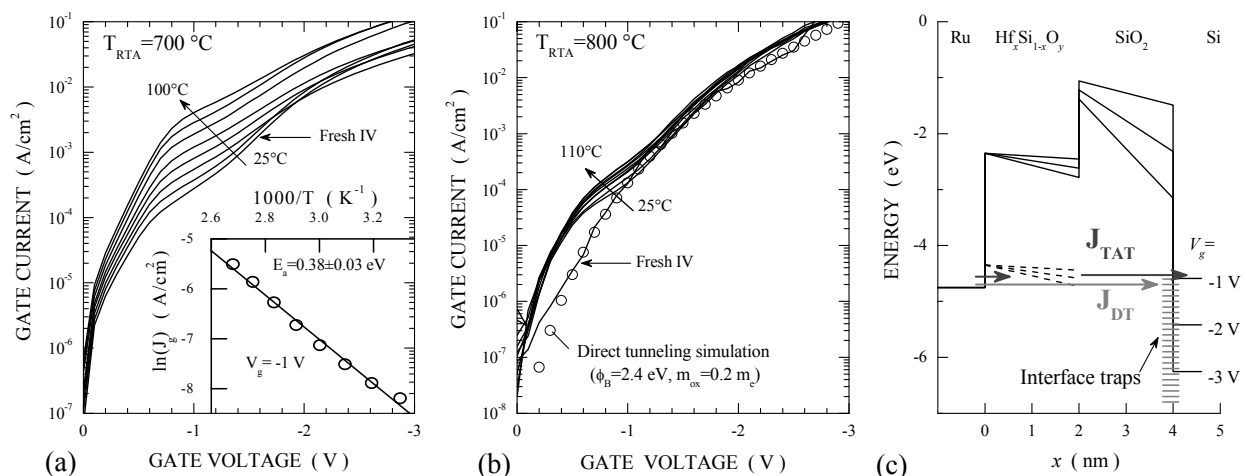


Fig. 1. IV - T characteristics of MOS capacitors with TD annealed at 700 (a) and 800 °C (b); (c) corresponding schematic band diagram illustrating TAT (dark grey arrow) and DT (light grey arrow) leakage current mechanism with charge trapping at the interface states for various V_g -data. Inset of (a): Arrhenius plot constructed at $V_g = -1$ V.

Effect of Ti doping on Ta₂O₅ stacks with Ru and Al gates

M. Ľapajna, E. Dobročka, and K. Fröhlich

Among the high- κ oxides investigated for memory device application, Ta₂O₅ has been identified as the strongest alternative to SiO₂-based dielectrics in storage capacitors of nanoscale DRAMs. The doping with a small quantity of a number of elements (Ti, Hf, Al, Zr) can extend the potential of pure Ta₂O₅ to allow further EOT scaling [1]. However, the results reported in the literature suggest that the doping-induced variation of the stack characteristics depends on the method of dopant introduction as well. In this work, the effect of introduction of Ti into the matrix of rf sputtered Ta₂O₅ is investigated varying the level and the method of Ti incorporation and using two types of top electrodes.

Ti incorporation into Ta₂O₅ was accomplished by rf sputtering of ultra-thin Ti film (0.7 or 2 nm) on the top (surface doping) or in between two Ta₂O₅ thin films (bulk doping) and subsequent annealing in N₂ atmosphere. Test structures were created by evaporating the Al or MOCVD growth of Ru films followed by patterning [2].

Structural properties were investigated by X-ray reflectivity (XRR) and time of flight secondary ion mass spectroscopy (ToF-SIMS) analysis. It was found that Ti was incorporated through the whole Ta₂O₅ film peaked at the dopant source and also into the part of ~3-nm-thick interfacial Ta-Si-O layer peaked close to Ta₂O₅/Ta-Si-O interface (Fig. 1). Interfacial layer thickness and Ti distribution in it is independent of the level and the

method of the doping.

From the capacitance-voltage (C - V) and current-voltage (I - V) characteristics we determined the effective dielectric constant, ϵ_{eff} , fixed oxide charge in the gate oxide, Q_f , and gate leakage current density, J , at gate voltage -1 V (accumulation regime) as summarised in Tab. 1. Only higher level of Ti doping (2-nm-thick Ti layer) leads to ϵ_{eff} increasing compare to pure Ta₂O₅. This was attributed to enhanced Ti incorporation to low- κ interfacial layer, resulting in its slight dielectric constant increasing. Oxide charge was found to be positive for Al-gated and negative for Ru-gated (except highly doped gate oxide) MOS capacitors. We suppose that different formation energy of oxygen vacancies for the two metals can lead to different metal-induced defect creation at the metal/oxide interface resulting in observed Q_f behaviour.

Leakage current was found to be higher for Ru-gated MOS capacitor, most likely due to a forementioned reaction of Ru with O. Surface doping offers systematically lower gate leakage as Ti doping at the Ta₂O₅ surface can effectively reduce the concentration of oxygen vacancies.

The work was supported by the grant APVV-0133-07.

[1] Cava, R.J., et al.: *Nature* **377** (1995) 215.

[2] Paskaleva, A., Ľapajna, M., Atanassova, E., Fröhlich, K., Vincze, A., and Dobročka, E.: *Appl. Surf. Sci.* **254** (2008) 5879.

Tab. 1. Thickness t_{ox} (estimated by XRR), effective dielectric constant ϵ_{eff} , net oxide charge Q_f (estimated from C - V curves) and comparison of current levels measured at -1 V for samples with Al and Ru gates.

Sample designation	t_{ox} (nm)	ϵ_{eff}		$Q_f \times 10^{12}$ (cm ⁻²)		J at -1 V (A/cm ²)	
		Ru gate	Al gate	Ru gate	Al gate	Ru gate	Al gate
0.7 nm Ti on Ta ₂ O ₅	7	6.7	6.3	-0.81	+1.7	1.5×10^{-5}	7×10^{-7}
2 nm Ti on Ta ₂ O ₅	8.9	10.2	8	-0.53	+1.4	2.5×10^{-5}	9×10^{-7}
Ta ₂ O ₅ /0.7 nm Ti/Ta ₂ O ₅	6	6.6	6	-0.6	+3.5	1.7×10^{-3}	2×10^{-6}
Ta ₂ O ₅ /2 nm Ti/Ta ₂ O ₅	9.1	9.3	9.1	+0.36	+2.5	4.3×10^{-5}	2×10^{-5}
pure Ta ₂ O ₅	7	9.3	6.9	-1.3	+3.5	0.59	2×10^{-5}

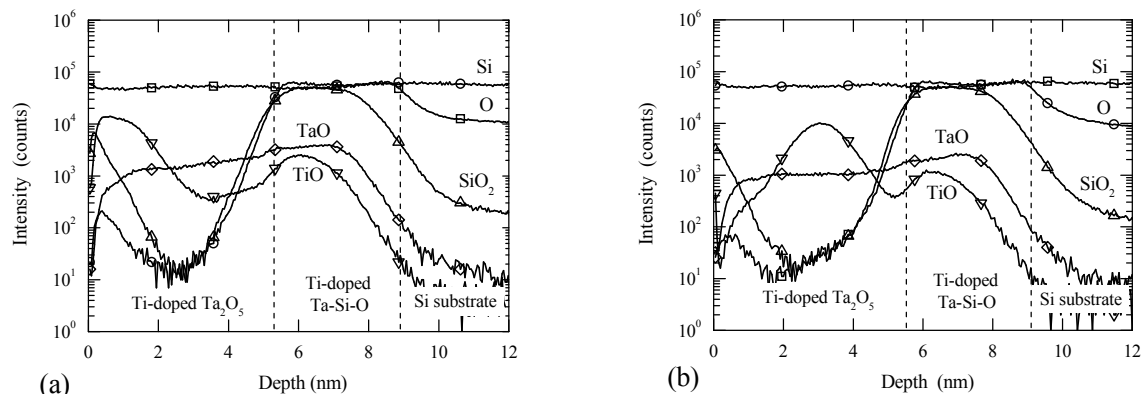


Fig. 1. ToF-SIMS depth profiles of (a) surface doped Ta₂O₅ with 2-nm-thick Ti film and bulk doped Ta₂O₅ (b) with 2-nm-thick Ti film.

Growth of high-dielectric-constant TiO₂ films in capacitors with RuO₂ electrodes

K. Fröhlich, M. Ľapajna, A. Rosová, E. Dobročka, B. Hudec, and K. Hušková

Titanium dioxide is attractive dielectric material for microelectronic applications. Depending on its growth conditions TiO₂ can be most easily prepared in amorphous, anatase and/or rutile phases. The rutile phase exhibits very high dielectric constant ranging from 90 to 170, depending on the lattice orientation. Due to the high dielectric constant the TiO₂ rutile phase is considered as a promising material for capacitors in future generation of dynamic random access memories (DRAM).

In a DRAM capacitor dielectric film should be combined with conductive electrodes. As the affinity of TiO₂ is about 4 eV, metals with high work function should be used as electrodes to prevent excessive leakage currents due to Schottky emission. We have recently demonstrated that the work function of ruthenium oxide is more than 5 eV. RuO₂ has high conductivity and crystallizes in the rutile structure with the lattice parameters close to that of the TiO₂ rutile phase. Therefore, RuO₂ is promising material for electrodes in capacitors with TiO₂ dielectric.

We have used bottom polycrystalline RuO₂ electrode grown by metal organic chemical vapour deposition (MOCVD). The films were grown at 290 °C using liquid injection of Ru(thd)₂(cod) precursor dissolved in iso-octane. In the second step TiO₂ rutile films were deposited by atomic layer deposition (ALD) at the Institute of Physics, University of Tartu, Estonia. The films were grown by ALD in a flow-type reactor at temperatures from 150 up to 600 °C. In order to synthesize the films, the substrates were exposed to the vapor of TiCl₄ (for 2 s), purged in the flow of pure nitrogen (for 2 s), exposed to the vapor of H₂O (for 2 s) and again purged in the flow of pure nitrogen (for 5 s).

The ALD cycle was repeated 200 – 1500 times to obtain 10 – 80 nm thick TiO₂ films.

Properties of the RuO₂/TiO₂/RuO₂ structures are described in [1]. X-ray diffraction showed strong effect of the bottom RuO₂ film resulting in the growth of rutile TiO₂ phase at temperatures above 275 °C. Figure 1 displays capacitance as a function of bias voltage of the RuO₂/TiO₂/RuO₂ capacitor with 20 nm TiO₂ film grown at 425 °C. Capacitance density of more than 60 fF/μm² with an equivalent oxide thickness (EOT) of 0.5 nm was attained. Determination of the dielectric constant using plot EOT vs. thickness (Fig. 2) revealed value 38 for the TiO₂ films grown at 150 °C, while dielectric constant as high as 155 was obtained for the films deposited at 275 °C and above. Extrapolation of the plot EOT vs. thickness to zero revealed absence of any interface layer between RuO₂ and TiO₂. We believe that high dielectric constant of the TiO₂ films grown at temperatures from 275 to 425 °C stems from high degree of crystalline perfection of the rutile phase achieved by local epitaxial growth on polycrystalline RuO₂ seed layers.

The authors acknowledge cooperation with J. Aarik and A. Aidla from the Institute of Physics, University of Tartu, Estonia. The work was supported by APVV (project APVT-51-017004) and VEGA (project 2/0031/08).

[1] Fröhlich, K., Ľapajna, M., Rosová, A., Dobročka, E., Hušková, K., Aarik, J., and Aidla, A.: *Electrochem. and Solid State Lett.* **11** (2008) G19.

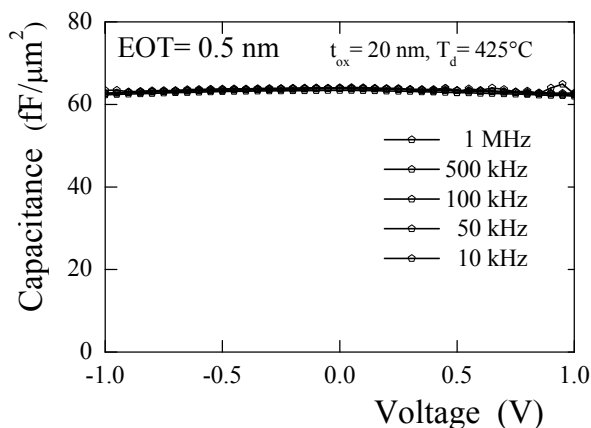


Fig. 1. Capacitance as a function of bias voltage of the RuO₂/TiO₂/RuO₂ capacitor.

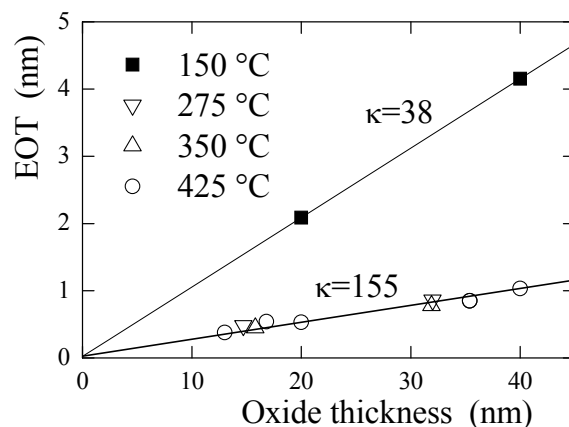


Fig. 2. Determination of the dielectric constant for the RuO₂/TiO₂/RuO₂ capacitor.

Leakage currents in $\text{RuO}_2/\text{TiO}_2/\text{RuO}_2$ structures with high-dielectric-constant TiO_2 rutile films

K. Fröhlich, M. Ľapajna, A. Rosová, E. Dobročka, and K. Hušková

Rutile phase of titanium dioxide is promising dielectric material for the dynamic random access memory (DRAM) application because of its very high dielectric constant. Employment of TiO_2 film with dielectric constant above 100 in a DRAM capacitor allows for scaling of the equivalent oxide thickness (EOT) below 0.5 nm.

Unfortunately, TiO_2 -based capacitor structures suffer from excessive leakage currents. TiO_2 is a semiconductor with relatively small band gap of 3.2 eV. Compositional variation (oxygen vacancies, titanium interstitials) creates n-type defects and contributes therefore to electrical conductivity. When prepared in a polycrystalline form, local defects concentrated around grain boundaries can act as effective path for leakage currents, resulting in unacceptable high leakage current density. It could be expected, that concentration of defects in epitaxial films will be lower. Therefore, we examined differences between electrical properties of polycrystalline and epitaxial TiO_2 layers [1].

Leakage current density as a function of bias voltage (J - V) for both polycrystalline and epitaxial $\text{RuO}_2/\text{TiO}_2/\text{RuO}_2$ structures is shown in Fig. 1. Typically, the J - V characteristics are asymmetric with lower current density for negative bias (top electrode injection). The leakage current density at the positive bias (bottom electrode injection) of 1 V is fairly high ($\sim 10^{-2}$ A/cm²) for the polycrystalline capacitor while it decreases down to 6×10^{-5} A/cm² for the epitaxial structure. For bias voltage 0.8 V, the leakage current density is about 6×10^{-6} A/cm² for epitaxially grown capacitor. This value is more than 3

orders of magnitude lower than that obtained for the same EOT in a recent paper of Kim et al. [2].

For negative gate bias (top electrode injection), we have fitted the J - V characteristics of both polycrystalline and epitaxial MIM structures using the equation derived for Schottky emission. Schottky emission represents the electrode limited mechanism as the current strongly depends on the barrier height ϕ_b between the metal Fermi level and the oxide conduction band edge. The deviation of the experimental data at low voltages (0 – -0.4 V) is due to the hopping mechanism reported by several authors. The mechanism takes place also at positive gate voltages in the same voltage range (0 – 0.4 V).

In the case of the epitaxial MIM structure, the leakage current at higher positive voltages can be accurately fitted by the Pool-Frenkel emission. In the case of polycrystalline stack, no feasible conduction mechanism capable to fit the J - V behaviour at higher positive voltages was found.

From the J - V curves measured at negative gate voltages, it seems that quality of the $\text{RuO}_2/\text{TiO}_2$ interfaces rather than presence of the grain boundaries plays an important role in the resulting leakage current mechanism. However, bulk limited conduction mechanism observed for epitaxial structure at positive voltages indicates the presence of the bulk traps in the TiO_2 . We suppose therefore, that observed asymmetry of the J - V characteristics in the case of epitaxial stack is connected with uneven distribution of the defects in the dielectric, while the difference in barrier heights at the $\text{RuO}_2/\text{TiO}_2$ interfaces is negligible.

The barrier height at ideal $\text{RuO}_2/\text{TiO}_2$ interface should be 1.2 eV. From the fitting of experimental values we found the barrier height value equal to 1 eV. It is likely that Fermi level pinning at the TiO_2 interface is responsible for the decreasing of the RuO_2 effective work function. Consequently, optimization of the TiO_2 deposition process and careful engineering of the $\text{RuO}_2/\text{TiO}_2$ interfaces is necessary to suppress leakage current density below 10^{-7} A/cm².

The authors acknowledge J. Aarik and A. Aidla from the Institute of Physics, University of Tartu, Estonia for the preparation of TiO_2 films. The work was supported by APVV (project APVV-0133-07) and VEGA (project 2/0031/08).

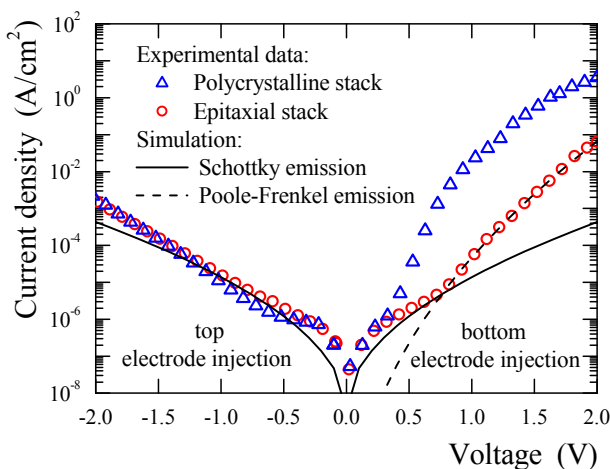


Fig. 1. Leakage current density as a function of bias voltage for polycrystalline and epitaxial $\text{RuO}_2/\text{TiO}_2/\text{RuO}_2$ capacitors.

- [1] Fröhlich, K., Aarik, J., Ľapajna, M., Rosová, A., Aidla, A., Dobročka, E., and Hušková, K.: *J. Vac. Sci. Technol. B* **27** (2009) 266.
- [2] Kim, S. K., Lee, S. Y., Seo, M., Choi, G.-J., and Hwang, C.H.: *J. Appl. Phys.* **102** (2007) 024109.

Transmission electron microscopy of epitaxially grown $\text{RuO}_2/\text{TiO}_2/\text{RuO}_2$ structures

A. Rosová, K. Fröhlich, M. Ľapajna, E. Dobročka, and K. Hušeková

Metal-Insulator-Metal (MIM) structures with dielectric layer with high dielectric constant are in demand for capacitors in ultra large scale integration dynamic random memories (DRAM). The combination of dielectric TiO_2 with metallic RuO_2 fulfills not only the imperative of sufficient energetic barrier for electrons but also enables deposition of pure rutile TiO_2 with very high dielectric constant at lower temperatures without any need of additional post-deposition annealing.

TiO_2 thin film deposition obviously results in coexistence of anatase with low dielectric constant of about 35 and rutile with high dielectric constant between 90 and 170 in dependence on crystal orientation. An additional annealing at temperature above $800\text{ }^\circ\text{C}$ is thus needful to eliminate anatase and increase resulting dielectric constant of the films.

Because RuO_2 crystallizes in very stable rutile phase with similar lattice parameters to rutile TiO_2 ($a_{\text{RuO}_2} = 0.4499\text{ nm}$, $c_{\text{RuO}_2} = 0.3107\text{ nm}$, $a_{\text{TiO}_2} = 0.4593\text{ nm}$, $c_{\text{TiO}_2} = 0.2959\text{ nm}$), RuO_2 electrode can act as a „seed layer“ stabilizing pure rutile growth of TiO_2 film. Indeed, we have shown that RuO_2 layer stabilizes the TiO_2 film to be grown in rutile form at deposition temperature from 275 to $600\text{ }^\circ\text{C}$ [1].

Local epitaxial growth was confirmed by transmission electron microscopy (TEM) on polycrystalline MIM structures deposited on Si substrates with SiO_2 layer (Fig. 1). The polycrystalline tri-layer shows columnar

structure, where RuO_2 and TiO_2 grains are oriented to each other in accord to the epitaxial relation $(001)_{\text{RuO}_2} \parallel (001)_{\text{TiO}_2}$ and $[100]_{\text{RuO}_2} \parallel [100]_{\text{TiO}_2}$. If one selects a diffraction spot corresponding to a certain grain orientation (Fig. 1b, c), the dark field image reveals the same orientation of grains in a column (Fig. 1d).

RuO_2 can grow epitaxially on R-plane sapphire substrate with the epitaxial relation $(001)_{\text{RuO}_2} \parallel (012)_{\text{Al}_2\text{O}_3}$ and $[100]_{\text{RuO}_2} \parallel [2\ 1\ 0]_{\text{Al}_2\text{O}_3}$. However, during a relatively high misfit accommodation the epitaxially grown tri-layer is split into mosaic block regions (Fig. 2) separated by low-angle boundaries [2]. In Fig. 2b the mosaic blocks are visualized and magnified by Moiré pattern, but the shape and structure of (300) diffraction spot (Fig. 2d) shows that the misorientation is very low.

We acknowledge ALD deposition of TiO_2 layers done by J. Aarik and A. Aidla, University of Tartu, Estonia. The work was supported by APVV (project APVV-0133-07) and VEGA (project 2/0031/08).

- [1] Fröhlich, K., Ľapajna, M., Rosová, A., Dobročka, E., Hušeková K., Aarik, J., and Aidla, A.: *Electrochem. Solid-State Lett.* **11** (2008) G19.
 [2] Fröhlich, K., Aarik, J., Ľapajna, M., Rosová, A., Aidla, A., Dobročka, E., and Hušeková K.: *J. Vac. Sci. Technol. B* **27** (2009) 266.

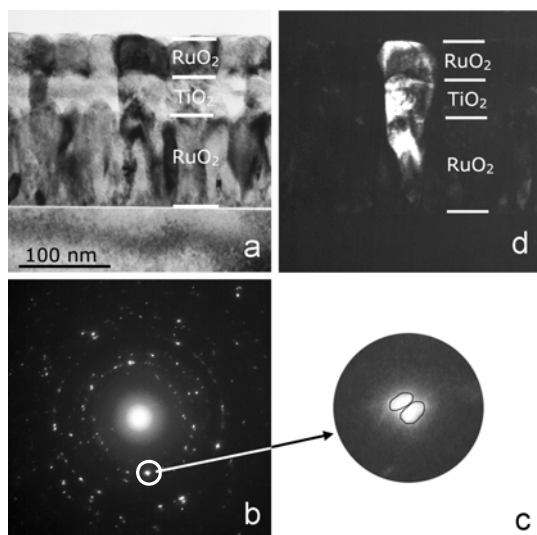


Fig. 1. Cross-sectional TEM micrograph of the poly-crystalline MIM structure deposited on Si (a) with the corresponding electron diffraction pattern (b). Diffraction spot selected by the aperture relates to RuO_2 and TiO_2 grains in a column (c). The corresponding dark-field image shows epitaxially grown grains in the column (d).

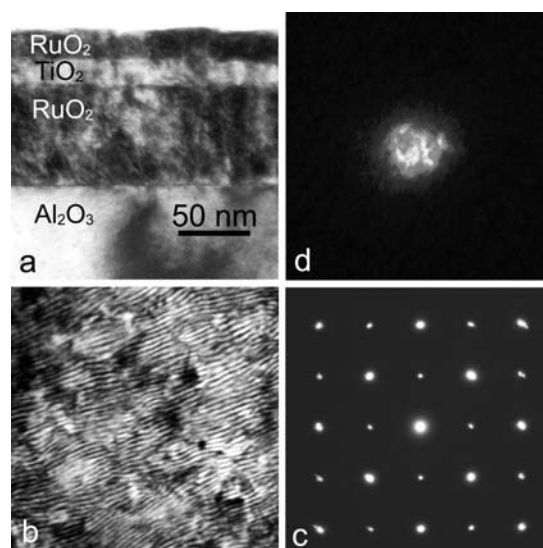


Fig. 2. Cross-sectional TEM micrograph of the MIM structure on R-plane sapphire (a). Its plane-view TEM micrograph (b) with the corresponding electron diffraction pattern (c) and detail on (300) diffraction spot (d).

Al₂O₃ insulating films grown by MOCVD using Ar or NH₃ carrier gas on InAlN/GaN heterostructures

K. Čičo, J. Kuzmík, K. Hušková, and K. Fröhlich

InAlN/GaN high electron mobility transistors (HEMTs) may become a key type of high frequency power devices [1]. However, these devices may suffer from thermal stability problem due to a possible high gate leakage current [2]. In previous reports, a variety of gate dielectrics such as SiO₂, ZrO₂ or Al₂O₃ have been used in metal-oxide-semiconductor HEMTs (MOSHEMTs) for reduction of the leakage current. On the other hand surface/interface-related imperfections may lead to collapse in the drain current. Therefore GaN-based devices are depending on surface treatment.

In our work we investigate InAlN/GaN MOSHEMT structures with Al₂O₃ gate insulation and surface passivation for reduction of leakage current and elimination of drain current collapse [3]. We tested NH₃ as an alternative carrier gas for replacing Ar in MOCVD deposition to facilitate supply of N in the pre-treatment period of the Al₂O₃ growth to fill possible N-vacancies in InAlN surface. We analyze the influence of the carrier selection on HEMTs electrical performance.

In experiment, In_{0.19}Al_{0.81}N/GaN heterostructure system was grown by Metal Organic Chemical Vapour Deposition (MOCVD) on sapphire substrate. 2DEG carrier density and mobility determined at room temperature by Hall measurements were $3 \times 10^{13} \text{ cm}^{-2}$ and $815 \text{ cm}^2 \text{ V}^{-1} \text{ s}^{-1}$, respectively. The wafer was divided into three parts for reference, Ar and NH₃ treated devices. The reference device is Schottky barrier (SB) diode with a Ni/Au contact directly deposited on InAlN.

Al₂O₃ thin films were prepared by liquid injection MOCVD using aluminium acetylacetonate precursor dissolved in toluene. Before deposition, the substrates were exposed either to ramp heating up to 600 °C in Ar atmosphere, or ramp heating up to 750 °C in NH₃ atmosphere. For the deposition, identical carrier gas as that for pretreatment was used with flow rate 100 ml/min. MOS HEMTs with a 2 μm long gate as well as circular MOS diodes were prepared.

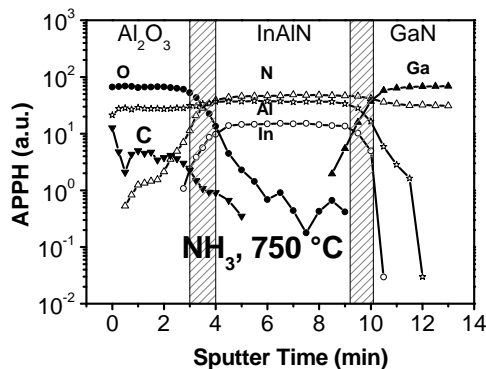


Fig. 1. AES depth profile of the sample prepared with NH₃ carrier gas. Shaded areas represent interface regions.

From current-voltage characteristics of MOS diodes, reduction of the leakage current was measured for both samples with Al₂O₃ film (NH₃ and Ar carrier gas) compared to the SB structure (not shown).

Auger electron spectroscopy (AES) depth profiles of the samples prepared with NH₃ or Ar carrier gas are depicted in Fig. 1 and Fig. 2, respectively. The carbon was detected in Al₂O₃ and InAlN layers. Sample with Ar pretreatment shows carbon only from the side of the Al₂O₃ surface due to the contamination from ambient and InAlN surface is carbon-free. If NH₃ is used, carbon is observed also on the InAlN surface (Fig. 1). Increased carbon concentration on InAlN can be explained by chemical reactions, which take place in reactor during deposition if NH₃ is used as a carrier gas. Decomposition of the precursor requires great amount of oxygen. On the other hand reaction between hydrogen from NH₃ and oxygen decreases oxygen partial pressure in a reaction atmosphere. Therefore we suppose that carbon traces on InAlN surface originate from the precursor incomplete decomposition if NH₃ is used as a carrier gas.

AES depth profile of carbon was found to correlate with the drain collapse measurement (not shown). We observed drain current collapse for NH₃ treated sample. We suggest that the current collapse is linked with the presence of deep carbon-related levels in InAlN surface region. Ar treated sample did not exhibit drain current collapse.

The authors would like to thank J. Liday, P. Vogrinčič from FEI STU Bratislava, Slovakia and J-F. Carlin, N. Grandjean from EPFL Lausanne, Switzerland for collaboration. This work was supported by the 6th FP project ULTRAGAN, No. 6903

[1] Kuzmík, J.: *Semicond. Sci. Technol.* **17** (2002) 540.

[2] Adivarahan., V., et al. : *IEEE Electr. Device Lett.* **26** (2005) 535.

[3] Čičo, K., et al.: *J. Vac. Sci. Technol. B* **27** (2009) 218.

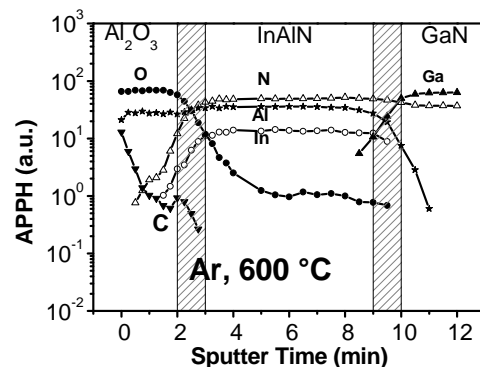


Fig. 2. AES depth profile of the sample prepared with Ar carrier gas. Shaded areas represent interface regions.

Current conduction and saturation in III-nitride MOS HEMTs

J. Kuzmík, K. Čičo, and K. Fröhlich

Gate leakage current is an important factor that limits the performance and reliability of conventional high-power III-nitride HEMTs. Thus a thin dielectric oxide layer is often inserted between the gate metal and the AlGaN barrier layer leading to the approach of the metal-oxide-semiconductor (MOS) HEMT. The dielectric was used also to cover the bare surface between the HEMT contacts. Consequently the barrier surface traps were passivated. On the other hand applying the gate insulation the gate to channel separation increases and a shift of V_T due to the gate-to-source capacitance C_{GS} decrease can be observed. Furthermore if we adopt $g_m = v_{sat} C_{GS} / L_G$ where g_m is the device intrinsic transconductance, v_{sat} the electron saturation velocity and L_G the gate length, g_m is supposed to decrease proportionally with C_{GS} . Surprisingly in recent reports the extrinsic transconductance ($g_{me} = g_m / (1 + g_m R_S)$) of III-nitride HEMTs increases after applying gate insulation and surface passivation [1-4].

The comparisons of g_{me} and transfer characteristics (at the drain-source bias $V_{DS} = 8$ V) of MOS and Schottky barrier (SB) InAlN/GaN HEMTs are shown in Fig. 1. For the explanation of the increase of g_{me} after the gate insulation, an analytical modelling of the g_{me} in dependence of channel mobility μ_{CH} was performed for both of experimental MOS and SB HEMTs with $L_G = 2 \mu\text{m}$ and for hypothetical devices with $L_G = 100$ nm, see Fig. 2. Two μ_{CH} regions are highlighted in Fig. 2: “A” represents typical GaN-based HEMTs ($\mu_{CH} < 2000 \text{ cm}^2\text{V}^{-1}\text{s}^{-1}$) while “B” corresponds to μ_{CH} of typical GaAs or InP-based HEMTs ($\mu_{CH} > 4000 \text{ cm}^2\text{V}^{-1}\text{s}^{-1}$). Results show that in the region “A” g_{me} may strongly depend on μ_{CH} and obviously is not proportional to C_{GS} . Moreover for $L_G = 2 \mu\text{m}$ (100 nm)

and $\mu_{CH} \leq 1000$ (500) $\text{cm}^2\text{V}^{-1}\text{s}^{-1}$ we see that if μ_{CH} is improved by the gate insulation, g_{me} of MOS HEMT may be even higher than for SB HEMT. Only in region “B” relation $g_m = v_{sat} C_{GS} / L_G$ holds without restrictions. These behaviors can be coupled to possible different I_{DS} saturation mechanisms valid for GaN and GaAs (InP)-based HEMTs. While a complete velocity saturation model may be justified for typical GaAs (InP)-based HEMTs, i.e. at the onset of the velocity saturation electrons drift in v_{sat} practically along the whole L_G , for some GaN-based HEMTs in a substantial part of the channel electrons may initially only accelerate, i.e. $v_d < v_{sat}$. The complete saturation model is justified only if $V_{PO} \gg 3 L_G \times v_{sat} / \mu_{CH}$ where V_{PO} is pinch-off voltage [5]. To fulfill this condition at e.g. $\mu_{CH} \sim 1000 \text{ cm}^2\text{V}^{-1}\text{s}^{-1}$ one may need $L_G \ll 1 \mu\text{m}$, see Fig. 2 for $L_G = 100$ nm. If the above is not fulfilled, then the onset of the velocity saturation is accompanied by μ_{CH} -dependent 2DEG depletion along the low-field mobility part of the channel and any μ_{CH} improvements such as by gate insulation lead to g_m increase.

We would like to thank to G. Pozzovivo, D. Pogany (TU Vienna, Austria) J.-F. Carlin, N. Grandjean (EPFL Lausanne, Switzerland) for collaboration. Support of ULTRAGAN EU project No. 6903 is also acknowledged.

- [1] Marso, M., et al.: *IEEE Trans. El. Dev.* **53** (2006) 1517.
- [2] Kordoš, P., et al.: *Appl. Phys. Lett.* **90** (2007) 123513.
- [3] Pozzovivo, G., et al.: *Appl. Phys. Lett.* **91** (2007) 043509.
- [4] Kuzmík, J., et al.: *IEEE Trans. El. Dev.* **55** (2008) 937.
- [5] Shur, M.S.: *GaAs Dev. and Circ.*, New York, Plenum 1987.

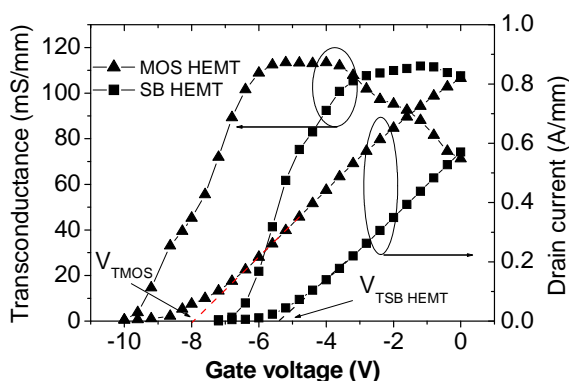


Fig. 1. I-V characteristics of 2 μm gate-length InAlN/GaN MOS and SB HEMTs.

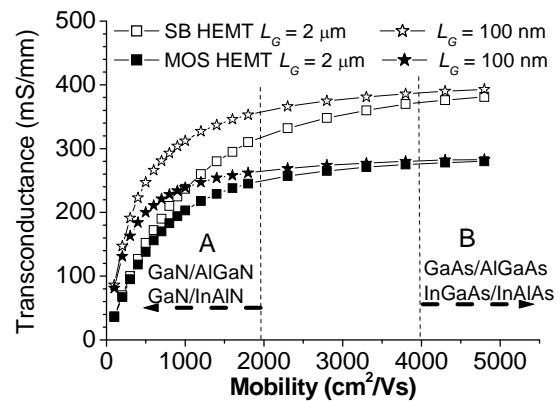


Fig. 2. Calculated transconductance dependencies of InAlN/GaN MOS and SB HEMTs on channel mobility for $L_G = 2 \mu\text{m}$ and 100 nm.

Evaluation of the interface state density on Ni/Al₂O₃/InAlN/GaN and Ni/ZrO₂/InAlN/GaN MOS contacts

M. Ľapajna, K. Čičo, J. Kuzmík, and K. Fröhlich

InAlN/GaN based high-electron mobility transistors (HEMTs) represent one of the most promising technologies for communication applications. Gate oxide integration (MOS-HEMT) can further improve the performance of these devices by means of gate leakage current suppression and surface states passivation, though, preparation of oxide/InAlN interface need to be carefully optimized. However, straightforward characterization of this interface is hindered by the InAlN/GaN interface with 2DEG. We present here an approach for interface state density, D_{it} , evaluation at the gate oxide/InAlN interface measured on metal-oxide-heterostructure (MOS-H) capacitor, hence on wafer measurement that can be directly correlated with MOS-HEMT's characteristics.

The proposed technique was applied to MOS-H capacitors with Al₂O₃ and ZrO₂ gate oxides grown by MOCVD with different InAlN/AlN/GaN surface pretreatment prior to gate oxide deposition. For Al₂O₃ gated samples, only HCl + H₂O surface cleaning was applied while for ZrO₂ gated samples, we employed HF + H₂O; HCl + H₂O; NH₃ + H₂O₂ cleaning recipe. Capacitance-voltage ($C-V$) and capacitance-time ($C-t$) measurements were performed in temperature range of 25 – 300 °C. $C-t$ transients were recorded on the MOS-H capacitors with gate voltage, V_g set to the beginning of the $C-V$ curve depletion region. After the positive V_g pulse, MOS-H capacitor was biased to the negative V_g corresponding to given capacitance and kept constant while capacitance transient recorded. D_{it} distribution was calculated from the transients following the constant-capacitance DLTS analysis recalculating ΔC to ΔV_g . DC and pulsed (100 ns pulse width) output MOS-HEMT characteristics were measured as well.

Figures 1a and 1b show the MOS-H capacitors $C-V$ curves measured at different ambient temperatures. In [1],

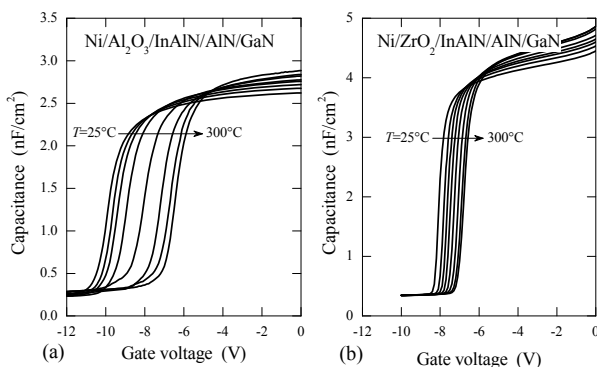


Fig. 1. $C-V$ curves of the Ni/Al₂O₃/InAlN/AlN/GaN (a) and Ni/ZrO₂/InAlN/AlN/GaN (b) MOS-H capacitor measured at temperature range from 25 to 300 °C.

it has been shown that the temperature-induced parallel shift of the $C-V$ curve is caused by a hole emission from the oxide/InAlN interface states promoted by a defect-related leakage current across the barrier layer. A hole emission process was monitored by $C-t$ curves shown in Fig. 2a and Fig. 2b for MOS-H capacitor with Al₂O₃ and ZrO₂, respectively. Corresponding distributions of oxide/InAlN D_{it} are depicted in Fig. 2c [2].

One may assess a very high difference between D_{it} distributions in the range of 1 – 1.3 eV above InAlN valence band edge. From comparison between DC and pulsed output characteristics, considerable current collapse was observed on MOS-HEMTs with Al₂O₃ gate dielectric while negligible collapse was seen on those transistors with ZrO₂ gate dielectrics, in accordance with D_{it} data evaluated on MOS-H capacitors.

This work was supported by the EU project ULTRAGAN, contract No. 6903, and by the project RPEU-0017-06.

- [1] Ľapajna, M., Čičo, K., Kuzmík, J., Pogany, D., Pozzovivo, G., Strasser, G., Carlin, J.-F., Grandjean, N., and Fröhlich, K.: *Semicond. Sci. Technol.* **24** (2009) 035008.
- [2] Ľapajna, M., Čičo, K., Kuzmík, J., Pogany, D., Pozzovivo, G., Strasser, G., Abermann, S., Bertagnoli, E., Carlin, J.-F., Grandjean, N., and Fröhlich, K.: *Proc. IWN'08, Montreux, Switzerland, 6-10 Oct. 2008*, p. 314.

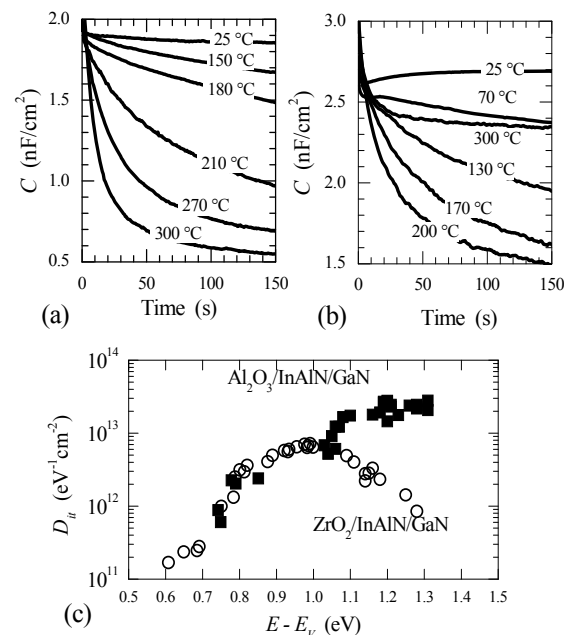


Fig. 2. $C-t$ transients of MOS-H capacitors with Al₂O₃ (a) and ZrO₂ (b) gate dielectrics at temperatures up to 300 °C and corresponding distribution of D_{it} at oxide/InAlN interface (c).

Department of Optoelectronics

Jozef Novák

Research scientists

Vladimír Cambel
Ján Fedor
Dagmar Gregušová
Peter Kordoš
Michal Kučera
Róbert Kúdela
Marián Morvic
Roman Stoklas
Ján Šoltýs
Pavel Štrichovanec

Technical staff

Peter Martiš
Pavol Mužík
Ivan Sabo

Research Engineers

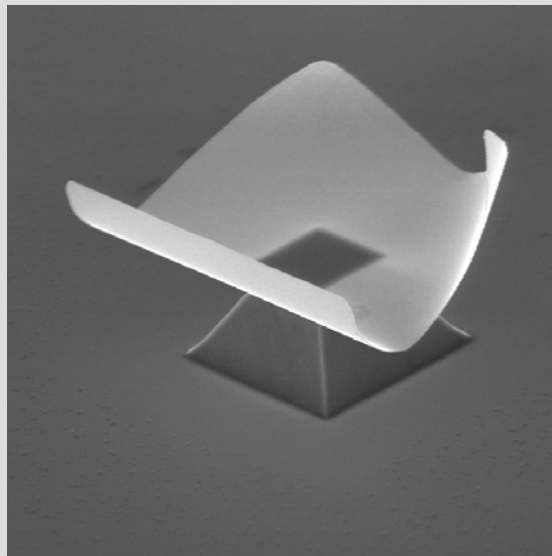
Peter Eliáš
Stanislav Hasenöhrl

PhD Students

Jozef Martaus

Students

Peter Telek



Research activities of the Department of Optoelectronics in 2007 and 2008 were traditionally focused on III-V semiconductors, namely their planar and patterned epitaxy, interfaces, processing, and device applications. We had the privilege to work on a few fresh areas that can be viewed as cutting edge technology: We (1) began work on the development of advanced tips for magnetic force microscopy, (2) processed and characterized GaN-based MOSHEMT devices, and (3) prepared materials for spintronics.

Our growth experiments were done with an Aixtron AIX 200 R&D MOVPE apparatus, used to prepare structures both for us and for researchers from other departments of the Institute.

The main financial supporter of our research in 2007 and 2008 was the Science and Technology Assistance Agency (APVV) in the Slovak Republic. It funded three of our projects. Their aim was to (1) develop novel active MFM tips; (2) grow and characterize the GaMnN material for spintronics; and (3) prepare semiconductor structures based on GaP by MOVPE.

The new tips were designed to measure electrical and magnetic fields, temperature, charge, etc. directly. They integrate in their facets sensitive layers, micro-magnets, and active electronic devices, including miniature transistors and Hall probes. The elements will be as close as possible to the tip apexes. With such tips, it is no longer necessary to evaluate physical quantities via transformation to a mechanical quantity, e.g. cantilever deflection. Members of the department worked intensively on a range of innovative technological approaches and processing techniques necessary to make such tips a reality.

The incorporation of manganese in some III-V semiconductors can provide a spintronics material. We worked towards this goal along with the FMPI within our second APVV-funded project. The project was finished in 2007. We went on with InMnAs epitaxy also in 2008 to prepare InMnAs layers and quantum dots on planar and patterned substrates. The material was also incorporated successfully in multi-quantum-well light-emitting diodes, designed to enable spintronics experiments.

A focus on GaP and its surface properties was the scope of the third APVV-funded project, which began in mid-2008. The project was linked with a EUREKA project entitled "*VGF GaP based optics for infrared sensors*".

Important results were achieved in our experiments with GaN/AlGaN-based HFET and MOSHFET transistors. We studied the phenomenon of current collapse in HFETs in relation to the surface and interface traps. Properties of the semiconductor-dielectrics interface and transistor characteristics (DC and pulse) were investigated versus technological steps, such as the deposition of dielectric films and subsequent annealing. We will use our expertise and experience with the technology and measurement of AlGaN-GaN transistors as members of the MORGaN project working group.

We have valued very much our participation in two APVV-funded Centres of Excellence: (1) the CENAMOST centre oriented on microelectronics and nanoelectronics (with the Faculty of Electrical Engineering and Informatics), and (2) the Centre of Cryophysics and Cryonanoelectronics (with the Institute of Experimental Physics).

In June 2007 we organized the 12th European Workshop on MOVPE technology in Bratislava (EW-MOVPE), a top European conference in the field. The conference helped to support the position of our MOVPE experts within the community of MOVPE growers in Europe. Its successful organization was made possible thanks to the efforts of every member of the department.

We have enjoyed fruitful international co-operation, as most of our activities are usually part of broader international efforts. In 2007 and 2008 we co-operated with the following institutions: the Institute for Thin Films and Ion Technology Research Centre Jülich (Germany), the Institute of Materials Research CSIC, Barcelona (Spain), the Institute of Physics Prague (Czech Republic) and with the Argonne National Laboratory (USA).

Also vital for our work has been close co-operation among members of the department. I would like to express my gratitude to all of them for their fruitful work and enthusiasm in 2007 and 2008.

Jozef Novák

Formation of AlGaAs/InGaP interfaces

R. Kúdela, J. Šoltýs, and M. Kučera

A GaAs/AlGaAs/InGaP structure can combine advantages of the AlGaAs/GaAs and InGaP/GaAs systems. One can expect a standard AlGaAs/GaAs structure with a high-mobility two-dimensional electron gas can become more stable if it is capped with an InGaP layer. The InGaP layer can also serve as an etch-stop layer. Such a combined structure can be exploited in devices with improved performance. To incorporate InGaP layers successfully into the AlGaAs/GaAs system, one needs to know well the AlGaAs/InGaP interface, including the band offset and other important characteristics.

The GaAs/Al_{0.3}Ga_{0.7}As/In_{1-x}Ga_xP structures were prepared by a conventional low-pressure MOVPE process in Aixtron AIX 200 equipment. We prepared structures with top InGaP layers (InGaP on AlGaAs) at first. A photoluminescence peak from the interface with a maximum of 1.77 eV was measured on the samples. The morphology of the interfaces was studied by AFM. Samples if 800, if 802 and if 803 were prepared on pieces of the same GaAs wafer, together with the reference AlGaAs layer for comparison. The thickness of the top InGaP was reduced to a nominal value of 0.8 nm. The samples were scanned immediately after preparation. Figure 1 shows the results. It depicts the underlying AlGaAs material with monolayer growth steps. Monolayer steps can be identified also in sample if 803, with a simple AlGaAs/InGaP interface. The formation of "islands" is evident in if 800 together with an increased

surface roughness. This sample was prepared with a 0.3 nm thick GaP interlayer. The roughness was reduced in sample if 802 (with 0.83 nm GaP) and the step structure of the surface was not detected.

The reverse AlGaAs-on-InGaP structure is more sensitive to the As/P exchange effect. Phosphorus atoms from the surface of the InGaP layer are replaced by As atoms. Consequently, low band gap InGaAs or InGaPAs interlayers can be formed at the interface. Because they have lower band gaps compared with that of InGaP or AlGaAs, the position of the PL peak from the interface is not fully determined by the band offset between InGaP and AlGaAs. Sample #085 was prepared with a simple InGaP/AlGaAs interface. A PL peak of 1.47 eV from the interface was measured in this sample, and a strong clustering in the interface can be seen in the AFM scan in Fig. 2. A comparison of various samples shows that the duration of arsine pre-flow during the growth process has a significant impact on the PL shift. It is a consequence of the As/P exchange process and diffusion of As into the InGaP. The intentionally grown GaP or AlGaP interlayers at the interface can restrict the formation of a low band gap interlayer during the arsine pre-flow in spite of the fact that the exchange process and the diffusion are still present. The sample with a 0.83 nm thick GaP interlayer shifted the PL peak to a value of 1.67 eV and with a 0.83 nm thick layer of AlGaP to 1.735 eV. The AlGaP interlayer with a nominal thickness of 1.37 nm prevented the PL shift nearly completely. Therefore, one can estimate the thickness of the spontaneously modified interlayer between 0.69 and 1.37 nm.

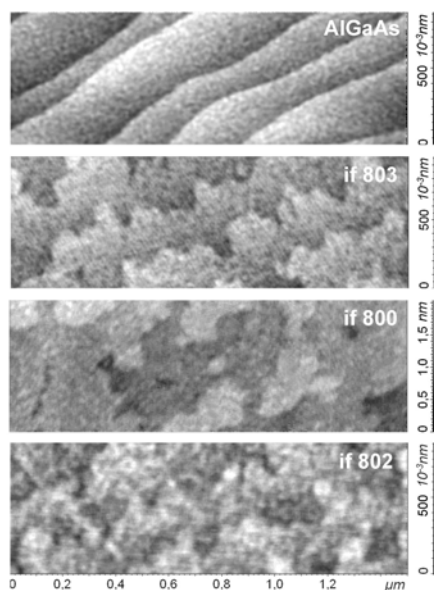


Fig. 1. AFM scans from the InGaP on AlGaAs interfaces.

- [1] Cambel, V., Karapetrov, G., Novosad, V., Bartolome, E., Gregušová, D., Fedor, J., Kúdela, R., and Šoltýs, J.: *J. Magnetism Magn. Mater.* **316** (2007) 232.

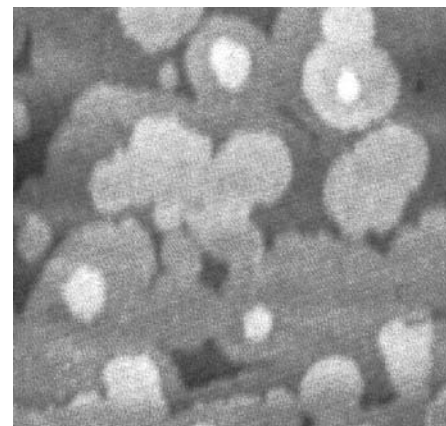


Fig. 2. Clustering in the AFM scan from the AlGaAs-on-InGaP interface.

50-nm local anodic oxidation technology of semiconductor heterostructures

J. Martaus, V. Cambel, D. Gregušová, R. Kúdela, and J. Fedor

Local anodic oxidation (LAO) induced by the tip of an atomic force microscope (AFM), represents the simplest way to reproducibly manufacture nanostructures.

The typical base width of oxide lines prepared by LAO on AlGaAs/GaAs heterostructures is ≈ 130 nm, and has not decreased significantly in recent years. The relatively wide oxide lines result from the use of low-conducting GaAs cap layers and from a deep oxidation of samples. Our calculations [1,2] pointed out the difficulties in the preparation of narrow oxide lines on conventional AlGaAs/GaAs heterostructures.

Based on the calculation, a novel approach to LAO was proposed [3,4]. It uses a shallow heterostructure with an InGaP cap layer. LAO is used to oxidize only the cap layer. The oxide lines are then etched away to expose underlying AlGaAs to the air, on which it naturally oxidizes. Native oxides in the AlGaAs layer are subsequently removed by a wet etching process. The process of the native oxide formation and its removal can be repeated several times to transfer the LAO patterns into a 2DEG. Trenches as narrow as ≈ 50 nm were prepared using the technique [4]. We utilized the novel approach to the LAO technique for the definition of the

quantum point contact (QPC) on a low-mobility semiconductor heterostructure.

Firstly, a shallow semiconductor heterostructure was prepared. The 2D electron gas layer was located only 23.5 nm below the surface. The sheet concentration and the mobility of 2D electrons were $n_e \approx 8.8 \times 10^{15} \text{ m}^{-2}$ and $\mu_e \approx 3 \text{ m}^2/\text{Vs}$ at 4.2 K, respectively.

Secondly, an initial Hall bar with 10 μm wide arms was defined on the heterostructure by standard optical lithography and wet etching.

Finally, a T-shaped QPC was defined on the Hall bar by LAO and subsequent sequential wet etching.

Figure 1 shows AFM surface topography of the QPC prepared. The 1D constriction is lithographically ≈ 60 nm long and ≈ 360 nm wide (see profiles in Fig. 1).

The conductance of the QPC (Fig. 2) shows a sequence of quantized plateaus at multiplies of $2e^2/h$. The plateaus deterioration was mainly caused by relatively high temperature during measurement and by short mean-free path (~ 300 nm) of the 2D electrons. The quantized conductance of the QPC was observed on the low-mobility sample at 4.2 K thanks to a very short (≈ 60 nm) 1D constriction prepared by the LAO technique.

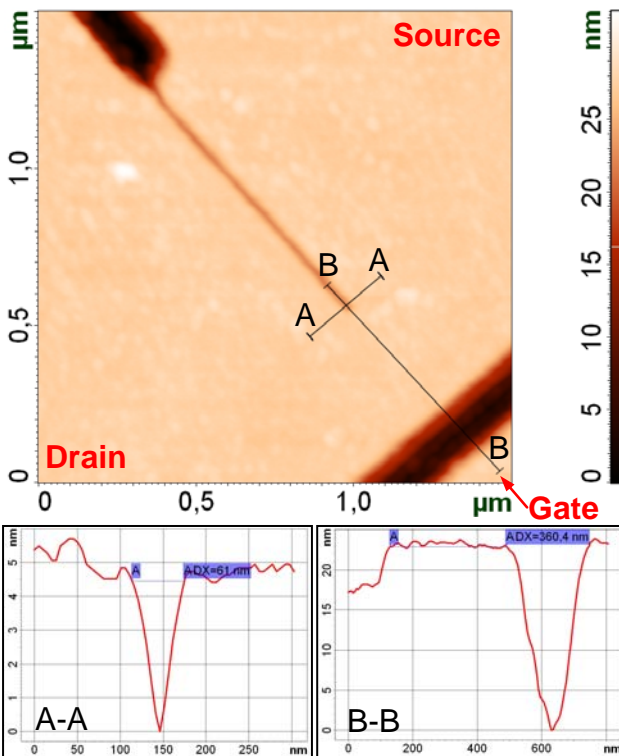


Fig. 1. AFM surface topography of the T-shaped QPC defined by LAO technique. 1D constriction has a lithographic length and width of ≈ 60 nm and ≈ 360 nm, respectively (see profiles).

- [1] Cambel, V. and Šoltýs, J.: *J. Appl. Phys.* **102** (2007) 074315.
- [2] Cambel, V., Martaus, J., Šoltýs, J., Kúdela, R., and Gregušová, D.: *Surf. Sci.* **601**, (2007) 2717.
- [3] Cambel, V., Martaus, J., Šoltýs, J., Kúdela, R., and Gregušová, D.: *Ultramicroscopy* **108** (2008) 1021.
- [4] Martaus, J., Gregušová, D., Cambel, V., Kúdela, R., and Šoltýs, J.: *Ultramicroscopy* **108** (2008) 1086.

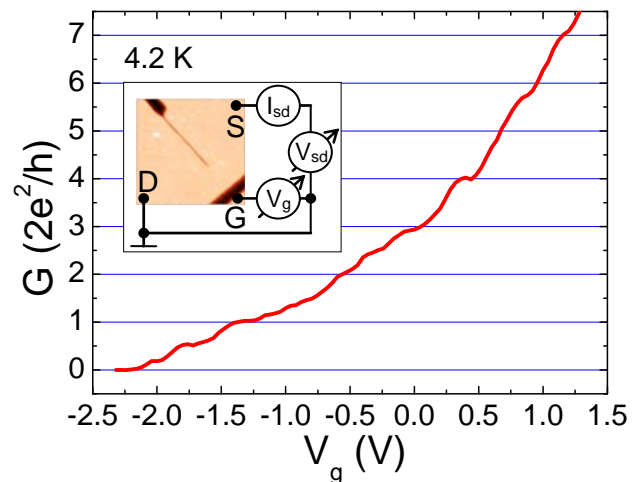


Fig. 2. Quantized conductance of the QPC in zero magnetic field at 4.2 K. The conductance was obtained from the I-V measurements performed on the three-terminal device (inset) after subtraction of a constant series resistance of 6 k Ω .

Wet-etch revelation of $\{n11\}$ -related facets in (100) GaAs at dynamic mask pattern edges

P. Eliáš, R. Kúdela, and J. Novák

When (100) GaAs substrate is locally etched in acidic hydrogen dioxide water solutions, e.g. $\text{H}_3\text{PO}_4:\text{H}_2\text{O}_2:\text{H}_2\text{O}$, facets tilted at $\sim 54^\circ$ to (100) and related to $\{111\}$ A are revealed at $[0\bar{1}1]$ -oriented edges of etching mask patterns. They emerge because they are the slowest etching ones in the (100)-(111)A section of the $[0\bar{1}1]$ crystallographic zone. Less steep and steeper facets do not emerge provided chemical reactions between GaAs and the etching solutions play the main role in the etching process. However, if mask erosion, mask delamination, and an interfacial layer are allowed to affect the process, the substrate will be etched differently. In general, if there is a layer of a different material between the mask and a substrate, its concurrent lateral etching will alter the dissolution of the substrate: A facet will be exposed at a higher rate compared with that of an identical facet emerged without the influence of the interlayer [1], or a different facet will be exposed instead [2]. The phenomenon has been used to facilitate reliable metallic interconnects and to reveal three-dimensional objects unreachable by conventional etching methods [3-5].

We have used the phenomenon to reveal ordinary mesas confined to $\{n11\}$ A-related facets with $n > 1$ in (100) GaAs substrates in $x\text{H}_3\text{PO}_4 : y\text{H}_2\text{O}_2 : z\text{H}_2\text{O}$. The mesas were revealed through $[0\bar{1}1]$ -oriented stripes of etching mask composed of (1) a semiconductor structure, (2) a titanium layer (100 nm), and (3) a top AZ5214-E resist layer (1.4 μm). The structure, grown by organometallic vapour phase epitaxy, consisted of a GaAs buffer layer (100 nm), an AlAs layer (100 nm), and a top GaAs layer (2 μm). The pattern definition was done using optical lithography and the transfer into the Ti layer in a HF-based solution.

The substrate was initially etched in 7 H_3PO_4 (85 % w/w) : 7 H_2O_2 (30 % w/w) : 10 DI H_2O at $20^\circ\text{C} \pm 0.1^\circ\text{C}$ (a 7:7:10 solution) during 35, 45, 50, 60, and 120 s [6]. Shallow mesas confined to $\{111\}$ A-related facets were revealed in the top GaAs layer before the solution reached

the AlAs layer. Upon cutting through it, the top GaAs layer and the GaAs buffer layer and substrate began to be locally etched at the $[0\bar{1}1]$ -oriented edges of the AlAs layer. As it dissolved laterally, the edges were moving to one another along $[011]$ and $[0\bar{1}\bar{1}]$. As a result, three new facets (f_2, f_3 and f_4) emerged in each mesa side: f_2 and f_3 squeezed into the top part above AlAs and f_4 emerged under AlAs from the buffer layer and the substrate (Fig. 1). While f_2 and f_3 were from the B section of the $[0\bar{1}1]$ crystallographic zone, f_1 and f_4 were from the A section of the zone. With etching duration, f_1, f_2, f_3 and f_4 changed their size as they differed in etching rates; $r(f_1) \approx 18 \text{ nm/s} < r(f_2)$ and $r(f_3) \approx 78 \text{ nm/s}$. The AlAs layer dissolved at $\sim 128 \text{ nm/s}$. Facet f_1 was tilted at $\sim 53^\circ$ to the (100) surface, and f_4 at $\sim 27.6^\circ$ at 35 s and $\sim 30.7^\circ$ at 120 s. Facet f_2 closed $\sim 87.5^\circ$ to $(\bar{1}00)$, and $f_3 \sim 51.4^\circ$ at 35 s and $\sim 48.5^\circ$ at 120 s. More data is necessary to evaluate how f_3 and f_4 changed their tilt during etching. While the (7:7:10) solution delivered f_4 lying roughly in the middle between $\{211\}$ A and $\{311\}$ A, the (18:7:10) and (10:10:65) ones revealed f_4 close to $\{211\}$ A and $\{311\}$ A, respectively [7]. This research was sponsored under projects APVV-51-045705 and VEGA 2/6096/26. The authors would like to thank Mr. I. Kostič (II SAS, Bratislava, Slovak Republic) for co-operation.

- [1] Notten, P.H.L.: *J. Electrochem. Soc.* **138** (1991) 243.
- [2] Huo, D.T.C., et al.: *J. Electrochem. Soc.* **135** (1988) 1231.
- [3] Wang, J., et al.: *J. Electrochem. Soc.* **145** (1998) 2931.
- [4] Huang, H., et al.: *J. Vac. Sci. Technol. B* **20** (2002) 1107.
- [5] Cambel, V., Gregušová, D., and Kúdela, R.: *J. Appl. Phys.* **94** (2003) 4643.
- [6] Eliáš, P., Kostič, I., Kúdela, R., and Novák, J.: *Proc. 7th Inter. Conf. Advanced Semicond. Dev. and Microsyst. Eds. Š. Haščík and J. Oswald. Piscataway, 2008, p. 303.*
- [7] Novák, J., Šoltýs, J., Eliáš, P., Hasenöhrl, S., and Vávra, I.: *Mat. Sci. in Semicond. Proc.*, (2009), in print.

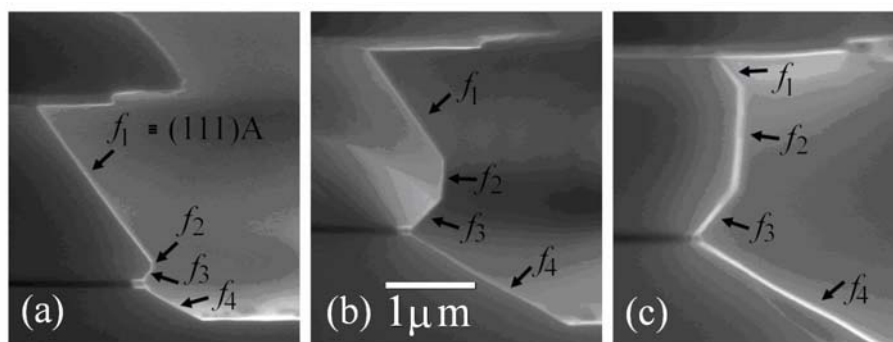


Fig. 1. $[0\bar{1}1]$ -oriented cleavage view of mesas revealed in (100) GaAs by etching in 7 H_3PO_4 : 7 H_2O_2 : 10 H_2O at dynamic edges of an AlAs sacrificial layer for (a) 35 s, (b) 45 s and (c) 60 s.

Study of the growth and structural properties of InMnAs dots grown on high-index surfaces by MOVPE

J. Novák, P. Eliáš, J. Šoltýs, S. Hasenöhrl, and I. Vávra

A high lattice mismatch between InAs (or InMnAs) and GaAs substrates (above 7 %) is the driving force for the formation of quantum dots. The Stranski-Krastanow (S-K) growth mode is based on strain relaxation that makes initially formed two-dimensional (2D) islands transform into three-dimensional quantum dots. It is a very promising, simple technique that can lead to the formation of defect-free nanostructures. The S-K mode is therefore widely used for the preparation of quantum dots in various III-V material systems, using either MBE or MOVPE. As quantum dots are growing, they are self-organized in a two-dimensional wetting layer. Their formation is determined by a number of growth parameters. To grow the dots controllably, the growth conditions must be precisely defined. It is especially true for InAs dots grown under the presence of Mn. In this paper, we report on the MOVPE growth of an InMnAs/GaAs heterostructure over $[0\bar{1}1]$ -oriented mesas and ridges confined at sides to facets related to $\{211\}A$ and $\{311\}A$ crystallographic planes.

The InMnAs/GaAs heterostructure overgrew the mesas and ridges differently because tops of the mesas contained (100)-oriented strips of original substrate surface while the ridges had their (100)-oriented tops eliminated. The difference between the mesas and ridges is exemplified for the ones confined to $(311)A$ - and $(3\bar{1}\bar{1})A$ -related facets. Both GaAs buffer layers overgrew the ridges continually at growth rates that differed along $\langle 311 \rangle$ and $[100]$. The rate close to $[311]$ and $[3\bar{1}\bar{1}]$ was about 0.13 nm/s, which was about 1.3 times the rate in $[100]$. As a result, the ridges grew into mesas, because (100)-related surfaces formed on their

tops. Their originally triangular cross-section thus changed to a trapezoidal one. By contrast, the mesas (of originally trapezoidal cross-section) retained their cross-sectional shape during growth.

Densities of the InMnAs dots on the $\{311\}A$ -related facets were about 5-7 times lower compared with those on reference planar (100) substrates. On the average, the dots on the facets were larger than those formed on the reference substrates. The lateral size of the dots varied between 100 and 180 nm. The dots were too large, and they may have contained more defects compared with ideal ones made of an ideal crystal prepared by the S-K growth mode. This property indicates that the growth conditions (wetting layer thickness and waiting time) for InMnAs dots with high Mn content should be modified to be able to fully utilize the potential of the S-K growth mode.

In addition, the dots were unevenly distributed along the facets from tops downwards: The densities were higher close to intersections of the $\{311\}A$ -related facets with the concave bottom sections of the ridges. The strain concentrated in the bottom sections increased the probability for the formation of dots along such intersections [1].

By contrast, almost no dots were grown on the (100)-related strips that formed during growth by self-faceting on tops of the triangular ridges. It indicates that the strips contained surfaces of high crystallographic quality without nucleation centres.

[1] Novák, J., Šoltýs, J., Eliáš, P., Hasenöhrl, S., and Vávra, I.: *Material Science in Semiconductor Processing (in print)*.

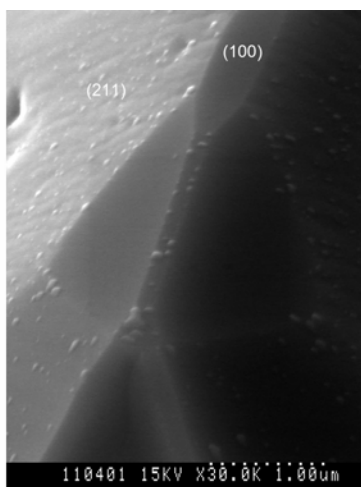


Fig. 1. SEM image of the mesa ridge after growth of GaAs buffer and InMnAs dots. This picture clearly shows a (100) top facet without dots.

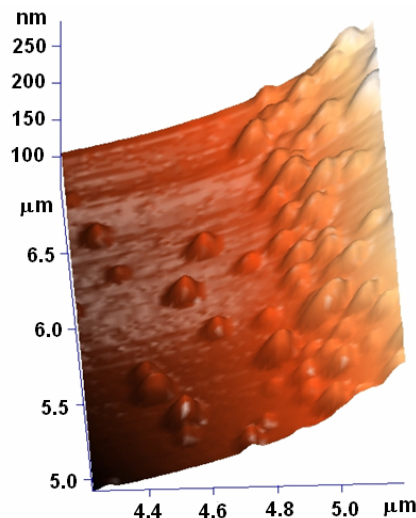


Fig. 2. AFM scan of the area covering intersection of (311) and (511) planes.

Technology of ‘active’ tips for magnetic and electric force microscopy

J. Šoltýs, R. Kúdela, M. Kučera, I. Vávra, J. Novák, and V. Cambel

Using standard scanning probe microscopy techniques, physical quantities are mapped indirectly. The force acting on the tip changes the mechanical state of the vibrating cantilever, shifts laser spot on the photodetector which transforms the change into electrical signal processed by the electronics. By this approach the absolute value of the quantity measured is mostly lost.

We have developed a non-planar technology of ‘active’ tips for the direct measurement of a physical quantity. To achieve a high space resolution of the measurements, the active elements (Hall probe, field effect transistor, etc.) have to be placed to the tip apex, i.e. on the tilted sidewalls of the tips. In this contribution, we report on the micromachining of pyramid structures and the subsequent epitaxial overgrowth. Such 3D objects will serve as the basic elements for active tips.

We prepared regular pyramids by wet chemical etching that utilizes a sacrificial AlAs layer [1]. The pyramids were overgrown by an AlGaAs/GaAs heterostructure to create an active layer (quantum well - QW) on them. The surface quality of the sidewalls was evaluated by SEM, TEM and AFM measurements. The quality of the tilted QW was tested by energy-dispersive X-ray analysis (EDX) and photoluminescence measurements (PL).

At first, we prepared pyramids with the base lines parallel with the $[001]$ and $[010]$ directions. The sidewalls were close to the (110) , $(1\bar{1}0)$, (101) and $(10\bar{1})$ crystallographic planes, which are oriented at 45° to (100) . The advantage of such oriented pyramids is their perfect symmetry. We experimentally found out that sidewall growth rate was much lower than that on (100) . Our aim was to deposit a 5 nm thick quantum well on the sidewalls. We decided to grow layers 10 times thicker than the nominal ones. However, PL measurements did

not confirm the presence of a quantum well at the sidewalls. The likely cause is that Al atoms can build into the sidewalls only with a difficulty. We have confirmed this assumption with an element analysis. The EDX spectrum shows that the content of aluminum on a (110) -related sidewall is 10 times lower than that on (100) .

In the following experiments, we prepared pyramids with base lines parallel with the $[011]$ and $[0\bar{1}1]$ directions. Such objects are of asymmetric shape with the sidewalls tilted at 30° and 45° to (100) , respectively (Fig. 1). It is better to have a steeper sidewall for an active tip. Therefore, we focused on determining optimized conditions for growth over the 45° tilted sidewalls. We found out that to be able to create a quantum well at the sidewall, the grower needs to deposit layers 15 times as thick as the original ones. The pyramids were overgrown with layers: a GaAs buffer (750 nm), AlGaAs (500 nm), GaAs (75 nm), AlGaAs (300 nm) and a GaAs cap layer (5 nm). The low temperature PL showed that the QW was 7 nm wide, which is in good agreement with results from TEM. Figure 2 depicts a TEM image of the epitaxial heterostructure with a 10 nm wide GaAs QW. More detailed PL diagnostics is described in the next contribution. The PL and TEM study showed that a heterostructure with a 2DEG grew on sidewalls tilted at 45° . Such a structure is usable for the preparation of the active elements.

We would like to thank to M. Záhoran, FMPI Comenius University, Bratislava, Slovakia, and I. Kostič, II SAS, Bratislava, Slovakia for collaboration. This work was supported by APVV-51-045705.

[1] Cambel, V., Gregušová, D., and Kúdela, R.: *J. Appl. Phys.* **94** (2003) 4643.

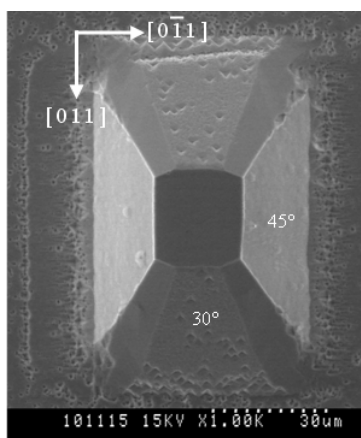


Fig. 1. SEM picture of an overgrown pyramid.

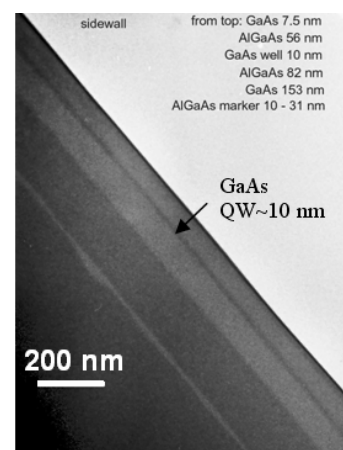


Fig. 2. TEM cross-sectional view on heterostructures grown on the sidewall with 45° .

Photoluminescence diagnostics of AlGaAs/GaAs/AlGaAs QWs prepared on non-planar, wet-etch-formed objects of pyramidal shape

M. Kučera, J. Šoltýs, R. Kúdela, and V. Cambel

Micrometer- and sub-micrometer-scale electronic devices placed on pyramidal tips can serve as physical sensors in ‘active-probe’ microscopy. A tip of a vector Hall-probe microscope was realised by this way [1].

In this work, our goal was to prepare AlGaAs/GaAs/AlGaAs quantum wells (QW) on the facets of pyramidal, wet-etch-formed objects. Such QWs with a two dimensional electron gas (2DEG) can be processed into a microscopic field effect transistor or a Hall bar. Photoluminescence (PL) spectroscopy was used to identify QW electron-hole transitions and to estimate the quality of the wells.

Pyramids and ridges were formed by a wet-etching procedure in (100) GaAs substrates [1]. The angles of the sidewalls with the substrate plane were close to 30° or 45° , and the baselines were parallel with the [011], $[0\bar{1}1]$ or, alternatively, [001], [010] crystallographic directions. After completing the etching procedure, the pyramids were overgrown with AlGaAs/GaAs/AlGaAs heterostructures with GaAs QWs. As the growth rate strongly depends on the growth plane orientation, the main task was to adapt the MOCVD growth sequence in order to grow 5 nm wide QWs on the respective pyramidal facets. In PL, an Ar^+ ion laser beam was focused to the diameter of approx. $20\ \mu\text{m}$ and with the help of a microscope it was targeted on a pyramid wall. PL signal was filtered by a quarter-meter monochromator and detected by a silicon photodiode.

The experiments started on pyramidal objects with the [001]- and [010]-oriented baselines, because they have a perfectly symmetrical shape and nearly 45° slope of their facets (which would be almost ideal). We did not observe any PL signal corresponding to a QW. EDX diagnostics and a microscopy of the pyramid profile proved that the

sidewall growth was very poor.

As a next step, the QW growth on the pyramids with the [011]- and $[0\bar{1}1]$ -oriented sidewall baselines was tested. The specific feature of the pyramids are the pairs of opposite facets with the slopes close to 30° (the baseline direction [011]) and 45° (the direction $[0\bar{1}1]$). PL spectra of sample MO1058 (with a growth sequence corresponding to the (100) planar QW width of 5 nm) are shown in Fig. 1. We observed a fairly good QW signal on the 30° -tilted facets. No signal was observed on the 45° -tilted facets. It corresponds to the investigations performed in [2], where a rather low growth rate on 45° -tilted facets was observed. A QW-related peak at 1.572 eV corresponds to a well width of approximately 7 nm according to e. g. [3].

In the following, we adapted the growth sequence to grow structures that had $5\times$ and $15\times$ wider epitaxial layers than those of sample MO1058. In Fig. 2, one can see PL spectra corresponding to the QWs on the 45° -tilted facets. The QW signals at 1.573 eV (MO1067) and 1.532 eV (MO1083) correspond to QW widths of 7 and 15 nm, respectively. A broadening of the QW peaks indicates a poorer quality compared with that of planar wells. The PL results were supported by SEM observations. The work showed that it was possible to grow QWs with a 2DEG, suitable for further processing into microelectronic devices on the tilted pyramid walls.

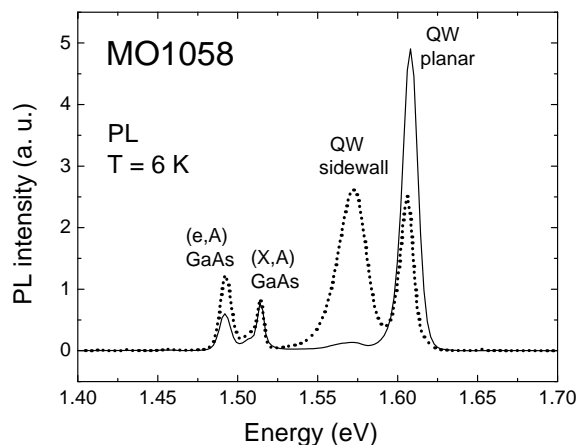


Fig. 1. PL spectra of sample MO1058. The full line corresponds to the top of the pyramid (or the planar reference sample), the dotted line to the sidewall with the [011] baseline orientation.

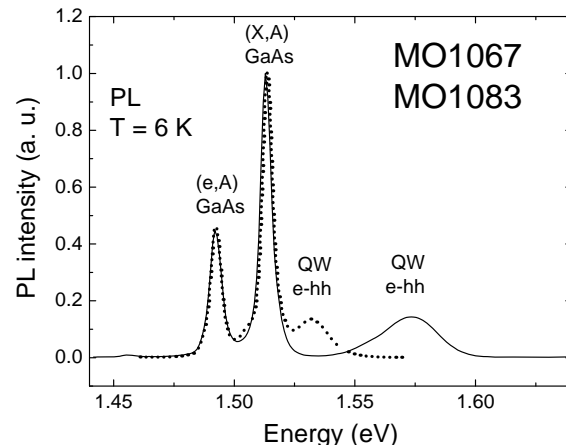


Fig. 2. PL spectra of samples MO1067 (well width in the corresponding planar growth 25 nm, full line) and MO1083 (75 nm, dotted line). The baseline orientation $[0\bar{1}1]$, tilt $\sim 45^\circ$.

Investigation of structural properties of GaAs based heterostructures by EDX and FIB

P. Štrichovanec, J. Novák, S. Hasenöhrl, and I. Vávra

In many compound semiconductors, the addition of dilute concentrations of impurities leads to dramatic changes in the electronic, optical, and magnetic properties. For example, the introduction of a few per cent of nitrogen into GaAs leads to a band gap reduction of hundreds of meV. Furthermore, the incorporation of a few per cent of manganese into GaAs enables a combination of semiconducting and ferromagnetic behaviour. The resulting narrow gap nitride and dilute magnetic semiconductors are promising for several applications ranging from long-wavelength light emitters and high-efficiency solar cells to spin-electronics and spin-optoelectronics. In all cases, nanometer-scale details of impurity incorporation are critical to the understanding and controlling of the observed properties. Strain can play an important role in control of magnetic atoms incorporation. Single-phase ferromagnetic $\text{In}_{1-x}\text{Mn}_x\text{As}$ with x close to 0.14 was recently prepared using MOCVD. The material exhibited room temperature ferromagnetic behaviour with a Curie temperature close to 330 K, which was explained as a consequence of Mn metal clustering at the atomic level.

Figure 1 presents a cross-section of an InMnAs epitaxial layer prepared with a high value of the MnAs molar fraction ($x \sim 0.9$). The cross-section was prepared using focused ion beam (FIB) equipment from the layer that was covered with Au. The experiments were done with commercial dual-beam equipment (Nova 200 NanoLab), which included a 30 kV field-emission electron column and a Ga-based 30 kV ion column. The FIB experiments allowed for a detailed study of the layer, namely its thickness variation, structural defects, and MnAs clusters.

Figure 2 shows an experimentally evaluated

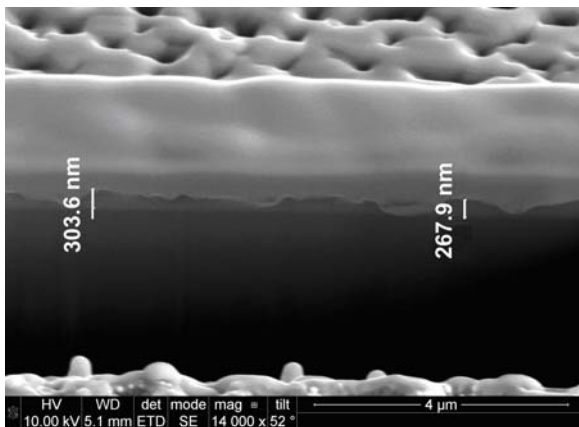


Fig. 1. SEM cross-sectional view of an InMnAs membrane prepared by a focused ion beam technique.

dependence of the InMnAs layer composition versus ratio of partial pressures of the Mn and In precursors. As follows from HRXRD measurements, a misfit related to the InAs lattice was very low up to a partial pressure ratio of 0.1. This indicates the growth of high doped InAs:Mn or strained InMnAs. A further increase of the partial pressure ratio led to a standard linear relation between the partial pressure ratio and MnAs molar fraction in the ternary compound. All data calculated were evaluated under the condition that the zinc-blende MnAs lattice constant value is equal to 0.601 nm. However, the ternary composition evaluated from EDX measurements showed a slightly higher value of x compared with the HRXRD results (see Fig. 2). The reason for the difference is unknown. In addition, the EDX measurements on InMnAs quantum dot structures showed that in InMnAs dots the x value is the highest one compared with the EDX and HRXRD results obtained on the planar layers. The difference may have come from the Stranski-Krastanow growth mode used for the preparation of the InMnAs dots.

- [1] Novák, J., Vávra, I., Hasenöhrl, S., and Šoltýs, J.: 14th Inter. Conf. on MOVPE, 2008, Metz, France.
- [2] Novák, J., Šoltýs, J., Eliáš, P., Hasenöhrl, S., and Vávra, I.: 7th Inter. Workshop on Epitaxial Semiconductors on Patterned Substrates and Novel Index Surfaces, 2008, Marseille, France.

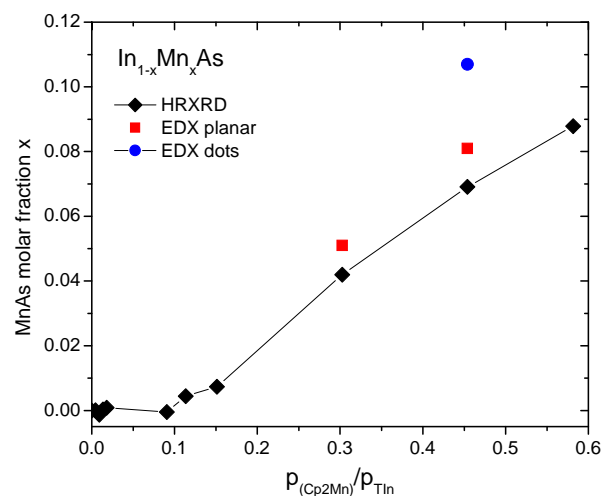


Fig. 2. InMnAs composition evaluated by HRXRD and EDX on planar and dot structures.

Switching magnetization magnetic force microscopy – an alternative to conventional lift-mode MFM

V. Cambel, D. Gregušová, J. Fedor, J. Martaus, P. Eliáš, and R. Kúdela

We propose a new magnetic force microscopy (MFM) technique called switching magnetization MFM (SM-MFM) [1]. The method is expected to eliminate the drawbacks of standard MFM. Its principle is explained in Fig. 1. The tip is scanned over a sample in two passes in the tapping mode with its magnetization orientation reversed between them. Signals received with the opposite tip magnetization orientations are added and subtracted. The former represents atomic (plus electric if present) forces and the latter the magnetic forces only.

The space resolution of SM-MFM should be increased and the force mixing lowered as compared with those in standard MFM techniques. If tips with low magnetization are used, the new approach will be less invasive to the sample. Such tips have yet to be developed.

MFM tips are basically prepared by the simple evaporation of soft or hard magnetic materials onto standard tips used for atomic force microscopy. The magnetization and switching field of such tips are defined only roughly by the selection of evaporated magnetic material and its thickness, and by the shape of the tip.

As the magnetic state of proposed SM-MFM tips must be easily controlled, well-defined and stable during scanning, more sophisticated technology has to be used for their fabrication. The tips must show the following magnetic properties: (1) Their magnetization must be very low (non-invasive tips in the tapping mode) and a soft magnetic material (Permalloy, Py) has to be used for their fabrication; (2) the magnetization has to be reversed easily by a low external magnetic field to keep the sample in the same magnetic state, i.e. the tips with a low switching field have to be developed.

The properties can be achieved with a magnetic object of precise shape located close to the tip apex to guarantee a high space resolution of the SM-MFM technique, i.e. the magnetic object has to be placed on one of the sidewalls of the tip.

We have calculated the switching field of Py objects

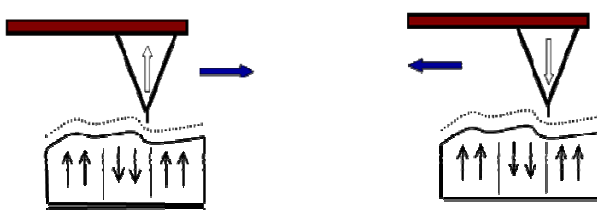


Fig. 1. Switching magnetization MFM principle. The tip magnetization is reversed within the scanning.

to optimize the tips magnetic properties (low magnetization, low switching field) by solving the micromagnetic problem. The objects simulated differ in their shape: thickness, length and width. The dimensions of the objects are limited by the dimensions of the tips, the pyramid sidewalls. In our experience – 10 μm high atomically smooth pyramids can be prepared by our technology quite easily and reproducibly.

We have calculated the magnetization reversal of the Py objects. The micromagnetic simulations were performed using the software package object oriented micromagnetic framework (OOMMF) [2], which solves the micromagnetic problem using the Landau–Lifshitz–Gilbert (LLG) equation. We used 10 nm \times 10 nm \times 10 nm cells for calculations of magnetic state in objects of variable shape and size with length $L = 100 \text{ nm} - 10 \mu\text{m}$, width $w = 40 \text{ nm} - 3 \mu\text{m}$, and thickness $t = 20 - 50 \text{ nm}$. The parameters used for Permalloy are listed below: saturation magnetization = $8.6 \times 10^5 \text{ (A/m)}$, exchange stiffness = $1.3 \times 10^5 \text{ (J/m)}$, crystalline anisotropy constant is zero and damping coefficient = 0.5.

We have found in our micromagnetic calculations that magnetic objects of hexagonal shape are the optimum ones yielding switching fields as low as 6 mT (Fig. 2). Such objects will be defined on tilted facets of the future SM-MFM tips.

- [1] Cambel, V., Karapetrov, G., Belkin, A., Novosad, V., Eliáš, P., Gregušová, D., Fedor, J., Kostič, I., Kúdela, R., and Šoltýs, J.: *International Scanning Probe Microscopy Conference, 22-24 June, 2008, Seattle, Washington, USA.*
 [2] <http://math.nist.gov/oommf>.

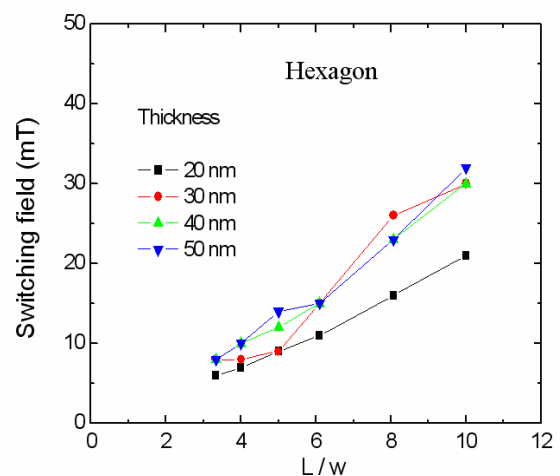


Fig. 2. Switching field for hexagon of the length fixed to 5 μm , and thickness as a parameter.

On-tip sub-micrometer Hall probes for magnetic probe microscopy prepared by non-planar optical and AFM lithography

D. Gregušová, J. Martaus, J. Fedor, R. Kúdela, and V. Cambel

Magnetic force microscopy (MFM) is a state-of-the-art technique used to study sub-micrometer magnetic domain structures, written bit patterns in recording media, and physical effects in superconductors. As it is a tip-based method, MFM can be invasive depending on the type of magnetic sample explored. Additionally, it does not image absolute values of local magnetic fields, but it shows only local magnetic forces between the tip and a sample. We developed a technology of sub-micrometer heterostructure-based Hall probes operated at room temperature (RT) for future application in scanning Hall probe microscopy (SHPM) and MFM.

The heterostructure consisted of an undoped GaAs substrate and a 500 nm buffer, a 17 nm thick AlGaAs spacer, a silane-doped delta-layer, a 3 nm thick AlGaAs top and a 3.5 nm thick InGaP cap layers. Its active layer was located only 23 nm below the surface, which is important for the formation of a sub-micrometer Hall probe using AFM tip-induced local anodic oxidation (LAO) [1,2].

Optical lithography and LAO were combined to fabricate sub-micrometer Hall probes on the top of high-aspect ratio mesas [3]. The processing included (1) the definition of an AZ 5214-E etching mask pattern to transfer the active layer into the plateau of a pyramid; (2) the definition of an AZ5214-E lift-off mask pattern to transfer the topology of ohmic contacts to the probes; (3) the evaporation and lift-off of metallic films for the ohmic contacts based on an AuGe eutectic alloy and Ni; (4) the alloying of the metallic films; (5) the definition of an AZ 5214-E lift-off mask pattern to transfer the topology of metallic strips to connect the ohmic contacts and pads, (6) the evaporation and lift-off of the metallic films based on Ti and Au. A draping technique [4] was used to deposit AZ 5214-E on the non-planar substrates to realize the lithographic process. To make the devices usable at RT, LAO was applied to the InGaP cap layer of the heterostructure in the following way:

At first, oxide lines were formed by LAO in the InGaP

cap layer. The oxide lines were subsequently etched away leaving narrow line openings in the InGaP layer through which the underlying AlGaAs became exposed to the air and oxidized. The openings in the InGaP layer served as a mask for the subsequent wet etching. Narrow AlGaAs were prepared this way.

The magnetic-field resolution was evaluated at the planar Hall probes at 140 Hz for the 500 nm and 200 nm wide Hall probes and at 10 kHz for the 5 μm and 2 μm Hall probes. Figure 1 summarizes the evaluated magnetic-field resolution of the downscaled Hall probes at 4.2, 77, and 300 K.

In the last step, we have applied the LAO technique to lower the dimensions of the probes defined on the top of the prepared sharp pyramids (Fig. 2).

- [1] Martaus, J., Gregušová, D., Cambel, V., Kúdela, R., and Šoltýs, J.: *Ultramicroscopy* **108** (2008) 1086.
- [2] Cambel, V., Martaus, J., Šoltýs, J., Kúdela, R., and Gregušová, D.: *Surface Sci.* **601** (2007) 2717.
- [3] Gregušová, D., Martaus, J., Fedor, J., Kúdela, R., and Cambel, V.: *Ultramicroscopy* (2009), accepted.
- [4] Gregušová, D., Eliáš, P., Ószi, Zs., Kúdela, R., Šoltýs, J., Fedor, J., and Cambel, V.: *Microelectronics J.* **37** (2006) 1543.

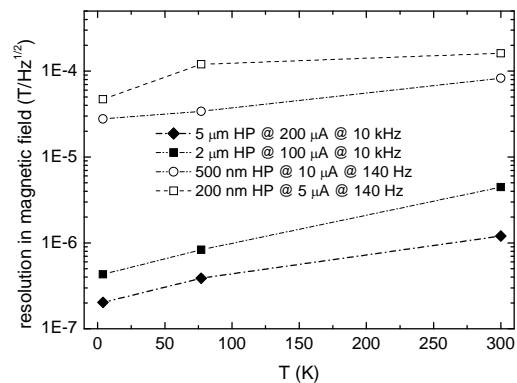


Fig. 1. Resolution in the magnetic field of the downscaled Hall probes.

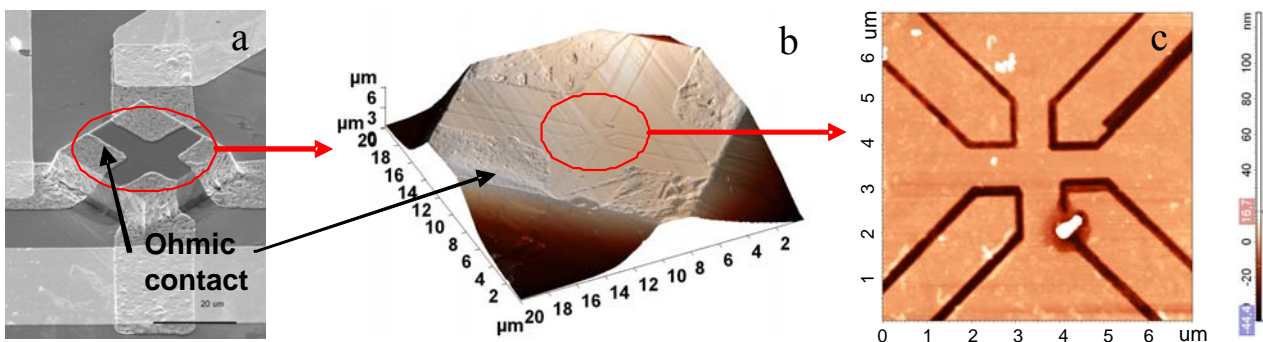


Fig. 2. a) SEM image of a pyramidal 3D object before downscaling; b) AFM image of a downscaled, submicron Hall probe on the top of the pyramidal mesa structure; c) AFM image of the central part (800-nm-sized Hall probe).

Micromagnetic permalloy element on a Hall probe: design and technology

P. Eliáš, V. Cambel, R. Kúdela, Š. Gaži, J. Šoltýs, and J. Martaus

Micro- and nano-magnetic elements made of soft and hard magnetic materials exhibit remanent magnetism of self-organised magnetic domains that take shape with respect to the geometry of the objects and external magnetic fields [1]. The structure of the domains can be re-configured when exposed to an external magnetic field of appropriate direction and magnitude.

We studied micro-magnetic elements of elliptical shape made from Permalloy with a focus on those exhibiting a single domain magnetic state with a low coercivity.

The length, width and thickness of the elliptical elements were varied. They were nominally 10 μm long and 6, 5, 4, 3, 2 and 1 μm wide or 5 μm long and 3.5, 3, 2.5, 2, 1.5, 1, and 0.5 μm wide. Their thickness was 25, 30, 40, and 50 nm.

The elements were defined on a (100) GaAs substrate (for lithography tests) and on Hall probes (Fig. 1) based on an InGaP/AlGaAs/GaAs heterostructure with a two-dimensional electron gas (for switching magnetization tests). The heterostructure, grown by organometallic vapour phase epitaxy on a standard (100) semi-insulating GaAs substrate, consisted of a cap InGaP layer (5 nm), a top AlGaAs layer (20 nm), a Si delta-doping layer, an AlGaAs spacer layer (20 nm), a GaAs buffer layer (200 nm). Processing of the arrays included (1) the formation of standard ohmic contacts by means of evaporation, lift-off and alloying of an AuGe/Ni metallic system; (2) dry-etch mesa definition by milling with neutral Ar atoms; and (3) formation of Au contact pads and alignment marks for electron beam lithography (EBL).

The elements were carved out by acetone lift-off from NiFe layers thermally evaporated onto a 200 nm thick layer of PMMA in which elliptical windows were opened by EBL. The elements were positioned centrally over

active areas of the Hall probes with their long axis at a 45° to the orthogonal topology of the Hall probe legs.

Their magnetization and switching behaviour were studied by magnetic force microscopy (MFM) and pulsed current Hall voltage measurement. The results were correlated with micromagnetic simulations of the elements using the Landau-Lifshitz-Gilbert equation [2].

Both the theoretical calculations and experimental results have shown that the length-to-width ratio (l/w) is a crucial parameter that characterizes the magnetic behaviour of the elements. The MFM evaluation demonstrated that the 50 nm thick elements exhibited the following domain arrangements depending on their aspect ratio: (1) diamond state $l/w = 10/6$; (2) cross-tie state $l/w = 10/3$; (3) single state $l/w = 5/0.7$ (Fig. 2). The results agreed with those from micromagnetic calculations. The calculations also showed 30 nm thick NiFe elliptical elements with $l = 5 \mu\text{m}$ and $w \leq 1.25 \mu\text{m}$ ($l/w \geq 4$) should possess a single domain state. Such elements with $l = 5 \mu\text{m}$ and $w = 1.25 \mu\text{m}$ should theoretically exhibit a single domain state with a switching field lower than 10 mT. The initial switching experiments using the Hall probes indicated that the switching fields of such an element could even be as low as 4.5 mT [2].

This research was sponsored under projects APVV-51-045705. The authors would like to thank Mr. I. Kostič (II SAS, Bratislava, Slovak Republic) for co-operation.

- [1] Chang, C.C., Chang, Y.C., Chung, W.S., Wu, J.C., Wei, Z.H., Lai M.F., and Chang, C.R.: *IEEE Trans. Magnetics* **41** (2005) 947.
- [2] Cambel, V., Karapetrov, G., Belkin, A., Novosad, V., Eliáš, P., Gregušová, D., Fedor, J., Kostič, I., Kúdela, R., and Šoltýs, J.: *International Scanning Probe Microscopy Conference, Seattle, Washington, USA, June 22-24, 2008*.

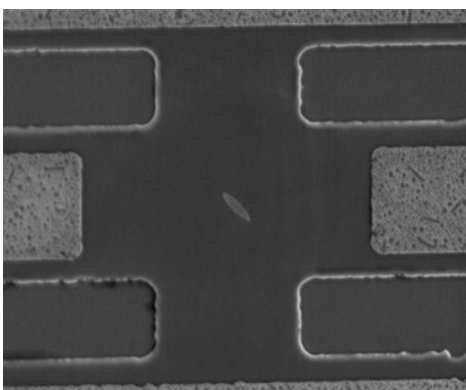


Fig. 1. 50 nm thick NiFe element on a Hall probe, $l = 5 \mu\text{m}$ and $w = 1 \mu\text{m}$.

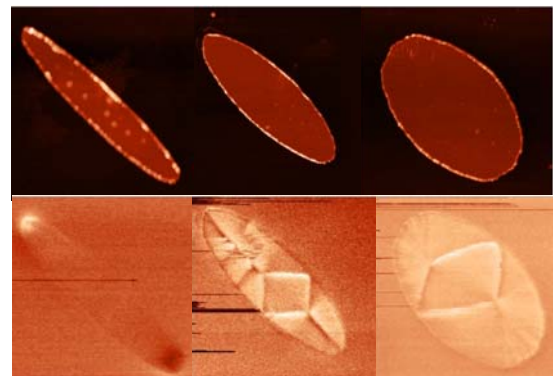


Fig. 2. 50 nm thick NiFe elements. Top row: topology by AFM. Bottom row: corresponding magnetic domains by MFM. Left: single domain state, $l = 5 \mu\text{m}$, $l/w = 7.1$; Middle: cross-tie state, $l = 10 \mu\text{m}$, $l/w = 3.3$; Right: diamond state. $l = 10 \mu\text{m}$, $l/w = 1.7$.

AlGaIn/GaN metal-oxide-semiconductor heterostructure field-effect transistors with Al₂O₃ gate oxide

D. Gregušová, R. Stoklas, K. Čičo, Š. Gaži, J. Novák, and P. Kordoš

AlGaIn/GaN heterostructure field-effect transistors (HFETs) have been extensively investigated because of their potential as highly-efficient sources of microwave power. The main obstacle for their wide application is the current collapse, i.e. the reduction of high-frequency drain current versus its static value. In general, a major technological limitation of GaN-based devices, including the AlGaIn/GaN HFETs, is high gate leakage currents [1]. This contribution reports on a study that compared two types of transistor based on an identical layer structure and prepared using the same procedure. One type was a metal-oxide-semiconductor HFET (MOSHFET) with a 4 nm thick Al₂O₃ gate oxide layer and the other was an unpassivated HFET. The devices were based on an AlGaIn/GaN structure that consisted of a 3 μm thick undoped GaN layer and a 30 nm thick undoped Al_{0.25}Ga_{0.75}N layer grown on sapphire substrates by metal-organic chemical vapor deposition (MOCVD). Their production included conventional FET fabrication steps. The Al₂O₃ layer was deposited between the source and drain contacts before the gate deposition by a low pressure MOCVD technique [2].

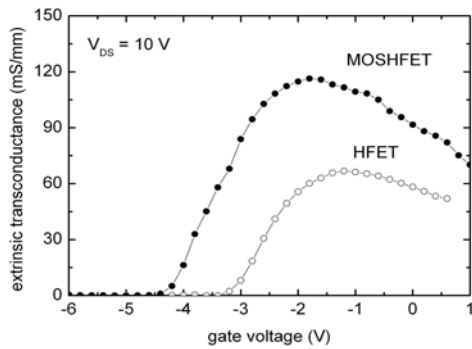


Fig. 1. Transconductance characteristics of an AlGaIn/GaN HFET (open circles) and an Al₂O₃/AlGaIn/GaN MOSHFET (full circles).

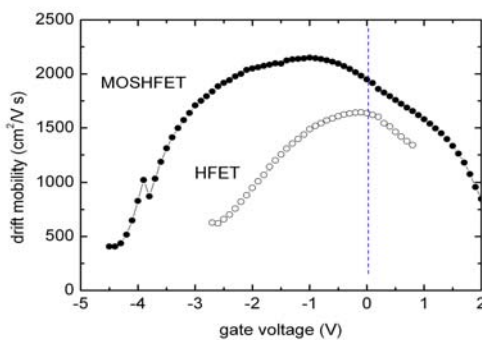


Fig. 2. Drift mobility of an HFET and a MOSHFET (based on AlGaIn/GaN) versus gate voltage.

The MOSHFETs with their gate oxide passivation exhibited a higher saturation drain current (about 40 %) than the HFETs. The enhancement was larger than expected. The extrinsic transconductance of the MOSHFETs was also higher than that of the HFETs, despite their wider gate-channel separation (Fig. 1). We also observed a similar but less expressed effect (up to 37 % increase of the peak values) in our previous study on MOSHFETs with 9 nm and 14 nm thick Al₂O₃ layers [3].

The MOSHFETs exhibited a significantly higher drift mobility compared with the HFETs. One can assume the structure with the gate oxide provided for a higher effective velocity of carriers [4]. Figure 2 shows the drift mobility of an HFET and a MOSHFET versus gate voltage.

The current collapse, evaluated from pulsed current – voltage (*I*–*V*) measurements, was highly suppressed in the MOSHFETs (Fig. 3). The static drain current decreased relatively markedly with an increased drain bias at higher gate voltage. It was because of self-heating effects, which are more pronounced if sapphire substrate is used for AlGaIn/GaN HFETs. Thus, higher pulsed drain currents compared with the static ones indicate the devices were cooled down better under pulse operation.

Further investigation is needed to fully understand the origin of the drift velocity enhancement and the impact of the series resistance.

- [1] Vetury, R., et al.: *IEEE Trans. Electron Devices* **48** (2001) 560.
- [2] Gregušová, D., Stoklas, R., Čičo, K., Lalinský, T., and Kordoš, P.: *Semicond. Sci. Technol.* **22** (2007) 947.
- [3] Gregušová, D., Stoklas, R., Čičo, K., Heidelberg, G., Marso, M., Novák, J., and Kordoš, P.: *Phys. Status Solidi c* **4** (2007) 2720.
- [4] Kordoš, P., Gregušová, D., Stoklas, R., Čičo, K., and Novák, J.: *Applied Phys. Lett.* **90** (2007) 123513.

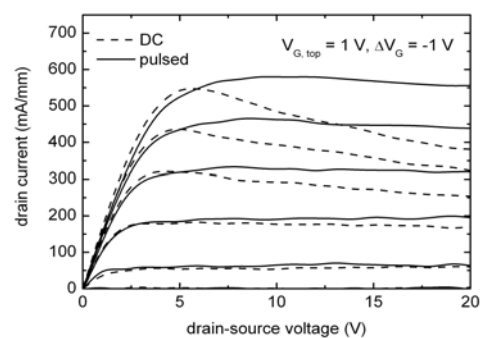


Fig. 3. Static (dashed lines) and pulsed (full lines) *I*–*V* characteristics of an Al₂O₃/AlGaIn/GaN MOSHFET.

Trapping effects in AlGaIn/GaN-on-Si field-effect transistors by frequency dependent capacitance and conductance measurements

R. Stoklas, D. Gregušová, J. Novák, P. Kordoš, K. Čičo, and K. Fröhlich

It is well known that surface trap states are responsible for the current collapse of AlGaIn/GaN heterostructure field-effect transistors (HFETs). The current collapse can be suppressed by applying a surface passivation and/or a gate insulator [1]. We recently investigated transport properties of AlGaIn/GaN MOSHFETs with an Al₂O₃ gate insulator [2]. However, the origin of the surface states is not clear yet. In this work, we investigated trapping effects in AlGaIn/GaN-on-Si HFETs and MOSHFETs [3].

The capacitance and conductance measurements in the frequency range from 1 kHz to 1 MHz were used to characterize the trapping effects in the HFETs and MOSHFETs. The capacitance vs frequency characteristics are shown in Fig. 1. The zero-bias capacitances (open and full stars for the HFET and MOSHFET, respectively) are nearly independent on frequency. However, a frequency dispersion can be observed for selected biases near the depletion, which is partially stronger for the HFET as compared to the MOSHFET. This indicates different trapping behavior in the two types of device investigated.

The equivalent parallel capacitance C_p and conductance G_p as functions of frequency, assuming a continuum of trap levels, can be expressed as

$$C_p = C_b + \frac{qD_T}{\omega\tau_T \tan(\omega\tau_T)},$$

and

$$\frac{G_p}{\omega} = \frac{qD_T}{2\omega\tau_T} \ln[1 + (\omega\tau_T)^2],$$

where D_T is the trap density, τ_T is the trap state time constant, C_b is the barrier capacitance and ω is the radial frequency. The D_T and τ_T can be extracted by fitting experimental $C_p(\omega)$ or $G_p(\omega)$ data. We used this procedure to analyze the conductance data, as in this case the barrier

capacitance C_s is not required to be known. Typical G_p/ω vs ω curves for the HFET, measured at selected biases near the threshold voltage, are shown in Fig. 2. The data show a significant G_p/ω increase at lower frequencies. This indicates that two different trap states, “fast” and “slow” with different densities and time constants, should be present. A detailed inspection of the MOSHFET data [3] indicated the existence of the same effect, although less pronounced. An excellent agreement between the measured data and fitted curves (full lines) was obtained assuming two different trap states. From the fitting resulting parameters for the HFET were: $D_{T(f)} = (2-3)\times 10^{12} \text{ cm}^{-2} \text{ eV}^{-1}$ and $\tau_{T(f)} = (0.1-1) \mu\text{s}$ for the fast trap states and $D_{T(s)} = (0.3-1.2)\times 10^{13} \text{ cm}^{-2} \text{ eV}^{-1}$ and $\tau_{T(s)} = 8 \text{ ms}$ for the slow trap states. On the other hand, fitting of G_p/ω data for the MOSHFET yielded the density of fast traps $D_{T(f)} \cong 1.5\times 10^{12} \text{ cm}^{-2} \text{ eV}^{-1}$ and of slow traps $D_{T(s)} = (2.5-4)\times 10^{11} \text{ cm}^{-2} \text{ eV}^{-1}$, with identical time constants as those for the HFET. The density of slow traps in the MOSHFET was nearly two orders of magnitude lower than that in the MOSHFET. This shows that the GaN/AlGaIn surface was successfully passivated after applying the oxide on the source-drain access region.

This work was performed in co-operation with the RWTH Aachen, Germany (Prof. A. Vescan) and supported by the Slovak Scientific Grant Agency VEGA (Contract No. 2/6099/27).

- [1] Kordoš, P., Heidelberger, G., Bernát, J., Fox, A., Marso, M., and Lüth, H.: *Appl. Phys. Lett.* **87** (2005) 143501.
- [2] Kordoš, P., Gregušová, D., Stoklas, R., Gaži, Š., and Novák, J.: *Solid. St. Electron.* **52** (2008) 973.
- [3] Stoklas, R., Gregušová, D., Novák, J., Vescan, A., and Kordoš, P.: *Appl. Phys. Lett.* **93** (2008) 124103.

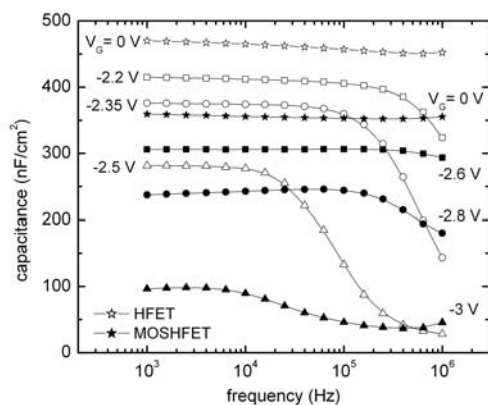


Fig. 1. Capacitance vs frequency for AlGaIn/GaN/Si HFET and Al₂O₃/AlGaIn/GaN/Si MOSHFET for selected V_G .

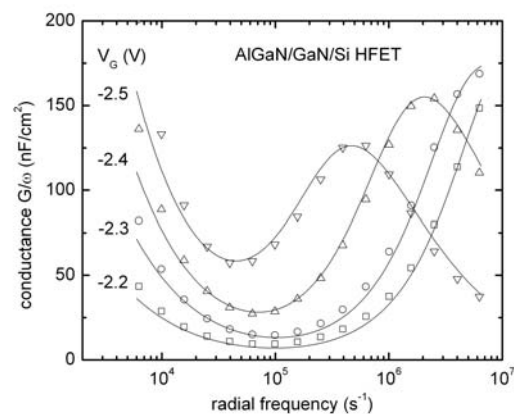


Fig. 2. Conductance vs frequency for AlGaIn/GaN/Si HFET at gate voltages near depletion (full lines are fitting curves).

Influence of InMnAs layer on the properties of GaAs/AlGaAs MQW LEDs

P. Telek, S. Hasenöhrl, J. Šoltýs, I. Vávra, and J. Novák

Great advances in the development of III-V diluted magnetic semiconductors (DMS) materials allow for the incorporation of ferromagnetic epitaxial layers into advanced device structures. In this contribution, we report on the growth of GaAs/InMnAs layers by metalorganic vapour phase epitaxy (MOVPE) over an AlGaAs/GaAs multi-quantum-well (MQW) light-emitting diode structure. In particular, results of electrical and structural characterization of the structures are presented [1].

We prepared a single-phase ferromagnetic $\text{In}_{1-x}\text{Mn}_x\text{As}$ ternary with x close to 0.075 on (100) GaAs substrates using MOVPE. The material exhibited room temperature ferromagnetic behaviour with a Curie temperature close to 340 K. In addition, all InMnAs ternary samples showed p -type conductivity. The ferromagnetic material was incorporated into an AlGaAs/GaAs LED structure. The LED structure was grown by MOVPE on n -type (100)-oriented GaAs substrates with a 350 nm thick n -type GaAs buffer layer. The active region consisted of three 9 nm thick undoped GaAs wells separated by an 18 nm thick AlGaAs barrier sandwiched between two 40 nm thick undoped AlGaAs spacer layers. A p -doped AlGaAs layer followed by a p^+ cap GaAs layer were grown on top of the MQW structure. The lattice mismatch between the GaAs-based heterostructure and the InMnAs layer was very high (up to 7%). The incorporation of such a strained layer into the LED structure led to the creation of misfit dislocations and to a decrease in the quality of the LED structure (Fig. 1). To cast more light on the problem, we prepared three LED structures with a variable position of the InMnAs layer: (i) 300 nm thick InMnAs layer was incorporated directly at the interface between the AlGaAs spacer and p -AlGaAs layer; (ii) a 100 nm thick InMnAs

layer with $x = 0.069$ was incorporated inside the p -AlGaAs layer. The distance from the interface to the undoped/ p -type AlGaAs layer was 100 nm; (iii) The third structure was similar to the second one, only the value of x was higher ($x = 0.88$).

The device processing consisted of conventional LED fabrication steps: (1) preparation of metallic systems for ohmic contacts Au + Zn on the p -side and Au + Sn on the n -side (substrate), (2) annealing of ohmic contacts at 420 °C for 60 s in a $\text{H}_2 + \text{N}_2$ ambient, (3) mesa separation by wet chemical etching, (4) chip separation and bonding with a 21 μm Au wire.

All samples exhibited room temperature electroluminescence maxima of varied intensity at an energy of 1.467 eV. Transmission electron microscopy revealed the presence of strain and dislocation loops in the active parts of the LEDs. It caused substantial changes in the current – voltage (I - V) characteristics: Reverse current increased by five orders of magnitude (measured at $V_r = -5$ V) from 10^{-8} A to a value close to 10^{-3} A. A small increase of the serial resistance R_s was detected in the forward I - V characteristics (Fig. 2).

[1] Telek, P., Hasenöhrl, S., Šoltýs, J., Vávra I., and Novák, J.: 17th International Workshop on Heterostructure Technology, 2008, Venice, Italy, Abstract book p. 27.



Fig. 1. TEM view of the MQW structure with an InMnAs layer incorporated at the interface, case (i). Dislocation loops are present inside the MQW active layer.

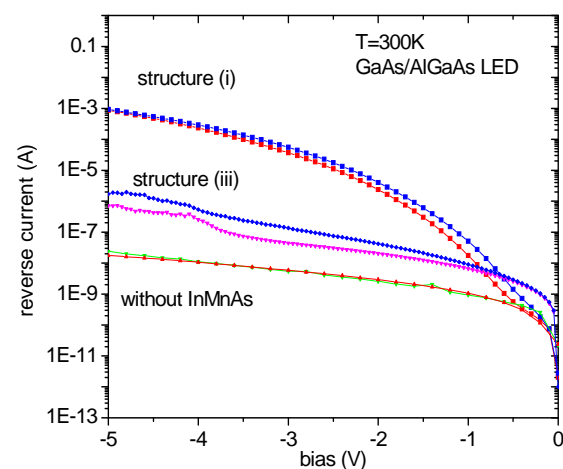


Fig. 2. Reverse I - V characteristics of multi quantum well LEDs. Structures without InMnAs layer and with InMnAs layer are compared.

Department of Microelectronics Structures

Tibor Lalinský

Research scientists

Jozef Osvald

Technical staff

Martin Grujbár

Jozef Vanko

Research Engineers

Štefan Haščik

Želmíra Mozolová

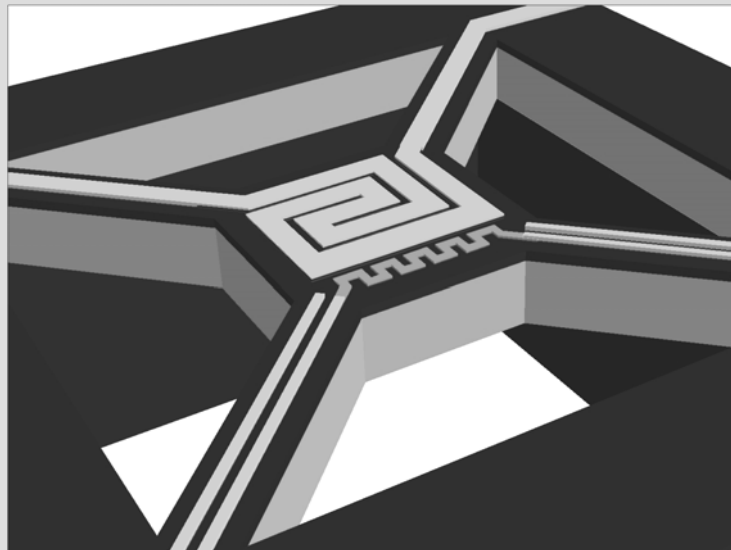
PhD Students

Gabriel Vanko

Students

Ivan Rýger

Vladimír Pira



Our research work in 2007 – 2008 was mainly focused on (1) the Design and development of HEMTs and MEMS devices based on AlGaIn/GaN heterostructures for a new generation of chemical sensors; and (2) the Numerical simulation of an AlGaIn/GaN heterostructure and GaN Schottky diodes (specific problems).

The first area was worked on within the following projects:

- 1) “*Micro(nano)electromechanical structures for new generation of electronic, sensoric and detection devices*”, funded by the Slovak Grant Agency for Science;
- 2) “*Advanced MEMS chemical sensors for extreme conditions*”, funded by the Science and Technology Assistance Agency;
- 3) “*Monolithically integrated HEMT-SAW chemical sensors based on the AlGaIn/GaN piezoelectric material system*”, a Slovak-French project funded by the Science and Research Assistance Agency;
- 4) “*Materials for Robust Gallium Nitride – MORGaN*”, large-scale integration project within the 7th framework programme, funded by the European Union.

The work involved the design, sophisticated technology and study of operation of advanced MEMS chemical sensors based on the AlGaIn/GaN piezoelectric material system.

Such MEMS-based chemical sensors may in principle constitute a new generation of devices suitable for the multifunctional monitoring and detection of gases and volatile toxic chemical substances. Such sensors will be reliable, highly sensitive, highly selective, and fast. The piezoelectric and semiconducting properties of AlGaIn/GaN allow for the design of monolithic MEMS sensors integrated on a chip with control electronics. The integration makes it possible to miniaturize detection regions of the sensors. It will also widen their function abilities and markedly lower the production costs.

Their basic construction and electronic material is the AlGaIn/GaN heterostructure system, grown by MBE and MOCVD on sapphire and silicon substrates. Specific (intrinsic), electro-physical and thermo-mechanical properties of the heterostructures are taken into account in the design of the sensors.

The sensors rest on mechanically supported and thermally insulating membrane structures (suspended membrane islands), released by surface and bulk micro-(nano)-patterning. The membranes are designed to be fully compatible with active inter-digitated electro-mechanical transducers and with micro-(nano)-electronic quantum devices, such as HEMTs.

Expertise acquired with the technology of the sensors, based on AlGaIn/GaN micromechanical structures (membranes, bridges, cantilevers), can be applied further in the design of other multifunctional sensors, exploiting other physical principles and mechanisms of sensing, detection and actuation. The sensors based on the

AlGaIn/GaN micromechanical structures (cantilevers, membranes) compatible with HEMTs can be used in the automotive industry (new generation of sensors of pressure, vibrations and acceleration), surface microscopy (new cantilever-based probes), metrology (new generation of sensors of electrical power for the microwave and millimetre frequency bands), and in satellite signal transmission (passive micromechanical electronic devices for the millimetre frequency band).

We have successfully solved the following relevant technological and physical aspects:

- 1) *Process technology development and characterization of AlGaIn/GaN HEMTs for use as thermal heaters or sensing and electronic devices in the MEMS-based sensors;*
- 2) *Formation of inter-digital transducers (IDTs) on an AlGaIn/GaN heterostructure for use as a source surface acoustic wave (SAW) at a zero DC bias voltage;*
- 3) *Influence of polarization charge at the surface of an AlGaIn barrier layer on the energy band diagram of the AlGaIn/GaN interface;*
- 4) *Numerical study of a large reverse leakage current (tunnelling current) generally observed in GaN Schottky diodes.*

The research staff of our department organized the 7th International Conference on Advanced Semiconductor Devices and Microsystems – ASDAM 2008. It was held at Smolenice Castle, Slovakia, on October 12 – 16, 2008. The conference was devoted to the latest results of the research, development and technology of advanced devices and microsystems.

Researchers at our department have also been involved in the Centre of Excellence Nano-/Micro-electronic, Optoelectronic and Sensoric Technologies (CENAMOST) at the Faculty of Electrical Engineering and Information Technologies of the Slovak Technical University in Bratislava. We are responsible for the development of sensoric technologies within the Centre.

We have done a lot of research in collaboration with domestic and foreign institutes and universities. This included co-operation with the Electron Beam Lithography Department at the Institute of Informatics (Bratislava), the Department of Micro-electronics, Slovak Technical University (Bratislava), the International Laser Center (Bratislava), the TIMA Laboratory in Grenoble, France, and the Department of Microelectronics, Czech Technical University in Prague, the Czech Republic. I would like to express gratitude to all our partners.

The contributions in this booklet are short reports on our research introduced above. Most of the results have been published in journals and at conferences.

Tibor Lalinský

Impact of SF₆ plasma on performance of AlGa_N/Ga_N HEMT structures

T. Lalinský, G. Vanko, Š. Haščík, I. Rýger, and Ž. Mozolová

High-electron-mobility transistors (HEMTs) based on GaN and its alloys have shown great promise in high-frequency and high-power applications. However, one key problem is related to high density of surface traps located in the gate range of the HEMTs, which increase leakage current through the Schottky gates, decrease the breakdown voltage and cause an important parasitic phenomenon of the rf current collapse. To reduce the influence of the surface traps various approaches were proposed including an insulating dielectric layer placed between the gate electrode and the AlGa_N barrier layer, a gate-terminated metallic field plate, and a thick epitaxial cap layer. Recently, a new simple approach based on a surface selective plasma treatment of the HEMT gate range using CF₄ plasma gas was introduced to reduce the gate leakage current and current collapse.

We introduce a modified approach in passivation of AlGa_N/Ga_N HEMTs. Instead of CF₄ plasma we have proposed SF₆ plasma to modify Schottky gate interface and two-dimensional electron gas (2DEG) density of the HEMTs. A comprehensive dc and microwave performance of the plasma treated AlGa_N/Ga_N HEMTs was investigated [1].

Undoped AlGa_N/Ga_N heterostructure grown by metal-organic chemical vapor-phase deposition (MOCVD) on (0001) sapphire substrate was used to define HEMT structures. The thicknesses of AlGa_N and Ga_N layers were 32 nm and 3 μm, respectively. The aluminum mole fraction of the AlGa_N layer was nominally 0.25. The concentration and the mobility of the 2DEG formed at the AlGa_N/Ga_N interface at room temperature were found to be $1 \times 10^{13} \text{ cm}^{-2}$ and $1600 \text{ cm}^2/\text{Vs}$, respectively.

The processing flow consisted of device "MESA"-isolation performed using a reactive ion etching (RIE) in CCl₄ gas. In the next step source-drain alloyed ohmic contacts based on Nb/Ti/Al metallic system were formed

at 850 °C for 35 s [2]. After gate windows with 2 μm length were opened by a contact photolithography, a specific surface plasma processing was performed. We have used a two-step surface plasma treatment of the AlGa_N barrier layer before the deposition and patterning of the Ni/Au Schottky gate contacts. In the first step, a shallow recess-gate etching of AlGa_N (~ 1-2 nm) is performed in CCl₄ plasma through the photoresist mask. Afterwards, in the second step the recess-gate etching is in situ followed by SF₆ plasma treatment at different plasma powers.

The comparison of dc transfer and transconductance characteristics of the conventional and plasma treated HEMT structures (SF₆ plasma at power of 250 W for 60 s) are shown in Fig. 1. It can be seen that the new approach in the forming of Schottky gate interface improves linearity in the transfer characteristic, decrease threshold voltage and increase maximum transconductance of the HEMT structure. The maximum transconductance as large as 150-160 mS/mm can be achieved for 2 μm gate length HEMT structure with the gate range additionally treated in SF₆ plasma.

In addition to dc characterization, on wafer S-parameter measurements from 100 MHz to 40 GHz as a function of drain and gate bias voltages were performed [2]. As a figure of merit current gain cut-off frequency (f_t), and maximum oscillation frequency (f_{max}) were chosen. It was found that SF₆ plasma treatment additionally performed under Schottky gate improves f_t and f_{max} almost about 60 %. Figure 2 shows f_{max} of HEMTs at different dc bias conditions.

- [1] Vanko, G., Lalinský, T., Haščík, Š., Rýger, I., Mozolová, Ž., Tomáška, M., Škriniarová, J., Kostič, I., and Vincze, A.: *accepted in Vacuum* (2009).
 [2] Vanko, G., Lalinský, T., Mozolová, Ž., Liday, J., Vogrinčič, P., Vincze, A., Uherek, F., Haščík, Š., and Kostič, I.: *Vacuum* 82 (2007) 193.

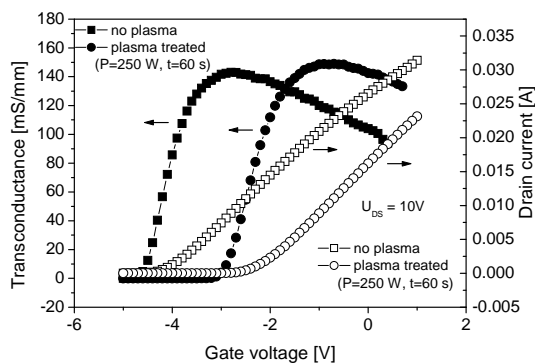


Fig. 1. Transfer and transconductance characteristics of 2 μm gate length AlGa_N/Ga_N HEMT structures.

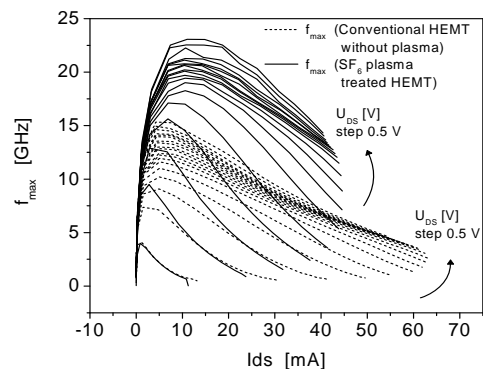


Fig. 2. f_{max} of HEMTs at different dc bias conditions.

Surface acoustic wave excitation on SF₆ plasma treated AlGa_{0.3}N/GaN heterostructure

T. Lalinský, I. Rýger, G. Vanko, Š. Haščík, and Ž. Mozolová

Nowadays, there is an increasing interest in identifying new piezoelectric materials where surface acoustic waves (SAW) devices can exhibit novel or improved characteristics. Among them, the epitaxially grown III-nitride semiconductor materials such as AlN, AlGa_{0.3}N and GaN combine high SAW velocity and piezoelectric coupling with excellent thermal and chemical stability. SAW propagation directly in AlGa_{0.3}N/GaN heterostructure material system that defines a two-dimensional electron gas (2DEG) of the high electron mobility transistors (HEMTs) is a topic of much interest because of possible monolithic integration of the SAW devices (filters, oscillators, sensors) with the HEMT based electronics.

The direct interaction of SAW with free carriers of 2DEG prevents the acousto-electric transduction in interdigital transducers (IDTs) due to additional insertion losses.

We introduce a new modified approach to the formation of IDT structures on an AlGa_{0.3}N/GaN heterostructure. The modified approach is based on the use of a shallow recess-gate plasma etching of the AlGa_{0.3}N barrier layer in combination with “in-situ” SF₆ surface plasma treatment applied under Schottky gate fingers of IDTs. It was proposed to achieve an improved performance of AlGa_{0.3}N/GaN-based HEMTs. Initial results of the processing technology and characterization are presented.

Undoped AlGa_{0.3}N/GaN heterostructure grown by metal-organic chemical vapor-phase deposition (MOCVD) on (0001) sapphire substrate was used to define IDT structures. The thicknesses of AlGa_{0.3}N and GaN layers were 25 nm and 2 μm, respectively. The aluminum mole fraction of the AlGa_{0.3}N layer was nominally 0.3. The cross-section through the plasma treated SAW structure is schematically shown in Fig. 1.

To modify high density of 2DEG in the range of IDTs, a shallow recess-gate plasma etching of AlGa_{0.3}N barrier layer (1-2 nm) in CCl₄ plasma is performed in combination with “in-situ” SF₆ surface plasma treatment.

SF₆ plasma treatment is there selectively applied in

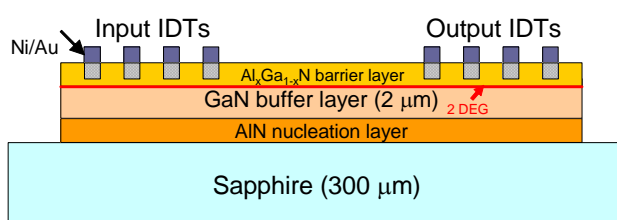


Fig. 1. Cross-section through plasma treated AlGa_{0.3}N/GaN based SAW structure.

two following steps before the deposition and forming of Ni/Au fingers of IDTs. In the first step it is applied at plasma power of 30 W for 30 s, and in the second step at plasma power of 350 W for 120 s. The two-steps SF₆ treatment enables to obtain homogenous distribution of F atoms (F⁻ ions) in the AlGa_{0.3}N barrier layer.

The measured depth profiles of the plasma-treated AlGa_{0.3}N/GaN heterostructure revealed that mainly F atoms were incorporated in the sample surface and AlGa_{0.3}N/GaN interface [2]. Because of a strong electronegativity of F⁻ ions, the incorporated F⁻ ions can provide immobile negative charges in the AlGa_{0.3}N barrier layer and effectively deplete electrons in the 2DEG channel.

Two IDTs, each with 80 pairs of interdigital fingers were designed for the working frequency of around 250 MHz. Both the width and the spacing between the fingers were designed to be 5 μm. Consequently, the SAW wavelength λ is equal to 20 μm.

Figure 2 shows an amplitude characteristics dependence of a SAW structure on variable bias DC voltage applied on IDTs. At a zero DC bias voltage applied between the fingers of the IDTs, we observed the SAW excitation with a relative stop-band rejection of 15 dB. The measured quality factor $Q = 1264$ corresponding to -3 dB bandwidth of 180 kHz. The center peak frequency was 227.57 MHz and the calculated phase velocity about 4551 m.s⁻¹. An extensive study of SAW propagation through the plasma treated AlGa_{0.3}N/GaN heterostructure can be found in [2].

- [1] Lalinský, T., Rufer, L., Vanko, G., Mir, S., Haščík, Š., Mozolová, Ž., Vincze, A., and Uherek, F.: *Appl. Surf. Sci.* **255** (2008) 712
- [2] Lalinský, T., Rýger, I., Rufer, L., Vanko, G., Haščík, Š., Mozolová, Ž., Tomáška, M., Vincze, A., and Uherek, F.: *accepted in Vacuum* (2009).

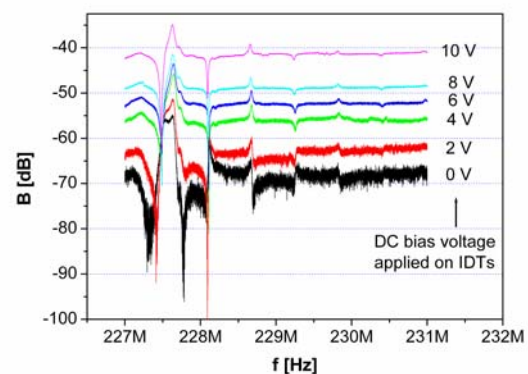


Fig. 2. Amplitude characteristics of SAW structure at different DC bias voltages.

Polarization effects and energy band diagram in AlGaIn/GaN heterostructure

J. Osvald

AlGaIn/GaN and generally III-nitrides heterostructures are well known candidates for high power and high frequency transistors. Spontaneous and piezoelectric polarization in such devices make possible to obtain electron concentration in the channel of the transistor in the order of 10^{13} cm^{-2} or even higher in undoped or unintentionally doped structures. The polarization fields caused by the spontaneous polarization in AlGaIn and the piezoelectric polarization are in order of 10^6 V/cm .

Currently the energy profile in AlGaIn/GaN structure and the carrier density are studied by the self-consistent solution of Poisson and Schrödinger equations. By the solution of this system of equations it is possible to find out eigenenergy states in the subband structure, their population in the channel region and finally the potential distribution in the system.

As was shown recently [1] the polarization charge at the AlGaIn/GaN interface can be simulated by insertion of very thin δ -doped layer. The sheet carrier concentration of such δ -doped layer is directly determined by the polarization charge. The δ -doped layer with the same sheet carrier concentration but with opposite charge must be put at the AlGaIn surface layer. This last effect was not taken into account in the previous work. We show in this contribution how the polarization charge at the surface of the AlGaIn barrier layer influences the energy band diagram and how the external bias changes the potential curve and the electron concentration near the AlGaIn/GaN interface.

In order to calculate the potential and the energy band diagram in thermodynamic equilibrium it is necessary to solve the Poisson equation. If an external bias is applied to the structure and the system is out of equilibrium, the continuity equation for electrons and holes must also be solved simultaneously with Poisson equation. We used basic semiconductor equations for study of such systems,

i.e., we solved simultaneously Poisson and continuity equations.

The polarization charge was simulated in our calculations by approximately one monolayer (0.25 nm) thick δ -doped layer and the Schottky barrier height was assumed to be 1 V. AlGaIn layer was 30 nm thick. The doping concentration of AlGaIn layer given as an input to the calculations was $2 \times 10^{18} \text{ cm}^{-3}$ and of GaN layer it was $1 \times 10^{16} \text{ cm}^{-3}$. The total polarization was assumed to be around $1 \times 10^{13} \text{ C/cm}^2$ with the same induced sheet charge concentrations. In Fig. 1 the potential of the conduction band minimum for three external voltages is shown.

In Fig. 2 the concentration of electrons near the heterointerface region is shown as a function of external bias. Analysis of this plot leads to the conclusion that the electron concentration directly at the AlGaIn/GaN interface is not seriously influenced by external bias. As a reaction to the applied voltage that simulates pinching-off the channel layer, the electron peak concentration remains almost the same and only the concentration outside the δ -doped layer in GaN layer is significantly influenced and diminished. The electrons move deeper into the semiconductor by decreasing the reverse voltage – the conduction channel is wider for these voltages. The electrons at the interface are in the lowest subband and their binding is stronger than that of electrons in higher energy subbands. The concentration diminishing proceeds with increasing reverse voltage from the bulk of GaN towards the AlGaIn/GaN interface.

The drift-diffusion approximation enables to find the energy band shape and the charge distribution. The method is certainly suitable for studying also of other III-nitride polar heterostructures.

- [1] Li, N., Zhao, D.G., and Yang, H.: *Solid State Commun.* **132** (2004) 701.

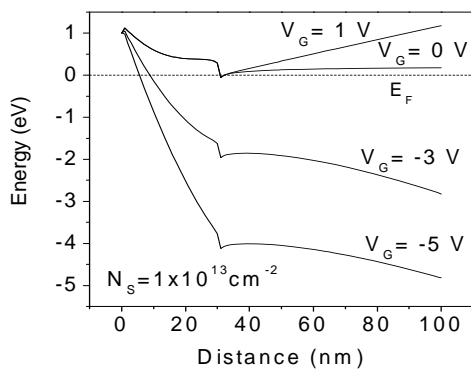


Fig. 1. Potential of the conduction band minimum of the AlGaIn/GaN heterostructure for different bias external voltages.

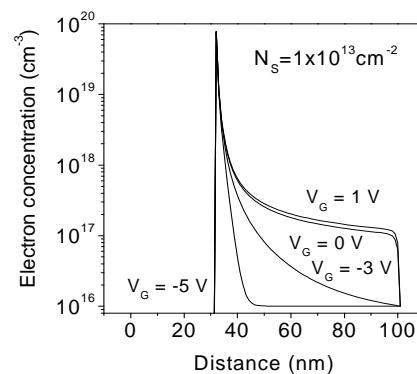


Fig. 2. Shape of the electron density function in GaN layer under the AlGaIn/GaN interface.

Numerical study of tunneling currents in GaN Schottky diodes

J. Osvald

In recent years the technology of GaN based high power and high frequency transistors has made a great advance. In spite of the fact, that the technology of AlGaIn/GaN HEMT transistors reached relatively high level of maturity, several points remained up to now unresolved. One of them is a large reverse leakage current that is commonly about two orders of magnitude higher than in AlGaAs/GaAs technology and several orders of magnitude larger than is predicted by the thermionic emission theory. Recently Kotani *et al.* analyzed especially the leakage current in AlGaIn diodes [1].

The aim of this contribution is to calculate the tunneling current along with the drift-diffusion current in a wide bias region and compare their contributions to the total current flowing through the GaN Schottky diodes. The charge transport through the metal semiconductor barrier by the drift and the diffusion is always present and it enables to calculate self-consistently the shape of the barrier. The potential in the structure and also the barrier shape can be calculated for every bias voltage by the simultaneous solution of Poisson and drift diffusion equations. Knowing the shape of this potential barrier we use Wentzel-Kramers-Brillouin approximation to calculate numerically the tunneling probability $T(E_x)$ for electrons. The tunneling current was calculated according to the expression

$$I = \frac{4\pi q m^*}{\hbar^3} \int_{E_{min}}^{E_{max}} T(E_x) \int_0^\infty [f_s(E_p + E_x) - f_m(E_p + E_x)] dE_p dE_x.$$

We have simulated current-voltage (I - V) characteristics of GaN Schottky diodes with three different doping concentrations $N_D = 1 \times 10^{17}$, 5×10^{17} , and $1 \times 10^{18} \text{ cm}^{-3}$. In Fig. 1 I - V curve for $N_D = 5 \times 10^{17} \text{ cm}^{-3}$. In the reverse bias region it is clearly seen that the tunneling

current does not saturate and increases more steeply with bias than the drift-diffusion current. Worth noting is also the fact, that by the forward bias the tunneling current is for almost every voltage lower or maybe comparable to the drift-diffusion current.

We have studied also the temperature dependence of the tunneling current for the same doping concentrations and compared it with the appropriate thermionic emission (TE) current. For lower temperatures and the doping concentration $N_D = 5 \times 10^{16} \text{ cm}^{-3}$ the tunneling current density is higher than the thermionic emission current density only for higher reverse voltages. For the doping concentration $N_D = 5 \times 10^{17} \text{ cm}^{-3}$ the tunneling current plays already the dominant role and is higher than the thermionic current for every studied temperature and the whole bias range. Further enhancement of the doping concentration to the value $N_D = 5 \times 10^{18} \text{ cm}^{-3}$ (Fig. 2) brings already described bowing of the reverse part of the I - V curve which is seen also at $N_D = 5 \times 10^{17} \text{ cm}^{-3}$ and 100 K.

We may say that according to the theory the thermionic emission is important only for the diodes with moderately doped GaN up to $N_D = 5 \times 10^{16} \text{ cm}^{-3}$. For higher doping concentration the tunneling current is the decisive conductance component. For the highest studied doping concentration the reverse tunneling current has typical bowed shape often observed in experiments. Certainly, in real structures non-idealities of the structure such as dislocation-related leakage paths, nitrogen vacancies, and other inhomogeneities may further enhance the total current flowing through the structure.

[1] Kotani, J., Kaneko, M., Hasegawa, H., and Hashizume, T.: *J. Vac. Sci. Technol. B* **24** (2006) 2148.

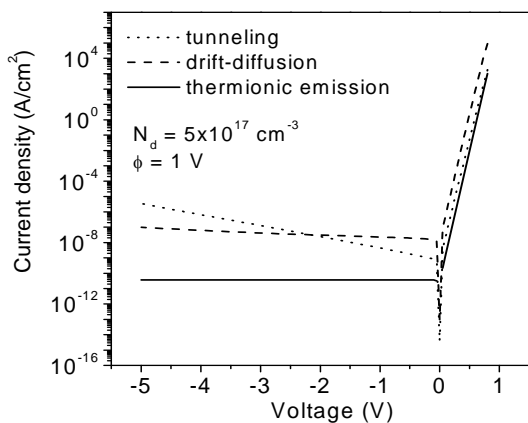


Fig. 1. Simulated I - V characteristic of GaN Schottky diodes for the tunneling, drift-diffusion and thermionic emission currents.

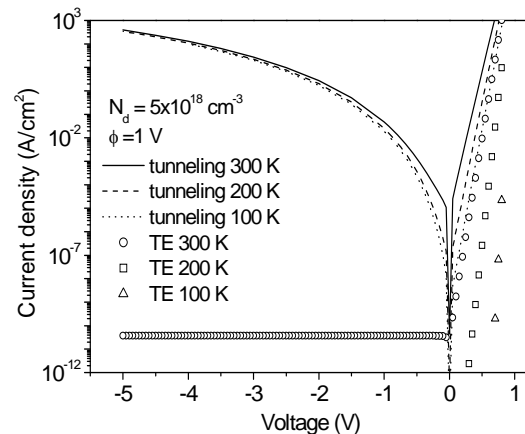


Fig. 2. The tunneling and thermionic emission GaN Schottky diodes currents at different temperatures.

Department of Semiconductor Technology and Diagnostics

František Dubecký

Research scientists

Pavel Boháček
Jozef Huran
Dušan Korytár
Bohumír Zaťko

Research Engineers

Mária Sekáčová

Technical staff

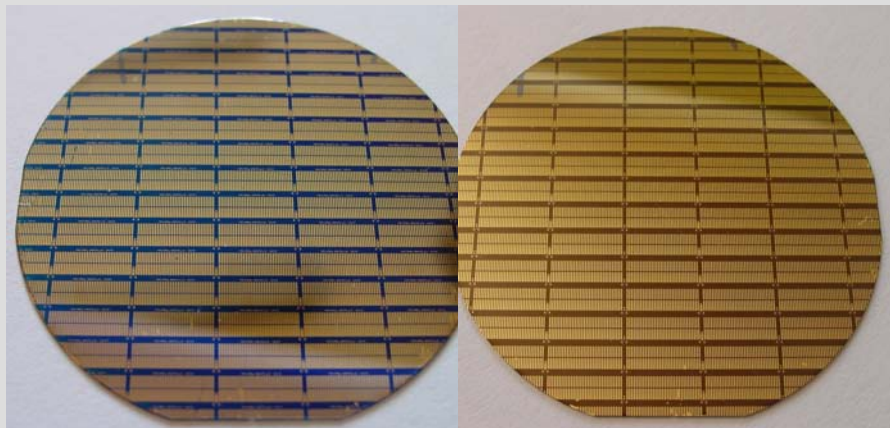
Miloslav Ruček
Viktor Štefanec
Anton Páldi

PhD Students

Andrea Šagátová
Patrik Vagovič
Milan Ladziansky

Students

Matej Makovník
Martin Pivarčí
Igor Trokšiar
Tomáš Šalát
Pavol Konopka
Tomáš Šugerek
Roman Bartoš



The research activities of the Department of Semiconductor Technology and Diagnostics have had an interdisciplinary character, covering semiconductor materials science, technology, applied physics, and applications:

(i) Characterisation and diagnostics of basic physical parameters of semiconductors, mainly those of GaAs and InP. We have been using a variety of measurement techniques to evaluate conductivity, Hall mobility, magnetoresistance, I - V and C - V characteristics. The department has also used other techniques, e.g. DLTS, Admittance Transient Spectroscopy, High Resolution X-ray Diffraction and Topography, EBIC, SEM, AFM, etc.;

(ii) Study of physical problems related to the development of III-V radiation and particle detectors, such as the transport of charge carriers, deep-level (radiation induced) defects, electric field distribution, etc.;

(iii) Study of the technology of III-V particle, X-ray and neutron detectors and fast photo- and opto-devices. It includes the preparation of contacts (Schottky, injecting, ohmic), optimization of device topology, treatment of interface and surface passivation. The detection properties of the devices are tested using sources of α -particles, X- and gamma rays and neutrons (fast and thermal);

(iv) Development of new generation radiology instrumentation. Study of X-ray digital imaging, in particular the single photon counting ("quantum") and "colour" imaging (photons separated in energy) techniques. The development of systems suitable for the detection of X- and gamma rays and neutrons emitted by hot plasmas (Tokamak);

(v) Investigation and development of X-ray diffraction and devices for X-ray optics;

(v) Study of special plasma technologies and the related phenomena. The technologies are developed for sensor applications (e.g. SiC) and devices passivation (silicone nitride).

Our **main goal** (staff of 8 people) is to develop, fabricate and apply semiconductor devices suitable for small-scale fabrication. We have been using the unique III-V technology facilities of the Institute based in the town of Piešťany (80 km from Bratislava).

The key department activities during 2007-2008 included:

Basic research projects

(1) "*Neutron detectors: technology of preparation, study of electrical and detection performance*", supported under VEGA project No. 2/7170/27 and headed by the principal investigator F. Dubecký;

(2) "*Thin nanocrystalline layer structures for sensorics and microsystem techniques*", supported under VEGA project No. 1/3095/05 with the principal investigator I. Hotový (SUT).

Application research projects

(3) "*Selected topics from X-ray technologies*", supported under APVV project No. APVV-0459-06 and headed by the principal investigator D. Korytár;

(4) "*A new generation digital radiology system kit*", supported under APVV project No. APVV-99-P06305 and led by the principal investigator J. Mudroň (MTC, a.s.).

International research projects

(5) "*X-ray beam conditioning and imaging*", supported by COST project MP 0601 "*Short wavelength laboratory sources*" headed by the principal investigator D. Korytár;

(6) "*Applications of semiconductor single crystals for X-ray optics, monolithic X-ray detectors and high efficiency solar cells*", co-ordinated by F. Dubecký (SK) and C. Ferrari (I) under a bilateral IEE SAS-IMEM CNR project; and

(7) "*Theoretical and experimental study and technology of plasma diagnostic sensors*", supported within EURATOM/CU (7FWP) and led by the principal investigator F. Dubecký.

The **technology equipment**, used for the fabrication of devices as small as 1 μm , is placed in a 100&1000 clean room (225 m^2). It consists of an automatic contact lithography aligner, a projection lithography system with a wet-chemical treatment line, a BALZERS UMS 500 UHV evaporation system, a BALZERS BAS 450 magnetron and reactive sputtering apparatus, an annealing furnace, a SECON XPD200 dry plasma system for the deposition of dielectric layers, and a SECON XPL 200P reactive ion etching system.

The key testing equipment includes: a HP 4192A PC-controlled low-frequency impedance analyzer, a DLS 82 PC-controlled deep-level spectrometer, an automatic test system (AVT 110) with 50 controlled needle probes, an X-ray diffractometer with a monolithic four-fold monochromator and attachments for the Lang and double crystal topography, an automatic I - V measurement system (D/S Lab, Ltd.) up to 1 kV, and a HP 54600 two-channel digital oscilloscope. A recently obtained microfocus Hamamatsu X-ray source, type 80 kV L6731, was installed to perform X-ray digital non-destructive evaluation, e.g. CT at a micro-scale resolution ($< 8 \mu\text{m}$).

We organized the 7th International Autumn School on X-Ray Scattering from Surfaces and Thin Layers, Smolenice, 2007. We also participated in the 8th ASDAM'08 International Conference (Advanced Semiconductor Devices and Microsystems), Smolenice, October 2008. In addition, we co-organized the XIVth Semiconducting and Insulating Materials Conference (University of Arkansas, Fayetteville, USA, May 2007).

Our research is based on a long-term fruitful collaboration with many research groups in Slovakia and abroad, e.g. the IMEM-CNR, Parma, Italy; the Institute of Physics and the Institute of Photonics and Electronics, the Czech Academy of Sciences and the Czech Technical University in Prague; the Institute of Plasma Physics and Laser Micro-fusion, Warsaw, Poland.

František Dubecký

Development of mobile X-CT & SCAN system with monolithic GaAs detectors working in single photon counting and photon energy separation mode

B. Zató, F. Dubecký, and D. Korytár

We are developing a quantum (single photon counting regime) X-CT & SCAN mini-system (XCTSMS) which utilizes a monolithic semi-insulating (SI) GaAs two lines of pixel detectors. The system allows for scanning objects as large as 180 mm in diameter and 250 mm in length at an estimated spatial resolution less than 150 μm .

The portable XCTSMS device consists of the: i) the X-ray source, ii) the detection unit, iii) two stepper motors, which control the rotation of the X-ray source coupled with the detection unit around the evaluated object and the linear movement, iv) a local high-performance PC with a touch-screen monitor allowing for comfortable control of all system elements. The overall block diagram of the XCTSMS is shown in Fig. 1. The X-ray source (Source-Ray Inc.: Model SB-80-500) with a W anode operates in a bias range of 35-80 kV at a maximum current of 500 μA with a maximum focal spot size smaller than 46 μm at a maximum power of 40 W. X-rays generated by the source pass through two filters, selectable from 2x8 positions fixed in two rotatable carousels, followed by a micro-adjustable slit, which restricts the width of the cone (into which X-ray photons are emitted) into a narrow beam. The detection dual line incorporates 2x1024 pixels for a total length of 261.5 mm based on SI GaAs with a thickness of 250 μm . The pixel detectors are dc-coupled by wire bonding to the inputs of two ASICs – DX64 readout chips. The readout chip has two discriminators and 20-bit counters for each channel, hence one energy window is available in one evaluation

scan [1,2]. The distance between the X-ray source and the detection unit is fixed at 380 mm. An examined object is located between the X-ray source and the detection unit. One of the stepper motors ensures a full rotation of the X-ray source & detection unit coupled system around the object. The other stepper motor allows for its linear positioning along the z direction over a distance of 250 mm. As a fan-beam configuration (diverging beam) is used, the maximum diameter of an object that can be examined is 180 mm. The radiation dose to evaluate an object is lower compared with the irradiation without slit (or fully open slit). The device can also be used to examine living objects (small animals or parts of the human body, including hand or leg). A photograph of the mechanical construction of the XCTSMS is shown in Fig. 2. The X-ray source, connected with the filter and the slit holder, is positioned in the top part of an aluminum wheel, driven by the stepper motor. The cylindrical holder is used to fix the tested objects. The detection unit is being currently developed, and it will be set-up and installed in the near future. The custom user-friendly software provides for setting of operational parameters, data collection and image reconstruction processing via a touch-screen monitor. A minimum time for acquiring projections in two slices is about 55 s. The evaluation of an object with the length of 250 mm requires 384 steps (768 slices) of obvious 0.65 mm pace.

This work was supported by the Slovak Research and Development Agency under No. APVV-99-P06305.

[1] Gryboš, P., et al.: *IEEE Nucl. Sci. Sypos. Conference Record*, N17-5 (2006) 693.
 [2] Zató, B., et al.: *Nucl. Instr. and Meth. in Phys. Res. A* 591 (2008) 101.

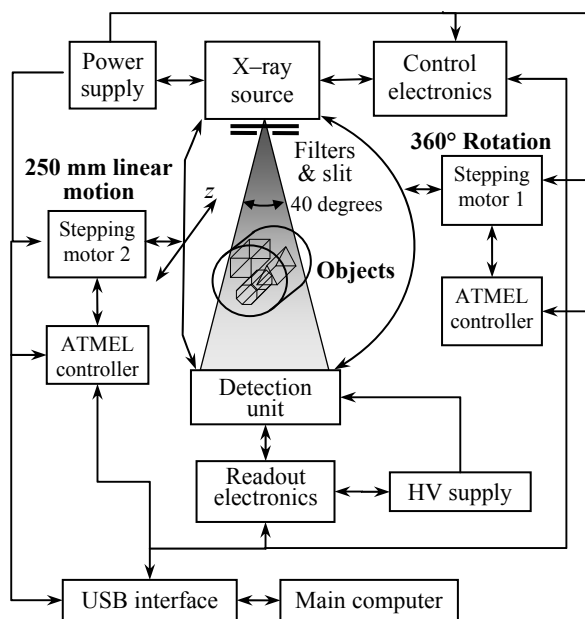


Fig. 1. Overall block diagram of the automatic control of the portable XCTSMS.



Fig. 2. Photo of constructed part of the portable XCTSMS with the personal computer and touch-screen monitor.

Concept and performance of 2×64 channel input mini-module with monolithic semi-insulating GaAs two-line X-ray detectors coupled to DX64 ASICs

B. Zato'ko, F. Dubecký, P. Boháček, M. Sekáčová, and J. Huran

The readout electronics is important part of digital X-ray radiography system operating in the single photon counting mode. The value of noise has to be low especially for detection of X-rays with energy below 20 keV. ASIC DX64 readout chip is suitable for the application due to its fast response at reasonable noise quality.

The main characteristics of ASIC DX64 readout chip are published in [1]. The chip with overall size 3.9 mm × 5.0 mm is designed in CMOS 0.35 μm process. Each of 64 channels consists of the charge sensitive preamplifier, shaping amplifier and two discriminators with two independent 20 bits counters. Power dissipation per channel is 5 mW. Peaking time of the shaped impulse is 160 ns and the equivalent noise charge for $C_{det} = 1$ pF is 110 e⁻ rms. The maximum counting rate of the readout chip is more than 1 MHz per channel. Semi-insulating (SI) GaAs detectors are wire bonded to the inputs of the readout chip. During testing the detectors operated at a reverse bias voltage of 220 V. The radioisotope ²⁴¹Am was used as a γ- (59.5 keV) and X-rays (13.9, 17.8 and 20.8 keV) source. Measurement of the integral spectra (dependence between the total counts of channel and adjusted threshold) of SI GaAs detectors and calculation of differential spectra of each tested channel was performed [2]. Typical energy resolution is depicted in Fig. 1. Lines of three X-ray photons are resolved and the

energy resolution of 59.5 keV gamma photons is 3.8 keV in FWHM (full width at half maximum). This value is achieved for SI GaAs detector with area of 0.09 mm², which is characteristic for detectors used in digital radiography.

The detection unit in our developed portable X-CT mini system consists of 16 input modules, each with 2×64 monolithic SI GaAs pixel detectors arranged along two lines on the chip assembled into an arc. The detection two-line incorporates 2×1024 pixels for a total length of 261.5 mm. The input mini-module (Fig. 2a) consists of the chip with the pixel detectors based on SI GaAs with a thickness of 250 μm (Fig. 2b). The pixel pitch is 250 μm and distance between two lines is 350 μm. The operational bias of the SI GaAs detectors is between 150 and 300 V. The pixel detectors are dc-coupled to the inputs of two ASICs – type DX64 readout chips, by wire bonding via pitch adapters, which adjust the pitch of the pixel detectors to the input pads of the ASICs. The PCB (printed circuit board) has dimension of about 16 mm × 120 mm and is fixed onto Peltier cooler which stabilize the working temperature of the detectors and the input electronic circuitry at about 15 °C using a thick Cu holder.

This work was supported by the Slovak Research and Development Agency under No. APVV-99-P06305 and APVV-0459-06.

[1] Gryboš, P., et al.: *IEEE Nucl. Sci. Sypos. Conference Record*, N17-5 (2006) 693.
 [2] Zato'ko, B., et al.: *Nucl. Instr. and Meth. in Phys. Res. A* 591 (2008) 101.

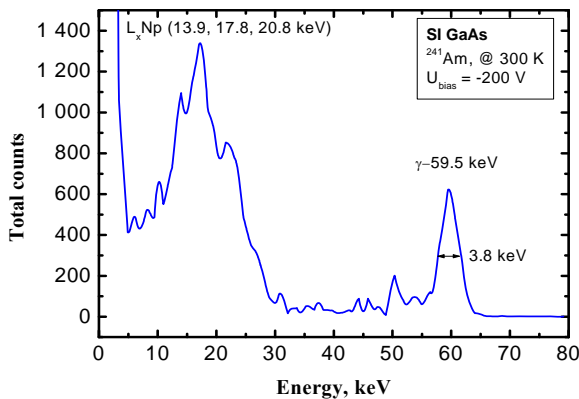


Fig. 1. Measured spectrum of the ²⁴¹Am by an SI GaAs pixel detector connected to the ASIC DX64 readout chip.

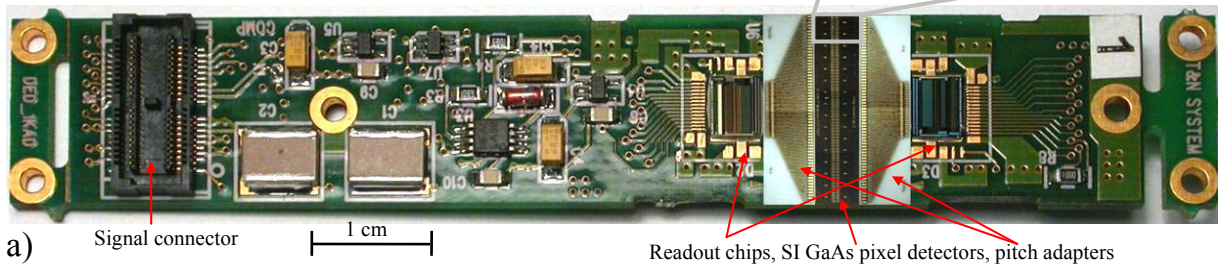


Fig. 2. Input readout mini-module with 2×64 SI GaAs pixel detectors, two pitch adapters and two readout chips (a) and 10× magnified part of two-line pixel detector chip (b).

Application of quantum digital X-ray scanner in CT reconstruction

B. Zat'ko and F. Dubecký

The work was focused onto application of our previously developed X-ray scanner [1] operating in the single photon counting mode in computed tomography (CT). The system is based on monolithical semi-insulating GaAs radiation detectors.

There are different methods used for image reconstruction from projections, e.g. filtered backprojection (FBP), reconstruction via frequency domain or many kinds of iterative algorithms. We use FBP because of sufficient speed to accuracy ratio [2]. Considering setup geometry, three different arrangements are possible: parallel beam (Fig. 1a), fan beam with equidistal detectors (Fig. 1b) and fan beam with equiangular detectors (Fig. 1c). In our case, fan beam with equidistal detectors geometry was used, whereas the way of data acquisition is usually referred to as third generation CT [3].

The output of transformation from spatial domain to Radon domain is called sinogram - $p(\tau, \theta)$:

$$p(\tau, \theta) = \int_{-\infty}^{\infty} \int_{-\infty}^{\infty} f(x, y) \delta(x \cos \theta + y \sin \theta - \tau) dx dy,$$

where θ is the angle of particular projection, τ is the target distance of each beam and $f(x, y)$ is a 2D function to be projected. Filtered backprojection can be expressed by the following equation

$$f(x, y) = \int_0^{\pi} q(x \cos \theta + y \sin \theta, \theta) d\theta,$$

where q is a 2D function of filtered projections. Filters implemented in our algorithms were Ram-Lak, Shepp-Logan, Hann, Hamming and cosine filter. The fan-type projections must be rebinned and interpolated to parallel-type before applying back projection algorithm. It follows from the figure geometry that for any ray $\tau = R \sin \alpha$ and consequently

$$r_{\beta}(\alpha) = p_{(\alpha+\beta)}(R \sin \alpha).$$

The experimental equipment used for testing X-ray CT imaging method consists of an active X-radiation source with energy of photons up to 80 keV, digital X-ray scanner consisting of 17 monolithic 24 strip line detectors based on bulk SI GaAs capable to scan area of 144 mm × 102 mm corresponding to 576 × 408 pixel, measured

sample positional system (movement in x-axis and rotation), CCD camera with infra LED lighting for condition monitoring inside of a scanning area, local (remote) PC computer for parallel control of all working devices (X-ray source, scanner, positional system and CCD camera) connected via serial or USB lines, main PC located in another place (office room) for distributed control of performed X-ray experiments connected via LAN network to the local PC. The whole X-ray scanning area is incased to a box shielded by 1.5 mm Pb plate. Achieved position resolution of our first testing X-CT mini platform was about 0.1 mm in x-axis, minimum rotation angle was 1.8 deg, and the investigated object can rotate in full interval of 0 ÷ 360 deg [4].

To demonstrate reconstruction process of FBP using Hamming filter was employed and low-pass filtration was performed to decrease the high frequency noise. The output matrix dimension was equal to 140×140 pixels. The photo and the reconstruction image of one slice from 100 projections are depicted in Fig. 2.

This work was supported by the Slovak Research and Development Agency under No. APVV-99-P06305 and APVV-0459-06.

- [1] Dubecký, F., et al.: *Nucl. Instr. & Meth. in Phys. Res. A* **546** (2005) 118.
- [2] Kak, A.C. and Slaney, M.: *Principles of Computerized Tomographic Imaging*. IEEE PRESS, (1988).
- [3] Jan, J.: *Medical Image Processing, Reconstruction and Restoration: Concepts and Methods*, Taylor & Francis Group, (2006).
- [4] Pribil, J., et al.: *Automated Positional Unit of Testing X-ray CT Mini System, Proc. of 7th Int. Conf. Applied Electronics 2007, Pilsen, Czech Republic*, (2007) p. 163.

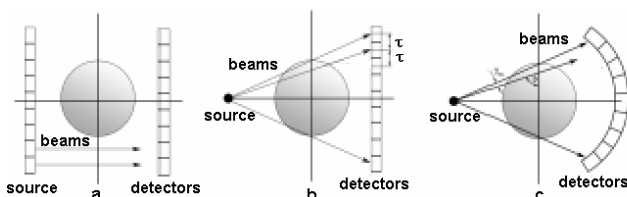


Fig. 1. Basic arrangement for different types of the projection measurement.

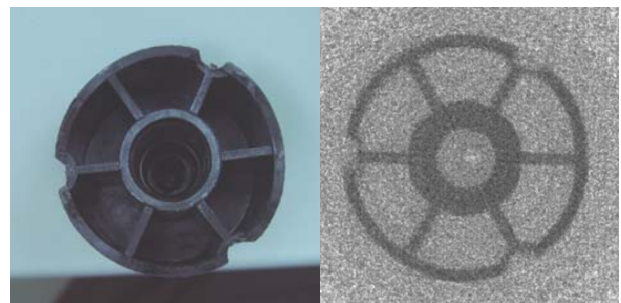


Fig. 2. Application of image reconstruction on the testing object: photography of plastic tube with six capsules, diameter 40 mm (a), finally reconstructed image by the parallel beam method – 100 projections.

Anomalous charge current transport in semi-insulating GaAs with a new quasi-ohmic metallization

F. Dubecký, B. Zat'ko, P. Boháček, J. Huran, and M. Sekáčová

Semi-insulating (SI) GaAs radiation detector performance mainly concerns the electrode metallization [1]. A special emphasis should be devoted to the ohmic electrode technology following the results of Alietti et al. [2] introducing new kind “non-alloyed” ohmic contact which improved performance of the SI GaAs detector.

Our idea of a non-injecting ohmic contact utilizes formation of a metal–semiconductor Schottky barrier using a metal with low enough work function in comparison with the semiconductor (4.5 eV for GaAs). Such a contact should block injected holes from anode, hence behaves as a non-injecting quasi-ohmic contact. The study deals with the measurement and evaluation of electrical characteristics of the detector structures with such a new “quasi-ohmic” contact metallization.

We fabricated SI GaAs detectors with Mg and Gd contacts (work functions 3.68 and 3.10 eV, respectively) and non-alloyed eutectic AuGeNi/Au as a reference contact. Detector structures were prepared from 2” bulk (100) undoped vertical gradient freeze SI GaAs wafer polished from both sides down to $250 \pm 10 \mu\text{m}$. Resistivity and the Hall mobility measured by the van der Pauw method at 295 K give values of $1.82 \times 10^7 \Omega\text{cm}$ and $7062 \text{ cm}^2/\text{Vs}$, respectively, fulfilling key requirements for a “detector-grade” bulk SI GaAs material [3]. Square Schottky electrodes of Ti/Pt/Au (10/40/70 nm) with 0.5 mm size were formed using photolithography masking onto top side of each sample. Just before evaporation the surface oxides were removed in a solution of $\text{HCl}:\text{H}_2\text{O} = 1:1$ at room temperature (RT) for 30 sec. The back side of samples was fully covered by a double layer of Mg/Au or Gd/Au (50/70 nm). AuGeNi/Au (50/70 nm) eutectic alloy was deposited on the back side of the reference sample. The metal contacts were evaporated in a dry high-vacuum system.

Current-voltage (I - V) characteristics of detectors measured at RT in the dark are shown in Fig. 1. The solid straight lines correspond to the linear-ohmic transport calculated from the SI GaAs bulk conductivity

measurements. The reverse characteristics (negative bias polarity applied to the top Ti/Pt/Au electrode) of detectors are similar but some quantitative differences are observable. The linear part of all characteristics in the voltage region under 0.1 V is about $1.5 \div 4$ times lower than that correspond to the calculated ohmic current. The deviation is larger for Mg and Gd contacts. The first sublinear part of the reverse characteristics between 0.1 \div 10 V corresponds to the value of the saturation current I_s of the thermionic field emission. The second sublinear part at voltages over 10 V, which represents the detector operation bias region, is characterized by unknown transport mechanisms. The forward characteristic of the reference detector with AuGeNi metallization (Fig. 1a) for low bias behave similarly. After an initial linear part, a superlinear injection region starts reaching the linear-ohmic current limit (the solid straight line). Such a tendency toward the electrical charge injection is not observed for Mg and Gd contacts. In fact, in the voltage range 0.1 \div 10 V, the detectors prepared with these contacts show always a sublinear character, which follows the initial linear characteristic, similarly to the reverse I - V branch. Finally for voltage values over about 100 V the forward current is almost identical for all structures. These anomalous characteristics are in contradiction with expectations: detectors with Mg and Gd contacts should exhibit the injection behaviour in comparison with the AuGeNi electrode due to the lower work function of used metals. Further detailed theoretical and experimental investigations will be carried out.

Authors acknowledge P. Hubík (IP CAS, Prague, Czech Republic) and E. Gombia (IMEM CNR, Parma, Italy) for helpful collaboration. This work was supported by the Slovak Research and Development Agency under No. APVV-99-P06305.

[1] Dubecký, F., et al.: *NIM A* **576** (2007) 87.

[2] Alietti, M., et al.: *NIM A* **362** (1995) 344.

[3] Dubecký, F., et al.: *NIM A* **576** (2007) 27.

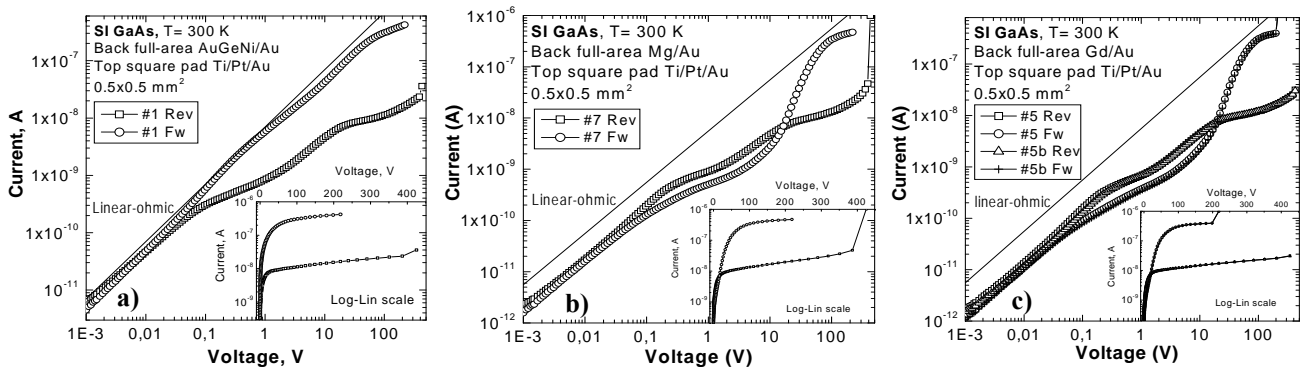


Fig. 1. I - V characteristics of SI GaAs structures in log-log and a log-lin scale (inset): a) Ti/Pt/Au-AuGeNi/Au, b) Ti/Pt/Au-Mg/Au, c) Ti/Pt/Au-Gd/Au.

Basic parameters of a high resolution X-ray system with a microfocus source

D. Korytár, P. Vagovič, F. Dubecký, and P. Boháček

Recent developments of X-ray imaging techniques at synchrotrons such as phase contrast imaging [1,2] present a strong driving force for the development of laboratory X-ray imaging techniques [3]. The brilliance of new microfocus sources combined with suitable source-side optics gives the possibility to transfer some demanding experiments from synchrotrons to laboratories. Concerning detection side, new approaches include single photon counting with semiconductor radiation detectors and so called “colour” imaging allowing evaluation in a pre-selected photon energy window [4]. These new techniques substantially improve overall diagnostic performance of new generation X-ray systems.

Based on our experience in X-ray crystal optics, in semiconductor detectors and in X-ray imaging we are developing a variable X-ray optical bench to study some of these modern imaging techniques.

The enclosed optical bench 2.6 m long contains a vertical stand for a Hamamatsu microfocus X-ray source (L6731-01 type), longitudinal slides for changing geometrical magnification and moving various components, a Newport goniometer to adjust and rotate the object or optics, and another stand for detector slides [5]. The focus size of the X-ray source with a transmission tungsten anode (declared as of 8 μm) has been measured using the technique of imaging a tungsten cross according to EN 12543-3 [6]. At the full power of 80 kV and 100 μA the technique has given focus size of 8.6 μm in horizontal and 6.2 μm in vertical direction.

One of the most important imaging parameters is spatial resolution. A technique using full width at half maximum (FWHM) of the absolute derivative of transmission function of a metal grid has been used for the purpose. See Fig. 1 for more details.

The advantage of contemporary microfocus sources is that some of their parameters are approaching those of

synchrotrons. Longitudinal coherence length $d_l = \lambda^2/2\Delta\lambda$, given by the spectral width $\Delta\lambda/\lambda$ and by the wavelength λ of monochromators is around 0.3 μm for a Si(111) monochromator. Transversal coherence length $d_t = \lambda/2D$, where D is the divergence in a point at the sample given by the ratio of focus size and focus-sample distance, is in our case about 12.5 μm (focus size 8 μm , distance 2 m, wavelength 0.1 nm), which is longer than that for a synchrotron radiation source with 300 μm focus size at the distance of 30 m ($d_t = 5 \mu\text{m}$). Despite the fact that the brilliance of a microfocus source is higher than that of a standard laboratory source, the increase of the coherence length is at the expense of a decrease of the intensity.

To assess the coherence properties of imaging we are simulating the Fraunhofer diffraction at a rectangular aperture using the BESSY raytracing program RAY [7]. Preliminary results show that ripples up to 100 μm distance from the edges are observable.

This work was supported by the Slovak Research and Development Agency under the contracts Nos. APVV-0459-06 and APVV-0713-07 and COST MP0601.

- [1] Cloetens P., et al.: *J. Phys. D: Appl. Phys.* **32** (1999) A145.
- [2] Baruchel J., et al.: *J. Synchrotron Rad.* **7** (2000) 196.
- [3] Davis, T.J., et al.: *Nature* **373** (1995) 595.
- [4] Dubecký F., et al.: *Nucl. Instr. and Meth. in Phys. Res. A* (2009), in print.
- [5] Korytár, D., Dubecký, F., Zaňko, B., Vagovič, P., and Áč, V.: *IEEE Workshop on X-ray Micro Imaging of Materials, Devices, and Organisms. Dresden, 2008, Book of abstracts.*
- [6] *The European Standard EN 12543-5:1999, European Committee for Standardization, CEN, Sept. 1999.*
- [7] Schäfers, F.: *RAY the BESSY raytrace program, ver. 24.5, 2008.*

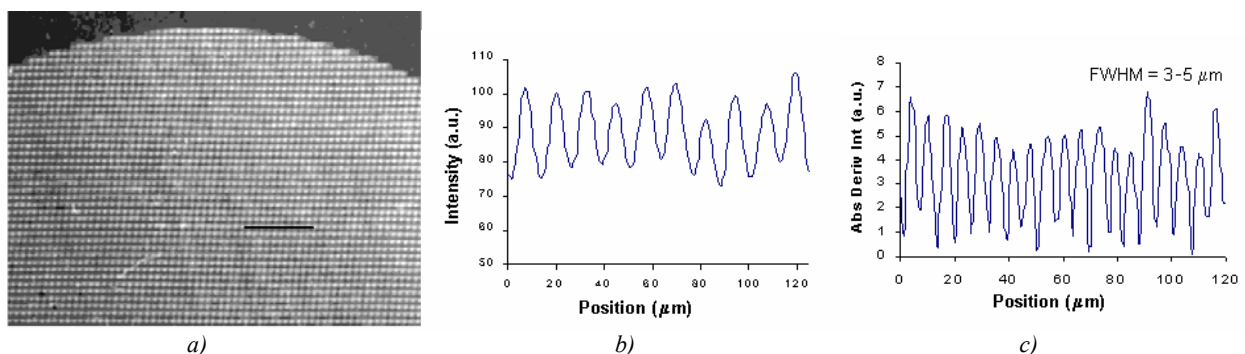


Fig. 1. a) X-ray image of a gold microscopic grid 4-5 μm stripes, 12.5 μm period taken with the geometrical magnification of 17. b) Transmitted intensity function from the black horizontal region indicated in a), c) Absolute value of the first derivative of the transmitted intensity profile and calculated FWHM of 3-5 μm .

Spectral-angular function of X-ray diffractive optics

P. Vagovič and D. Korytár

To design X-ray crystal optical systems, preceding computer analysis and optimization of optical, geometrical features and intensity throughput need to be done. For the spectral angular analysis of coplanar diffractors DuMond diagrams [1] are often used. But they do not take into account the vertical divergence of the incoming radiation and their results are only approximative. Improved method (Apparatus Function) which uses dynamical theory of X-ray diffraction for coplanar 4-bounce diffractors, considering only horizontal divergence, was used by Möller [2], for simulation of diffraction curves from crystal samples. Same approach (transmission function) for estimation of the energy bandwidth and the output divergence of four-bounce monochromator in coplanar plane was used by Toellner et al. [3]. For visualization of the spectral-angular space of coplanar diffractors Xu and Li [4] used modified 3D DuMond diagrams. However, all those approaches use some level of the approximation. We present an improved more general approach which uses two-beam X-ray dynamical theory of diffraction suitable for estimation of spectral and angular properties of the flat X-ray crystal optics. It takes into account both the vertical and the horizontal divergence of incoming beam and directly interconnects input with output divergences of the input and output beam for given successive crystal arrangements in reflection Bragg geometry. Using this

approach we can couple general non-coplanar diffractors and estimate their spectral-angular function (SAF). SAF is the spectral and angular distribution of the diffracted radiation of a given crystal arrangement. In another words we calculate total reflection coefficient of the given optical system as a function of three variables, wavelength, horizontal and vertical (input or output) divergence.

We applied SAF approach to study parameters of the monolithic monochromator [5] which was designed for Co $K\alpha_1$ spectral line. It uses four successive diffractions in Bartels-like configuration (+ n , - n , - m , + m) as is shown in Fig. 1.

Authors acknowledge Petr Mikulík (MU Brno, Czech Republic) for helpful discussions and collaboration on this topic. This work was supported by the Slovak Research and Development Agency through grant No. APVV-0459-06.

- [1] Bartels, W. J.: *J. Vac. Sci. Technol. B* **1** (1983) 338.
- [2] Möller, M. O.: *J. Appl. Cryst.* **27** (1994) 369.
- [3] Toellner, T.S., Alatas, A., Said, A., Shu, D., Sturhahn, W., and Zhao, J.: *J. Synch. Rad.* **13** (2006) 211.
- [4] Xu, S. and Li, R.J.: *Appl. Cryst.* **21** (1994) 213.
- [5] Vagovič, P., Korytár, D., Mikulík, P., and Ferrari, C.: *Nucl. Instr. Meth. in Phys. Res. B* **265** (2007) 599.

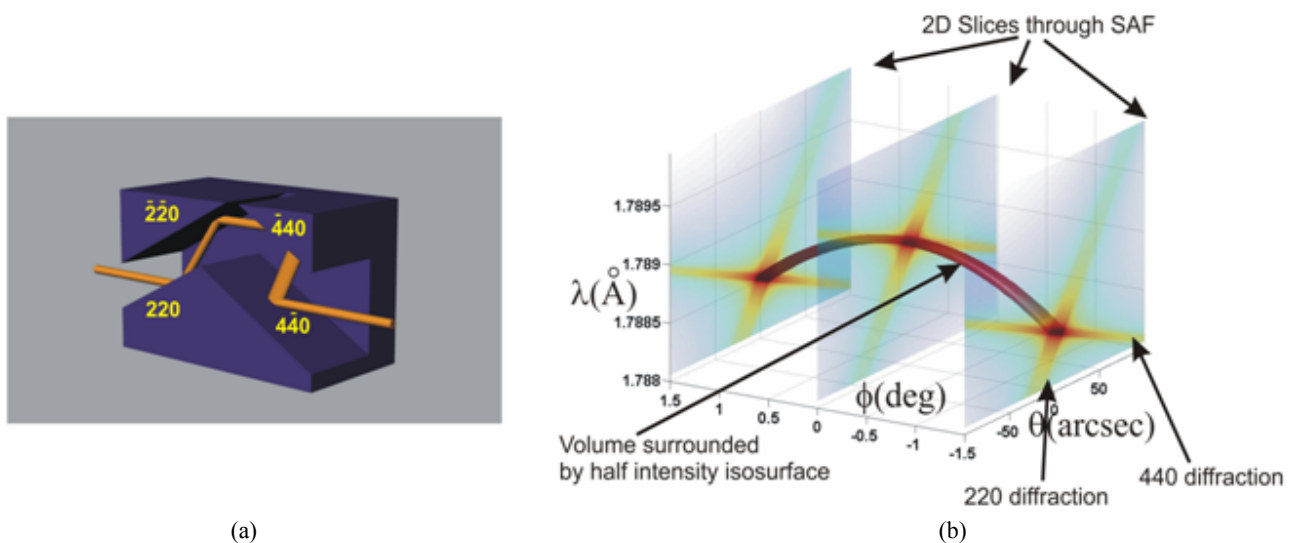


Fig. 1. Small size Ge monolithic X-ray 4-bounce high resolution monochromator (a) and its SAF (b).

Application of semi-insulating GaAs detectors in registration of fast neutrons emissions from hot plasmas

F. Dubecký, B. Zat'ko, P. Boháček, M. Sekáčová, and J. Huran

Semi-insulating (SI) GaAs detectors are proved to be very useful for detection of high-energetic charged particles and photons [1]. The relatively high resistance of bulk SI GaAs to the damage by neutrons and high energy photons predestines SI GaAs to be a perspective candidate for fabrication of *neutron* detectors. SI GaAs-based detectors of thermal as well as fast neutrons were successfully developed [2-4]. The development of SI GaAs fast neutron detector and accompanying electronic circuitry working and the application of the detection system to diagnostics of neutron emitted from hot plasmas are presented.

Detectors were fabricated from bulk vertical gradient freeze SI GaAs. The thickness of both-side polished wafer was about 300 μm , the resistivity $9.5 \times 10^7 \div 1.2 \times 10^8 \Omega\text{cm}$ and the Hall mobility $4990 \div 5120 \text{ cm}^2/\text{Vs}$ (room temperature). Blocking Schottky contact was prepared by evaporation of AuZn eutectic alloy (120 nm), whereas the full area back-side ohmic contact using an AuGeNi eutectic alloy. A large area ($2 \times 2 \text{ mm}^2$) top contact with a guard-ring maximizes the detection efficiency. Four detectors used later in the bridge circuit were glued by the silver epoxy onto a ceramic support and double wire-bonded using Al wire.

Two of four GaAs detectors assigned to registration of neutrons were coated with a converter layer which was a high density polyetylen (HDPE) foil of thickness about 140 μm . In order to improve sensitivity and achieve insensitivity to background X- and γ -rays, differential four-detector configuration was applied where two detectors were coated with the HDPE conversion layer and two other uncoated [5]. Moreover, this configuration could improve compensation of the X-ray flux non-uniformity. The evaluated detector response to the flux of 2.45-MeV neutrons emitted from the Plasma-Focus source applied in our experiment was the only 1.5 mV. The evaluation was made applying the following parameters: i) HDPE thickness 140 μm , ii) two detectors surface $\sim 10 \text{ mm}^2$, iii) load resistance 50 Ω , iv), neutron collision efficiency 0.002 (considering 2.59 barn scattering cross section), v) expected neutron flux 10^{13} n/s cm^2 , average energy transfer to semiconductor 0.3 MeV, vii) mean energy for creation of one electron-hole pair 4.2 eV (GaAs), viii) calculated charge generated per neutron: $2.29 \times 10^{-17} \text{ C}$, and ix) estimated pulse duration 50 ns. Having such a small signal from a detector an amplifier had to be used to extract it from noise existed in this experiment.

The developed system was applied in registration of neutrons emitted by hot plasmas generated in a small Plasma-Focus device, type PF6, installed at the IPPLM Warsaw (shown in Fig. 1a). The measuring system was placed in a shielded box. Examples of signals collected

by a fast oscilloscope are demonstrated in Fig. 1b and Fig. 1c. Detectors configured in the bridge circuit give a negative signal for irradiation by X-rays only (without neutrons) as shown in Fig. 1c which would mean a lack of equilibrium in the bridge. There is no influence of the HDPE converter in this case. This effect, which diminishes the quality of measurement, was possible to eliminate by using a lead shield against X-rays. The results obtained after shielding by the use a thick ($\sim 8 \text{ mm}$) lead plate in the front of detectors show the response from fast neutrons only. In such a case a strong background signal from X-rays was substantially eliminated and correct, positive signal from neutrons is detected (Fig. 1c).

To depress fully the signals from strong X-ray background lead shielding must be used. The use of a thinner SI GaAs base material (not more than 50 μm instead of 300 μm) and a larger area of the Schottky contact would give better conditions for measurement neutrons emitted by hot plasmas. Also applying a better optimized HDPE converter and detector bias would give a higher neutron signal.

This work was supported by the Slovak Research and Development Agency under No. APVV-99-P06305 and project within the EURATOM/CU multilateral FWP7 collaboration.

- [1] Schlessinger, T. E. and James, R. B.: *Semiconductors and Semimetals*, Vol. 43, Academic Press, San Diego (1995).
- [2] McGregor, D., et al.: *Nucl. Instr. and Meth. in Phys. Res. A* **466** (2001) 126.
- [3] Šagátová, A., et al.: *Nucl. Instr. and Meth. in Phys. Res. A* **576** (2007) 56.
- [4] Jakůbek, J., et al.: *Nucl. Instr. and Meth. in Phys. Res. A* **560** (2006) 143.
- [5] Dubecký, F., et al.: *Proc. of the ASDAM'08*, (2008) p. 29.

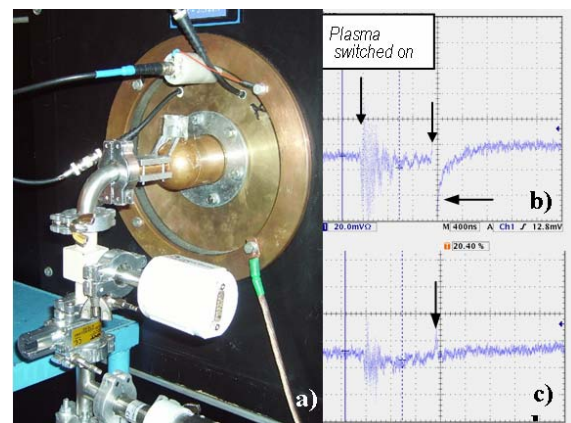


Fig. 1. Picture of the small Plasma-Focus system FP-6 (a), registered mixed signals from X-rays and neutrons (b) and pure positive signal from registered neutrons (c).

Silicon carbon nitride thin films prepared by plasma enhanced chemical vapour deposition

J. Huran and P. Boháček

The deposition of silicon carbon nitride SiCN has been widely studied due to their attractive properties, such as wear resistance, chemically inertness and wide band gap, which provide optical, electronic and other ambient applications. Significant progress in this area has been made due to advancement of the film fabrication technologies, in particular physical vapor deposition (PVD) and chemical vapor deposition (CVD), as well as the characterization technique. Most of the published work devoted to production of SiCN, refer to high temperature deposition processes (CVD). High temperature deposition (typically between 600 and 1200 °C) is a strong limitation for industrial applications. Only few works has been published about the synthesis of Si-C-N at low growth temperatures.

Amorphous silicon carbon nitride films were grown by plasma enhanced chemical vapour deposition (PE CVD) technique. All films were prepared on lightly doped *n*-type Si substrates (111). The films were deposited in a high frequency parallel-plate plasma reactor in which the frequency and the RF power were maintained at 13.56 MHz and 0.06 Wcm⁻², respectively. The flow rates of SiH₄, CH₄ and NH₃ gases were 10 sccm, 20 sccm and 15 sccm, respectively. The deposition temperatures were 250, 350 and 400 °C. The concentration of species in the SiCN films was determined by Rutherford backscattering spectrometry (RBS). Chemical compositions were analyzed by infrared spectroscopy. The IR spectra were measured from 4000 to 400 cm⁻¹. The hydrogen concentration was determined by the elastic recoil detection (ERD) method. For this purpose the ⁴He⁺ ion beam from a Van de Graaff accelerator at JINR Dubna was applied. The energy of 2.4 MeV was chosen.

The target was tilted at an angle of 15 ° with respect to the beam direction and the recoiled protons were

measured in forward direction at an angle of 30 °. For electrical characterization of the SiCN films vertical structures were formed on the prepared SiCN/Si samples. Circular Au dots with a diameter of 0.4 mm and a thickness of 70 nm were evaporated after the cleaning procedure of SiCN surface. Al served as large area back contact to Si substrate.

Figure 1 shows RBS spectra of samples A1, A2 and A3 with different deposition conditions of the deposited amorphous silicon carbon nitride. In the case of samples A1 and A2 the concentration of silicon, carbon and nitrogen are 25, 20 and 35 at. %, respectively. Concentration of Si, C and N in the sample A3 is 25, 22 and 37 at. %, respectively. Hydrogen was detected by means of elastic recoil detection. The ERD analyses (Fig. 2) show that the amount of incorporated H in samples A1 and A2 were 18 at. % and in samples A3 were 17 at. %.

There is no essential difference between the IR spectra of the samples. From current-voltage (*I-V*) characteristics of structure SiCN/Si for all samples we observed dispersion in characteristics that is due to the inhomogeneity of SiCN film parameters. At higher voltages, the current is limited by the series resistance due to ohmic contact and the bulk resistance of SiCN layer. It was found that with increased deposition temperature the conductivity of the amorphous SiCN films was increased from 3.2 × 10⁻¹⁴ S for samples A1 to 8.0 × 10⁻¹⁴ S for samples A3.

We would like to thank to A.P. Kobzev, JINR Dubna, Russia for RBS and ERD measurements. This work was supported by the Slovak Research and Development Agency under the contracts Nos. APVV-0459-06 and APVV-0713-07.

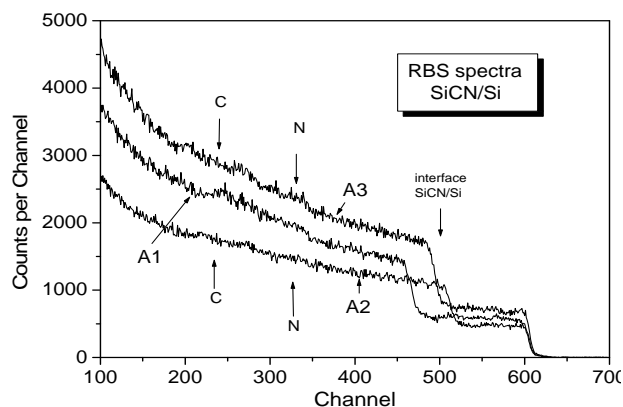


Fig. 1. RBS spectra of SiCN films deposited onto a silicon substrate for 2 MeV alpha particles detected at scattering angle of 170 °. The spectra are for samples A1 (thickness of film 250 nm), A2 (220 nm) and A3 (230 nm).

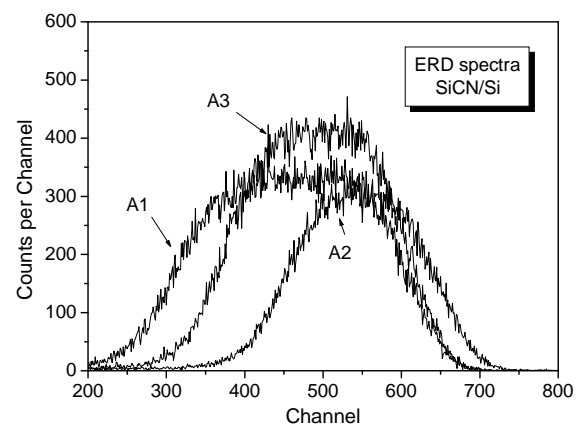


Fig. 2. ERD spectra of recoiled hydrogen obtained with 2.4 MeV ⁴He⁺. The concentration of hydrogen in samples A1 and A2 is 18 at. % and 17 at. % in the sample A3.

Department of Theory of Semiconductor Microstructures

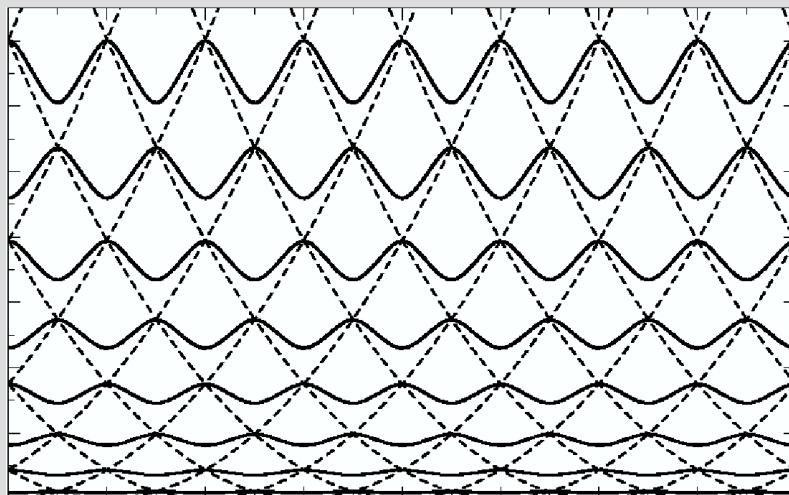
Martin Moško

Research scientists

Andrej Gendiar
Radoslav Németh

PhD students

Roman Krčmár
Juraj Feilhauer



In 2006-2008 the group focused on two topics: 1) Theoretical investigation of persistent current in mesoscopic rings; and 2) Simulation of statistical properties of various spin lattice models with spin-spin interaction. The activities were performed within the projects “*Coherence, decoherence and disorder in metallic and superconducting systems*” and “*Centre of cryophysics and cryonanoelectronics*”, supported by the Science and Technology Assistance Agency, and within the project “*Electron-electron interaction and coherent electron transport in mesoscopic wires and rings*”, supported by the Slovak grant agency VEGA.

Mesoscopic electron transport in thin conducting wires shaped into circular rings with both wire ends tied to each other has been intensively studied in the past twenty years. If a ring circumference is shorter than the coherence length, the ring is referred to as mesoscopic. An external magnetic flux applied through the opening of such a ring gives rise to a persistent equilibrium electron current circulating around the ring circumference.

Although persistent currents were measured in metallic mesoscopic rings twenty years ago, the values measured have not yet been explained theoretically. In a standard Green’s function theory of persistent currents, electrons in a normal metal multi-channel ring are assumed to be scattered by impurity disorder. The resulting current underestimates the measured persistent current by one to two orders of magnitude. More precisely, the measured currents are close to the theoretical value derived for a ballistic (disorder-free) single-channel metallic ring. This observation is surprising because the experimental rings involve several thousand conducting channels and are disordered, which is documented by conductance measurements of the equivalent metallic wires (the mean free path l extracted from the conductance is a hundred times smaller than the ring length L). In our work, we argued that electrons in the experimental rings are scattered by disordered (rough) sample edges rather than by impurity disorder. The fact that a disordered multi-channel ring of length $L/l=100$ supports the ballistic single-channel persistent current was explained as follows. The disordered edges scatter all conduction electrons except for a small number of those moving in parallel with the ring edge (mainly electrons in the lowest energy channel). Such electrons (ideally) avoid any scattering at the disordered edge and carry the single-channel ballistic current.

We also studied the persistent current in a ring made of a perfect crystalline insulator. A standard tight-binding model with nearest-neighbour hopping is known to predict a perfectly zero persistent current if the valence band of the crystal is fully filled and all higher energy bands are empty. In our model, we considered a one-dimensional crystalline ring consisting of one-dimensional “atoms”. To such a ring, we applied a method of localised atomic orbitals. However, we considered that any orbital can overlap with its own tail circulating around the ring. Although the overlap is

exponentially small, it gives rise to a non-zero persistent current despite the valence band being completely filled with the electrons and all higher bands being completely empty. Although the persistent current decays with increasing ring length exponentially, we suggest that it is measurable in rings made of properly chosen materials.

We further studied a one-dimensional ring with an interacting electron gas. We investigated how electron-electron (e-e) interaction influenced the persistent current. One-dimensionality of the electron gas combined with the e-e interaction gives rise to a correlated many-body state known as the Luttinger liquid. Our main goal was to perform a microscopic many-body calculation of the persistent current carried by the Luttinger liquid. We implemented several many-body methods capable of solving the problem numerically. We at first implemented the Hartree-Fock approximation, which ignores many-body correlations except for the Fock exchange. Then we developed the correlated many-body calculations based on a configuration-interaction method and quantum Monte Carlo method. With the methods, we solved the many-body Schrödinger equation for several tens electrons interacting via an exponentially screened electron-electron interaction. We focused on the ring with a single weak link where the Luttinger-liquid state is expected to cause a characteristic (power-law) dependence on the persistent current on the ring length. We reproduced most of the basic features predicted by the Luttinger-liquid and renormalization group models. However, we also found a few novel features related to the fact that our many-body model is continuous, with the single-particle energy dispersion being truly parabolic.

Finally, we studied magnetic properties of the spin models on negatively curved lattices. We developed a numerical algorithm using ideas of the density matrix renormalization group method. The algorithm enabled us to calculate ground-state properties by evaluating thermodynamic functions in the thermodynamic limit to a very high accuracy. Having calculated critical exponents related to a variety of spin systems, we concluded that a hyperbolic deformation of plain lattices resulted in the mean-field universality classification, as the Hausdorff dimension of such a system is infinite. By increasing the number of the spin degrees of freedom, we observed the creation of anomalous Schottky peaks in the specific heat that vanished algebraically towards the quantum XY model limit. We successfully applied the algorithm to frustrated spin systems, in which mutually competing ferromagnetic and antiferromagnetic interactions led to interesting new results: In particular, we found a tri-critical point.

Collaboration:

We cooperated with Professor Indlekofer from the University of Applied Science at Wiesbaden, Germany, Professor Mitas from the North Carolina State University, USA, and Professor Nishino from the Kobe University, Japan.

Martin Moško

Persistent current in mesoscopic multichannel ring with disordered edges

J. Feilhauer and M. Moško

Magnetic flux Φ applied through the opening of the mesoscopic conducting ring gives rise to the equilibrium persistent electron current I circulating along the ring [1]. A single electron at the energy level E_n carries the current $I_n = -\partial E_n(\Phi)/\partial \Phi$. At zero temperature the persistent current in a single ring reads $I = \sum I_n$ where we sum over all occupied electron states up to the Fermi level. The persistent current was observed in the disordered multichannel metallic rings [2] almost twenty years ago, but the measured values have so far not been explained theoretically. In the ensemble of disordered rings the current fluctuates at random from sample to sample. To compare with the measurements of a single ring [1], it is useful to calculate the typical current $I_{typ} = \langle I^2 \rangle^{1/2}$, where $\langle \dots \rangle$ is the ensemble average. A standard Green's function theory of persistent currents [3] assumes that the non-interacting electrons in the normal-metal multichannel ring are scattered by impurity disorder. For the typical current at $\Phi = 0.25h/e$, the Green's function theory gives the result $I_{Green} = 3.2(ev_F/L)(l/L)$, where L is the ring circumference, v_F is the electron Fermi velocity, and l is the electron mean free path. However, the persistent currents measured in the individual gold rings [1] are close to the value $I_0 = ev_F/L$ calculated for the ballistic (disorder-free) single-channel metallic ring. This result is surprising because the experimental rings [2] involve several thousands of conducting channels and the presence of disorder is clearly documented by the conductance measurements of equivalent metallic wires (the mean free path l extracted from the conductance is hundred times smaller than L). In our work we argue, that the electrons in the experimental ring samples are scattered by disordered (rough) sample edges rather than by impurity disorder. Indeed, it has been pointed out [4], that the mean free path l in very thin gold wires remarkably varies (decreases) with decreasing wire thickness. In our opinion, this decrease is consistent with electron scattering due to the disordered sample edges, unavoidably produced by the electron-beam lithography. We calculate the persistent current in a disordered multichannel ring made of the two-dimensional gold conductor

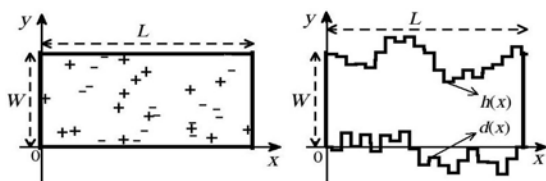


Fig. 1. The sample with impurity disorder (left figure) and the impurity-free sample with disordered edges (right figure), where $d(x)$ and $h(x)$ are the randomly fluctuating y -coordinates of the edge at $y = 0$ and $y = W$, respectively.

of width W and length $L \gg W$. We assume that the mean free path l is limited by two types of disorder (Fig. 1). First, impurity disorder is modeled by the δ -like-potential barriers with random positions and signs. Second, disorder due to the sample-edge roughness is modeled as rectangular steps added or subtracted at random at both sample edges. We simulate [5] transport across disorder by the scattering-matrix method [6,7] combined with searching for the single-electron eigenenergies E_n in the ring. After obtaining the E_n spectrum we obtain the single electron currents I_n and persistent current I . In Fig. 2 we show the resulting I_n and I for a gold ring with $l = L/20$. In the case of impurity disorder, I oscillates close to the theoretical value I_{Green} . However, in the case of disordered sample edges, maximum values of I are close to the ballistic value I_0 , which is consistent with experiment [2]. The fact [2] that a disordered multi-channel ring of length $L/l = 100$ supports the ballistic single-channel persistent current I_0 can be understood as follows. The disordered edges scatter all conduction electrons except for a small part of the electrons moving in parallel with sample edges (mainly the electrons in the lowest energy channel). Due to the parallel motion, these electrons (ideally) avoid any scattering by disordered edges and therefore tend to carry the single-channel ballistic current.

- [1] Imry, Y.: *Introduction to Mesoscopic Physics*, Oxford University Press, Oxford, UK, (2002).
- [2] Chandrasekhar, V., et al.: *Phys. Rev. Lett.* **67** (1991) 3578.
- [3] Cheung, H.F., et al.: *Phys. Rev. Lett.* **62** (1989) 587.
- [4] Mohanty, P., et al.: *Phys. Rev. Lett.* **78** (1997) 3366.
- [5] Feilhauer, J. and Moško, M.: *Physica E* **40** (2008) 1582.
- [6] Torres, J.A., et al.: *J. Phys. Soc. Jpn.* **73** (2004) 2182.
- [7] Cahay, M., et al.: *Phys. Rev. B* **37** (1988) 10125.

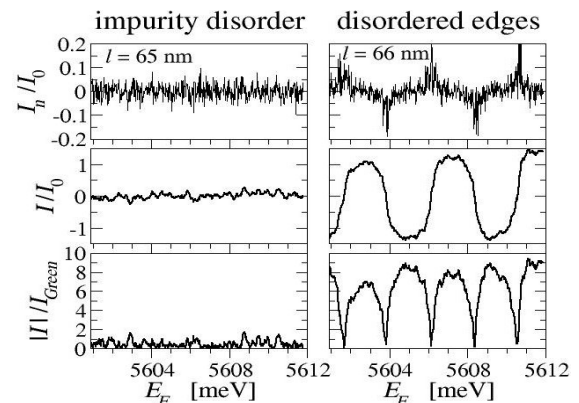


Fig. 2. Persistent current I versus Fermi energy in the disordered ring of length $L = 20l$ and width $W = 20$ nm. The top panels show the single electron current I_n . In the sample with impurity disorder I_n behaves almost chaotically, while in the sample with disordered edges I_n shows regular peaks. A closer inspection shows that these peaks are due to the quasi-ballistic motion in a few lowest energy channels.

Persistent current in a ring made of the perfect crystalline insulator

A. Mořková, M. Mořko, R. Németh, and A. Gendiar

A mesoscopic metallic ring pierced by magnetic flux ϕ is known to support the equilibrium persistent current [1,2]. In our work [3] we proposed possibility of the persistent current in a ring made of the perfect crystalline insulator like for instance the intrinsic silicon crystal. Consider the ring-shaped lattice of one-dimensional (1D) "atoms" in Fig. 1. The electron wave function $\psi(x)$ in such ring obeys the Schrödinger equation

$$\left[-\frac{\hbar^2}{2m} \frac{d^2}{dx^2} + V(x) \right] \psi(x) = E \psi(x) \quad (1)$$

with the cyclic boundary condition [2]

$$\psi(x+L) = \exp(i2\pi\phi/\phi_0) \psi(x), \quad (2)$$

where m is the free electron mass, x is the position along the ring, L is the ring length, $\phi_0 = h/e$ is the flux quantum, and $V(x)$ is the potential of the lattice. The persistent current is $I = -\partial \sum_n E_n(\phi) / \partial \phi$, where $\sum_n E_n$ is the ground-state energy of all N_e electrons in the ring. Solving equation (1) within the lattice model with nearest neighbor hopping one gets [2] for odd N_e the expression

$$I = -\frac{4\pi}{N\phi_0} U \frac{\sin(\pi N_e/N)}{\sin(\pi/N)} \sin\left(\frac{2\pi\phi}{N\phi_0}\right), \quad (3)$$

where U is the hopping amplitude. The persistent current (3) is nonzero in the metal ($N_e < N$) but zero in the insulator ($N_e = N$). To show that the persistent current is nonzero also in the insulator, we proceed as follows [3].

We express $\psi(x)$ via the isolated atomic orbitals. The atomic orbital $\varphi(x)$ and energy E^{at} in a single isolated atom at $x=0$ obey the Schrödinger equation

$$\left[-\frac{\hbar^2}{2m} \frac{d^2}{dx^2} + v(x) \right] \varphi(x) = E^{at} \varphi(x),$$

where $v(x)$ is the atomic potential - the same potential well as in Fig.1 but with the infinitely thick barriers. We notice that in the multi-atom ring of Fig. 1 the cyclic condition (2) holds together with the Bloch condition

$$\psi(x+a) = e^{(ika)} \psi(x). \quad (4)$$

We also note that the ring potential in Fig. 1 is formally

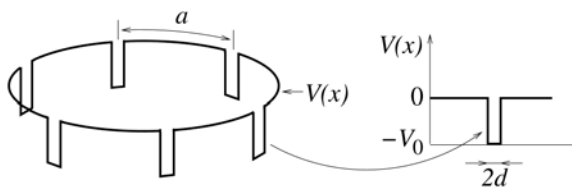


Fig. 1. Potential $V(x)$ in a ring-shaped periodic 1D lattice of atoms modeled by one-dimensional potential wells of width $2d$ and depth V_0 . The lattice period is a . The ring circumference is $L=Na$, where N is the number of atoms.

tractable as an infinite lattice potential with period a , given as $V(x) = \sum_{j=-\infty}^{\infty} v(x-ja)$. We expand $\psi(x)$ as

$$\psi_k(x) = \sum_{j=-\infty}^{\infty} e^{ikja} \varphi(x-ja). \quad (5)$$

Expansion (5) obeys the boundary conditions (2) and (4) for $k=(2\pi/Na)(\phi/\phi_0+n)$, where n is the integer. Using equation (5) we express $E_n = \langle \psi_{kn} | H | \psi_{kn} \rangle / \langle \psi_{kn} | \psi_{kn} \rangle$ as [3]

$$E_n = E^{at} - \gamma_0 - 2 \sum_{\Delta_j=1}^{\infty} \gamma_{\Delta_j} \cos(k_n \Delta_j a) \quad (6)$$

where $\gamma_{\Delta_j} = -\int_{-\infty}^{\infty} \varphi(x-\Delta_j a) [V(x)-v(x)] \varphi(x) dx$ is

the overlap integral, $\gamma_{-\Delta_j} = \gamma_{\Delta_j}$, and $\langle \psi_{kn} | \psi_{kn} \rangle \approx N$. We

set (6) into the single electron current $I_n = -\partial E_n / \partial \phi$. Then we sum $I = \sum_n I_n$ over $n=0, \pm 1, \pm 2, \dots, \pm(N_e-1)/2$ assuming odd N_e and spinless electron system. For $N_e=N$ we obtain the persistent current in the insulating 1D ring [3],

$$I = -(4\pi/\phi_0) N \gamma_N \sin(2\pi\phi/\phi_0). \quad (7)$$

We note that if we keep in (6) only the term with $\Delta_j=1$, the sum $I = \sum_n I_n$ gives the standard formula (3).

Figure 2 shows the persistent current (7) as a function of L . It decays with L exponentially and even the largest considered L is not feasible by present nanotechnology. However, our 1D atom based model is a minimum model. It shows that the persistent current in the insulator exists but it underestimates the effect. For realistic 3D insulators we expect larger persistent currents and technologically feasible sample sizes. In [4] we also proposed another possibility - an artificial insulating 1D ring prepared by applying an external periodic potential to the conducting 1D ring. It shows the nonzero persistent current as well.

We thank for the APVV grant APVV-51-003505.

- [1] Lévy, L. P., et al.: *Phys. Rev. Lett.* **64** (1990) 2074.
- [2] Cheung, H.F., et al.: *Phys. Rev. B* **37** (1988) 6050.
- [3] Mořková, A., Mořko, M., and Gendiar, A.: *Physica E* **40** (2008) 1991.
- [4] Németh, R. and Mořko, M.: *Physica E* **40** (2008) 1498.

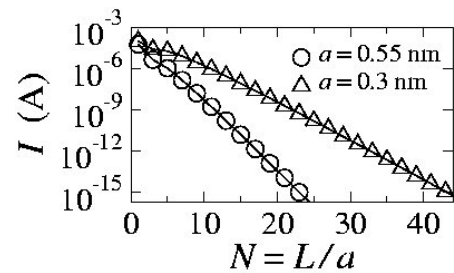


Fig. 2. Persistent current I versus ring length L for the 1D ring made of the perfect crystalline insulator.

Luttinger liquid and persistent current in continuous mesoscopic ring with weak link

M. Moško, R. Németh, R. Krčmár, and A. Gendiar

The electron-electron (e-e) interaction causes that the one-dimensional (1D) electron gas in a clean 1D wire away from the charge-density-wave instability is a Luttinger liquid [1]. The Luttinger-liquid state affects the electron conductance already when the wire contains a single scatterer. For non-interacting electrons the conductance is $(2e^2/h)|t_{kF}|^2$, where t_{kF} is the transmission amplitude through the scatterer and k_F is the Fermi wave vector [2]. For the Luttinger liquid, the conductance of the infinite wire with a single impurity or weak link varies with temperature as $\propto T^{2\alpha}$, where α depends only on the e-e interaction [3,4]. For $\alpha > 0$ (repulsive interaction) such wire is impenetrable at $T = 0$ K regardless of the strength of the scatterer. If $T = 0$ K and the wire length (L) is finite, the conductance shows the power law $\propto L^{-2\alpha}$. These power laws are a sign of the Luttinger liquid. A similar power law results for interacting electrons in a mesoscopic ring. Magnetic flux piercing the opening of the isolated ring gives rise to the persistent electron current [2]. For the interacting spinless electrons in the 1D ring containing a single weak link with transmission probability $|\tilde{t}_{kF}|^2$, it can be shown by combining the Luttinger-liquid [5] and renormalisation-group (RG) [6] models, that the persistent current at $T = 0$ K depends on the magnetic flux ϕ and ring length L as [5]

$$I \propto (ev_F / 2L) |\tilde{t}_{kF}| (L/d)^{-\alpha} \sin(2\pi\phi / \phi_0). \quad (1)$$

where $\phi_0 = h/e$, v_F is the Fermi velocity, and d is the range of the pair electron-electron interaction $V(x-x')$. As to the power α for weak e-e interaction ($\alpha_{RG} \ll 1$) the RG theory expresses α by means of the expression

$$\alpha_{RG} \equiv [V(0) - V(2k_F)] / 2\pi\hbar v_F, \quad (2)$$

where $V(q)$ is the Fourier transform of $V(x-x')$. For strong interaction (say $\alpha_{RG} = 0.5$) the theory [1,7] gives

$$\alpha = (1 + 2\alpha_{RG})^{1/2} - 1. \quad (3)$$

In our works [8,9] we analyzed the circular 1D ring of length L threaded by magnetic flux ϕ , with N spinless electrons interacting via the screened pair interaction

$$V(x-x') = V_0 \exp(-|x-x'|/d). \quad (4)$$

The ring was assumed to contain a single weak link modeled by the single-particle potential $\gamma\delta(x)$. By applying numerical microscopic methods, we solved the continuous N -electron Schrödinger equation

$$\hat{H} \Psi(x_1, x_2, \dots, x_N) = E \Psi(x_1, x_2, \dots, x_N), \quad (5)$$

where \hat{H} is the many-body Hamiltonian of the system and the wave function ψ obeys the cyclic boundary condition $\psi(x_1, \dots, x_i + L, \dots, x_N) = \psi(x_1, \dots, x_i, \dots, x_N)$. In turn, we calculated the persistent current at $T = 0$ K,

$$I = \langle \Psi_0 | \hat{I} | \Psi_0 \rangle, \quad (6)$$

where $\hat{I} = -(e/mL) \sum_{j=1}^N [(\hbar/i)(\partial/\partial x_j) + (e\phi L)]$ is the current operator and $\psi_0(x_1, x_2, \dots, x_N)$ is the ground-state wave function. We solved [8,9] the equation (5) by means of the configuration-interaction method and quantum Monte Carlo method, both of them providing a fully correlated many-body solution.

Our motivation was to verify the formulae (1), (2) and (3). Our major result was, that for $d < 1/2k_F$ the persistent current exhibits the asymptotic (large N) dependence

$$I = C \frac{ev_F}{2L} \frac{|\tilde{t}_{kF}|}{|\tilde{t}_{kF}|} N^{-\alpha} \sin(2\pi\phi / \phi_0), \quad \alpha > 0, \quad (7)$$

where N/L is a fixed density, $C = 1 + 1.66\alpha$, and α agrees with the formulae (2) and (3). The formula (7) shows the power law $LI/ev_F \propto N^{-\alpha}$, which depends on a single interaction parameter (α), while the formula (1) exhibits the power law $LI/ev_F \propto (L/d)^{-\alpha}$, which depends on both α and d . For $d > 1/2k_F$ we found the power laws depending on α and d , but α was not given by the formulae (2) and (3). We ascribed these distinctions to the fact that in our many-body model the single-particle energy dispersion is truly parabolic while in the Luttinger-liquid and RG models the dispersion is linearized. The linear energy dispersion is typical for carbon nanotubes [4] while the power law $N^{-\alpha}$ might be observable in the GaAs 1D systems where the dispersion is parabolic.

We also applied [8] the Hartree-Fock approximation, which ignores correlations except for the Fock exchange. Instead of the power law $N^{-\alpha}$, we found exponential decay of the current with N .

This work was performed in collaboration with K. M. Indlekofer and L. Mitás. We acknowledge support by the grants APVV-51-003505, VVCE-0058-07, and VEGA-2/6101/27.

- [1] Voit, J.: *Rep. Prog. Phys.* **57** (1994) 977.
- [2] Imry, Y.: *Introduction to Mesoscopic Physics*, Oxford University Press, Oxford, UK, 2002.
- [3] Kane, C.L. and Fisher, M.P. A.: *Phys. Rev. Lett.* **68** (1992) 1220.
- [4] Yao, Z., et al.: *Nature* **402** (1999) 273.
- [5] Gogolin, A. and Prokofev, N.: *Phys. Rev. B* **50** (1994) 4921.
- [6] Matveev, K.A., et al.: *Phys. Rev. Lett.* **71** (1993) 3351.
- [7] Polyakov, D.G. and Gornyi, L.I.: *Phys. Rev. B* **68** (2003) 035421.
- [8] Németh, R., et al.: *arXiv:0902.2225* (2009).
- [9] Moško, M., et al.: *submitted to Phys. Rev. B*.

A new algorithm based on renormalization group study for negatively curved lattices

R. Krčmár and A. Gendiar

Classification of various quantum-mechanical systems into universality classes helps in recognizing properties of the systems around their phase transitions. If significantly different systems belong to the same universality class, it is, of course, advantageous to study the simplest case, rather than to treat a complicated Hamiltonian of a fluid, for instance. It is also known that there exists a critical dimension above which all systems satisfy the so-called mean-field universality. We studied infinitely large two-dimensional spin models mapped onto lattices in a curved space which is characteristic for its constant and negative curvature. We call them the hyperbolic lattices. The corresponding Hausdorff dimension of such hyperbolic lattices is infinite, and for this reason, Poincaré disk representation is a useful scheme to visualize the lattice through a simple transformation into a circle of the unity radius, c.f. Fig. 1. The circumference of the circle represents the boundary of the infinitely large lattice.

Figure 1 shows the case in which the whole lattice is build out of tessellation of regular pentagons with the coordination number four (the four pentagons share the same lattice site). It is useful to describe a hyperbolic lattice by two numbers (p, q) , where the two variables correspond to the number of sides p in a polygon and to the coordination number q . The open circles denote the lattice sites where one can place an electron spin σ and study thermodynamic properties of the magnetic systems, for instance, using the Ising Hamiltonian

$$H = -J \sum_{\{i,j\}} \sigma_i \sigma_j - h \sum_{\{i\}} \sigma_i.$$

The overlap integral J describes ferromagnetic ($J > 0$) or anti-ferromagnetic ($J < 0$) spin coupling and h stands for an external magnetic field interacting with the spins. The phase transition is known to appear at non-zero critical

temperature T_c . The thermodynamic functions are related to calculation of the partition function $Z = Tr \exp(-H/k_B T)$. The two thick lines (geodesics) in Fig. 1 divide the system into four equivalent subsystems which simplifies our task.

In order to accomplish this, we developed a new, numerically highly accurate, algorithm [1] based on ideas of the density matrix renormalization group method [2]. The algorithm enables us to study phase transitions in various hyperbolic lattices $p \geq 4$ at fixed $q = 4$. Note that, the Bethe lattice can be treated as well and is related to the case if $p = \infty$ as shown in Fig. 2. We calculated the critical temperatures T_c in the model and found that with increasing p , quite fast convergence of the critical temperature towards the analytically known value in the Bethe lattice $T_c = 2/\ln 2$ was observed [3]. We also obtained the critical exponents $\alpha = 0$, $\beta = 1/2$, and $\delta = 3$ for the Ising model on hyperbolic lattices ($p \geq 5, 4$). Notice that the critical exponents α , β , and δ are related to singular behaviour of the specific heat, spontaneous magnetization and induced magnetization, respectively. We concluded unambiguously that the Ising model on the hyperbolic lattices belongs to the mean-field universality class. Our results were also compared to the known case of the Ising model on the Euclidean square lattice $(4, 4)$ resulting in the well-known magnetic exponent $\beta = 1/8$.

This work was carried out in collaboration with Prof. Nishino (Kobe University, Japan). The partial support of VEGA grant No. 2/6101/27 and APVV grant No. APVV-51-003505 is acknowledged.

- [1] Ueda, K., Krčmár, R., Gendiar, A., and Nishino, T.: *J. Phys. Soc. Jpn.* **76** (2007) 084004.
- [2] Schollwöck, U.: *Rev. Mod. Phys.* **77** (2005) 259.
- [3] Krčmár, R., Gendiar, A., Ueda, K., and Nishino, T.: *J. Phys. A: Math. Theor.* **41** (2008) 125001.

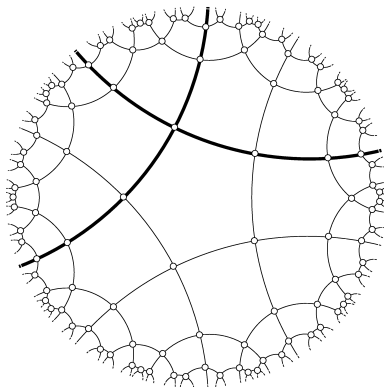


Fig. 1. Regular spin lattice on the hyperbolic plane $(5, 4)$ in Poincaré disk representation.

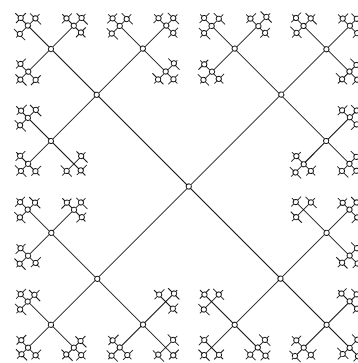


Fig. 2. Bethe lattice with the coordination number $q=4$ corresponds to the notation $(\infty, 4)$.

Determination of the tri-critical point and phase transition classification on hyperbolic lattices

R. Krčmár and A. Gendiar

Magnetic properties of frustrated spin systems have attracted interest of theoretical physicists for several decades. In this work we address the problem of mutually competing ferromagnetic and anti-ferromagnetic coupling in the J_1 - J_2 Ising model with Hamiltonian written as

$$H = -J_1 \sum_{\langle i,j \rangle = NN} \sigma_i \sigma_j + J_2 \sum_{\langle i,k \rangle = NNN} \sigma_i \sigma_k + h \sum_{\langle i \rangle} \sigma_i$$

with the nearest-neighbor ferromagnetic coupling (J_1), the next-nearest-neighbour anti-ferromagnetic coupling (J_2), and the external magnetic field h . The model is defined on a hyperbolic lattice (5, 4) which is made of pentagons with the coordination number four. The next-nearest-neighbour interactions require additional five interactions to be considered within each pentagon.

We applied a recently developed numerical method, the corner transfer matrix renormalization group [1], to study the phase transition of the model in detail. The resulting phase diagram is depicted in Fig. 1 and contains three phases [2]: the ferromagnetic at low temperatures T and at the frustration parameter $\kappa = J_2/J_1 < 1/4$, the anti-ferromagnetic at $\kappa > 1/4$ and low T , and finally the paramagnetic at high T . In this analysis, we focused on the region $\kappa < 1/4$ where the second order phase transition between the ferromagnetic and paramagnetic phases is known to be present in the flat (Euclidean) square lattices (4, 4). This scenario is, however, violated if the model is defined on hyperbolic lattices resulting in the existence of the tri-critical point along the phase transition line. This point separates the second order phase transition at lower κ from the first order transition at higher κ . We located the tri-critical point at $\kappa_c = 0.203$ as indicated by the open circle in Fig. 1.

We analyzed the tri-criticality by mean-field theory

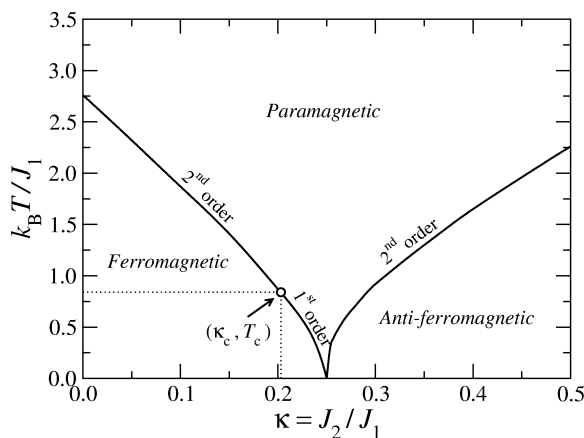


Fig. 1. Phase diagram of the J_1 - J_2 Ising model on the (5, 4) hyperbolic lattice. The tri-critical point is denoted by the open circle at $\kappa_c = 0.203$.

both on the pentagonal (5, 4) and Bethe (∞ , 4) lattices and found that the observed tri-critical behaviour around κ_c could be described by the Landau free energy [2]

$$F(M, T) = aM^6 + b(\kappa_c - \kappa)M^4 + c(T - T_c)M^2.$$

At the tri-critical point, we calculated the related critical exponents $\alpha = 1/2$, $\beta = 1/4$, and $\delta \approx 7$ which are well-understood by the above formula except for the case when the external magnetic field h is applied.

Another interesting problem was solved on the (5,4) lattice where we studied the spin system by a subsequent increase of the number of spin degrees of freedom [3].

The system is described by the N -state clock model

$$H = -J \sum_{\langle i,j \rangle} \cos[2\pi(\xi_i - \xi_j)/N],$$

where the spin variable ξ has N degrees of freedom, $\xi = 0, 1, \dots, N-1$. If $N = 2$, the Ising model is resulted. The first order phase transition is found for $N = 3$. Schottky peaks in the specific heat arise if $N \geq 5$ as shown in Fig. 2 (the inset shows the case of $N = 10$). We found a scaling formula showing that temperature maxima of Schottky peak vanish as N^{-2} . We found no indication for the Kosterlitz-Thouless phase transition in the model.

We acknowledge support of grants VEGA 2/6101/27, APVV-51-003505, and AvH foundation. Prof. Tomotoshi Nishino from Kobe University, Japan collaborated in this work.

- [1] Ueda, K., Krčmár, R., Gendiar, A., and Nishino, T.: *J. Phys. Soc. Jpn.* **76** (2007) 084004.
- [2] Krčmár, R., Ihagari, T., Gendiar, A., and Nishino, T.: *Phys. Rev. E* **78** (2008) 061119.
- [3] Gendiar, A., Krčmár, R., Ueda, K., and Nishino, T.: *Phys. Rev. E* **77** (2008) 041123.

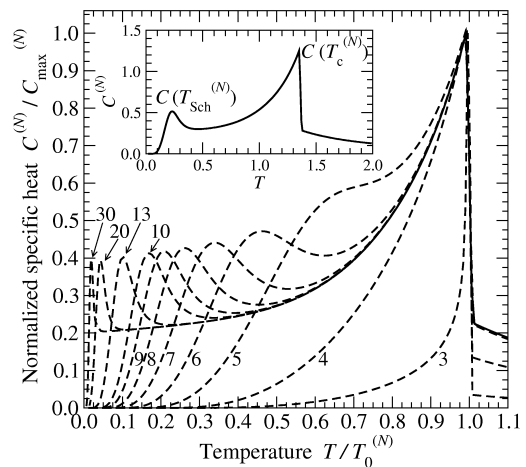


Fig. 2. Specific heat exhibits two maxima: the first one is related to the Schottky peak (left) whereas the second one corresponds to the phase transition (right).

III Projects

National projects

Project	Agency	Responsible	Duration
Centre of electronic and electrotechnique advanced devices - CENG	Centre of Excellence SAS	Dr. F. Gömöry	2005 - 2008
Centre of nanostructured materials - NANOSMART	Centre of Excellence SAS	Dr. I. Vávra	2007 - 2011
Educational Centre for Information Technology and Power Engineering - VCITE	EC - ESF & Ministry of Education SR	Dr. V. Cambel	2005 - 2008
Establishment of research-development and innovative network for materials and technology of their combination - MatNet	EC - ESF & Ministry of Education SR	Dr. K. Fröhlich	2005 - 2008
Gas sensing microsystem based on GaAs microstructures	VEGA	Dr. J. Huran	2004 - 2007
Thin films and structures perspective for electronics	VEGA	Dr. Š. Chromik	2005 - 2007
Superconducting MgB ₂ wires with artificial pinning centers	VEGA	Dr. P. Kováč	2005 - 2007
Temperature aspects of dissipative processes in high T _c superconductors YBCO and BSCCO-2223	VEGA	Dr. P. Ušák	2005 - 2007
Nanocrystalline thin layer structures for sensors and microsystem techniques	VEGA	Dr. J. Huran	2006 - 2008
Electron-electron interaction and coherent electron transport in mesoscopic wires and rings	VEGA	Dr. M. Moško	2006 - 2008
Nanocomposite thin films and coatings	VEGA	Dr. I. Vávra	2006 - 2008
Influence of passivation on the properties of AlGaIn/GaN HEMT's	VEGA	Dr. D. Gregušová	2006 - 2008
Nanodimension and its influence on properties of MOVPE semiconductor layers and structures	VEGA	Dr. J. Novák	2006 - 2008
Micro(nano)electromechanical structures for new generation of electronic, sensoric and detection devices	VEGA	Dr. T. Lalinský	2006 - 2008
The effect of magnetic field on the properties of superconductors with ac transport current	VEGA	Dr. S. Takács	2006 - 2008
Josephson effects in structures from unconventional superconductors	VEGA	Dr. V. Štrbik	2007 - 2009
Neutron detectors: technology of preparation, study of electrical and detection performances	VEGA	Dr. F. Dubecký	2007 - 2009
Perspective thin films and structures for cryoelectronics on semiconducting substrates	VEGA	Dr. Š. Chromik	2008 - 2010
Microstructure of very thin films for advanced microelectronics	VEGA	Dr. K. Fröhlich	2008 - 2010
Integrated MEMS sensors based on magnetoresistive thin films	APVT	Dr. P. Lobotka	2004 - 2007
Gas-sensitive microsystem based on GaAs micromechanical structures	APVT	Dr. T. Lalinský	2004 - 2007
Thin oxide films for advanced MOS structures	APVT	Dr. K. Fröhlich	2005 - 2007
Monolithically integrated microsystem for gas detection based on GaAs micromechanical structures	APVT	Dr. T. Lalinský	2005 - 2007

Preparation of high quality GaMnN thin layers for spintronics	APVT	Dr. J. Novák	2005 - 2007
A new generation digital radiology system kit	APVT	Dr. F. Dubecký	2005 - 2009
Electro-thermal converter monolithically integrated with HEMT-SAW chemical sensors	APVV	Dr. T. Lalinský	2006 - 2007
Superconductors for future technologies	APVV	Dr. Š. Haščík	2004 - 2007
Superconducting wires in the conditions of power electric devices	APVV	Dr. F. Gömöry	2006 - 2009
Pinning in the new types of superconducting wires	APVV	Dr. F. Gömöry	2006 - 2009
Monolithically integrated circuits based on GaAs (GaN) with passive superconducting filters for millimeter wave band	APVV	Dr. Š. Chromik	2006 - 2009
The study of electric current distribution processes in superconducting conductors at DC and AC applications	APVV	Dr. P. Ušák	2006 - 2009
Preparation of "active" tips for probe microscopy by MOCVD	APVV	Dr. V. Cambel	2006 - 2010
Coherence, decoherence and disorder in metallic and superconducting systems	APVV	Dr. M. Moško	2006 - 2009
Selected topics from X-ray technologies	APVV	Dr. D. Korytár	2007 - 2009
Thin oxide films for GaN heterostructures	APVV	Dr. K. Fröhlich	2007 - 2008
Centre of cryophysics and cryonanoelectronics	APVV	Dr. V. Cambel	2008 - 2011
Centre of Excellence in nano-/micro-electronic, optoelectronic and sensoric technologies	APVV	Dr. J. Novák	2008 - 2011
Transport and microwave characteristics of magnesium diboride, a novel superconducting material for practical applications	APVV	Dr. Š. Chromik	2008 - 2009
Electromagnetic properties of composite tapes superconductor-ferromagnetic	APVV	Dr. J. Šouc	2008 - 2009
Research work on formation and properties of pyrolytic boron nitride	APVV	Dr. J. Novák	2008 - 2009
Structure metal-insulator-metal for nanoscale DRAM memories	APVV	Dr. K. Fröhlich	2008 - 2010
Technology and characterization of modern semiconductor thin films for microelectronics and optoelectronics	APVV	Dr. J. Huran	2008 - 2010
High temperature superconducting films and structures for microwave	APVV	Dr. Š. Chromik	2008 - 2010
Advanced MEMS chemical sensors for extreme conditions	APVV	Dr. T. Lalinský	2008 - 2010
Carbon nanocomposites for chemical sensing	APVV	Dr. P. Lobotka	2008 - 2010
Epi-ready substrates VGF GaP (S)	APVV	Dr. J. Novák	2008 - 2010
Advanced filamentary composite MgB ₂ superconductors	APVV	Dr. P. Kováč	2008 - 2010

International projects

Project	Type	Agency	Responsible	Duration
Superconducting coated conductor cable – SUPER3C	STREP	EC, 6 th Framework Programme	Dr. F. Gömöry	2004 - 2008
Nano-and micro-scale engineering of higher-performance MgB ₂ composite superconductors for macro-scale applications - HIPERMAG	STREP	EC, 6 th Framework Programme	Dr. P. Kováč	2004 - 2008
InAlN/(In)GaN Heterostructure Technology for Ultra-high Power Microwave Transistor - ULTRAGAN	STREP	EC, 6 th Framework Programme	Dr. K. Fröhlich	2005 - 2008
AC losses measurements on high temperature superconductors	CSA	EC, 6 th Framework Programme	Dr. F. Gömöry	2005 - 2008
Nano-Engineering Superconductors for Power Applications - NESPA	Training Network	EC, 6 th Framework Programme	Dr. F. Gömöry	2006 - 2010
Materials for Robust Gallium Nitride - MoRGaN		EC, 7 th Framework Programme	Dr. K. Fröhlich	2008-2011
Theoretical and experimental study and technology of plasma diagnostic sensors		EC, 7 th Framework Programme	Dr. F. Dubecký	2008-2011
Development qualification of HTSC conductors for fusion magnets		EC, 7 th Framework Programme	Dr. F. Gömöry	2008-2011
Arrays of quantum dots and Josephson junctions (AQDJJ)	Network	European Science Foundation	Dr. Š. Beňačka	2004 - 2009
Nanoscience and engineering in superconductivity		European Science Foundation	Dr. Š. Chromik	2007 - 2012
VGF GaP based optics for infrared sensors		EUREKA	Dr. J. Novák	2007-2010
Thin films for novel oxide devices - THIOX	Network	European Science Foundation	Dr. K. Fröhlich	2003 - 2007
Short wavelength laboratory sources		COST	Dr. D. Korytár	2007-2011
Superconducting coils for AC currents using YBCO coated conductors		European Office of Aerospace Research Development (EOARD)	Dr. M. Polák	2005 - 2007
Nuclear physics – fundamental and applied investigation		JINR	Dr. D. Machajdík	2004-2007

IV Invited presentations

Invited presentations at international conferences

Gömöry, F., Vojenčiak, M., Pardo, E., and Šouc, J.: Influence of ferromagnetic substrate on the properties of coated conductor. In: International Workshop on Coated Conductors for Applications - CCA 2008. Houston 2008.

Gömöry, F., Vojenčiak, M., Pardo, E., and Šouc, J.: Magnetic flux penetration and AC loss in a composite superconducting wire with ferromagnetic parts. In: International Conference on Superconductivity and Magnetism - ICSM 2008. Side (Turecko) 2008.

Chromik, Š.: Perovskite YBCO and LSMO films on advanced semiconducting substrates. In: 6th International Conference Solid State Surfaces and Interfaces 2008, Smolenice.

Kuzmik, J.: Advances and prospects of InAlN/GaN HEMTs. In: 17th International Workshop on Heterostructure Technology. Venice 2008.

V Publications

2007

Boháček, P., Dubecký, F., and Sekáčová, M.: *Simulation of the reverse I-V characteristics of the Schottky barrier radiation detector structures prepared on semi-insulating GaAs*, *Semicond. Sci Technol.* **22** (2007) 763-768.

Cambel, V. and Šoltýs, J.: *The role of surface-layer conductivity in local anodic oxidation by AFM tip*, *J. Applied Phys.* **102** (2007) art.no. 074315.

Bartolome, E., Pavau, A., Guitierrez, J., Granados, X., Pomar, A., Puig, T., Obradors, X., **Cambel, V., Šoltýs, J., Gregušová, D.,** Chen, D.-X., and Sanchez, A.: *Artificial magnetic granularity effects on patterned epitaxial $YBa_2Cu_3O_{7-x}$ thin films*, *Phys. Rev. B* **76** (2007) art. no. 094508.

Cambel, V., Martaus, J., Šoltýs, J., Kúdela, R., and Gregušová, D.: *AFM nanooxidation process – technology perspective for mesoscopic structures*, *Surface Sci.* **601** (2007) 2717-2723.

Cambel, V., Karapetrov, G., Novosad, V., Bartolome, E., Gregušová, D., Fedor, J., Kúdela, R., and Šoltýs, J.: *Novel Hall sensors developed for magnetic field imaging systems*, *J. Magnetism Magn. Mater.* **316** (2007) 232-235.

Bartolome, E., Navau, C., Sanchez, A., Chen, D.-X., Puig, T., Obradors, X., and **Cambel, V.:** *Imaging current percolation and ac losses in artificially granular YBCO thin films*, *IEEE Trans. Applied Supercond.* **17** (2007) 3223-3226.

Aboľshev, A., Aboľsheva, I., Gierlowski, P., Lewandowski, S.J., Konczykowski, M., Rizza, G., and **Chromik, Š.:** *Effect of pulsed UV laser irradiation on the properties of crystalline $YBa_2Cu_3O_{7-\delta}$ thin films*, *Supercond. Sci Technol.* **20** (2007) 433-440.

Li, X., Khafizov, M., **Chromik, Š., Valeriánová, M., Štrbik, V.,** Odier, P., and Sobolewski, R.: *Ultrafast photoresponse dynamics of current-biased Hg-Ba-Ca-Cu-O superconducting microbridges*, *IEEE Trans. Applied Supercond.* **17** (2007) 3648-3651.

Čičo, K., Kuzmík, J., Gregušová, D., Stoklas, R., Lalinský, T., Georgakilas, A., Pogany, D., and **Fröhlich, K.:** *Optimization and performance of Al_2O_3/GaN metal-oxide-semiconductor structures*, *Microelectr. Reliability* **47** (2007) 790-793.

Demenčík, E., Ušák, P., Takács, S., Vávra, I., Polák, M., Levin, G.A., and Barnes, P.N.: *Visualization of coupling current paths in striated YBCO-coated conductors at frequencies up to 400 Hz*, *Supercond. Sci Technol.* **20** (2007) 87-91.

Demenčík, E., Ušák, P., and Polák, M.: *Hall probe based system for study of AC transport current distribution in YBCO coated conductors at frequencies up to 700Hz*, *IEEE Trans. Applied Supercond.* **17** (2007) 3175-3178.

Dubecký, F., Ferrari, C., Korytár, D., Gombia, E., and Nečas, V.: *Performance of semi-insulating GaAs-based radiation detectors: Role of key physical parameters of base materials*, *Nuclear Instr. and Methods in Phys. Res. A* **576** (2007) 27-31.

Šagátová-Perďochová, A., **Dubecký, F., Zaťko, B.,** Chodák, I., Ladzianský, M., and Nečas, V.: *Detectors of fast neutrons based on semi-insulating GaAs with neutron converter layers*, *Nuclear Instr. and Methods in Phys. Res. A* **576** (2007) 56-69.

Dubecký, F. and Nečas, V.: *Study of radiation detectors based on semi-insulating GaAs and InP: aspects of material and electrode technology*, *Proc. SPIE* **6706** (2007) 67061D.

Dubecký, F., Boháček, P., Sekáčová, M., Zaťko, B., Lalinský, T., Linhart, V., Šagátová-Perďochová, A., Mudroň, J., and Pospíšil, S.: *Role of electrode metallization in performance of semi-insulating GaAs radiation detectors*, *Nuclear Instr. and Methods in Phys. Res. A* **576** (2007) 87-89.

Dujavová, A., Valeriánová, M., Štrbik, V., Matkovičová, Z., Plesch, G., and Kostič, I.: *Influence of the reaction conditions on the formation of Tl(Re)-Ba-Ca-Cu-O superconducting thin films by thallination in open system*, *Central European J. Phys.* **5** (2007) 229-235.

- Eliáš, P., Šoltýs, J., and Kostič, I.:** *Study of ordinary facets revealed in (100) InP by etching in HCl*, Mater. Sci Engn. B **138** (2007) 172-179.
- Gömöry, F., Šouc, J., Vojenčiak, M., and Klinčok, B.:** *Phenomenological description of flux pinning in non-uniform high-temperature superconductors in magnetic fields lower than self-field*, Supercond. Sci Technol. **20** (2007) S271-S277.
- Rostila, L.J., Lehtonen, J.R., Masti, M.J., Mikkonen, R., **Gömöry, F., Melišek, T., Seiler, E., Šouc, J., and Usoskin, A.:** *AC loss and current sharing in an YBCO cable*, IEEE Trans. Applied Supercond. **17** (2007) 1688-1691.
- Gömöry, F., Šouc, J., Seiler, E., Klinčok, B., Vojenčiak, M., Alamgir, A.K.M., Han, Z., and Gu, Ch.:** *Performance improvement of superconducting tapes due to ferromagnetic cover on edges*, IEEE Trans. Applied Supercond. **17** (2007) 3083-3086.
- Klinčok, B., **Gömöry, F., and Dhalle, M.:** *Study of BSCCO/Ag tapes with the help of voltage signal analysis*, IEEE Trans. Applied Supercond. **17** (2007) 3129-3132.
- Gömöry, F., Šouc, J., Vojenčiak, M., Alamgir, A.K., Han, Z., and Gu, Ch.:** *Reduction of ac transport and magnetization loss of a high- T_c superconducting tape by placing soft ferromagnetic materials at the edges*, Applied Phys. Lett. **90** (2007) 092506.
- Pardo, E., **Gömöry, F., Šouc, J., and Ceballos, J.M.:** *Current distribution and ac loss for a superconducting rectangular strip with in-phase alternating current and applied field*, Supercond. Sci Technol. **20** (2007) 351-364.
- Bartolome, E., **Gömöry, F., Granados, X., Puig, T., and Obradors, X.:** *Universal correlation between critical current density and normal-state resistivity in porous $YBa_2Cu_3O_{7-x}$ thin films*, Supercond. Sci Technol. **20** (2007) 895-899.
- Gregušová, D., Stoklas, R., Čičo, K., Lalinský, T., and Kordoš, P.:** *AlGaIn/GaN metal-oxide-semiconductor heterostructure field-effect transistors with 4nm thick Al_2O_3 gate oxide*, Semicond. Sci Technol. **22** (2007) 947-951.
- Gregušová, D., Stoklas, R., Čičo, K., Heidelberg, G., Marso, M., Novák, J., and Kordoš, P.:** *Characterization of AlGaIn/GaN MOSHFETs with Al_2O_3 as gate oxide*, Physica Status Solidi c **4** (2007) 2720-2723.
- Gregušová, D., Kučera, M., Hasenöhrl, S., Vávra, I., Štrichovanec, P., Martaus, J., and Novák, J.:** *Impact of growth conditions on the spatial non-uniformities of composition in InGaP epitaxial layers*, Physica Status Solidi c **4** (2007) 1419-1422.
- Haščík, Š., Hotový, I., Lalinský, T., Vanko, G., Řeháček, V., and Mozolová, Ž.:** *Preparation of thin GaAs suspended membranes for gas microsensors using plasma etching*, Vacuum **82** (2007) 236-239.
- Holúbek, T., Dhallé, M. and Kováč, P.:** *Current transfer in MgB_2 wires with different sheath materials*, Supercond. Sci Technol. **20** (2007) 123-128.
- Huran, J., Hotový, I., Balalykin, N.I., and Starikov, A.M.:** *Physical and bonding characteristics of N-doped hydrogenated amorphous silicon carbide films grown by PECVD and annealed by pulsed electron beam*, J. Phys.: Conf. Ser. **61** (2007) 430-431.
- Kordoš, P., Gregušová, D., Stoklas, R., Čičo, K., and Novák, J.:** *Improved transport properties of Al_2O_3 /AlGaIn/GaN metal-oxide-semiconductor heterostructure field-effect transistor*, Applied Phys. Lett. **90** (2007) art. no. 123513.
- Kordoš, P., Marso, M., and Mikulics, M.:** *Performance optimization of GaAs-based photomixers as sources of terahertz radiation*, Applied Phys. A **87** (2007) 563-567.
- Áč, V. and **Korytár, D.:** *Analysis of SR thermal load studied by FEA*, Physica Status Solidi (a) **204** (2007) 2804-2828.

- Kováč, P., Hušek, I., Melišek, T., and Holúbek, T.:** *Properties of stabilized MgB₂ composite wire with Ti barrier*, Supercond. Sci Technol. **20** (2007) 771-776.
- Kováč, P., Hušek, I., Pachla, W., and Kulczyk, M.:** *Properties of seven-filament in-situ MgB₂/Fe composite deformed by hydrostatic extrusion, drawing and rolling*, Supercond. Sci Technol. **20** (2007) 607-610.
- Stenvall, A., Korpela, A., Mikkonen, R., and **Kováč, P.:** *Discrepancies in modeling magnets utilizing MgB₂ conductor with ferro- and non-magnetic matrix configurations*, IEEE Trans. Applied Supercond. **17** (2007) 2369-2372.
- Kováč, P., Hušek, I., Skákalová, V., Meyer, J., Dobročka, E., Hirscher, M., and Roth, S.:** *Transport current improvements of in-situ MgB₂ tapes by the addition of carbon nanotubes, silicon carbide or graphite*, Supercond. Sci Technol. **20** (2007) 105-111.
- Ueda, K., **Krčmár, R., Gendiar, A., and Nishino, T.:** *Corner transfer matrix renormalization group method applied to the ising model on the hyperbolic plane*, J. Phys. Soc. Japan **76** (2007) art. no. 084004.
- Pinčík, E., Kobayashi, H., Hajossy, R., Glesková, H., Takahashi, M., Jergel, Ma., Brunner, R., Ortega, L., **Kučera, M., Král, M., and Rusnák, J.:** *On interface properties of ultra-thin and very-thin oxide/a-Si:H structures prepared by oxygen based plasmas and chemical oxidation*, Applied Surface Sci **253** (2007) 6697-6715.
- Pozzovivo, G., **Kuzmík, J., Golka, S., Schrenk, W., Strasser, G., Pogany, D., Čičo, K., Ťapajna, M., Fröhlich, K., Carlin, J.-F., Gonschorek, M., Feltin, E., and Grandjean, N.:** *Gate insulation and drain current saturation mechanism in InAlN/GaN metal-oxide-semiconductor high-electron-mobility transistors*, Applied Phys. Lett. **91** (2007) 043509.
- Abermann, S., Pozzovivo, G. J., **Kuzmík, J., Strasser, G., Pogany, D., Carlin, J.-F., Grandjean, N., and Bertagnolli, E.:** *MOCVD of HfO₂ and ZrO₂ high-k gate dielectrics for InAlN/AlN/GaN MOS-HEMTs*, Semicond. Sci Technol. **22** (2007) 1272-1275.
- Kuzmík, J., Bychikhin, S., Lossy, R., Würfl, H.-J., di Forte Poisson, M.-A., Teyssier, J.-P., Gaquiere, C., and Pogany, D.:** *Transient self-heating effects in multifinger AlGaIn/GaN HEMTs with metal airbridges*, Solid-State Electronics **51** (2007) 969-974.
- Kuzmík, J., Carlin, J.-F., Gonschorek, M., Kostopoulos, A., Konstantinidis, G., Pozzovivo, G., Golka, S., Georgakilas, A., Grandjean, N., Strasser, G., and Pogany, D.:** *Gate-lag and drain-lag effects in (GaN)/InAlN/GaN and InAlN/AlN/GaN HEMTs*, Physica status solidi (a) **204** (2007) 2019.
- Kuzmík, J., Bychikhin, S., Pogany, D., Gaquiere, C., Pichonat, E., and Morvan, E.:** *Investigation of the thermal boundary resistance at the III-Nitride/substrate interface using optical methods*, J. Applied Phys. **101** (2007) 054508.
- Zanino, R., Astrov, M., Bagnasco, M., Baker, W., Belina, F., Ciazynski, D., Egorov, S., Kim, K., **Kvitkovič, J., Lacroix, B., Martovetsky, N., Mitchell, N., Muzzi, L., Nunova, Y., Okuno, K., Polák, M., Ribani, P.L., Salpietro, E., Savoldi Richard, L., Sborchia, C., Takahashi, Y., Weng, P., Wesche, R., Zani, L., and Zapretilina, E.:** *Predictive analysis of the ITER poloidal field conductor insert (PFCl) test program*, IEEE Trans. Applied Supercond. **17** (2007) 1353-1357.
- Držík, M., Chlpík, J., and **Lalinský, T.:** *Thermomechanical response of membrane-like MEMS component*, Microelectr. Engn. **84** (2007) 1274-1277.
- Jakovenko, J., Husák, M., **Lalinský, T., and Držík, M.:** *Micromechanical GaAs hot plates for Gas sensors*, Sensors & Transducers J., Special Iss. (2007) 84-92.
- Jakovenko, J., Husák, M., and **Lalinský, T.:** *Design and characterization of MEMS thermal converter*, Sensors & Transducers J., Special Iss. (2007) 101-110.
- Lobotka, P., Dérer, J., Vávra, I., de Julián Fernandez, C., Mattei, G., and Mazzoldi, P.:** *Single-electron transport and magnetic properties of Fe-SiO₂ nanocomposites prepared by ion implantation*, Phys. Rev. B **75** (2007) Art. No. 024423-1-7.

- Machajdík, D.**, Kobzev, A. P., **Hušeková, K.**, **Ťapajna, M.**, **Fröhlich, K.**, and Schram, T.: *Thermal stability of advanced gate stacks consisting of a Ru electrode and Hf-based gate dielectrics for CMOS technology*, *Vacuum* **81** (2007) 1379-1384.
- Majchrák, P.**, **Vávra, I.**, **Lobotka, P.**, **Dérer, J.**, Frait, Z., and Horváth, D.: *FMR in nanosystems – discontinuous multilayers Fe/SiO₂/Fe*, *Modern Phys. Lett. B* **21** (2007) 1201-1206.
- Majchrák, P.**, **Dérer, J.**, **Lobotka, P.**, **Vávra, I.**, Frait, Z., and Horváth, D.: *Ferromagnetic resonance study of exchange and dipolar interactions in discontinuous multilayers*, *J. Applied Phys.* **101** (2007) Art. No. 113911.
- Novák, J.**, **Hasenöhrl, S.**, **Vávra, I.**, **Sedláčková, K.**, **Kučera, M.**, and Radnóczy, G.: *Role of the V-III ratio and growth rate in decomposition of In_{0.27}Ga_{0.73}P/GaP grown by MOVPE*, *J. Crystal Growth* **298** (2007) 76-80.
- Novák, J.**, **Hasenöhrl, S.**, **Vávra, I.**, and **Kučera, M.**: *Influence of surface strain on the MOVPE growth on InGaP epitaxial layers*, *Applied Phys.* **87** (2007) 511-516.
- Reparaz, J. S., Bernardi, A., Goni, A. R., Alonso, M. I., Garriga, M., **Novák, J.**, and **Vávra, I.**: *Phonon pressure coefficient as a probe of the strain status of self-assembled quantum dots*, *Applied Phys. Lett.* **91** (2007) 081914.
- Novák, J.**, **Hasenöhrl, S.**, **Kučera, M.**, **Vávra, I.**, **Štrichovanec, P.**, Kovác, J., and Vincze, A.: *Photoluminescence and TEM characterization of (Al_yGa_{1-y})_{1-x}In_xP layers grown on graded buffers*, *Physica Status Solidi c* **4** (2007) 1503-1507.
- Osvald, J.**: *Numerical simulation of tunneling current in GaN Schottky diodes*, *J. Applied Phys.* **101** (2007) 103701.
- Osvald, J.**: *Polarization effects and energy band diagram in AlGaIn/GaN heterostructures*, *Applied Phys. A* **87** (2007) 679-682.
- Polák, M.**, **Kvitkovič, J.**, **Mozola, P.**, Barnes, P.N., and Levin, G.A.: *Characterization of individual filaments in a multifilamentary YBCO coated conductor*, *IEEE Trans. Applied Supercond.* **17** (2007) 3163-3166.
- Polák, M.**, **Kvitkovič, J.**, **Mozola, P.**, Ušák, E., Barnes, P.N., and Levin, G.A.: *Frequency dependence of hysteresis loss in YBCO tapes*, *Supercond. Sci Technol.* **20** (2007) S293-S298.
- Polák, M.**, **Kvitkovič, J.**, Formisano, A., and Martone, R.: *Impact of experimental uncertainties on the reconstruction reliability for CCIC cable current*, *Inter. J. Applied Electromagn. Mechanics* **26** (2007) 273-283.
- Sedláčková, K.**, Ujvári, T., Grasin, R., **Lobotka, P.**, Bertóti, I., and Radnóczy, G.: *C-Ti nanocomposite thin films: structure, mechanical and electrical properties*, *Vacuum* **82** (2007) 214-216.
- Sedláčková, K.**, **Lobotka, P.**, **Vávra, I.**, Czigány, Zs., Grasin, R., Ujvári, T., Bertóti, I., and Radnóczy, G.: *Structural, electrical and mechanical properties of carbon-nickel nanocomposite thin films*, *Acta Metallurgica Slovaca* **13** (2007) 168-172.
- Šoltýs, J.**, **Cambel, V.**, **Kúdela, R.**, and **Eliáš, P.**: *Study into the shape of oxide lines formed by LAO – influence an oxidized material*, *Surface Sci* **601** (2007) 2876-2880.
- Rostila, L.J., Lehtonen, J.R., Mikkonen, R., **Šouc, J.**, **Seiler, E.**, **Melišek, T.**, and **Vojenčiak, M.**: *How to determine critical current density in YBCO tapes from voltage-current measurements at low magnetic fields*, *Supercond. Sci Technol.* **20** (2007) 1097-1100.
- Šouc, J.**, **Gömöry, F.**, Klinčok, B., **Frolek, L.**, **Vojenčiak, M.**, Usoskin, A., and Rutt, A.: *AC loss measurement of the YBCO cable model*, *IEEE Trans. Applied Supercond.* **17** (2007) 1718-1721.
- Španková, M.**, **Chromík, Š.**, **Vávra, I.**, **Sedláčková, K.**, **Lobotka, P.**, Lucas, S., and Stanček, S.: *Epitaxial LSMO films grown on MgO single crystalline substrates*, *Applied Surface Sci* **253** (2007) 7599-7603.

Matkovičová, Z., Štrbik, V., Plesch, G., Valeriánová, M., and Dujavová, A.: *Tl-based superconducting films prepared by aerosol spray deposition and thallinated in an open system*, Central European J. Phys. **5** (2007) 398-404.

Nurgaliev, T., Štrbik, V., Miteva, S., Blagoev, B., Mateev, E., Neshkov, L., Beňačka, Š., and Chromik, Š.: *Electrical characteristics of HTS/manganite double layers*, Central European J. Phys. **5** (2007) 637-649.

Matkovičová, Z., Nguyen Xuan, H., Galez, Ph., Beauquis, S., Štrbik, V., and Plesch, G.: *The influence of the reaction conditions on the formation of Tl-2223 superconducting films deposited by spray pyrolysis*, J. Phys. Chemistry Solids **68** (2007) 1230-1233.

Štrichovanec, P., Kúdela, R., Vávra, I., Kováč, J., Šoltýs, J., and Novák, J.: *Characterization of corrugated MQW heterostructure prepared on patterned (001) GaAs substrate by MOVPE*, Physica Status Solidi c **4** (2007) 1499-1502.

Takács, S.: *Current transfer between superconductor and normal layer in coated conductors*, Supercond. Sci Technol. **20** (2007) 180-185.

Takács, S.: *Hysteresis losses in superconductors with an out-of-phase applied magnetic field and current: slab geometry*, Supercond. Sci Technol. **20** (2007) 1093-1096.

Takács, S.: *Low coupling losses in YBa₂Cu₃O₇ coated conductors with current sharing between the superconducting stripes*, Applied Phys. Lett. **90** (2007) art. no. 242505.

Takács, S.: *Coupling losses in superconductors with twisted filaments, stripes, or striations*, IEEE Trans. Applied Supercond. **17** (2007) 3151-3154.

Ťapajna, M., Rosová, A., Hušeková, K., Roozeboom, F., Dobročka, E., and Fröhlich, K.: *Evidence of hafnia oxygen vacancy defects in MOCVD grown Hf_xSi_{1-x}O_y ultrathin gate dielectrics gated with Ru electrode*, Microelectr. Engn. **84** (2007) 2366-2369.

Ušák, P., Polák, M., Demenčík, E., Kvitkovič, J., Levin, G.A., and Barnes, P.N.: *The current distribution in a striated YBCO tape subjected to both a magnetization and a transport current*, Supercond. Sci Technol. **20** (2007) 994-1001.

Ušák, P., Polák, M., and Demenčík, E.: *Current distribution in thermally degraded superconductor of 2nd generation*, Physica C **455** (2007) 67-70.

Vagovič, P., Korytár, D., Mikulík, P., and Ferrari, C.: *On the design of a monolithic 4-bounce high resolution X-ray monochromator*, Nuclear Instr. Methods in Phys. Res. B **265** (2007) 599-604.

Misiuk, A., Surma, B., Bak-Misiuk, J., Londos, C.A., Vagovič, P., Kovacevic, I., Pivac, B., Jung, W., and Prujarczyk, M.: *Revealing the radiation-induced effects in silicon by processing at enhanced temperatures–pressures*, Radiation Measurements **42** (2007) 688-692.

Valeriánová, M., Odier, P., Chromik, Š., Štrbik, V., Polák, M., and Kostič, I.: *Influence of the buffer layer on the growth of superconducting films based on mercury*, Supercond. Sci Technol. **20** (2007) 900-903.

Valeriánová, M., Chromik, Š., Odier, P., and Štrbik, V.: *Role of the mercury pressure during reaction synthesis of Hg(Re)-based superconducting films*, Central European J. Phys. **5** (2007) 446-456.

Vanko, G., Lalinský, T., Mozolová, Ž., Liday, J., Vogrinčič, P., Vincze, A., Uherek, F., Haščík, Š., and Kostič, I.: *Nb-Ti/Al/Ni/Au based ohmic contacts to AlGaIn/GaN*, Vacuum **82** (2007) 193-196.

Aliev, F.G., Guerrero, R., Pryadun, V., Villar, R., Cebollada, A., Anguita, J., Schad, R., and Vávra, I.: *Enhanced magnetic viscosity at low temperatures in [Fe/Cr(0 0 1)]₁₀ multilayers*, J. Magnetism Magnetic Mater. **316** (2007) 344-347.

Závišová, V., Koneracká, M., Štrbák, O., Tomašovičová, N., Kopčanský, P., Timko, M., and Vávra, I.: *Encapsulation of indomethacin in magnetic biodegradable polymer nanoparticles*, J. Magnetism Magnetic Mater. **311** (2007) 379–382.

Zat'ko, B., Dubecký, F., Ščepko, P., Mudroň, J., and Stranovský, I.: *Imaging performance study of the quantum X-ray scanner based on GaAs detectors*, Nuclear Instr. and Methods in Phys. Res. A **576** (2007) 66-69.

Zat'ko, B., Dubecký, F., Procházková, O., and Nečas, V.: *Role of electrode metallization in the performance of bulk semi-insulating InP radiation detectors*, Nuclear Instr. and Methods in Phys. Res. A **576** (2007) 98-102.

2008

Boháček, P., Zat'ko, B., Dubecký, F., Chromik, Š., Huran, J., and Sekáčová, M.: *Role of new ohmic electrode metallization in detection performance of bulk semi-insulating GaAs radiation detectors*, Nuclear Instr. and Methods in Phys. Res. A **591** (2008) 105-108.

Cambel, V., Martaus, J., Šoltýs, J., Kúdela, R., and Gregušová, D.: *Local anodic oxidation by AFM tip developed for novel semiconductor nanodevices*, Ultramicroscopy **108** (2008)1021-1024.

Beňo, J., Weis, M., Dobročka, E., and Haško, D.: *Mixed 2D molecular systems: Mechanic, thermodynamic and dielectric properties*, Applied Surface Sci **254** (2008) 6370-6375.

Ryć, L., Dobrzański, L., Dubecký, F., Kaczmarczyk, J., Pfeifer, M., Riesz, F., Słysz, W., and Surma, B.: *Application of MSM InP detectors to the measurements of pulsed x-ray radiation*, Radiation Effects Defects in Solids **163** (2008) 559-567.

Feilhauer, J. and Moško, M.: *Persistent current in a disordered mesoscopic ring with many channels: Scattering-matrix based calculation*, Physica E **40** (2008) 1582.

Fröhlich, K., Ťapajna, M., Rosová, A., Dobročka, E., Hušeková, K., Aarik, J, and Aidla, A.: *Growth of high-dielectric-constant TiO₂ films in capacitors with RuO₂ electrodes*, Electrochem. Solid-State Lett. **11** (2008) G19-G21.

Frolek, L., Gömöry, F., and Seiler, E.: *A special sample holder for AC susceptibility measurements of superconducting samples in high magnetic fields at various temperatures*, Supercond. Sci Technol. **21** (2008) 105009.

Frolek, L., Oravec, J., and Šouc, J.: *Impulse measurement of dynamic current-voltage curves of superconducting tape at various lengths and shapes of current waves*, J. Phys. - Conf. Series **97** (2008) 012085.

Gendiar, A., Krčmár, R., Ueda, K., and Nishino, T.: *Phase transition of clock models on a hyperbolic lattice studied by corner transfer matrix renormalization group method*, Phys. Rev. E **77** (2008) art. no. 041123.

Gömöry, F., Vojenčiak, M., Šouc, J., and Seiler, E.: *Influence of ferromagnetic layer on critical current of a superconducting wire*, Acta Physica Polonica **113** (2008) 605-608.

Gömöry, F., Šouc, J., Seiler, E., Vojenčiak, M., and Granados, X.: *Modification of critical current in HTSC tape conductors by a ferromagnetic layer*, J. Phys. - Conf. Series **97** (2008) 012096.

Donoval, D., Florovič, M., Gregušová, D., Kováč, J., and Kordoš, P.: *High temperature performance of AlGaIn/GaN HFETs and MOSHFETs*, Microelectron. Reliab. **48** (2008) 1669.

Holúbek, T., Kováč, P., and Hušek, I.: *Relation between current transfer length and stability of Fe/ MgB₂ and Fe/Nb/MgB₂ conductors*, Acta Physica Polonica A **113** (2008) 367-370.

Holúbek, T., Kováč, P., Takács, S., Hušek, I., and Melišek, T.: *Current sharing and the stability of composite MgB₂ superconductors*, Supercond. Sci Technol. **21** (2008) art. no. 065013.

Hušek, I. and Kováč, P.: *Filament and interface structure of in-situ MgB₂ wires*, J. Phys. - Conf. Series **97** (2008) 012106.

Chromik, Š., Španková, M., Vávra, I., Liday, J., Vogrinčič, P., and Lobotka, P.: *Preparation and structural properties of MgO films on GaAs substrate*, Applied Surface Sci **254** (2008) 3635-3637.

Chromik, Š., Valeriánová, M., Štrbik, V., Gaži, Š., Odier, P., Li, X., Xu, Y., Sobolewski, R., Hanic, F., Plesch, G., and Beňačka, Š.: *Hg-based cuprate superconducting films patterned into structures for ultrafast photodetectors*, Applied Surface Sci **254** (2008) 3638-3641.

Kopera, L., Kováč, P., and Melišek, T.: *Electromechanical characterization of selected superconductors*, Supercond. Sci Technol. **21** (2008) art. no. 115001.

Kopera, L., Šmatko, V., Prusset, W., Polák, M., Semerad, R., Štrbik, V., and Šouc, J.: *In situ patterning of filamentary YBCO coated conductors*, Physica C **468** (2008) 2351-2355.

Kordoš, P., Donoval, D., Florovič, M., Kováč, J., and Gregušová, D.: *Investigation of trap effects in AlGaIn/GaN field-effect transistors by temperature dependent threshold voltage analysis*, Applied Phys. Lett. **92** (2008) art. no. 152113.

Kordoš, P., Gregušová, D., Stoklas, R., Gaži, Š., and Novák, J.: *Transport properties of AlGaIn/GaN metal-oxide-semiconductor heterostructure field-effect transistors with Al₂O₃ different thickness*, Solid-State Electr. **52** (2008) 973-979.

Mikulics, M., Marso, M., Wu, S., Fox, A., Lepsa, M., Grützmacher, D., Sobolewski, R., and **Kordoš, P.:** *Sensitivity enhancement of metal-semiconductor-metal photodetectors on low-temperature-grown GaAs using alloyed contacts*, IEEE Photon. Technol. Lett. **20** (2008) 1054.

Florovič, M., **Kordoš, P.**, Donoval, D., **Gregušová, D.**, and Kováč, J.: *Performance of AlGaIn/GaN heterostructure field – effect transistors at higher ambient temperatures*, J. Electr. Engn. **59** (2008) 53-56.

Korytár, D., Ferrari, C., Mikulík, P., Germini, F., Vagovič, P., and Baumbach, T.: *High resolution 1D and 2D crystal optics based on asymmetric diffractors*. In: Modern Developments in X-Ray and Neutron Optics. Series: Springer Series in Optical Sciences, Vol. 137. Eds. Erko, A. et al. Berlin: Springer 2008. ISBN: 978-3-540-74560-0. P. 501-512.

Áč, V., Perichta, P., **Korytár, D.**, and Mikulík, P.: *Thermal effects under synchrotron radiation power absorption*. In: Modern Developments in X-Ray and Neutron Optics. Series: Springer Series in Optical Sciences, Vol. 137. Eds. Erko, A. et al. Berlin: Springer 2008. ISBN: 978-3-540-74560-0. P. 513-524.

Kováč, P., Pachla, W., **Hušek, I.**, Kulczyk, M., **Melišek, T.**, **Holúbek, T.**, Diduszko, R., and Reissner, M.: *Multicore MgB₂ wires made by hydrostatic extrusion*, Physica C **468** (2008) 2356- 2360.

Kováč, P., **Hušek, I.**, and **Melišek, T.:** *MgB₂ cable made from two-axially rolled wires*, Supercond. Sci Technol. **21** (2008) 125003.

Zola, D., Polichetti, M., Adesso, M.G., **Kováč, P.**, Martini, L., and Pace, S.: *Thermomagnetic instability and critical current density in MgB₂ monofilamentary tapes*, Physica C **468** (2008) 761-764.

Kováč, P., Birajdar, B., **Hušek, I.**, **Holúbek, T.**, and Eibl, O.: *Stabilized in situ rectangular MgB₂ wires: the effect of B purity and sheath materials*, Supercond. Sci Technol. **21** (2008) 045011.

Kováč, P., **Hušek, I.**, **Dobročka, E.**, **Melišek, T.**, Haessler, W., and Herrmann, M.: *MgB₂ tapes made of mechanically alloyed precursor powder in different metallic sheaths*, Supercond. Sci Technol. **21** (2008) 015004.

- Krčmár, R.**, Iharagi, T., **Gendiar, A.**, and Nishino, T.: *Tricritical point of the J_1 - J_2 Ising model on a hyperbolic lattice*, Phys. Rev. E **78** (2008) art. no. 061119.
- Krčmár, R.**, **Gendiar, A.**, Ueda, K., and Nishino, T.: *Ising model on a hyperbolic lattice studied by the corner transfer matrix renormalization group method*, J. Phys. A **41** (2008) art. no. 125001.
- Krčmár, R.**, **Gendiar, A.**, **Moško, M.**, **Németh, R.**, Vagner, P., and Mitas, L.: *Persistent current of correlated electrons in mesoscopic ring with impurity*, Physica E **40** (2008) 1507-1509.
- Pinčík, E., Brunner, R., Kobayashi, H., Takahashi, M., and **Kučera, M.**: *Photoluminescence of very thin oxide/a-Si:H structures passivated in HCN solutions*, Appl. Surf. Science **254** (2008) 3710-3714.
- Pinčík, E., Kobayashi, H., Brunner, R., Takahashi, M., **Kučera, M.**, Rusnák, J., and Jergel, M.: *Electrical, optical and structural properties of different Si-based structures prepared on a-Si:H/c-Si, porous Silicon/c-Si, and c-Si*, Metallurg. Analysis **28** Suppl. 2 (2008) 1229-1237.
- Brunner, R., Kobayashi, H., **Kučera, M.**, Takahashi, M., Jergel, M., and Pinčík, E.: *On the relation between structural and photoluminescence properties of passivated a-Si:H / glass samples*, Metallurg. Analysis **28** Suppl. 2 (2008) 1248-1253.
- Kuzmík, J.**, Pozzovivo, G., Abermann, S., Carlin, J.-F., Gonschorek, M., Feltin, E., Grandjean, N., Bertagnolli, E., Strasser, G., and Pogany, D.: *Technology and performance of InAlN/AlN/GaN HEMTs with gate insulation and current collapse suppression using ZrO_2 or HfO_2* , IEEE Trans Electron Devices **55** (2008) 937-941.
- Pozzovivo, G. J., **Kuzmík, J.**, Golka, K., **Čičo, K.**, **Fröhlich, K.**, Carlin, J.-F., Gonschorek, M., Grandjean, N., Schrenk, G., Strasser, W., and Pogany, D.: *Influence of GaN capping on performance of InAlN/AlN/GaN MOS-HEMT with Al_2O_3 gate insulation grown by CVD*, Physica Status Solidi c **5** (2008) 1956-1958.
- Kvitkovič, J.**, **Polák, M.**, and **Mozola, P.**: *Distribution of magnetic field inside the winding of a BSCCO coil*, IEEE Trans. Applied Supercond. **18** (2008) 1621-1624.
- Lalinský, T.**, Rufer, L., **Vanko, G.**, Mir, S., **Haščík, Š.**, **Mozolová, Ž.**, Vincze, A., and Uherek, F.: *AlGaIn/GaN heterostructure based surface acoustic wave structures for chemical sensors*, Applied Surface Sci **255** (2008) 712-714.
- Hotový, I., Řeháček, V., Mika, F., **Lalinský, T.**, **Haščík, Š.**, **Vanko, G.**, and Držík, M.: *Gallium arsenide suspended microheater for MEMS sensor arrays*, Microsyst. Technol. **14** (2008) 629-635.
- Lalinský, T.**, Držík, M., Jakovenko, J., **Vanko, G.**, **Mozolová, Ž.**, **Haščík, Š.**, Chlpík, J., Hotový, I., Řeháček, V., Kostič, I., Matay, L., and Husák, M.: *GaAs based micromachined thermal converter for gas sensors*, Sensors Actuators A **142** (2008) 147-152.
- Martaus, J.**, **Gregušová, D.**, **Cambel, V.**, **Kúdela, R.**, and **Šoltýs, J.**: *New approach to local anodic oxidation of semiconductor heterostructures*, Ultramicroscopy **108** (2008) 1086-1089.
- Mošková, A.**, **Moško, M.**, and **Gendiar, A.**: *Possible persistent current in a ring made of the perfect crystalline insulator*, Physica E **40** (2008) 1991-1993.
- Indlekofer K. M., **Németh, R.**, and Knoch J.: *Many-body approach to the terahertz response of Wigner molecules in gated nanowire structures*, Phys.Rev. B **77** (2008) 125436.
- Németh, R.** and **Moško, M.**: *One-dimensional ring with Kronig–Penney periodic potential: Persistent currents at full filling*, Physica E **40** (2008) 1498.
- Osvald, J.**: *Numerical analysis of gate leakage current in AlGaIn Schottky diodes*, Applied Surface Sci **255** (2008) 793-795.

Srnánek, R., Irmer, G., Donoval, D., **Osvald, J.**, McPhail, D., Christoffi, A., Sciana, B., Radziewicz, D., and Tlaczala, M.: *Application of micro-Raman spectroscopy for the evaluation of doping profile in Zn δ -doped GaAs structures*, Microelectr. J. **39** (2008) 1439-1443.

Pardo, E.: *Modeling of coated conductor pancake coils with a large number of turns*, Supercond. Sci Technol. **21** (2008) art. no. 065014.

Polák, M., Barnes, P.N., **Kvitkovič, J.**, Levin, G.A., **Mozola, P.**, and **Ušák, P.**: *Properties of an experimental coil wound with YBCO coated conductor carrying an AC current with frequencies up to 864 Hz*, IEEE Trans. Applied Supercond. **18** (2008) 1240-1244.

Sedláčková, K., Grasin, R., and Radnóczy, G.: *Carbon – metal (Ni, Ti) nanocomposite films as protective coatings*. In: New Research on Nanocomposites. Eds. Luis M. et al. ISBN 10: 1604567996. Nova Sci Pub Inc. 2008. P. 223-246.

Balázsi, C., Ionescu, R., and **Sedláčková, K.**: *Hexagonal WO_3 films with carbon nanotubes for sensing applications*, Materials Sci Forum **589** (2008) 67-71.

Balázsi, C. Bishop, A. Yang, J., **Sedláčková, K.**, Wéber, F., and Gouma, P.I.: *Biopolymer-hydroxyapatite nanocomposite from eggshell for prospective surgical applications*, Materials Sci Forum **589** (2008) 61-65.

Seiler, E. and **Frolek, L.**: *AC susceptibility of the $YBa_2Cu_3O_7$ coated conductor in high magnetic fields*, Acta Physica Polonica **113** (2008) 379-382.

Seiler, E. and **Frolek, L.**: *AC loss of the YBCO coated conductor in high magnetic fields*, J. Phys. - Conf. Series **97** (2008) 012028.

Stoklas, R., **Gregušová, D.**, **Novák, J.**, Vescan, A., and **Kordoš, P.**: *Investigation of trapping effects in AlGaIn/GaN/Si field-effect transistors by frequency dependent capacitance and conductance analysis*, Applied Phys. Lett. **93** (2008) art. no. 124103.

Stoklas, R., **Gaži, Š.**, **Gregušová, D.**, **Novák, J.**, and **Kordoš, P.**: *Enhancement of effective carrier velocity in AlGaIn/GaN MOSHFETs with Al_2O_3 gate oxide*, Physica Status Solidi c **5** (2008) 1935-1937.

Šouc, J., **Gömöry, F.**, **Vojenčiak, M.**, **Frolek, L.**, Isfort, D., Ehrenberg, J., and Bock, J.: *AC loss of the short coaxial superconducting cable model made from ReBCO coated tapes*, J. Phys. - Conf. Series **97** (2008) 012198.

Šouc, J., **Gömöry, F.**, **Vojenčiak, M.**, and **Frolek, L.**: *DC characterization of the coaxial superconducting cable*, Acta Physica Polonica A **113** (2008) 375-378.

Takács, S.: *Acceptable coupling losses in coated conductors at industrial frequencies without twisting the superconducting stripes*, J. Applied Phys. **103** (2008) art. no. 053907.

Paskaleva, A., **Ťapajna, M.**, Atanassova, E., **Fröhlich, K.**, Vincze, A., and **Dobročka, E.**: *Effect of Ti doping on Ta_2O_5 stacks with Ru and Al gates*, Applied Surface Sci **254** (2008) 5879-5885.

Ťapajna, M., **Rosová, A.**, **Dobročka, E.**, **Štrbik, V.**, **Gaži, Š.**, **Fröhlich, K.**, Benko, P., Harmatha, L., Manke, C., and Baumann, P.K.: *Work function thermal stability of RuO_2 -rich Ru-Si-O p-channel metal-oxide-semiconductor field-effect transistor gate electrodes*, J. Applied Phys. **103** (2008) art. no. 073702.

Ušák, P., **Polák, M.**, **Kvitkovič, J.**, **Mozola, P.**, Barnes, P.N., and Levin, G.A.: *Current distribution in the winding of a superconducting coil*, IEEE Trans. Applied Supercond. **18** (2008) 1597-1600.

Kadlečíková, M., Breza, J., Jesenák, K., Pastorková, K., Luptáková, V., Kolmačka, M., Vojačková, A., Michalka, M., **Vávra, I.**, and **Křižanová, Z.**: *The growth of carbon nanotubes on montmorillonite and zeolite (clinoptilolite)*, Applied Surface Sci **254** (2008) 5073-5079.

Timko, M., Džarová, A., Kopčanský, P., Závěšová, V., Konečná, M., Kováč, J., Šprincová, A., Vaclavíková, M., Ivaničová, L., and **Vávra, I.**: *Magnetic properties of magnetite formed by biomineralization and chemical synthesis*, Acta Physica Polonica A **113** (2008) 573-576.

Gregor, M., Mičunek, R., Plecenik, T., Roch, T., Lugstein, A., Bertagnolli, E., **Vávra, I.**, Štefečka, M., Kubinec, M., Leporis, M., Gašparík, V., Kúš, P., and Plecenik, A.: *Nano – bridges based on the superconducting MgB_2 thin films*, Physica C **468** (2008) 785-788.

Timko, M., Džarová, A., Závěšová, V., Konečná, M., Šprincová, A., Kopčanský, P., Kováč, J., **Vávra, I.**, and Szlaferek, A.: *Magnetic properties of bacterial magnetosomes and chemosynthesized magnetite nanoparticles*, Magnetohydrodyn. **44** (2008) 113-120.

Džarová, A., Timko, M., Šprincová, A., Kopčanský, P., Kováč, J., Konečná, M., Vaclavíková, M., and **Vávra, I.**: *Formation of magnetic properties of magnetosomes*, Mater. Struct. Chemistry, Biology, Phys. Technol. **15** (2008) 10.

Korenko, M., Kucharík, M., **Vincenc Oboňa, J.**, Janičkovič, D., Córdoba, R., De Teresa, J. M., and Kubíková, B.: *Nanotubes made from deeply undercooled cryolite/alumina melts*, Helvetica Chimica Acta **91** (2008) 1389-1399.

Vojenčíak, M., Šouc, J., Gömöry, F., and Seiler, E.: *Influence of DC magnetic field on AC loss of YBCO coated conductor with ferromagnetic substrate*, Acta Physica Polonica A **113** (2008) 359-361.

Zaťko, B., Dubecký, F., Štěpko, P., Grybos, P., Mudroň, J., Maj, P., Szczygiel, R., and Frollo, I.: *On the detection performance of semi-insulating GaAs detectors coupled to multichannel ASIC DX64 for X-ray imaging applications*, Nuclear Instr. and Methods in Phys. Res. A **591** (2008) 101-104.





INSTITUTE OF ELECTRICAL ENGINEERING

Slovak Academy of Sciences
Dúbravská cesta 9
841 04 Bratislava
Slovak Republic

Phone: (421 2) 54 77 58 06

Fax: (421 2) 54 77 58 16

<http://www.elu.sav.sk>